Self-assembly of hybrid microgels for interferential and responsive photonic applications

Nicolas Benoot

THÈSE

UNIVERSITÉ DE PAU ET DES PAYS DE L'ADOUR

École doctorale des Sciences Exactes et leurs Applications

Soutenue le 15 septembre 2020

par **Nicolas BENOOT**

Pour obtenir le grade de docteur

De l'Université de Pau et des Pays de l'Adour

Spécialité : Physico-Chimie des Polymères

Self-assembly of hybrid microgels for interferential and responsive photonic applications

MEMBRES DU JURY

RAPPORTEURS

- Elodie BOURGEAT-LAMI — Directrice de Recherche CNRS / C2P2 Laboratory, Lyon
- Virginie PONSINET — Directrice de Recherche CNRS / Centre de Recherche Paul Pascal, Pessac

EXAMINATEURS

- Valérie ALARD — Responsable Innovation Matériaux / LVMH Recherche, St Jean-de-Braye
- Kamel CHOUGRANI — Responsable Pôle Polymère / LVMH Recherche, St Jean-de-Braye
- Stéphanie REYNAUD — Directrice de Recherche / Université de Pau et des Pays de l'Adour, Pau

DIRECTEUR

- Laurent BILLON — Professeur / Université de Pau et des Pays de l'Adour, Pau

A mon épouse, mon fils,

ma famille, mes amis, à tous ceux qui ont été présents et bienveillants,

Ces travaux n'auraient jamais eu cette couleur sans vous.

Remerciements

A mes respectueux rapporteurs qui m'ont fait l'honneur de relire mes travaux, et pour leurs commentaires constructifs et pertinents.

A mes passionnés examinateurs pour leurs vifs intérêts et leurs questions ayant fait de cette soutenance un riche moment d'échange.

Je tiens particulièrement à remercier *l'Ecole Doctorale Sciences Exactes et Appliquées de l'UPPA* pour son accompagnement, l'*IPREM* pour son accueil mais surtout le centre *LVMH Recherche* qui a permis en collaboration avec l'*ANRT* le financement de ce projet de thèse ambitieux et passionnant. Ce fut une chance et un honneur d'être partie prenante de cette aventure.

Etudiant ayant soif d'apprendre, j'ai eu la chance d'être accueilli et guidé, me voyant offrir le cadre rigoureux indispensable à des résultats concrets et la possibilité d'expérimenter librement. *Laurent*, pour ton soutien, ta vision éclairée et tes précieux conseils, ces quelques lignes ne résument que maladroitement ma gratitude et mon profond respect.

A *Adèle* et *Eva* avec qui j'ai eu le bonheur de partager un bureau rempli d'excellents souvenirs (et de nos magnifiques plantes !).

A mes compagnons de route, *Guillaume, Thibault, Ahmed, Emile, Laura, Coste*, et ceux dont les noms ne sont pas cités ici mais que je garde chaleureusement en mémoire.

A ceux sans qui la vie au laboratoire n'aurait pas été la même, merci à *Virginie* pour sa passion communicative et les heures passées ensembles en AFM, *Saadia* pour ses précieux éclairages, *Laurence* pour ta sympathie et ta générosité, *Pierre* pour ton audace, ta créativité et ton acuité scientifique source d'inspiration.

Les derniers mots reviennent à ma moitié, mon épouse, sans qui je ne serai pas devenu celui que je suis et à notre fils, qui m'aura fait le bonheur et la fierté d'être présent pour ma soutenance.

Introduction

Into the changing industrial context of skincare and cosmetic, the necessity of preventing the next formulation constraints has never been truer than today. Taking its source in nature, “structural coloration” is bio-inspired from specimen as butterfly and chameleon which present “photonic crystals” interfering with visible light and producing colors without pigments. Nowadays, mineral pigments are the main source of colors in cosmetic application, their replacement is a critical challenge to limit the exposure of the nanometric objects that may be hazardous. Concomitantly, innovation is written in the DNA of the skincare and cosmetic market, with a constant need of renewal. The elaboration of easy in hand “photonic crystals” may develop the possibility of iridescent and responsive colored skincare products.

Open to these concerns, the company LVMH Perfumes & Cosmetics leader in the luxury sector has collaborated with the IPREM lab from the University of Pau and Pays de l’Adour and CNRS, through successive collaborations. They have led to the elaboration of an innovative and biocompatible material which is here the objects of development for making structural colors.

Thence, the purpose of this thesis settles in the line of previous works a material presenting a dual pH- and thermo- responsiveness made of biocompatible microgels based on oligo(ethylene glycol) copolymers[1,2]. These microgels have shown their encapsulating properties with hydrophobic and hydrophilic materials allowing their uses as delivery systems for skincare applications[3–5]. Moreover, the films produced thanks to the simple evaporation of the aqueous solvent exhibit two exciting properties. First, an outstanding cohesion of the films in the dried or wet state. Second, an excellent self-assembling property of the microgels leading to organized structures in space[6,7]. This outstanding cohesion has been identified as a consequence of the microgels entanglement after drying[8]. Nevertheless, the second pointed property of these microgel raise a question: *Would it be possible to develop the self-assembling properties of the microgels to make dried photonic*

crystal, with controllable and responsive interferential colors toward the conception of a skincare application?

Herein we intend to integrate the microgel material into the design of a colloidal sphere for the elaboration of films with responsive and iridescent coloration. Keeping in mind the development of a skincare product, a substantial attention is brought on the transferability of the synthesis process and the coloring technology toward an industrial scale and home use, respectively. Furthermore, a particular interest is carried on the understanding of the self-assembly mechanism and the relation between the colloidal arrangement and the coloring properties.

The first chapter present a bibliographic overview about the bio-inspiration behind the structural coloration concepts, and the ways to artificially mimic such optical properties. A first part is dedicated to the comprehension and the definition of the physical concepts related to photonic crystal. The second part focuses on the synthetic ways to reproduce them, especially through the self-assembly of colloidal building blocks (**BBs**) by solvent evaporation. Potential synthetic methods to integrate the microgel material into a colloidal BBs are described

The second chapter is dedicated to the effective conception of hybrid BBs integrating the multi-responsive microgel. Seeded precipitation polymerization methods are discussed for the conception of different colloidal designs. Firstly, the syntheses of core-interlayer-shell particles (**CIS**) are investigated, made of a *polystyrene* (**PS**) core surrounded by an interlayer of *poly(butyl acrylate)* (**PBA**) and a shell of *poly(oligo(ethylene glycol) methacrylate)* (**POEGMA**) based microgel. Secondly, a simpler core-shell (**CS**) design of PS core surrounded by a shell of POEGMA-based microgel is presented. A specific attention is led on the confirmation on the morphological control of the designed colloids, especially through the grafting rate evaluation of the POEGMA phase.

The third chapter covers the experimental tuneability as well as the responsiveness of the films' colors and is related to the characteristics of the colloidal self-assemblies. The characterization of the photonic crystals allows an identification of the three-dimensional crystalline structure, opening the

discussion about the self-assembly mechanism. This section ends with prospective modifications on the POEGMA-based copolymer composition and on the core size to evaluate the consequences on the optical properties.

The fourth chapter focuses on an applied point of view, with the evaluation of formulation attempts to elaborate a skincare formulation. In a first part, the perturbating roles of essential additives on the structural color formation is probed. In a second part, a control on the casting conditions of the hybrid microgel suspension is performed with a specific interest on the raise of the suspension's concentrations and viscosities, and their limiting effects on the self-assembly mechanism.

As nano"plastics" are an emerging societal concern appearing in this PhD work, *the fifth chapter* suggest a novel hybrid colloidal design as perspective that could overcome both 1) the spontaneous self-assembly limitations and 2) the colloids becoming and environmental impact in the context of a skincare application.

Finally, details about characterization/synthesis technics and methods are described in appendix.

1. Boularas, M. Synthèse de microgels hybrides, biocompatibles et stimulables pour des applications cosmétiques. (Université de Pau et des Pays de l'Adour, 2015).
2. Boularas, M., Gombart, E., Tranchant, J.-F., Billon, L. & Save, M. Design of Smart Oligo(ethylene glycol)-Based Biocompatible Hybrid Microgels Loaded with Magnetic Nanoparticles. *Macromolecular Rapid Communications* **36**, 79–83 (2015).
3. Aguirre, G. *et al.* Versatile oligo(ethylene glycol)-based biocompatible microgels for loading/release of active bio(macro)molecules. *Colloids and Surfaces B: Biointerfaces* **175**, 445–453 (2019).
4. Aguirre, G. *et al.* Smart self-assembled microgel films as encapsulating carriers for UV-absorbing molecules. *Polym. Chem.* **9**, 1155–1159 (2018).
5. Aguirre, G., Khoukh, A., Chougrani, K., Alard, V. & Billon, L. Dual-responsive biocompatible microgels as high loaded cargo: understanding of encapsulation/release driving forces by NMR NOESY. *Polym. Chem.* **9**, 757–768 (2018).
6. Boularas, M. *et al.* Dual stimuli-responsive oligo(ethylene glycol)-based microgels: insight into the role of internal structure in volume phase transitions and loading of magnetic nanoparticles to design stable thermoresponsive hybrid microgels. *Polym. Chem.* **7**, 350–363 (2016).

7. Boularas, M. *et al.* Functional film by trigger-free self-assembly of adhesive soft microgels at skin temperature. *Materials & Design* **147**, 19–27 (2018).
8. Dieuzy, É. Relationship between structural and rheological properties of dual-stimuli responsive microgel films for cosmetic and biomedical applications. (Université de Pau et des Pays de l'Adour, 2019).

Glossary

Chemical compounds

EGDMA: (ethylene glycol) dimethacrylate
MBA: N,N-methylenebisacrylamide
SDS: Sodium dodecyl sulfate
DVB: Divinyl benzene
PEG: poly(ethylene glycol)
KPS: potassium persulfate
POEGMA: poly(oligo ethylene glycol methacrylate)
MAA: methacrylic acid
PMMA: poly(methyl methacrylate)
MEO_2MA: 2-(2-methoxyethoxy) ethyl methacrylate
S: Styrene
BuA: *n*-butylacrylate
PNIPAM: poly(N-isopropyl acrylamide)
NIPAM: N-isopropylacrylamide
PBA: poly(*n*-butyl acrylate)
OEGDA: oligo(ethylene glycol) diacrylate
PS: polystyrene
OEGMA: oligo(ethylene glycol) methacrylate
SiO_2: Silicon dioxide or Silica
MPS: 3-methacryloxypropyl trimethoxysilane

Characterization techniques

AFM: Atomic Force Microscopy
SLS: Static Light Scattering
DLS: Dynamic Light Scattering
FTIR-ATR: Fourier Transform InfraRed Spectroscopy
DSC: Differential Scanning Calorimetry
TGA: ThermoGravimetric Analysis
NMR: Nuclear Magnetic Resonance Spectroscopy
TEM: Transmission Electron Microscopy
SEM: Scanning Electron Microscopy
UV-Vis: UltraViolet-Visible Spectroscopy

Acronyms and symbols

En: Energy

h: Planck constant

c: Celerity of light

λ: Wavelength

n: Refractive index of material

θ: angle between incident light and normal to the surface

Q: scattering efficiency

a: lattice parameter

b: reciprocal lattice parameter

E: Electric field

H: Magnetic field

ω: Electromagnetic pulsation

ε: Dielectric permittivity

t: Time

$\vec{\mathbf{r}}$: Position vector

$\vec{\mathbf{k}}$: Wave vector

$\mathbf{d_{hkl}}$: Distance between the the family of Reticular plan h,k,l

V: Volume

D: Diameter

BCP: Block copolymer

χ: Flory-Huggins interaction parameter

N: Degree of polymerization

BB: Building Block

CNC: Cellulose nanocrystal

$\mathbf{k_b}$: Boltzmann constant

T: Temperature

m: Mass

A: Hamaker constant

κ: Double layer thickness

$\mathbf{c_0}$: Ion concentration

e: Electronic charge

Φ: Surface potential

z: Valence of counter ions

I: Intensity

r: Separation between particles

$\Delta \boldsymbol{H_{mix}}$: Enthalpic mixing difference

$\Delta \boldsymbol{S_{mix}}$: Entropic mixing difference

k: Number of layers

U: Withdrawal rate

φ: Particle volume fraction

j_e: *Solvent evaporation rate*

ΔG: Free enthalpic difference

g: Acceleration from gravity

σ : Surface tension

Pe: Peclet number

$\mathbf{V_{DLVO}}$: DLVO potential

R: particle radius

CMC: Critical micellar concentration

VPTT: Volume phase transition temperature

Tg: Glass transition temperature

CS: Core-shell

CIS: Core-interlayer-shell

Abs: Absorbance

wt%: Weight percentage

vol%: Volume percentage

l%: Length percentage

EM: Electromagnetic

Dh: Hydrodynamic diameter

Chapter I: Bibliographic analysis

Introduction

Color is an important part of our daily perception of the world and found a critical value in plenty of objects constituting our environment. In the light of this, the discovery of news ways to make colors comes a key issue in the development of innovative products. As always, Nature is a wonderful source of inspiration, proposing multiples examples of specimens, embellished with fascinating colors. In this part, we will firstly investigate the secrets behind the apparition of such iridescent, and sometime responsive colorations. After a brief overview of the processes behind the light/matter interactions, we will expose the different ways to mimic those natural materials.

1. Structural colors: from the Nature to its understanding

In the nature, several species display intriguing colors, being red from a certain observation angle, or maybe green from another one. This angle-dependence of the coloration, or iridescence, has pushed the scientific community to set up new characterization technics. With the emergence of the electronic microscopy in the 1930s', new possibilities came to investigate the intimate architecture of such colored materials. It appeared then these iridescent colorations were systematically associated with well-organized arrays in space[1,2], with repeating units between 1 to 1000 nm, typically in the same range as the colloidal scale. Few decades later, Yablonovitch and John published the first works[3–5] that would described for the first time the concept of photonic bandgap and set a milestone to the formalism of this kind of structures, nowadays called photonic crystals.

But before entering in such details, we have to define what's color and what are the light-matter interactions involved in the production of colored light.

1.1. *Structural colors: bio-inspired concept*

From the material design point of view, there are many elements to bring together to attain such complex optical effects: the reflecting elements must be on a subwavelength scale, need to be produced on large distance, and must be sufficiently ordered to produce the desired color and reflectivity. According to the

dimensions in which the material is ordered, three main classes of architecture producing these "structural colors" are distinguished.

1.1.1. One-dimensional natural Photonic crystal

Many insects of the Coleoptera order display impressive structural colors, which often have a metallic appearance[6]. The wood-boring beetle *Chrysochroa fulgidissima*, from the family of *Buprestidae*, better known as the ''Japanese jewel beetle'', is found in the woods and forests of Japan during summer.

The shell of this beetle shows a remarkable metallic iridescence on its elytra, *i.e.*, the hardened forewings of beetles that protect the hindwings, which are used for flying (Figure 1*a* - *up*). The structure responsible for the bright iridescent colors is a multilayer arrangement in the epicuticle of the beetle shell, *i.e*, the outermost portion of its exoskeleton of the beetle shell[7]. This layer structure, shown in the transmission electron microscope TEM (Figure 1*a* - *bottom*) is made up of ~20 alternating layers[8] with refractive indices $n_1 = 1.5$ and $n_2 = 1.7$.

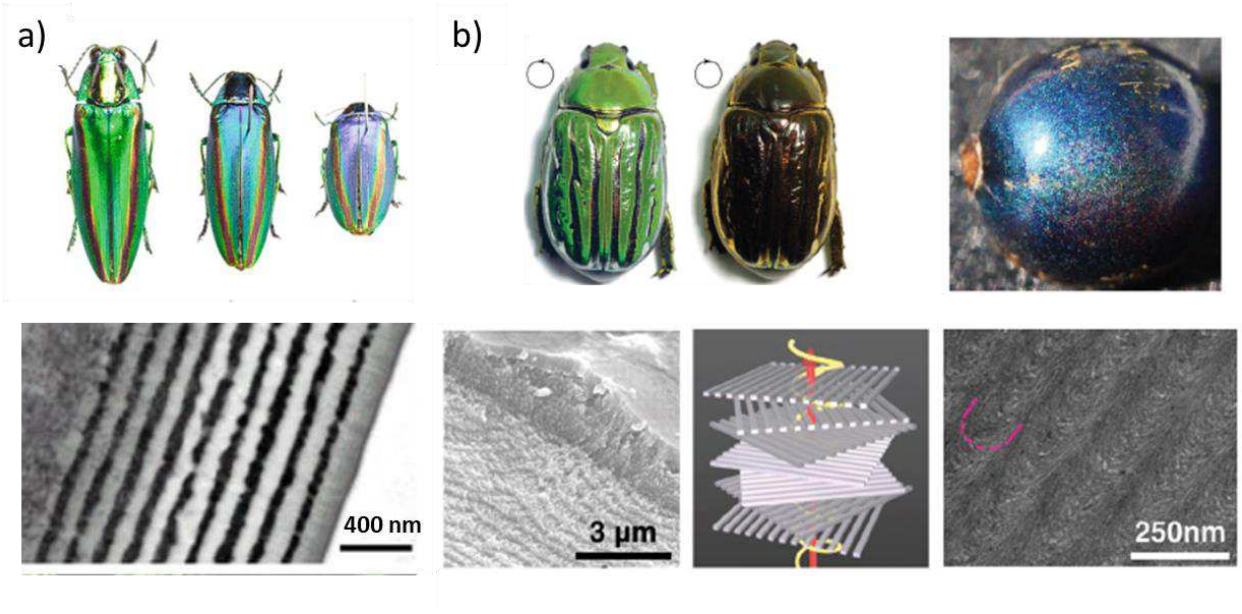

Figure 1. (a) Macroscopic pictures of a "Chrysochroa fulgidissima" (up) with corresponding TEM picture of the shell seen in cross-section, adapted from Kinoshita et al. [7]. (b) Macroscopic pictures of a "Chrysina gloriosa" beetle and a "Pollia condensata" fruit with corresponding scanning electron microscopy (SEM). A Schematic representation of the twisted nematic structure is represented between both SEM pictures. Adapted from Sharm et al & Vignolini et al.[9,10].

Some species of *Jewelled Beetles* (*Chrysina gloriosa*)[9] and the *Pollia condensata*[10] fruit display circularly-polarized iridescence thanks to a structure of

chitin (Figure 1*b* - *left micrograph*) and cellulose (Figure 1*b* - *right micrograph*) fibrils, respectively, similar to assemblies found in a twisted nematic liquid crystal.

1.1.2. Two-dimensional natural Photonic crystal

The work of Mason *et al.*[11] rightly focused in on the most striking characteristic of this class of material: their iridescence. These structures exhibit a visual stunning metallic-like luster and some for example, appear purple at normal incidence and proceed through to red, yellow and then green as the angle is reduced to near grazing incidence. Mason *et al.* identified that the color is located in the barbules of feathers and analysis on cross-sections of peacock feather barbules were performed. *Figure* 2 *a & b* shows a macroscopic image of a peacock feather and a TEM cross section showing the 2D photonic crystals of melanin rods embedded in keratin matrix responsible for the iridescence coloration.

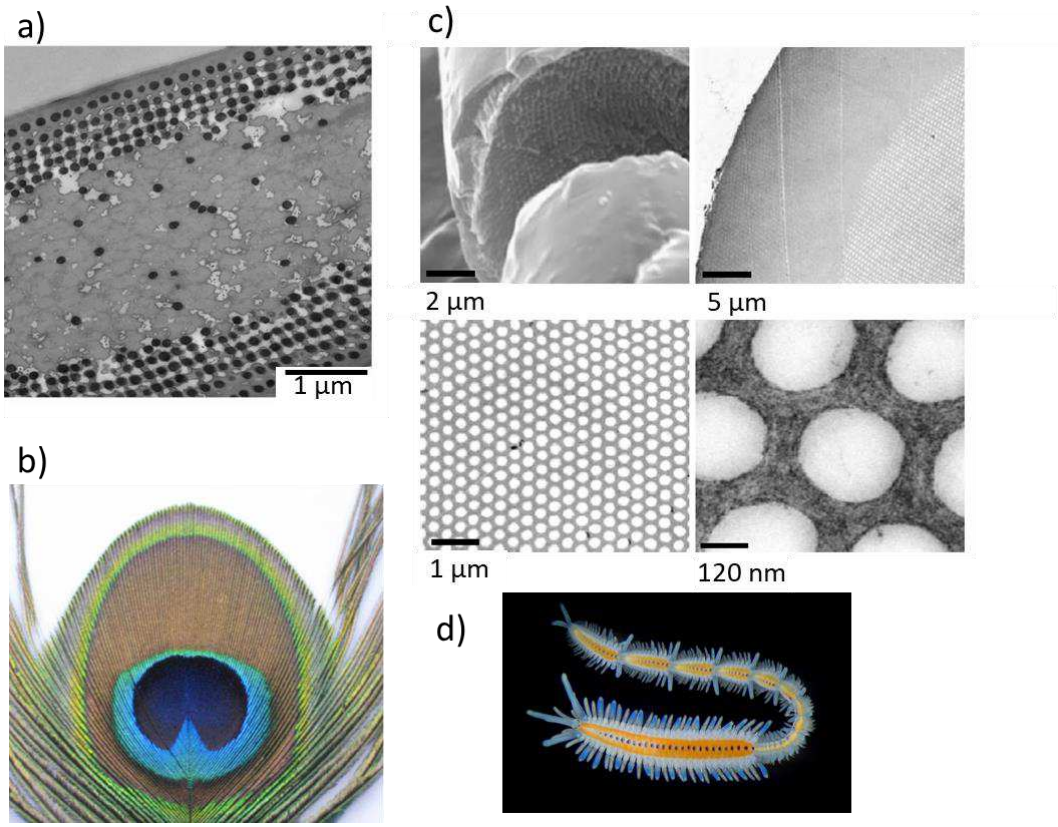

Figure 2 Male peacock and iridescent setae from "polychaete" worms. (a) Macroscopic photo of one of the tail feathers and (b) a TEM cross section of a barbule. Adapted from Medina et al.[12]. (c) Scanning electron micrograph (SEM) in the top-left and transmission electron micrograph (TEM) images of transverse sections through a single iridescent seta. (d) Macroscopic of a iridescent "polychaetae" worm. Adapted from Vukusic et al.[13]

Equally fascinating are the nanostructures found in the hair-like *setae* of many species of *polychaete* worm (Figure 2 *c & d*). In these creatures, a two-dimensional (2D) hexagonal lattice of voids within the cross-section of each seta creates a natural pseudo-photonic crystal fiber along its full length. In other words, periodic voids cylinders are embedded in a high-refractive-index solid medium. The high spatial periodicity of this lattice generates a partial photonic bandgap (PBG) by which color is strongly diffracted in certain directions. As a consequence of this, strong iridescence is observed laterally [13].

1.1.3. Three-dimensional natural Photonic crystal

Nevertheless, some examples of birds' plumage colorations are made thanks to more intricated, spongy structures[14]. For instance, colors of the plumage in the Eastern Bluebird (*Sialia sialis*, left) originate from a quasi-order of *β*-keratin

tubular nanostructures, while in the *Plum-throated Cotinga* (*Cotinga maynana*, centre), the structures are spheres.

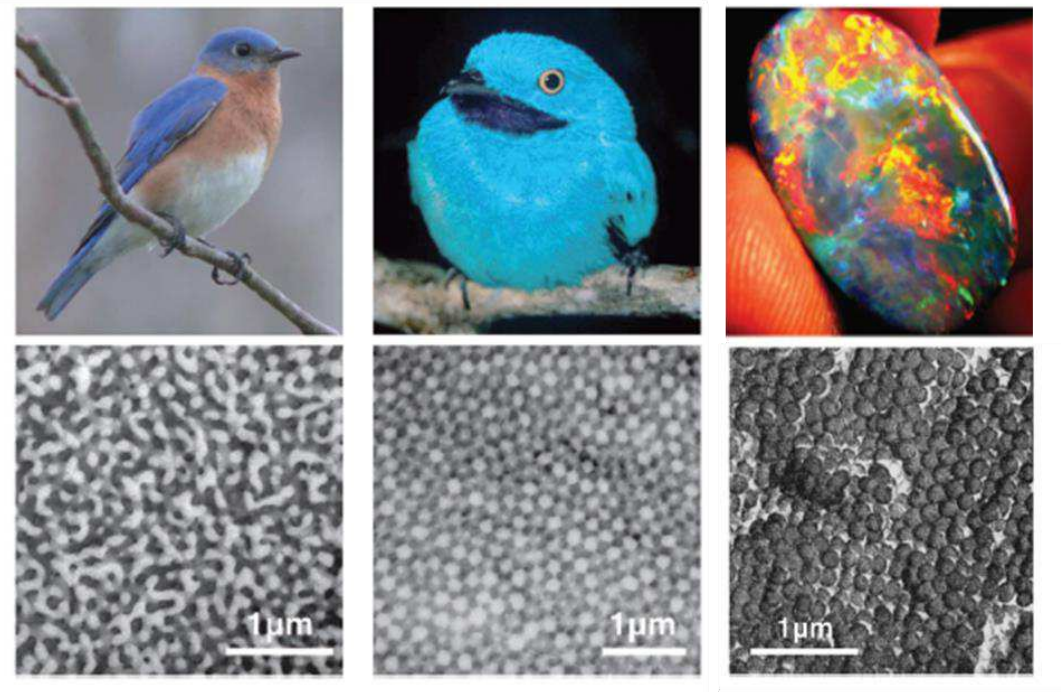

Figure 3 (up) Macroscopic pictures, from left to right of a Sialia sialis and Cotinga maynana birds and a natural opal. The corresponding TEM pictures are displayed below. Adapted from Dufresne et al.[14] & Jones et al. [2].

Iridescent colors may also be found from some peculiar gemstones: opals. Natural opals display iridescent colors because of the periodic organization of silica beads in air. [2]. The photonic coloration from this three-dimensional photonic crystal come from the crystallin arrangement of the beads and the refractive index difference between air (n=1) and silica ($n_{SiO2} = 1.46$) or keratin ($n_{keratin} = 1.51$) for natural opals and birds, respectively.

One of the most studied species, in terms of structural color production and biomimetics, is the *Morpho* butterfly, whose wing-scales exhibit a unique metallic-blue color. *Morpho* is an excellent example of the combined diversity of physical mechanisms in color production (*Figure* 4), hence it is all the more challenging to mimic.

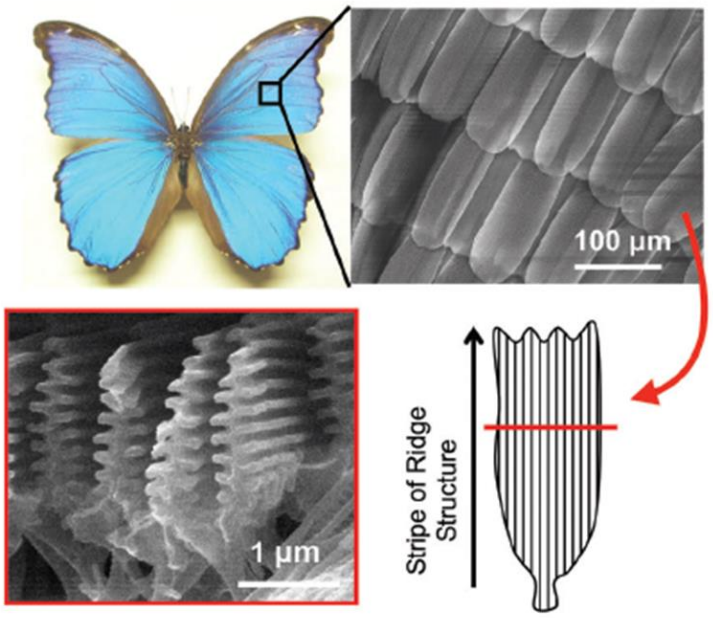

Figure 4 Typical Morpho butterfly (Morpho didius) and SEM images of the scale, each covered with ridges whose lateral profile has the typical "Christmas tree" shape; the ridges are supported by a gyroid crystal structure that also produces structural colors. Adapted from Saito et al.[15]

The iridescent blue color with high reflectivity is a result of coherent scattering in the periodic arrays of scales[16,17]. Periodic structures, such as gratings or multilayers, produce colors with high dependency on the angle of reflection. However, for the Morpho species, the reflected blue color has a low angle-dependency due to the presence of multilayer surfaces that exhibit a distribution of tilts with respect to the scales' substrate. The strong diffraction is further caused by a second layer of periodic ridges above the layer of highly iridescent ground.[18] As a result, Morpho butterfly wings exhibit a complex optical response by combining multilayer interference, diffraction, scattering, and even pigment induced absorption, to produce its singular, angle-independent brilliant blue color.

More interestingly, the structural colors are also produced from color changing animals.

1.1.4. Responsive coloration

Many chameleons, and panther chameleons in particular, have the remarkable ability to exhibit complex and rapid color changes during social interactions such as male contests or courtship[19]. It is generally interpreted that these changes are due to dispersion/aggregation of pigment-containing organelles,

within dermal chromatophores. Those chromatophores, or pigment cells, are known as iridophores due to their iridescent coloring properties. For instance, in the case of a panther chameleon *(Furcifer pardalis)*, its iridophores are made of guanine nanocrystals arranged into a three-dimensional photonic crystal, right under its skin. The work of Teyssier *et al.*[20] shows the guanine nanocrystal inter-distance can be increased or reduced with the osmotic pressure inside the iridophore, bringing an insight about the biological mechanism triggering this responsive coloring properties (Figure 5).

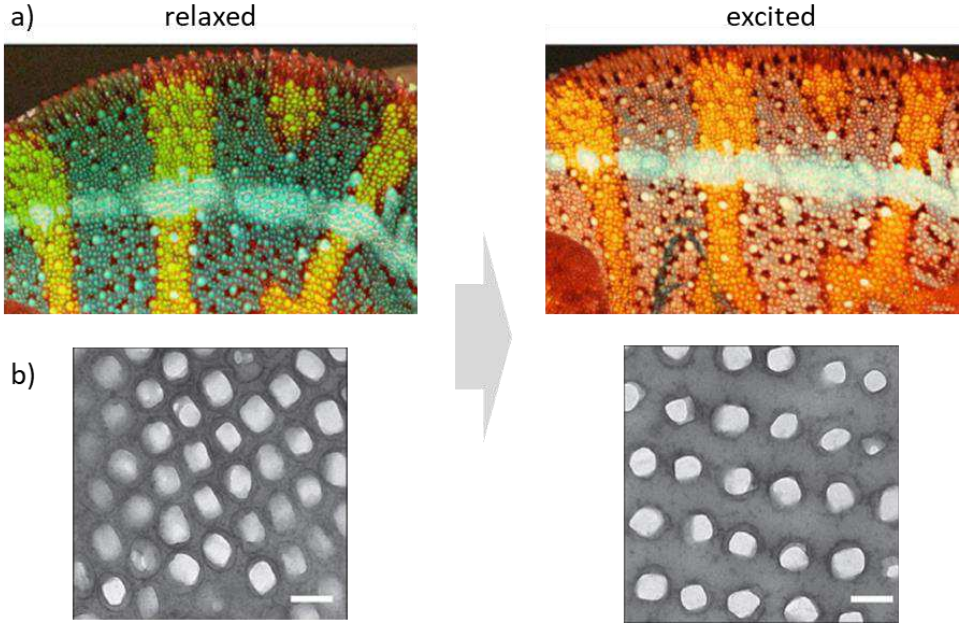

Figure 5 Macroscopic pictures of the skin of a Furcifer pardalis. On the left, the relaxed animal displays a green/yellow coloration. On the right, the skin of the excited animal shows a color shift toward orangish hues. SEM pictures of skins samples leading to similar hues are displayed below. The ex-vivo stimulation in therefore triggered through its wetting with a solution with a controlled osmotic pressure. Adapted from Teyssier et al[20]

All those examples give an overview about what's nature spontaneously produce, most of the time in soft conditions, without high pressure/ temperature and in water. Those iridescent coloration can appear from a multitude of ordered material. What we saw until now, is such structural colors require two elementary conditions to exist: order and refractive index differences. More, the modification of lattice, can induce a color modification, as in the case of the panther chameleon.

A more in-depth investigation about the nature of light and its interaction with matter is the key to understand how such phenomena are produced. In the

following section, we will focus on those points and more especially on the light's interaction with periodically organized matter, and how it can be controlled.

1.2. ***Understanding of the color***

1.2.1. The light

Since the works of Planck and Einstein, the light is known to exhibit a wave-particle duality[21]. Due to its particle behavior, photon, is characterized by a defined quantity of energy quantum of energy established by the Planck equation (Equation 1). This equation associated the photonic energy, *En*, with *h*, the Planck constant; *c*, the speed of light and λ, the wavelength associated to the wave behavior of the particle.

Equation 1

$$En = \frac{h \times c}{\lambda}$$

As an electromagnetic wave, its behavior can be described through the resolution of the Maxwell differential equations[22,23].

1.2.2. Absorption

As an electromagnetic wave, photons can interact with others electro-magnetic systems. As it's known from the beginning of the XX's century[24], matter is elementary composed by electrons surrounding nucleus made of proton & neutrons. According to De Broglie, all possess a similar wave/particle duality through a generalization of the Planck equation. Around those nuclei, electrons can explore several energy levels, depending of the charge of the nucleus or the environment of the atoms. Those discrete level of energy are separated by defined energy differences. In environmental conditions, the atoms are the most of the time involved in physical or chemical bonds through their electrons[25]. Quantum physics tell us those bonds define the electronical energy levels occupied or accessible in molecular structures. When an electro-magnetic wave, as photons, interact with matter, its energy can be transferred to the electronic system to increase the energy level of electrons. Because the energy level accessible to the electrons are discrete, only photons associated with a defined amount of energy can be absorbed.

In this such case, a color is produced through an energy absorption mechanism. It can happen in a lot of case but require each time the same condition:

an electronic vacancy of higher level in the electronic bonding, offering the possibilities to electron to absorb photonic energy. It happens everywhere, all the time, with metallic materials, molecules interacting with ligands, absorbent chemical functions… just to cite. A part of the incoming light, that's not absorbed, can reach our eye: the perceived color is then the complementary color of the absorbed one. It's the mechanism usually involved for the colors perceived from pigments and dyes.

1.2.3. Dispersion

However, the case where the light is non-absorbed is not a dead end. Indeed, depending of macroscopic physical properties of the materials as the dielectric permittivity, or similarly its refractive index, the light rays are reflected without energy loss or transmitted. When the light with a certain wavelength passes through the material, its wavefunction is altered by the present matter. From this alteration results a modification of its speed propagation and its trajectory: the light is refracted. This well-known phenomenon has been mechanically described in the 17th century through the Snell-Descartes equation.

Equation 2

$$n_1 \times \sin(\theta_1) = n_2 \times \sin(\theta_2)$$

Because of the refraction phenomenon, photons trajectories and speeds are altered differently in function of their wavelength/energy. When a rectilinear ray of light composed of photons associated with wavelength covering the whole visible range pass through a transparent medium: the light is then decomposed. This light decomposition in function of the wavelength is the phenomena called dispersion. In particular, it's what happens when rainbow appears in the sky: the day light being dispersed by the myriad of small atmospheric water droplets.

In parallel of theses phenomena, the photons absorbed by the electronic system may also re-emitted, but in another direction than the one expected by the Snell-Descartes equation: it's the scattering (Figure 6). Two different cases have been distinguished:

1) The less frequent is when light is re-emitted with a loss of energies due to electronic recombination, inelastically: it's the *Raman scattering*.

2) In most of situations, the photons are scattered elastically, without a loss of energy: it's the *Rayleigh scattering*.

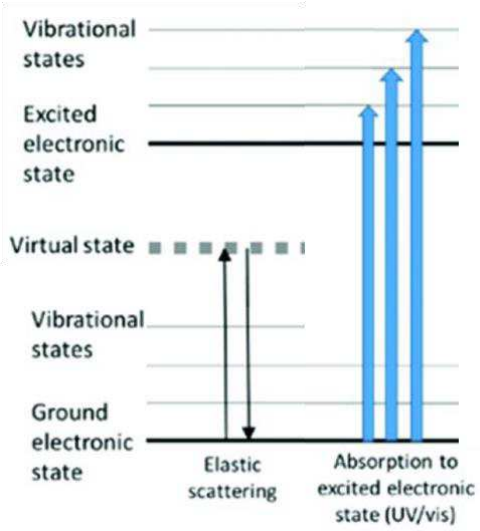

Figure 6 Energy level diagram comparing different light–matter interactions. Adapted from Wiester et al.[26]

1.2.4. Scattering

In our daily life, the *Rayleigh scattering* is the cause of the color of the sky. It affects objects largely smaller is size than the wavelength of radiations in contact with them, at least 10 times smaller[27]. Moreover, the intensity of the scattered radiations is proportional to λ^{-4}, scattering 16 times more blue light than red light for instance. Below the equation of the intensity, I of the light scattered from an unpolarized beam. With I_0, the incident intensity, θ the scattering angle, R the distance to the particle, λ the wavelength of the incident light, d the diameter of the spheres and n their refractive index.

$$I = I_0 \frac{1 + \cos^2 \theta}{2R^2} \left(\frac{2\pi}{\lambda}\right)^4 \left(\frac{n^2 - 1}{n^2 + 2}\right)^2 \left(\frac{d}{2}\right)^6$$

Factually, the Rayleigh scattering can be perceived as a particular case of a more general definition known as *Mie scattering*. Indeed, the Mie or Lorenz-Mie scattering comes from the resolution of Maxwell equations for interactions between light, *i.e.* EM waves, and objects with defined geometry, usually spheres. However, the Mie scattering description deviates significantly for objects with a size close or bigger than the wavelength of the incident beam. For instance, with

comparable geometries, the resulting intensity distribution in space changes drastically, with a more intense scattering phenomenon in the direction of the incident beam. Moreover, scattering intensity loss its wavelength dependence with the increase of the object size. For instance, for a sphere of polystyrene in water; with a diameter of 1.8 µm, the scattered intensity variation is closely independent from the wavelength in the visible range (mx= [12; 24] for λ= [400; 750 nm]– Figure 7). That's the reasons why clouds appear white in the sky: they are made of a myriad of disordered droplets of water, scattering in a multitude of directions equally each wavelength of the sunlight.

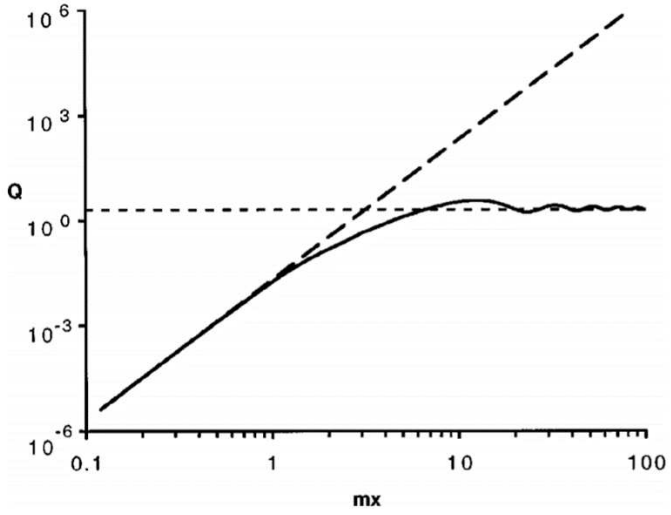

Figure 7. Scattering efficiency Qversus mx ($x = (2\pi n_0 r)/\lambda$ and $m = n/n_0 = 1.59/1.33$) for Rayleigh (dashed curve) and Mie (solid curve) scattering. The dotted line indicates the limiting value of Q = 2. Adapted from Cox et al.[28]

1.2.5. Diffraction

Among the scattering's effects, there is a special case that appears when colloidal objects are organized. In such case, the scattered light waves can develop constructive or destructive interactions leading to another optical effect: the diffraction. Such phenomena can be described from several ways. The first one come the resolution of the Maxwell equations applied to the translation of an electromagnetic wave into a material displaying a periodic modification of its dielectric permittivity[29]. The periodicity of the dielectric permittivity can be described in function of it dimension, separating so called photonic crystal (Figure 8).

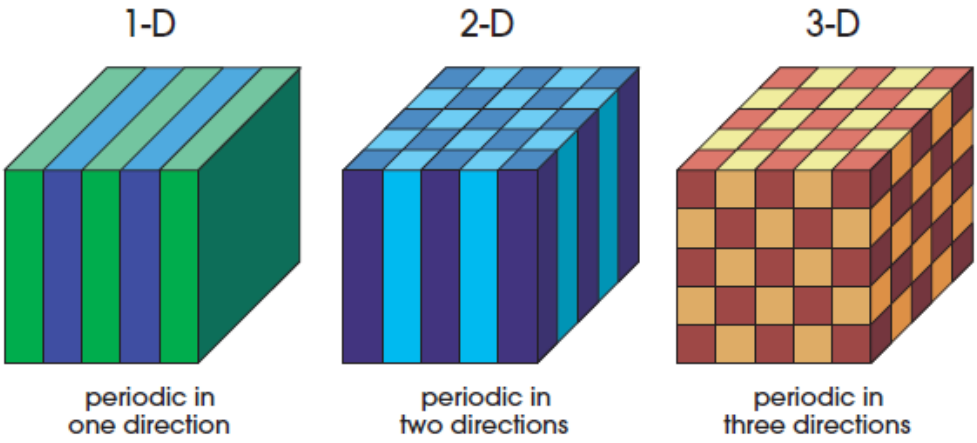

Figure 8. Schematic examples of one-, two- and three-dimensional photonic crystals. The different colors represent materials with different dielectric constants. Adapted from Joannopoulos et al.[29]

For 3D photonic crystals, the periodicity of the system is considered from a crystallographic point of view. Those Crystalline structures can be defined by their repeating pattern, called the unit cell and are characterized by translation vectors ($\overrightarrow{a_1}$, $\overrightarrow{a_2}$, $\overrightarrow{a_3}$). Also known *as lattice parameters*, those translation vectors are characterized by symmetric relations applied on them. Another useful representation of the unit cell in the reciprocal space which can be introduced. It leads to the construction of a reciprocal unit cell, characterized by its *reciprocal lattice parameters* ($\overrightarrow{b_1}$, $\overrightarrow{b_2}$, $\overrightarrow{b_3}$) expressed as:

$$\overrightarrow{b_1} = \frac{2\pi\overrightarrow{a_2} \times \overrightarrow{a_3}}{\overrightarrow{a_1} \cdot (\overrightarrow{a_2} \times \overrightarrow{a_3})} \qquad \overrightarrow{b_2} = \frac{2\pi\overrightarrow{a_3} \times \overrightarrow{a_1}}{\overrightarrow{a_1} \cdot (\overrightarrow{a_2} \times \overrightarrow{a_3})} \qquad \overrightarrow{b_2} = \frac{2\pi\overrightarrow{a_3} \times \overrightarrow{a_1}}{\overrightarrow{a_1} \cdot (\overrightarrow{a_2} \times \overrightarrow{a_3})}$$

For instance, in the case of a transparent material, the Magnetic and Electronic Field in a periodic medium, derived from the Maxwell equations for a periodic medium, can be expressed as:

Equation 3

$$\nabla \times \left(\frac{1}{\varepsilon(\vec{r})} \nabla \times H(\vec{r}) \right) = \left(\frac{\omega}{c} \right)^2 H(\vec{r})$$

Equation 4
$$E(\vec{r}) = \frac{i}{\omega\varepsilon_0\varepsilon(\vec{r})}\nabla \times H(\vec{r})$$

With H and E, respectively the magnetic and electric field, ω the electromagnetic pulsation, ε_0 the dielectric permittivity of the void, a scalar dielectric function ε(r) referring to the dielectric relative permittivity and c the celerity of the light.

H(r) and E(r) carry the spatial information about the evolution of the electromagnetic wavelength, also called "vibration modes". They may re-integrate in the expression below to recover the time (t) information:

Equation 5
$$\mathrm{H}(\vec{\mathrm{r}},\mathrm{t}) = H(\vec{r})e^{-i\omega t}$$

Equation 6
$$E(\vec{r},t) = E(\vec{r})e^{-i\omega t}$$

$$\hat{\theta} = \nabla \times \frac{1}{\varepsilon(\vec{r})}\nabla \times$$

The Equation *3* can be then considered as an *eigenvalue problem* to solve the expression of the magnetic field with the corresponding Hermitian operator $\widehat{\Theta}$. Once done, the magnetic field solution is injected in the Equation 4 to solve the expression of the electric field.

For instance, we can consider a plane wavelength defined as: $H(\vec{r}) = H_0 e^{i\vec{k}\cdot\vec{r}}$ propagating along a direction defined by the wave vector, $\vec{k}$. Due to the periodic organization of the objects in space the vibration modes may be degenerated: for one vibration mode, several wave vectors may exist, according to the symmetry of the periodic organization.

Related to the consideration of the periodic symmetries of the lattice, the *Bloch's theorem* allows a new expression of the *vibration mode*, defined as a "*Bloch's state*":

$$H_k(\vec{r}) = e^{i\vec{k}\cdot\vec{r}}u_k(\vec{r})$$

With $u_k(\vec{r})$, a periodic function on the lattice as $u_k(\vec{r}) = u_k(\vec{r} + \vec{R})$ for all lattice vector $\vec{R}$ with $\vec{R} = l\overrightarrow{a_1} + m\overrightarrow{a_2} + n\overrightarrow{a_3}$; l, m and n being integers. The *Bloch's*

states of a three-dimensional periodic system are then associated with a *Bloch wave* vector $\vec{k} = k_1\overrightarrow{b_1} + k_2\overrightarrow{b_2} + k_3\overrightarrow{b_3}$, with k restrained in the *first Brillouin's zone* (Figure 9). Each wave vector k inside the first Brillouin zone identifies an eigenstate $\hat{\theta}$ of with a frequency ω(k) and an eigenvector H_k. All the information about the electromagnetic wave inside a photonic crystal is then carried by the Boch wave vector $\vec{k}$, and the periodic function $u_k(\vec{r})$.

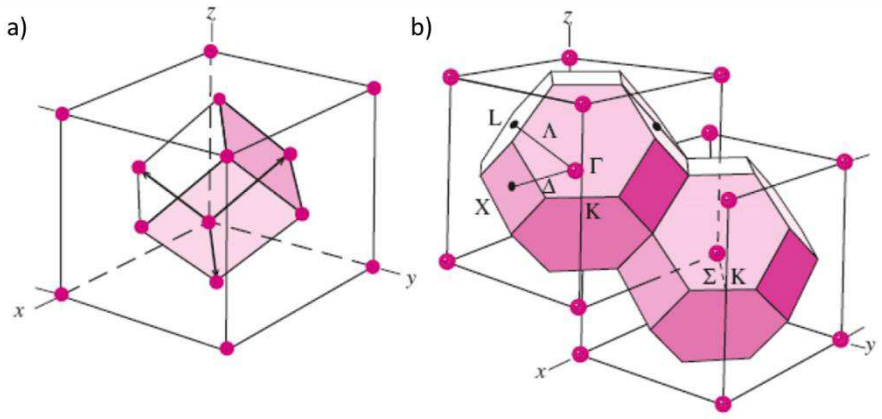

Figure 9. Schematic representation of (a) an FCC lattice and (b) the reciprocal lattice of the FCC with a representation of the first Brillouin Zone. Special symmetry point used in the construction of the band structure diagram are noted. Adapted from Yu et al.[30]

The resolution of $u_k(\vec{r})$ is done through the insertion of the *Bloch's state* expression into the *eigenvalue problem* (Equation *3*). The resolution of this Hermitian eigenvalue problem to a finite volume leads to a discrete spectrum of eigenvalues. For each value of *k* there is an infinite set of modes with discretely spaced frequencies, labelled by a band index *n*. In this way, we describe the electromagnetic vibrations modes of a photonic crystal as *photonic band structures*. It represents a family of continuous function, $\omega_k(k)$, indexed in order of increasing frequency by the band number. The information contained in these functions is called the "*band structures*".

In few words, the band structures model the electromagnetic frequency that can cross this transparent photonic crystal in function of directions defined by the *first Brillouin's zone*. In certain circumstances, a "*photonic band gap*" may appear. It requires usually a difference of refractive index/dielectric permittivity high enough and a favorable crystalline structure. Here, a photonic band gap corresponds thus to electromagnetic frequencies, or light wavelengths, that cannot

cross the photonic crystal, they are diffracted. With light, it means that photons associated with a specific wavelength range corresponding to the band gap are selectively reflected.

For a given photonic crystal, defined by $\varepsilon(\overrightarrow{r})$, the calculation of the band structures functions $\omega_k(\overrightarrow{k})$ require powerful computational resources, especially for three-dimensional photonic crystals. Several teams performed such calculations for classic crystallographic structures, as for instance *Face-Centered Cubic* (FCC), *Hexagonal Compact* (HC) or Diamond-like arrays. It is worth noting that the higher the refractive difference between the crystalline structure, the larger the *photonic band gap*[31]. Moreover, all the structure doesn't lead necessarily to *a complete photonic band gap*. Band structures may overlap along several crystalline directions, corresponding to directions where light is not diffracted and can cross the photonic crystal (Figure 10).

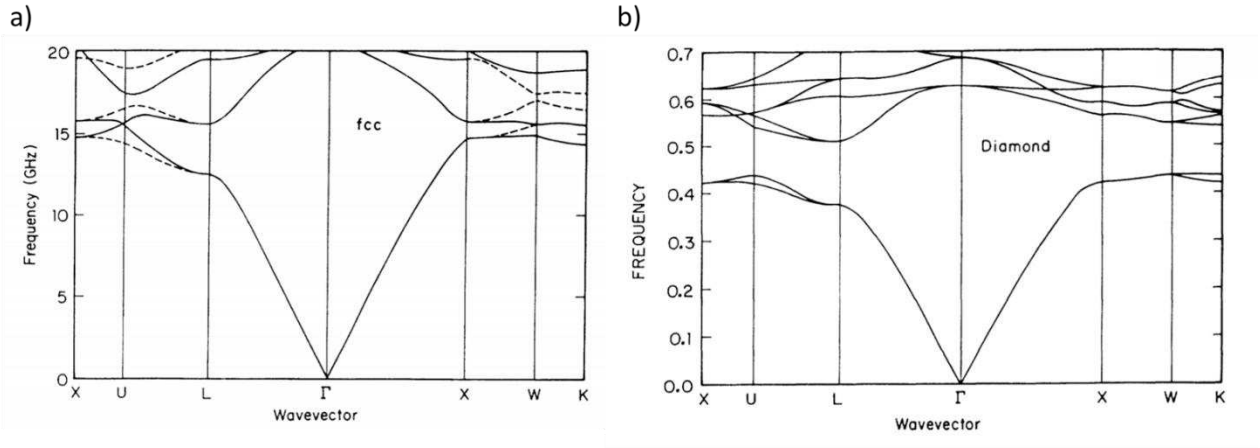

Figure 10. Calculated photonic band structure in the first Brillouin zone for (a) a fcc dielectric structure composing of air spheres in a dielectric background of refractive index 3.5, with a filling ratio of 86% for air and for 14% dielectric material. (b) diamond dielectric structure consisting of dielectric spheres of refractive index 3.6 in an air background. The filling ratio of the dielectric material is 34%. The frequency is given in units of c/a, where a is the cubic lattice constant of the diamond lattice.

Another approach of the diffraction phenomena worth to be mentioned, especially adapted in the case of stacked spheres. Borrowed from the X-Ray diffraction theory, the Bragg equation describe how the diffracted wavelength of maximum intensity (λ), the inter-reticular distance (d_{hkl}) and the incident beam angle with the normal (θ) are associated.

Equation 7

$$m\lambda = 2d_{hkl}\cos(\theta)$$

The Snell-Descartes's equation (Equation 2) of the refraction can be integrated to the equation to consider the effective refractive index of the material (n_{eff}). The equation 7 become then what's called usually the *"Snell-Bragg equation"*:

Equation 8

$$m\lambda = 2d_{hkl}\left(\left[\left[n_{eff}^2 - \sin(\theta)^2\right)\right]\right]^{\frac{1}{2}}$$

For instance, in the case of the stacking of spherical object into a medium, the effective refractive index can be considered as an averaged value of the refractive index of the particles (n_{part}) and the refractive index of the medium (n_{med}) in function of volume fraction of particle and of the medium, respectively V_{part} and V_{med}.

Equation 9

$$n_{eff}^2 = V_{part}n_{part}^2 + V_{med}n_{med}^2$$

In the case of colloidal spheres self-assembly, simulations show the most stable organization from a thermo-dynamical point of view would be *FCC* crystallographic structure. This consideration implies a geometric relation between the inter-particles distance (D) and the inter-reticular distance (d_{hkl}). This inter-reticular distance is the repeating distance separating each crystalline plans in space of a plan's family characterized by their Miller indices *h*,*k* and *l*:

Equation 10

$$\sqrt{\frac{2}{3}}D = d_{hkl}$$

By injecting the Equation 9 and the Equation 10 into the Equation 8, we achieve the equation below. It considers the refractive index differences in the photonic crystal through the expression of n_{eff}, and the geometry of the self-assembly through the relation between the inter-particle and the inter-reticular distances.

Equation 11

$$m\lambda = \sqrt{\frac{8}{3}}D\left(\left(V_{part}n_{part}^2 + V_{med}n_{med}^2\right) - \sin(\theta)^2\right)^{\frac{1}{2}}$$

This *Equation 11* appears as a useful and accessible tool to foresee the reflective color accessible to the material in function of experimentally controllable

parameters. In a first approximation, the impact of the possible additives on the refractive index of this particle/medium model can be pondered by using the *Equation 9* in larger expression as presented below. However further development could be needed.

Equation 12

$$n_{eff}^2 = \sum_i V_i \times n_i^2$$

All the (hkl) plans of a crystalline structure don't necessarily diffract light. Those diffractions conditions depend here again of operations of symmetry operating in the unit cell. The set of symmetry's operations for a defined *unit cell* define a "*space group*" associated with a collection of diffraction conditions on the *h, k* and *l* Miller indices of a family of reticular plan. In other term, for one of the 230 defined space group associated to a *unit cell*, only the reticular plans answering to the diffraction conditions are able to diffract light. And thus, only the d_{hkl} inter-reticular distances associated to those (*hkl*) family plans would be considered in the *Bragg-Snell equation*.

In such conditions, the Bragg-Snell approach offers the possibility to evaluate the diffracted wavelength position associated to a photonic crystal. However, it's an approach presenting some limitations in comparison with the Maxwell approach: there is no evaluation of the width of the bandgap and so no considerations about the width of the diffracted peak (Figure 11). Nevertheless, the Snell-Bragg's approach gives satisfying results with both experimental and expected data from the band structure analysis, but with more accessible computational resources.

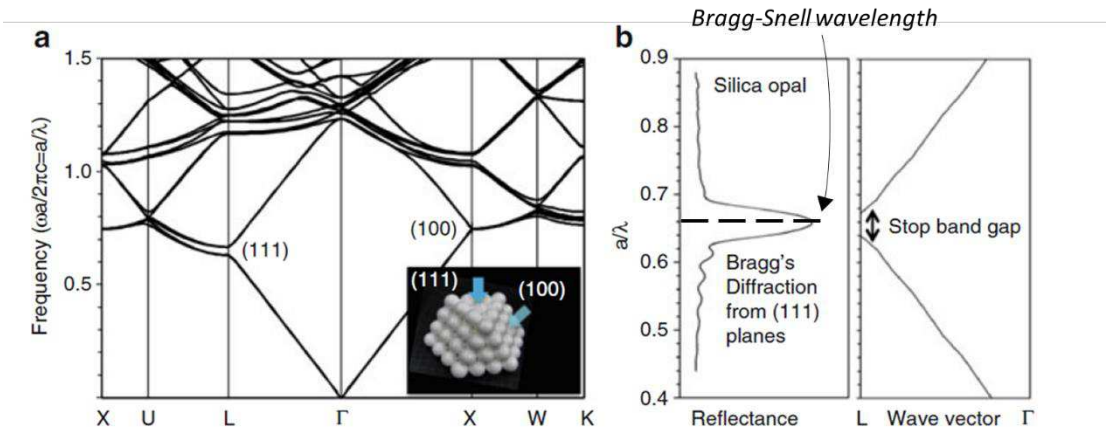

Figure 11. Photonic band structure of a silica opal film. (a) Photonic band diagram for FCC packed silica particles in air. (b) Comparison of the theoretical calculation and the experimental Bragg diffraction from (111) colloidal planes of the silica opal film. The wavelength given by the Bragg-Snell equation is indicated by a dashed line. Adapted from Bardosova et al.[32]

After this concise overview of the optical effect able to isolate ranges of light wavelength, the corresponding photons must be absorbed by the human eye to create the sensation of color. To create this sensation, the photons must be firstly absorbed by the photoreceptor localized in the eye's retina[33,34]. Those cells are divided in two types because of their morphology: rods sensitive to light levels and cone cells, giving the color perception. Those cone cells are divided into 3 categories: Small (S), Medium(M) and Large(L) still related to their form. This morphological specialization involves sensibility differences about their ability to absorb light. Thus, S, M and L cones cells develop respectively absorption peaks at about 560, 530 and 420 nm.

The diffraction can be conceived as a powerful optical tool to the production color, and has been widely naturally developed among a lot of species. Somehow, it gave a pulse to several teams around the world to mimic such phenomena into bio-inspired photonic crystals

2. Bio-inspired artificial self-assembled photonic crystals

The elaboration of artificial photonic crystals is not straightforward, among variety of methods, two different philosophies can be opposed. The first one is the "Top-down", involving the fabrication of a photonic crystal usually through the carving of macroscopic piece by X-ray, plasma or laser etching[35–39]. With the progress of the 3D printings came new promising perspective. The main

advantages of these technics lie in the possibility of making exotic architecture (Figure 12) and crystals with a high regularity[40].

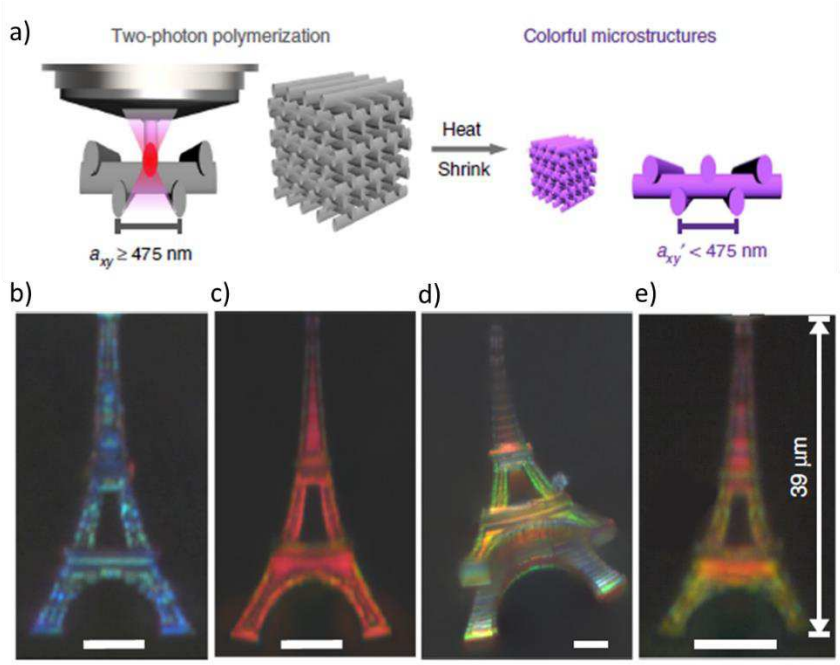

Figure 12. (a) Heat shrinking induced colors of 3D-printed woodpile photonic crystals. a Schematic of the fabrication process. Left: woodpile photonic crystal written by two-photon polymerization at dimensions well above the resolution limit of the printer to prevent structures from collapsing. Right: after heat treatment, the dimensions of the photonic crystal are reduced below the resolution limit of the printer, and colors are generated. The colors change with different degrees of shrinkage. Micrographs of 3D-printed model of the Eiffel Tower in structural blue (b) and structural red (c). (d) Oblique view of an Eiffel Tower printed with intentional gradient of colors. (e) Further down-scaled multi-color 3D print of the Eiffel Tower. Scale bars represent 10 µm. Adapted from Liu et al.[40]

However, these "top-down" technics require a lot of energy and time in comparison with size of the crystal achieved. They use technologies hardly transferable to the elaboration of healthcare/cosmetic applications.

On the opposite the "Bottom-up" approach count on the self-assembly properties of small objects. Usually made from a dispersion of solid objects with a size between 1 and 1000 nm in a liquid phase, the bottom-up way involves the arrangement of these colloidal object to a periodic lattice.

2.1. *Artificial colloidal crystals made from self-assembly*

In the bottom-up philosophy, 1D & 2D artificial photonic crystal are usually designed through the self-assembly of Block copolymers (BCPs).

BCPs are a specific class of copolymers, in which the chemically distinct monomer units are grouped in discrete blocks along the polymer chain[41]. Thanks to the advancement of polymer synthetic strategies and techniques, e.g., controlled polymerization techniques with facile post-polymerization functionalization, BCPs with precisely controlled molecular weights and defined macromolecular architectures can be prepared[42–45].

One of the ubiquitous features of BCPs is their ability to form a plethora of nanoscale ordered structures. By manipulating the molecular parameters such as the Flory-Huggins interaction parameter (χ), the degree of polymerization (N), and the volume fraction (f), various morphologies including spherical, cylindrical, lamellar, and others have been revealed both experimentally and theoretically[46,47]. For instance, BCPs made of poly(styrene)-*b*-poly(2-vinylpyridine)[48,49] can be self-assembled into lamellar phase to make 1D photonic crystals. More, the poly(2-vinylpyridine) phase can be filled with gold nanoparticles through *in situ* precipitation of Auric acid to elaborate films displaying exotics optical properties[50]. Similarly, the χN ratio of the BCPs can be adjusted to produce 2D photonic crystals. For instance, Deng *et al.* synthesized a high molecular weight polystyrene-*b*-polyisoprene copolymer by anionic living polymerization to produce phase separation of standing cylinders[51]. Even if nowadays the elaboration of block copolymer with high molecular weight has been eased, their conception still lies in anionic living polymerization. This rigorous synthesis approach is not easily transferable toward industrial production, as it require an environment free from oxygen and protic solvent, as water[52].

Three-dimensional photonic crystals from a bottom-up approach are usually made from the self-assembly of colloidal objects. According to their shape and size, plenty of configurations are achievable[53–56]. In the next section, we focus on crystalline architecture based on organic materials.

2.1.1. Twisted nematic photonic crystals.

This self-assembly of is made of anisotropic building blocks (BBs). Here, the BBs can be considered as rod-like objects, that follow a self-assembly pattern well-known from liquid crystal studies. The Twisted nematic pattern is mode of an arrangement of BB describing a layered structure, with BB tilted by a finite angle

with respect to the normal layer. This twist is associated to a pitch, referring to the distance over which the BB undergo a full 360° twist. The structure pattern is thus reproduced every half-pitch. Due to this periodicity, diffraction phenomena may occur. For instance, one mostly investigated BBs are the *cellulose nanocrystals* (CNC) to produce such photonic films[57,58]. They require usually a slow drying of the solvent for the CNC can have the time to self-assemble. Otherwise, they also be treated for a long time with an intense magnetic field to promote a long-range ordering[59].

2.1.2. Opal-like material

Matrix can be: air or an organic/inorganic material. The colloids and the matrix must present a refractive index difference, with a low absorption coefficient in the visible range. The easiest way to make a photonic crystal is thus through the fabrication of colloidal spheres with a controlled size and refractive index. For the refractive index, the materials chosen are usually PS or SiO_2 spheres for the versatility of their production. In both cases, their synthesis leads usually to a suspension of these colloidal objects dispersed in solvent. The photonic crystal is therefore obtained by the self-assembly through the controlled drying of theses suspensions. The lattice achieved can be described as an organized array of spheres with air between them; in other words, organized spheres in an air matrix.

However, the refractive index difference between of the spheres/matrix can also be tuned by adjusting the refractive index of the matrix. To do so, two strategies are achievable.

The first one consists in the modification of an already self-assembled lattice in air. In such case the free-space between particles can be infiltered with a solution leading to the synthesis of a filling material. For instance, Waterhouse *et al.*[60] used an inorganic filler, leading to the formation of silica through condensation of organosilanes in basic condition infiltered in the lattice. At the opposite, Zhang *et al.*[61] designed a self-assembly of inorganic spheres, with an organic filler made from a polymerizable monomers solution also infiltered in the lattice. In such case, the polymerization can be initiated thermally[62] or photo-chemically[63].

The second strategy lies in the conception of core-shell colloidal objects. Indeed, the purpose here is the shell material could act as the filling material previously described.

2.1.3. Inverse Opal-like material

This kind of architecture can be produced from the previously described opals structures where the free-space between spheres/cores is filled. Inverse opal-like are made by using the spherical lattice as a template: the final photonic crystal is made by the remaining filling material after the template has been removed. To this purpose, chemical etching[64–66]or annealing[60] are usually performed to remove the template, according to the sphere/matrix natures. The final material obtained can thus be described here as an array of spheres made of air, within a matrix than can be made of organic/inorganic material (Figure 13).

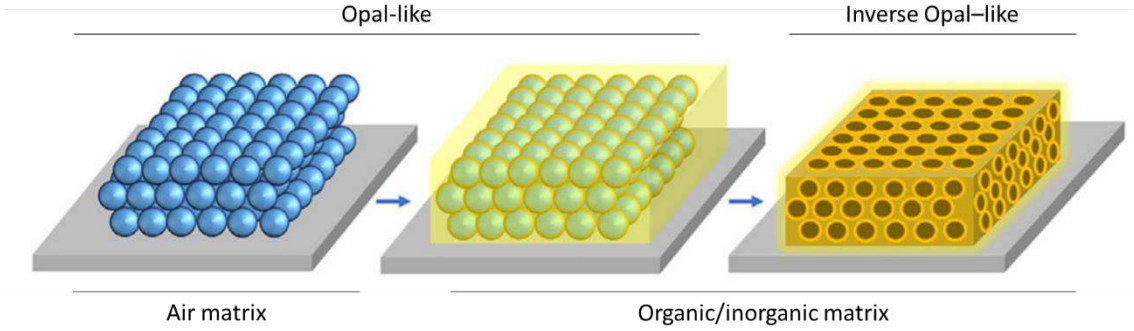

Figure 13. Schematic representation of opal-like an inverse opal like matter organization. From left to right, the surrounding matrix is either made of air or of a material different from the self-assembled beads. On the right side, the beads have been removed, replaced with air. Adapted from Yan et al.[64]

From a photonic point of view, the optical properties of a *twisted nematic crystals* are parameterized by the pitch of the self-assembly. In *opal* and *inverse-opal* like material, the diffracted wavelength is mainly controlled by the spheres size and the inter-particle distances, according the *Bragg-Snell theory*. From the point of view of the ordering conditions, twisted nematic self-assemblies require constraints on the positions and the orientations of the anisotropic BBs. However, due to their isotropic shape, spheres require only constraints on their positions to be periodically organized in a colloidal crystal. Because these geometric reasons, we believe the isotropy of spherical building blocks may facilitate their self-assembly for the development of a cosmetic applications.

More especially, our attention is turn to the fabrication of photonic crystal from spherical core-shell for different reasons. Firstly, in a one controlled drying step, the isotropic colloids can be organized in a periodic pattern. Second, the physical parameters governing the optical properties are experimentally tunable, depending on the core/shell refractive indexes related to their chemical nature and on inter-particles distances, related to the shell thickness.

The self-assembly of colloidal building blocks is the subject of physical forces operating for or against it. Since decades, numerous studies carried on their fundamental understanding.

2.2. *Self-assembly methods & forces involved*

Several works inspired this section. The works of Ng *et al.*[67] and Dommelen *et al.*[68] offers an overview about the colloidal stability and the forces involved in their self-assembly. Concerning self-assembly forces, the work of Li *et al.*[69] give a more exhaustive review of usable physical forces. In complement, the works of Yu *et al.*[70] exposed a synthetic description of mechanism underlying the organization of organic colloids under an evaporation-driven process. Those works were used as guideline to the conception of the following sections.

2.2.1. Colloidal stability

The first concept to consider about these dispersed objects is the small size of colloidal particle suspended in continuous phase, usually liquid. Because of their size, between 1 and 1000 nm, the colloidal objects are exposed to random motions. This is caused by the momentum transfer from the thermal activities of the molecules of the suspending medium. Discovered by the British biologist Robert Brown in 1827, this Brownian motion is driven by thermal energy $k_B T$ on the basis of the kinetic gas theory giving: $\frac{1}{2} m_p v^2 = \frac{3}{2} k_B T$ with m_p being the particle mass, v the particle translational velocity and T the temperature. This Brownian motion will be a key feature, involved in each aspect of the self-assembly mechanism.

Sphere model

As first consideration, colloidal particles may be conceived as hard and electrically neutral particles. Besides van der Waals forces, they only interact through steric repulsion when they are close enough to experience a physical

contact. For monodisperse spherical particles, the close-packing limit is 0.74 and would be in those conditions the most stable form of colloidal crystal at equilibrium. In practice, the higher the concentration of colloidal suspension, the higher the chance that colloids flocculate before than maximum packing limit should be reached. Brownian motion allows particles to gain thermal energy easily and collide with each other to form clusters. If many aggregates form upon collision (especially at high temperature and high concentration), there is a high chance that amorphous colloidal aggregates will form, preventing further packing.

Charged spheres

Almost all colloidal particles are not electrically neutral. They may contain a large number of acids, base or other functional groups which are susceptible to dissociation in a polar solvent. Their functional groups are normally determined by the synthesis path or catalysts used. For instance, polystyrene beads synthesized using KPS (Potassium persulfate) initiator will give rise to negatively charged particles. Hence, hard sphere model using exclusively steric repulsion is only a good approximation, but not an accurate approach to address real colloidal system.

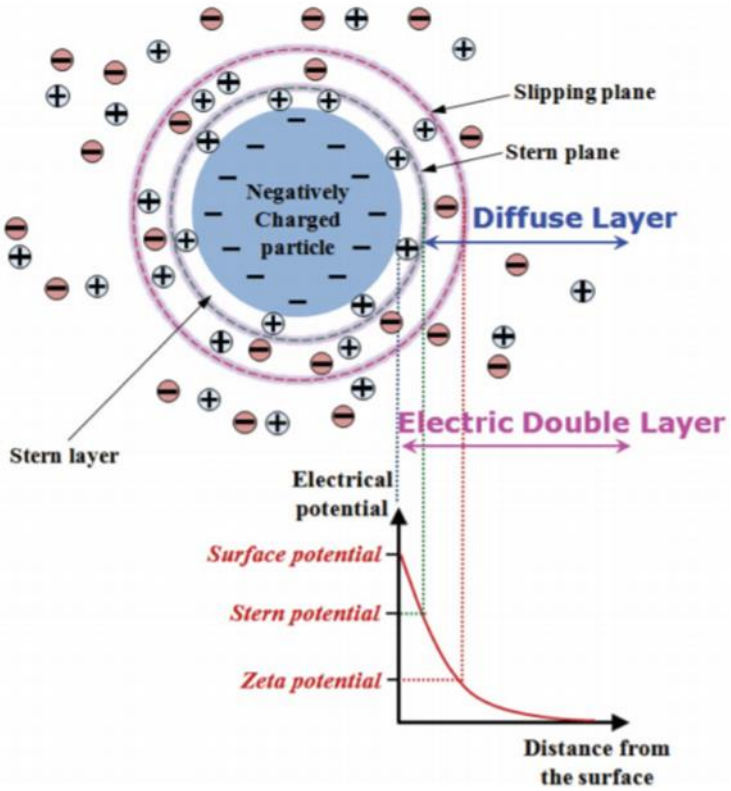

Figure 14. Diagram of electric double layer. Different values of the electrical potential are referenced: the surface potential of the particle, the Stern potential in the close vicinity and farther from the surface, the zeta potential. Adapted from Park et al.[71]

DLVO model

The further description of charged spheres has been largely described and reviewed[72]. On some point, this description is comparable to the interactions between atoms through a Leonard-Jones potential. In the case of charged colloids Derjaquin, Landau, Verwey and Overbeek described analogues and different possible interactions through the well-known DLVO theory. This theory describes the interaction forces between charged surfaces in a liquid medium (Figure 14). It combines both the van der Waals forces and electrostatic interaction of charged surface. Here, it is assumed that:

- Each colloidal particle is surrounded by its own double layer and behaves as if it was electrically neutral unless it approaches another particle closely enough.
- The potential energy of an elementary charge on a surface is much smaller than the thermal energy, $k_B T$.

- The particles are allowed to change position and find their own equilibrium states.

The DLVO potential can thus be expressed as:

Equation 13

$$V_{DLVO} = \frac{64\pi R c_0 \Gamma_0^2 k_B T}{k_B} e^{-\kappa r} - \frac{AR}{12r}$$

With R being the particle radius, c_0 the ion concentration, k_B the Boltzmann constant, T the temperature, κ the inverse double layer thickness, r is separation between particles, and A is the Hamaker constant. The surface potential of particles, Γ_0 can be described by:

Equation 14

$$\Gamma_0 = \tanh\left(\frac{ze\Phi_0}{4k_B T}\right)$$

With z being the valence of counter ions, e the electronic charge, and Φ is the surface potential. The first part of the Equation 13 is related to electric double layer interaction (repulsion by similar charge between particles) whereas the second part can be referred to attractive van der Waals interaction.

The electric double layer provides an energy barrier against irreversible agglomeration. This energy barrier, as indicated in Figure 15 (*right*) as V_{max}, normally has a magnitude ranging from 0 ~ 100 k_bT, depending on the suspension parameters. Unlike the atomic model, two minima exist between two approaching colloidal particles, which are irreversible (primary) and reversible (secondary) respectively. In atomic crystals, atoms are held strongly in the single equilibrium position (Figure 15 - *left*). High energy barrier or chemical bonds must be broken to disrupt the ordering. A brief comparison of interaction potential between atoms and colloidal particles side-by-side is illustrated in Figure 15.

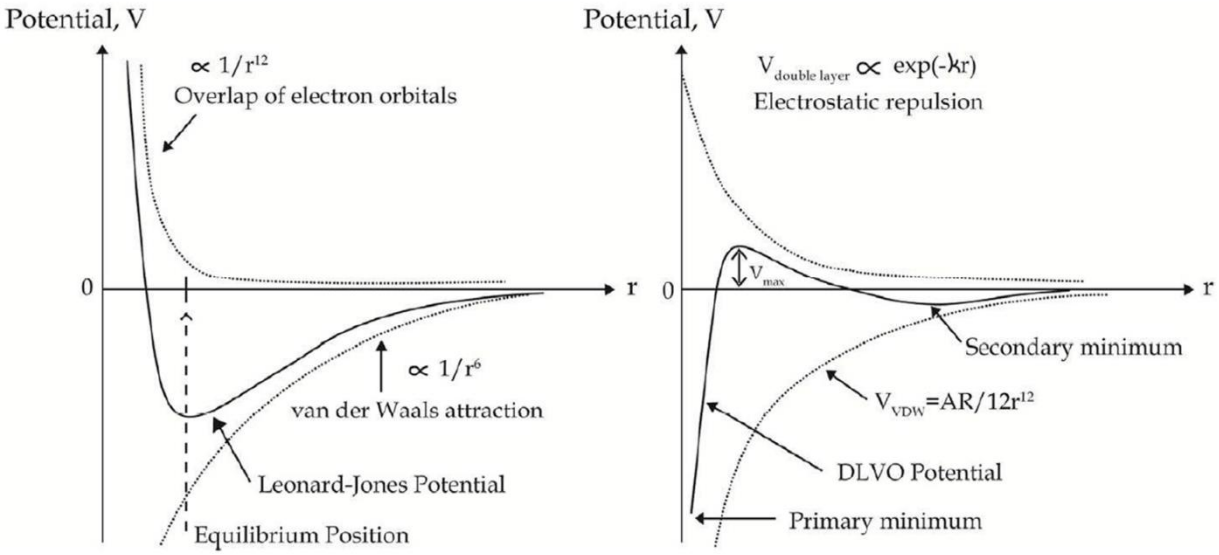

Figure 15 A comparison of interaction potentials between atoms (left) and colloidal particles (right) in close proximity, described respectively by Leonard-Jones potential and DLVO potential. Adapted from Ng et al.[67].

Surprisingly, the existence of secondary minimum allows scientists to "anneal" or remove defects in ordered arrays of wet colloidal crystal at this metastable state, before reaching the final irreversible dry state of colloidal crystal

For crystallization to occur, van der Waals forces must exceed double layer repulsion. This could only happen when particles are close enough, overcoming the energy barrier V_{max}. This is possible as double-layer interaction energy is finite or increases slowly when r approaches zero, while V_{vdw} decreases exponentially when $r \rightarrow 0$. Unlike electrostatic interaction, van der Waals interaction is highly insensitive to the change of pH and electrolyte concentration. Small addition of salt may change the magnitude of V_{max} significantly and remove the secondary minimum. Thus, no ordering in long range is ever possible if this situation happens.

Steric stabilization

The colloidal stability of a suspension can also be achieved through another non-electronic interactions which requires to take a step away from the sphere model developed so far. This stabilizing interaction is called steric stabilization[73] and is brought by molecular chains at the surface of the colloidal object. It can involve for instance the adsorption of nonionic surfactants[74] or polymers[75] on the surface of particles, or the covalent grafting of macromolecules on their surface[76]. It produces an adsorbed layer with a thickness δ. This layer can be strongly

solvated, or hydrated the solvent when this one is a good solvent of the layer's molecules.

From a thermodynamic point of view[77], the free energy of two layers interacting can be expressed as function of the related enthalpy (ΔH_{mix}) and entropy changes (ΔS_{mix}):

$$\Delta G_{mix} = \Delta H_{mix} - T\Delta S_{mix}$$

If the free energy is null, the adsorbed layer has no impact on the flocculation, whereas with a negative value, the layers interaction would promote the flocculation processes. The steric stabilization is achieved only if ΔG_{mix} is positive. To do so, three cases are possible:

1. Both entropy ($T\Delta S_{mix}$) and enthalpy terms are *negative*, with $T\Delta S_{mix} < \Delta H_{mix}$. The steric interactions are dominated by the *entropic stabilization* effects, due to the reduction in the configurations' number of the adsorbed molecules in the adsorbed layer
2. Both terms are *positive,* with $T\Delta S_{mix} < \Delta H_{mix}$. The steric interaction is thus driven by the *enthalpic stabilization*
3. $\Delta H_{mix} > 0$ and $T\Delta S_{mix} < 0$ and therefore both terms contribute to the stabilization – *combined stabilization*

When two particles with a radius R approach to distance h that is smaller than 2δ, the adsorbed layers can either overlap or be compressed without overlapping. Both mechanisms involve a reduction in the configurational freedom of the adsorbed molecules, inducing a repulsive force ($T\Delta S\_mix < 0$). If a high surface coverage is essential to achieve such effect, the solvency of these stabilizing molecules with the liquid phase remain critical.

Those mixing effect can be interpreted according to polymer solution theory, applied when $h < 2\delta$. The layer overlapping and elastic compression described mentioned above follow then the equation derived by Napper[78] from the free energy expression:

$$\Delta G_{mix} = \frac{2\pi RkTn^2\zeta^2 V_s^2}{V_i}\left(\frac{1}{2} - \chi\right)S_{mix} + 2\pi RkT\zeta S_{el}$$

The first and second terms refer respectively to the mixing of the adsorbed layers and the elastic compression effect. With V_s and V_i being the volumes of polymer segment and solvent molecule respectively; n the number of segments per polymer chain; ζ the number of chains per unit area of surface; χ the Flory interaction parameter and S_{mix} and S_{el} positive geometrical terms.

When the stabilizing chains are in a good solvent environment ($\chi < \frac{1}{2}$), the mixing term is positive (*enthalpic stabilization*). However, when $\chi > \frac{1}{2}$, its sign changes the steric interaction induces an attractive force between colloids. In such case, the elastic term remains repulsive and still operate at short distance. The flocculation behavior depends thus on the structure of the adsorbed layer and the magnitude of the repulsive/attractive interactions arising from the overlap of the adsorbed layers.

2.2.2. Ordering of colloidal particles – Solvent evaporation

Nevertheless, the ordering and kinetics of colloidal particles could be quite different from atomic crystals. The medium (solvent) of colloidal dispersion gives rise to the dynamic motion of particles through Brownian motion and exerts capillary forces on the particles near the interfaces[79]. Fluid instability at interface (*e.g.* dewetting) further complicates the kinetics of crystallization process[80,81]. Hence, it is important to address the relevant critical forces involved in particle ordering. First, the proposed mechanisms will be mostly focused on assembly process induced by capillary forces. It differs from other, assembly methods like field induced assembly[82–85] and spin-coating assembly[86]. As mentioned before, self-assembly *via* gravitation force is rather slow, and limits its application. Besides, the particles will only settle if their size and density is sufficiently high. This sedimentation tendency is best characterized by the *Peclet number* [87](Equation 15).

Equation 15

$$Pe = \frac{\frac{4}{3}\pi(\rho_p - \rho_f)gR^4}{k_b T}$$

With m_p being the mass of a particle with a radius R, g the gravitational acceleration, ρ_f and ρ_p respectively the density of the fluid and the particle. This number is a good indicator to determine the stability of a colloid suspension. For

$Pe >> 1$, the particles will tend to sediment and form agglomerates. For instance, polystyrene spheres of 0.1 µm and 10 µm in water solvent at a temperature of 23°C give Peclet number of 5×10^{-5} and $\approx 5 \times 10^{3}$ respectively. Therefore, this practical issue led to the studies on filtration and centrifugation[88,89] which however as drawbacks in terms of packing quality and thickness of the crystal grown.

Nevertheless, the formation of polycrystalline domains with different lattice orientation in colloidal crystals is commonly found, possibly due to nucleation at different locations of the interface and the subsequent growth of crystal domains in different directions[90].

Several casting technics involving the control of the self-assembly through capillary forces may catch our attention, as drop-casting, dip-coating, doctor blade or Langmuir-Blodget deposition. All those technics presents pros and cons, but more importantly similitudes due to evaporation forces occurring in each of them. The drop-casting technique can serve as a good example of the implication of a liquid evaporating among moving colloidal solids.

Drop-casting

Drop-casting can be considered as quite straightforward approach. The suspension is poured or cast drop by drop, on a substrate. The film is prepared when the solvent is fully evaporated. It' a process mainly driven by evaporation and capillary force. A well-known daily phenomenon is currently observed in such experiment, known as the "coffee-ring" effect[91]. When a drop of coffee is spilled onto a solid substrate, a dense ring of stain will be formed upon drying, leaving the center of the initial droplet empty. This dense deposition of coffee solids near the outer ring is related to an intense movement of solid particles from the droplet interior to the drying perimeter. This driving force is mainly attributed to evaporation, causing outward capillary flow (both solvent and solids) to the pinned contact line of the drying droplet, in order to replenish solvent loss from the edge[92]. The mechanism and stages of evaporation-induced assembly was first investigated in detail using an experimental cell containing a thin well of monodisperse micrometer-size latex particles, which allowed *in-situ* microscopic observations[93]. Similar to coffee-ring experiment, the particles were brought convectively to the edge of evaporation front (Figure 16), and the ordering of particles was found to

be initiated when the thickness of water layer approached the underlying diameter of particles[67].

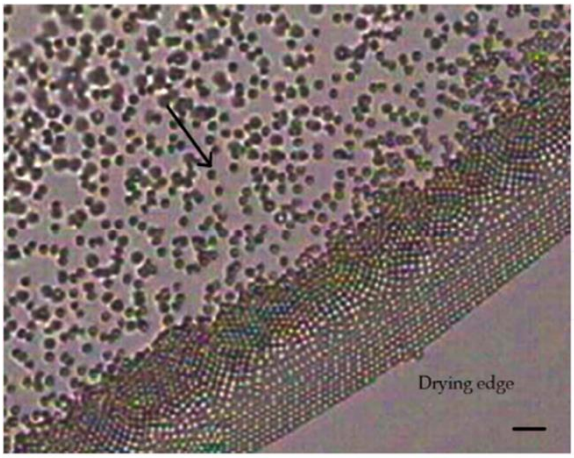

Figure 16 Evaporation driven self-assembly in a trapped droplet. Polystyrene particles (860 nm) move convectively to the drying edge, forming monolayer crystal at the outer perimeter. Transitional phases (e.g. buckling, square) are observed few particle diameters away from the perimeter. Arrow indicates the direction of particle movement. Adapted from Ng et al.[67].

Examples of particles moving to the drying edge of water film are shown in Figure 17. In those conditions, self-assembly starts when water thickness is close to the particle diameter. In evaporation-induced self-assembly, much attention is paid to the drying stage when the thickness of water layer is close to particle diameter. As evaporation proceeds, thinning of water layer causes deformation of menisci between particles at the drying front.

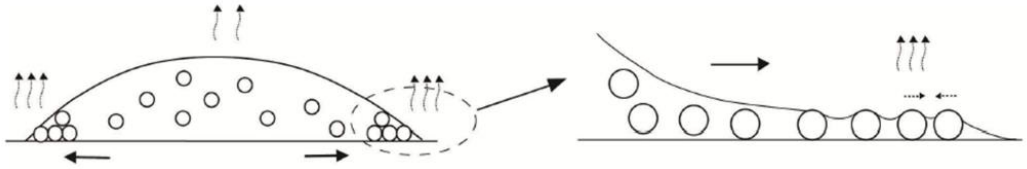

Figure 17. Schematic representation of drying edge confinement effect on colloidal assembly. Adapted from Ng et al.[67].

Further evaporation from the concave menisci increases the curvature and local capillary pressure, driving more water influx from thicker water layer to thinner region. However, depending on other experimental conditions, convective force can introduce a significant modification in the self-assembly dynamic.

Marangoni effect

Those convection forces have been furtherly investigated and studied, giving rise nowadays to the Marangoni effect. This effect holds his name from the Italian physicist Carlo Giuseppe Matteo Marangoni who investigated the spreading of oil drops on a water surface in the 1860s. This behavior was explained as being the macroscopic manifestation of a liquid flow resulting from local differences (gradients) in interfacial tension. Indeed, a liquid with a high surface tension pulls more strongly on the surrounding liquid than one with a low surface tension. Therefore, the presence of a gradient of surface tension cause the fluid to flow toward regions of high surface tension. Moreover, this surface tension gradient can be also caused by a concentration gradient or by a temperature gradient.

Bhardwaj and co-workers[94] showed that this effect can be overcome by altering the pH value of the suspension. To that purpose, they studied films made from aqueous dispersion of Titanium dioxide particle. The pH value of the suspension was lowered or increased, respectively either with an addition hydrochloric acid or sodium hydroxide. As result, the DLVO force was adjusted, either attractive at low pH values, or repulsive at high pH values leading to the formation of a uniform surface (low pH) or well-defined ring (high pH). The macroscopic organization of the film is thus strongly dependent on the repulsive or attractive nature of the DLVO force. They proposed a phase diagram putting into relation three competitive flow patterns: a radial flow driven by the liquid evaporation, a Marangoni flow driven by surface tension gradient and a flow transporting the object to the substrate through attractive DLVO interactions (Figure 18).

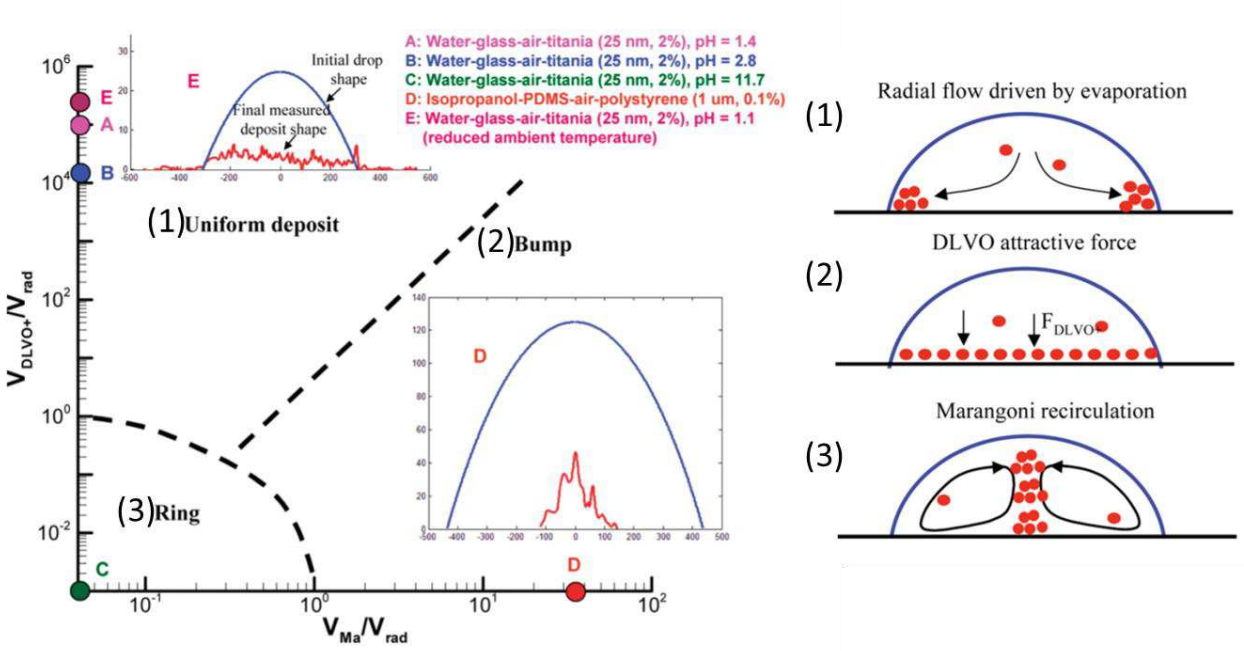

Figure 18. Phase diagram for self-assembly of nanoparticles during drop drying on a solid surface. The ratio of three characteristic velocities (V_{rad}, V_{DLVO+}, and V_{Ma}) determines the final pattern shape. V_{rad} is the radial flow velocity scale caused by the maximum evaporation rate at the pinned wetting line, V_{DLVO+} is the velocity scale caused by an attractive DLVO force, and V_{Ma} is the Marangoni velocity scale. Adapted from Bhardwaj et al[94]

The Marangoni effect may develop also interesting self-assembly patterns when it concerns particles which may tend to aggregate preferentially at near the water/air interface because of their low density. The work of Lee *et al.*[95] shows that convection forces can be promoted to achieve photonic crystals. To do so, they let to dry poly(styrene) aqueous suspension on a heating plate. The gradient of temperature between the bottom and the higher level of the drying suspension generated a gradient of surface tension. The promoted Marangoni effect allowed to achieve a more homogeneous deposit and inhibit the formation of the "coffee stain" pattern (Figure 19).

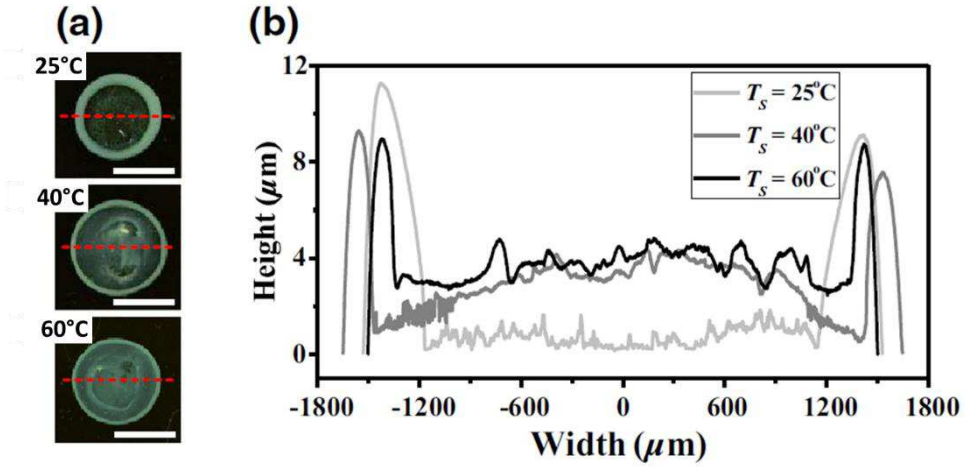

Figure 19. Thermal Marangoni effects on the final deposition pattern. (a) Comparison of the dried mark of an ethanol-water mixture (50:50 vol. %) containing PEO-coated silica nanoparticles (d = 228 nm) and remaining PEO at different substrate temperatures. The scale bars are 2 mm. (b) Comparison of thickness profiles along the red dashed line of (a); the light gray solid line, Ts = 25□C, the dark gray solid line, Ts = 40□C, and the black solid line, Ts = 60□C. Adapted from Lee et al.[95]

Drying of the suspension

The drying process of an hard spheres dispersion in a liquid has been intensively studied and can be separated has been separated in three different stages[96–101]:

(1) The constant rate period,
(2) The first falling rate period
(3) The second falling rate period

In the constant rate period (1), the volume reduction of the particle network equal simply to the volume of liquid lost through evaporation. At this stage, the evaporation rate per unit area of drying surface is constant. Indeed, a layer of liquid covers entirely the solid spheres, the liquid between them does not take affect the evaporation speed, and mechanical stress accumulation can be negligible. The air-liquid interface is macroscopically flat during this first stage of drying. The duration of this stage is therefore proportional to the initial volume fraction of solvent in the suspension[98]. Eventually the particle volume fraction in the drying film increases until a three-dimensional particle network is formed, it's the gel point[101]. At this moment of the drying process, the particle network develops some compressive yield stress, which increases as the drying continues. However, the particle network is able to remain undeformed if the applied isostatic compressive

consolidation pressure is less than the compressive yield stress. As the liquid evaporate, the liquid-air interface attempts to penetrate into the top of the arrangement of solid particles. To do so, it forms a curved meniscus between neighboring particles. These curved menisci between particles create an isostatic consolidation pressure on the particle network and a pressure gradient between the liquid at the surface, and the liquid in the interior of the drying dispersion. The liquid rises to the surface as a result of this pressure gradient and continues to evaporate at a constant rate.

During the second stage of constant rate drying (2), the top of the particle network and the air-water interface recede at the same rate. This is because the consolidation pressure applied to the particle network due to the capillary forces is sufficient to consolidate particle arrangement. As the network continues to consolidate, its compressive yield stress increases until the particle network has sufficient strength to withstand the capillary pressure and further consolidation is not possible at the capillary pressure determined by the curvature of the air-water interface.

At this point the third and final stage of drying begins (3). The liquid/vapor interface penetrates into the compacted arrangement and the evaporation no longer occurs at a constant rate as the liquid/vapor interface recedes into the pores between the particles. At this step, the capillary pressure decreases in the same time as the liquid/solid interfacial area. Eventually, the shrinkage of the solid particle network stops at this stage.

After the constant rate period, the first falling rate period describes the process of liquid flowing through the space between arranged particles, and the second falling rate period describes the final stage of drying, when liquid can escape only by diffusion *via* the vapor phase to the surface.

It is also worth noting that large and partially submerged particles can be immobilized by the thinning water layer as the vertical component of surface tension force pressing the particles against the horizontal substrate is huge. This phenomenon also serves as a condition for contact line pinning, which we will discuss later in section 4.2. Besides, formation of multilayer colloidal crystal is

possible if wetting angle is large or thickness of water layer is large[102]. Due to the almost fixed contact line formed by colloidal droplet on horizontal substrate, a variation of colloidal crystal thickness is commonly observed, from one single layer near the edge to multilayer further away from the contact line. In spite of evaporation, slight reduction of water layer thickness over time does not help in the uniformity.

Langmuir-Blodget deposition

The formation of monolayers is a well-known process, achievable an experimental approach called the Langmuir-Blodgett deposition[103]. The principle (Figure 20*a*) is commonly used with surfactants, such as oil and is quite straightforward. It can be also applied to colloidal materials as well, as long as they allow the formation of a monolayer at an interface. In such case, the dispersion of colloidal suspension at the interface will induce the spreading of the colloids, forming a spaced monolayer on the surface. In a second time, this spaced monolayer compressed through a barrier to reduces the available surface area, resulting in a rise of the surface tension. *Capillary forces* drive then the preliminary self-assembly of the colloidal at the interface air/liquid. The self-assembled compact monolayer of colloidal sphere can finally be gathered with a substrate. The lower surface tension provided by the substrate will cause the colloids to transfer from the interface.

The surface chemistry of the substrate on the colloidal crystal formation has been investigated by Reculusa and co-workers[104]. To do so, they tested several *hydrophobic* substrates by trying to form colloidal crystals using variously functionalized silica particles. Nonetheless, none of the silica particles were able to attach onto the hydrophobic surface, implying that the interaction between the liquid phase and substrate dominates the interaction between particles and substrate. Thus, the *hydrophilicity* of the substrate plays a fundamental role during self-assembly with a Langmuir- Blodgett method. The technique has its limits in terms of particle size and functionalization.

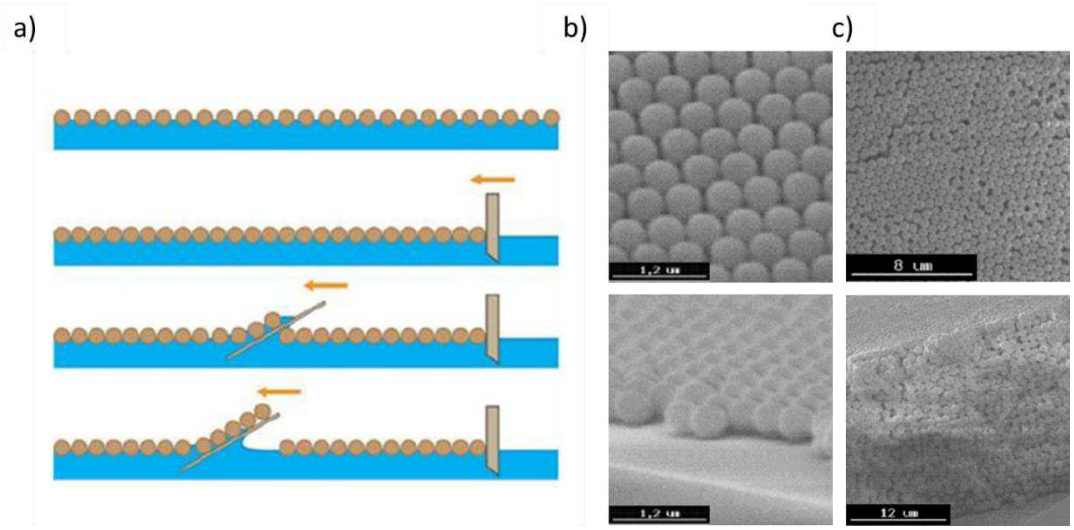

Figure 20. (a) Schematic representation of the Langmuir-Blodgett deposition method, adapted from Dommelen et al.[68] SEM picture of self-assembled films made from 680 nm SiO_2 spheres. (b) 1-layer deposition forming a 2D photonic crystal. (c) 25-layer film by successive Langmuir-Blodgett depositions, forming a 3D photonic crystal. Adapted from Reculusa et al.[104]

The technics was extensively developed, allowing nowadays the formation of stacked monolayers of colloidal crystal up to meters by roll-to-roll method, as developed by Parchine *et al.*[105]. In principle, the substrate is continuously withdrawn from a fluid supporting the compressed monolayer of self-assembled colloids. Multilayers are achieved by repeating the method on a covered substrate. The deposit self-assembled layers is not limited to planar substrate, as shown the works of Kohoutek *et al.*[106] (Figure 21) . They showed the coverage of three-dimensional object was achievable at the condition to control rigorously the continuous compression of the compressed monolayer at the liquid's interface, in parallel the withdrawn of the substrate. However, the Langmuir-Blodgett technics suffers from limitations: the self-assembly, as mostly driven by surface tension interactions, doesn't allow the spontaneous formation of multilayers in one deposition. Indeed, several succession Langmuir-Blodgett are required to form 3D photonic crystal. Even if a high regularity is achievable with this approach, it nevertheless required a substantial experiment set-up.

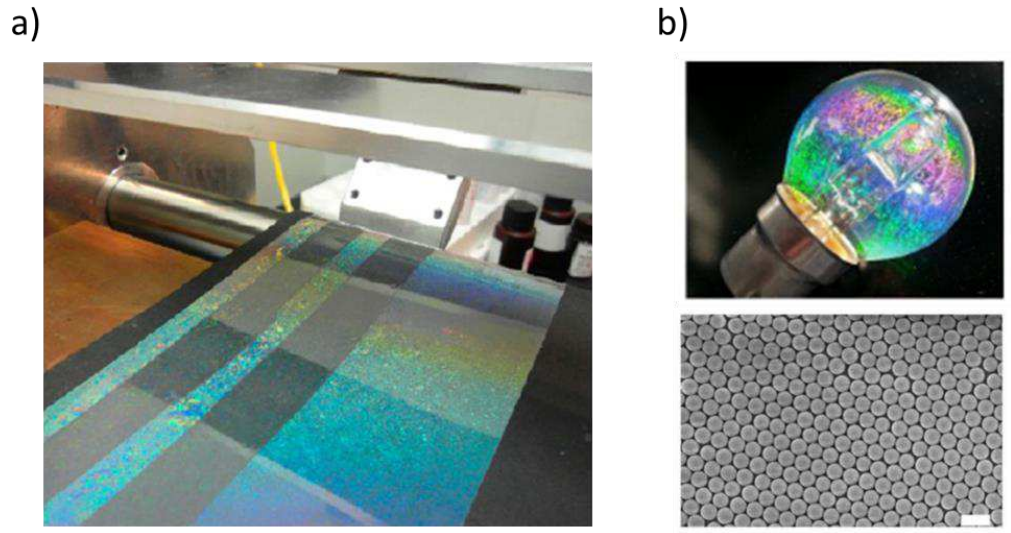

Figure 21. (a) Photograph of the roll-to-roll slot-die coating with strips of optical adhesive NOA164 on the PET substrate with the LB monolayer of silica spheres. Adapted from Parchine et al.[105](b) Photographic images of the 2D photonic crystal formed from 600 nm diameter silica particles assembled into a single-layer film on a light bulb and corresponding SEM image showing the close-packed ordering of the particles. The scale bar on the SEM image represents 1 µm. Adapted from Kohoutek et al.[106]

Vertical deposition / Dip-coating

The vertical deposition technic is also known as the Colvin method[102]. It can be easily set up with conventional lab tools. Briefly, the substrate is maintained partially immerged vertically into a colloidal suspension. The substrate's position is fixed whereas the suspension evaporates, letting ideally a self-assembled colloidal crystal thanks to the forces induced through the evaporation. Two inherent issues are related to this method: the increase of the particle layer number with time and the flocculation's risk due to the particle concentration increase, because of the gradual solvent evaporation. In response, Wong *et al.*[107] developed the technic to reduce the risk of flocculation with the addition of convection movement induced by a heat source. The mains advantage of this approach is the high regularity of the colloidal crystal achievable (Figure 22), however the process remains quite slow, as it could take from several days to weeks to form a dry film.

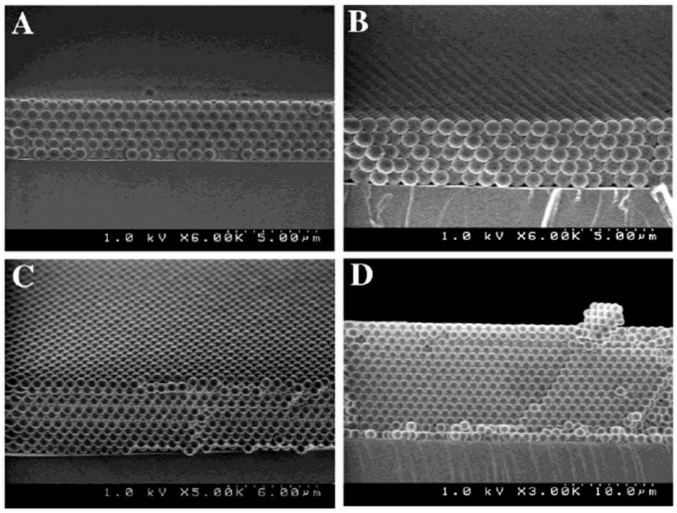

Figure 22. SEM images of the cross sections of the silica colloidal crystal films using thermally assisted vertical deposition (A) and (C) 635 nm, (B) 850 nm and (D) 1.0 µm spheres. From Wong et al.[107]

The dip-coating technic is a coating method which share several common points with vertical deposition. The experimental set-up barely the same, at the exception that the substrate is no longer static: it's withdrawn at a controlled speed. In 1996, Nagayama and Dimitrov suggested a model[108], confirmed later by Gu *et al.*[109], to control the *film thickness*:

$$k = \frac{2\beta h j_e \varphi}{0.605 R U (1-\varphi)}$$

Where k is the number of layers, U is the withdrawal rate, φ is the particle volume fraction, j_e is the solvent evaporation rate, R is the radius of the particles, h is the meniscus height and β is a ratio between the particle and the solvent velocity, generally close to 1. The main information brought by this equation is the number of layers is decreased when the withdrawal rate increase. It appears as a real issue for the formation of multilayers, *i.e.* 3D colloidal crystal, in a short period of time.

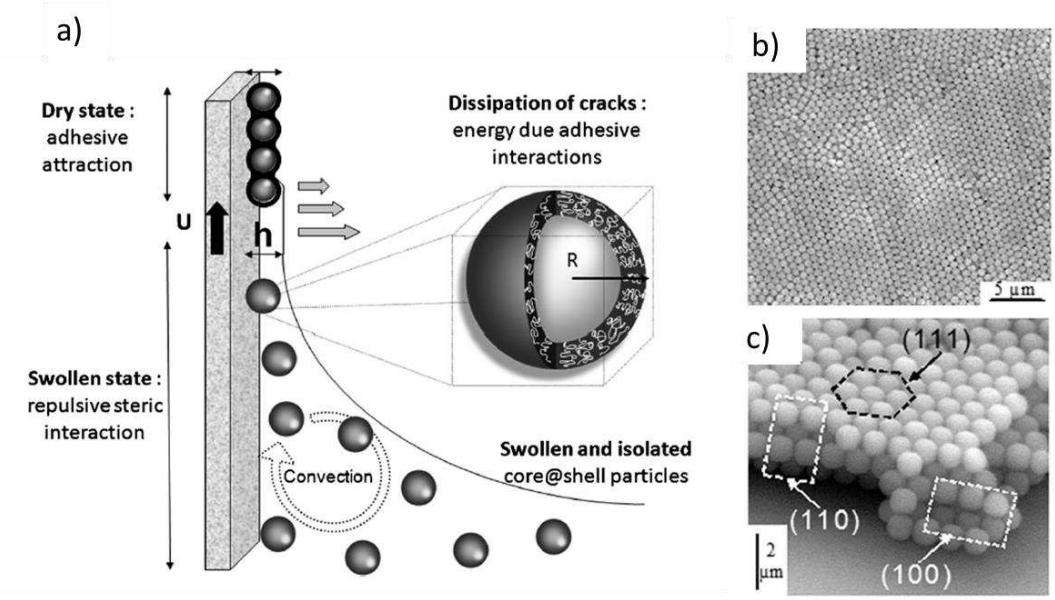

Figure 23 (a) grafted adhesive shell influence on the Dip Coating process (b) 3D hybrid photonic crystal from SEM observations on a top view, (c) a side view of (111), (110) and (100) plan of 3 stacked layers. Adapted from Deleuze et al.[110]

Nonetheless, a speed up of the fabrication was achieved by Deleuze *et al.*[110] in adjusting the deposit parameters (Figure 23). The solvent was wisely chosen to get a high boiling point and a low surface tension during the capillarity bridge evaporation, with here, N-Methyl Pyrrolidinone. The withdrawal rate was then significantly increased, from generally around 1 µm.s^{-1} to a maximum of 4000 µm.s^{-1}, and giving rise to three-dimensional photonic crystals ordered into a FCC lattice.

Doctor blade casting

A doctor blade is a device commonly used to print highly uniform films in the printing industry and used as well to create ceramic coatings. With this method, a blade applies a unidirectional shear force to a liquid that passes through the small gap between the blade and the substrate. The perpendicular blade moves thus closely along the substrate, leaving only a thin film of the initially deposited material. Prevo *et al.*[111] developed this doctor blade casting to elaborate self-assembled colloidal crystal, build on the same model than the one previously described with vertical deposition. In this way, they achieved a phase diagram of the structure achievable, using a dispersion of micrometric hard PS spheres as model. Controlling the blade speed with regard to the substrate, and the

suspension solid content, they achieve the controlled stacking of multilayered colloidal crystal (Figure 24).

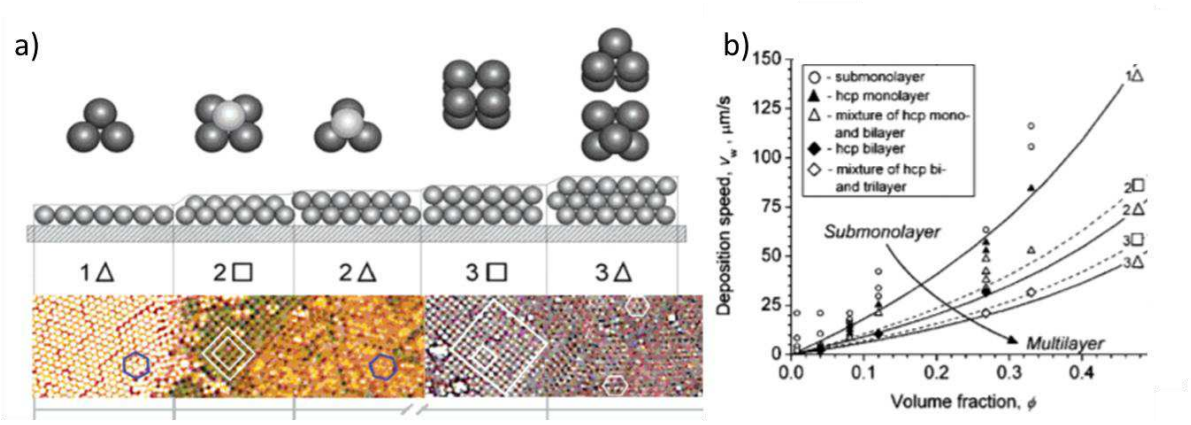

Figure 24 Layering transition schematic for monodisperse spheres. The experimental micrographs from this study on the bottom are made from polystyrene latex dispersions with a average of diameter 1.1 μm. The different colors of each layer are due to optical interference of the transmitted light. The polygons are to aid the eye. Adapted from Prevo et al.[111]

Yang and co-workers[112] extended this technique to produce close packed colloidal crystals. An amount of 1mL of silica particles suspended in Ethoxylated trimethylolpropane triacrylate (ETPTA), with a 20-50% volume fraction, was deposited on one side of the blade. The blade was then moved with a controlled speed and a thin layer was deposited with a long-range ordering in three dimensions. The ordered structures are a result of the *shear force* which, for viscous fluids, has a linear profile expressed as: $\tau = -\mu\frac{\delta v}{\delta h}$; where μ is the viscosity of the suspensions, v the speed of the blade and h the thickness of the film.

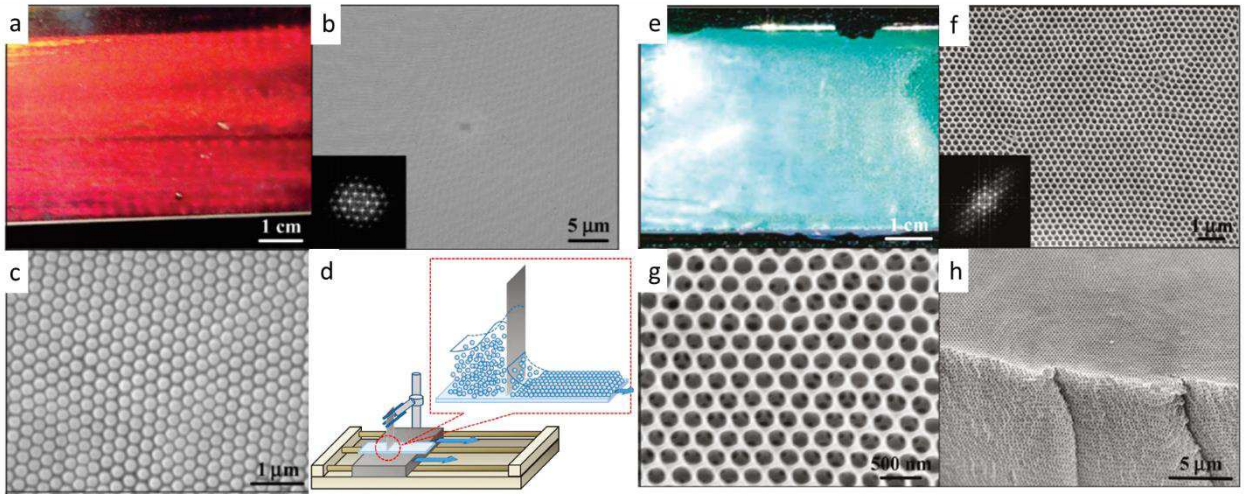

Figure 25. ***(Left)*** *Colloidal crystal-polymer nanocomposites fabricated by the doctor blade coating technique. (a) Photograph of a multilayer nanocomposite consisting of 290 nm silica spheres embedded in an ETPTA matrix coated onto a glass substrate. (b) Top-view SEM image of the sample in A. Inset showing a Fourier transform of a 40x40 µm² region. (C) Magnified SEM image of (B).*

(Right) *Macroporous polymer membrane after the selective removal of templating silica spheres. (a) Photograph of a free-standing, macroporous ETPTA film templated from 290 nm silica spheres. (b) Top-view SEM image of the sample in A. (c) Magnified SEM image of B. (d) Cross-sectional SEM image of the sample in (e). The samples were prepared by DB coating 50 vol % colloidal suspensions at a speed between 0.1-5 µm/s. Adapted from Yang et al.*[112]*.*

The silica template was then removed by a short hydrofluoric acid bath to from an inverse photonic crystal (Figure 25 *e to h*). The cross-section SEM images of the achieved structure shows the high degree of regularity achievable through doctor blade casting. As expected a significant change of the optical properties appears after the template removal, the high refractive index of SiO_2 being replace with the lower refractive index of air.

Nevertheless, the simplicity of this method is counterbalanced by its sensitive to dust and debris, which can easily inhibit the colloidal formation.

Among all those approaches observed in the previous section, all involved two elementary concepts to generate a self-assembly of colloidal objects: the nucleation of a small aggregate of particle called nuclei and the growth of these nuclei

2.2.3. Nucleation and Growth theory

The concept of nucleation has a general applicability in a variety of phase transition problems[113–115], including crystallization, melting, boiling, condensation,

precipitation, etc. In terms of nucleation, two dominant mechanism can be distinguished. First, *homogeneous nucleation* that happens freely in the surrounding medium when the concentration of objects is high enough force: their interaction leads to the formation of the aggregates giving rise of nuclei. However, the nuclei induced from the presence of dust particles, impurities or any interface, as the vessel walls, are considered as produced from *heterogeneous nucleation*.

The Classical Nucleation Theory (CNT) is the most common theoretical model used to understand the nucleation mechanism and can give a reasonable estimation of the nucleation rates. In the case of the homogeneous nucleation of colloidal object, the quantity of nuclei produced over time can be expressed as an Arrhenius's law following[116]:

Equation 16

$$J = J_0 e^{-\frac{\Delta G^*}{k_B T}} = \frac{\beta n D}{l^2} e^{-\frac{\Delta G^*}{k_B T}}$$

With ΔG^* is the nucleation barrier, n the particle number density, D the particle diffusion constant and l a typical length scale, k_B the Boltzmann constant, T the temperature and β, a proportionality constant, usually close to the unity. Two parameters of the Equation 16 may be noticed: First, the homogeneous nucleation rate is function of the diffusion of the colloidal object in the dispersion. According to Stokes-Einstein law[117] due to the Brownian motion, the smaller the object, the higher the diffusion constant. Second, there is an energy barrier ΔG^* to overlap in order produce nuclei.

The expression of the free energy of the system during a *homogeneous nucleation*[118] of a spherical crystallite for a colloidal object is given by (Figure 26):

$$\Delta G = \frac{4}{3}\pi r^3 \Delta g + 4\pi r^2 \sigma$$

Where r is the nuclei radius, σ the surface tension of the nuclei-liquid interface per unit area, Δg is the free energy difference between objects involved in an aggregate an those dispersed in the medium. Thus, the nucleation barrier corresponds to $\frac{\partial \Delta G}{\partial R} = 0$, and imply that $\Delta G^* = \frac{16\pi\sigma^3}{3\Delta\, g^2}$ defining a critical size under which the nuclei is not stable expressed as: $r^* = \frac{2\sigma}{\Delta g}$. It is worth noting that this

critical size depends then strongly on the surface tension of the nuclei. As the situation considered involves a high concentration of colloids usually assumed negative. The more attractive the interaction between colloids, the higher the $|\Delta g|$ value, thus the lower the nuclei critical size, allowing the start of the growth step.

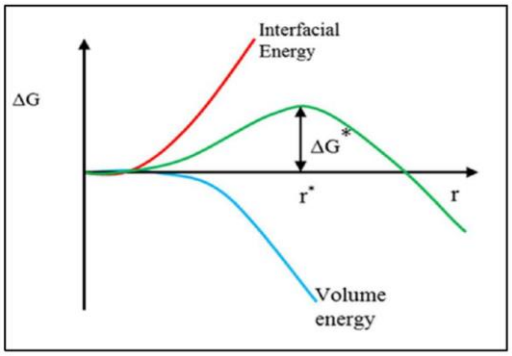

*Figure 26. Schematic representation showing the dependence of nucleation barrier ΔG*on the radius r according to classical nucleation theory. Adapted from Karthika et al. [119]*

Recently, Gasser *et al.*[118] worked on the nucleation of colloidal crystal of poly(methyl methacrylate) beads (R= 0.8 µm). They highlighted the polycrystallinity of nuclei in the very first stage of a *homogeneous nucleation* by confocal microscopy studies. More, isotropic are the colloidal objects, the faster is the growth of the nuclei.

The heterogeneous nucleation is phenomenon appears as a bit more complex. Sandomirski *et al.*[120] investigate the heterogeneous crystallization of hard-spheres near an interface, here a glass wall, over time (Figure 27).

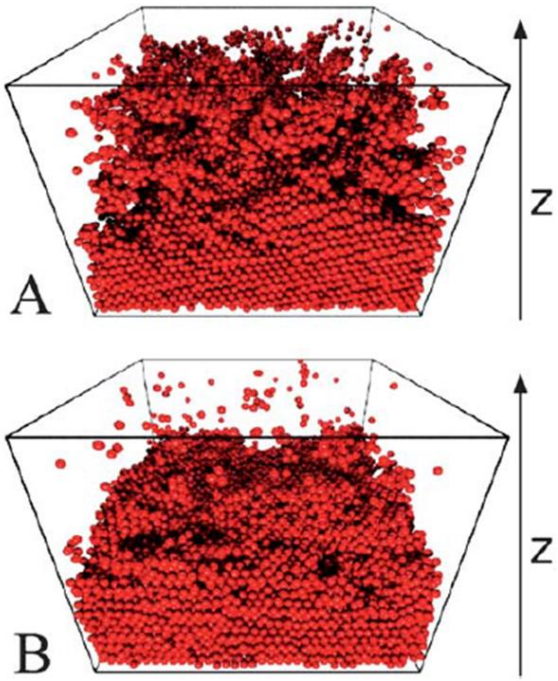

Figure 27 Snapshots based on (A) confocal microscopy and (B) simulations of a sample. In this reconstruction, only crystalline particles are shown and the simulation box is reduced in the z direction. Adapted from Sandomirski et al.[120]

In their study the driving force was gravity thanks to the size of their building blocks (colloidal beads with a radius of 0.9 µm). The crystallization process was followed here again by confocal microscopy and compared with Brownian dynamic simulations. In both case, colloidal arrangement with a higher degree of crystallinity was found close to the walls, while more disorganized arrangement was found in more distant area. The loss of compacity with the increasing distance from the wall was associated to a phenomenon of "caging" when the volume fraction of colloids become too high. The caging effect has especially a strong impact on the growth step of the crystal, inducing a decrease of the coefficient constant of the particle, limiting its possibility to contribute to the growth of a crystalline plan.

In complement, the works of Palberg *et al.*[116] the growth velocity of a planar interface can be expressed as a:

$$v = v_{\infty}\left(1 - e^{\left(\frac{\Delta g}{k_B T}\right)}\right)$$

Where $v_\infty = \frac{Dd}{l^2}$ is the limiting velocity and is given by the self-diffusion of particles to their target place, characterized by the particle coefficient constant *D*, through an interface of thickness *d.* According to the expression, the growth is thus limited by the mobility of the coefficient constant of the particle, in keeping with the Sandomirski's experimental results[120].

The Terrace, Ledge, Kink theory[121] is usually known in classical atomic crystal field for describing the surface defects on a crystal plane, triggered by temperature increase. It involves the consideration of several be atomic configuration (Figure 28*a*). Briefly, each atomic position in associated with the number of neighbors; its coordination number. The higher the coordination number, the higher are the energy holding the atom at its place. According to Nozawa *et al.*[122] the TLK theory take part of the growth of colloidal crystals. They studied the distribution of kinks sites in function the intensity of depletion forces to simulate attractive forces between PS particles (Figure 28 *b & c*). The kinks sites trends to decrease when the attractive force between particle increase. It indicates the surface of a growing crystallin plane appears less regular, with more kink sites, under weak attraction forces. In other words, the intensity of the attraction forces between colloidal sphere may impact the final crystalline structure.

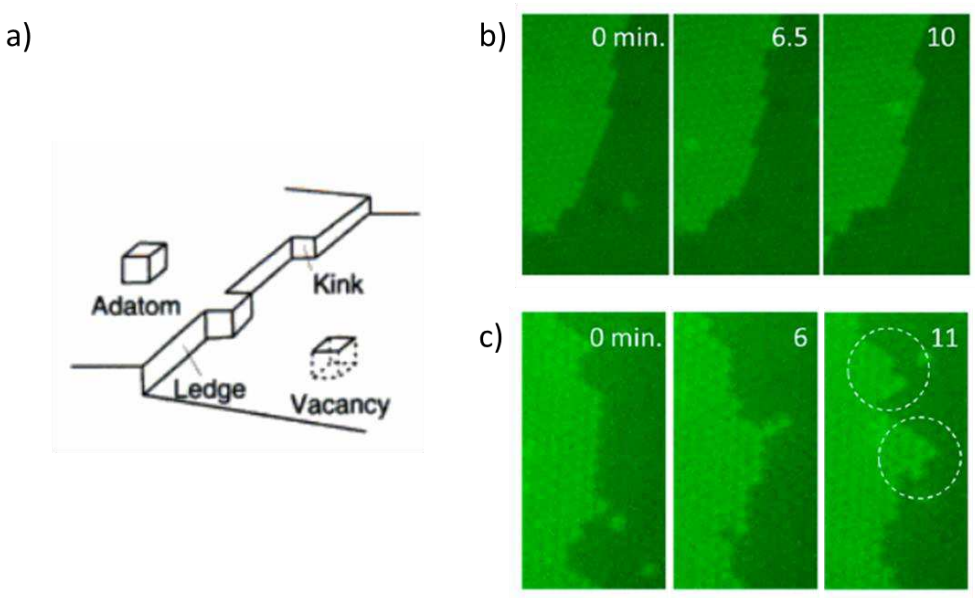

Figure 28. Schematic simple representation of the TLK sites, adapted from Lan et al.[121]. Detailed growth process of steps under high and low surfactant concentration (Cp). Snapshots of growing steps under (a) high Cp (0.15 g/L). and (b) low Cp (0.10 g/L). The dashed circles show the mounds formation. Adapted from Nozawa et al.[122]

The control of the self-assembly forces operating on building blocks leaded several teams to innovative materials. Possibly inspired by the skin of the chameleon, several scientific teams conceived responsive photonic crystals, playing with the optical rules governing the diffraction phenomenon.

2.3. ***Responsive self-assembled 3D photonic crystals***

Those innovative materials possess a diffraction- dependent coloration. As the structural colors are extremely sensitive to refractive index changes, and deformation, several teams elaborated color responsive material based on these physical characteristics.

2.3.1. Temperature responsive materials

Park *et al.*[123] succeeded to produce a thermo-responsive self-assembled photonic crystal. They designed core-shell colloids made of polystyrene for the core and poly(N-isopropylacrylamide) – PNIPAM – for the shell. The colloidal crystal was self-assembled thanks to depletion interaction against glass walls. The depletion forces were due to Polyacrylamide with a high molecular weight ($Mw = 5.10^6 – 6.10^6$ $g.mol^{-1}$) dispersed with colloidal building blocks (Figure 29)

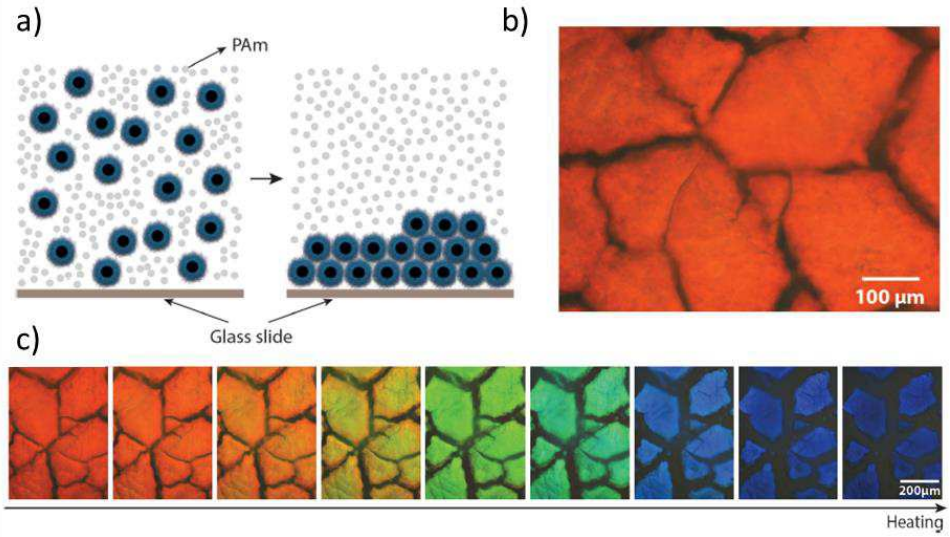

Figure 29. Polystyrene@PNIPAM core-shell nanoparticles self-assemble into photonic crystals through a depletion attraction (a) Self-assembly of colloidal crystals is driven by a depletion attraction induced by the presence of non-adsorbing polymer (gray dots). (b) An optical micrograph of the photonic crystals formed on a glass substrate shows highly uniform structural colors. (c) Series of optical micrographs of the photonic crystals taken during heating shows the uniform change in structural color upon heating. Adapted from Park et al.[123]

The photonic crystal achieved was then kept confined in the glass chamber used to its formation thanks to an epoxy sealing, preventing the evaporation of water. Because of the Low Critical Solubility Temperature behavior of the PNIPAM, it turns hydrophobic, when the temperature reaches its Volume Phase Transition Temperature (VPTT). The temperature has thus a strong impact on the size of the building blocks, the shell collapsing on the core when T>VPTT. As the inter-particle distance is correlated to reticular distances between crystalline plans with core-shell BBs, a modification of the temperature induces here a shift of the diffracted colors as expected from Bragg-Snell theory. The cohesion of the film here is assumed to be brought by the depletion forces occurring on the colloidal crystal against the glass wall.

2.3.2. Solvent-chromic materials

A color shift is thus expected each time the reticular distances are affected: in other terms, a swelling of the matrix separating can induce a sufficient deformation of the lattice to induce a red-shift (increase of d_{hkl}). In their works, Fudouzi *et al.*[124] self-assembled poly(styrene) beads with a size between 170 – 200 nm through a controlled evaporation process of an aqueous dispersion. The achieved photonic crystal was the filled in its interstices with a mix of

polydimethylsiloxane (PDMS) precursors. After a curing of one night at ambient temperature, and 6 hours at 55 °C, the material is achieved (Figure 30).

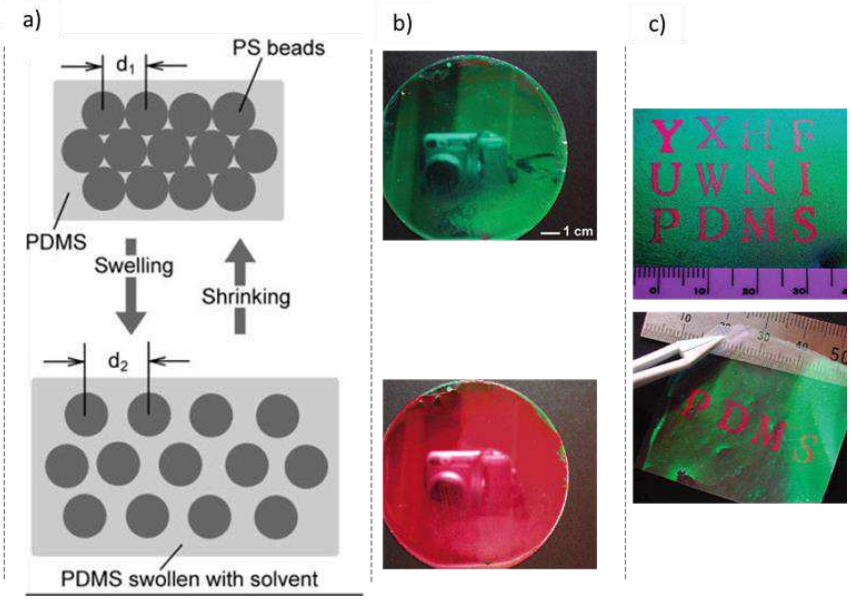

Figure 30 (a) A schematic illustration of the process in which the lattice is increased by swelling the poly(dimethylsiloxane) (PDMS) matrix with an appropriate liquid. The PDMS matrix will shrink back to its original state once the liquid has completely evaporated. (b) Photographs of a photonic paper before and after its color had been changed by covering the surface with 2-propanol liquid (c)Patterns generated on the surfaces of photonic papers with silicone fluid as the ink. The photonic papers were assembled from 202nm PS beads in a PDMS matrix.

The photonic crystal is thus composed of organized poly(styrene) beads embedded in a matrix of PDMS. The swelling of the lattice can be operated locally, defining the kind of materials as a photonic paper. The color change is more produced by a modification of the paper structure itself than by the ink. For instance, Zhao *et al.*[66] and Zhang *et al.*[61] exposed the possibility to use respectively invers opal and opal-like 3D photonic crystals as chemical sensors to probe specific concentrations of solvent, in function of the color shift of the material. In such case, the color shift is also impacted by the refractive index of the chemical probed, altering the average refractive index of the matrix.

2.3.3. Mechano-chromic materials

- *Hybrid colloidal mixture between organic and inorganic objects*

Wu *et al.*[125,126] made mechano-chromic films from the drying of a batch mix of nanosized silica (20 nm) and colloidal copolymer of poly(styrene-butyl acrylate) (Figure 31). The styrene presence into the colloidal copolymer promotes a

refractive index difference between the beads and the matrix. On the counter part, the butyl acrylate increases the mobility of the chains constituting the beads at ambient temperature and ensuring the film cohesion through their intertwining. However, the use of such nanosized silica (20 nm) may be controversial in the context of a cosmetic application[127]. Indeed, due to their size, they may increase of the risks of inflammatory reactions and may have a potential genotoxicity.

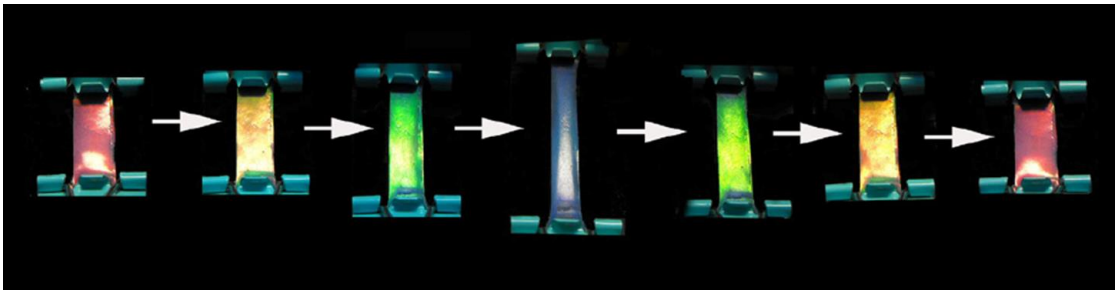

Figure 31 Optical images of the crystal film during a stressing and releasing cycle. Adapted from Duan et al.[126]

- *Swelling and photocuring of photonic crystals*

Foulger *et al.*[128] proposed to freeze a self-assembled photonic crystal of crosslinked poly(styrene) beads through, first, a photoinitiated polymerization of methacrylate functionalized poly(ethylene glycol). Then, the dried organic composite was swollen with 2-methoxyethyl acrylate and a photo-initiator (2,2-diethoxyacetophenone) before an UV curing. Here, the PEGMA matrix/PS beads system insures the required refractive index difference to get photonic properties. The photochemically crosslinking allowed here non-destructive deformations of the arrays, and thus mechano-chromic properties.

Inomata *et al.*[62] made a self-assembly of poly(ethyl acrylate-methyl methacrylate), successively swollen by an aqueous solution of ethyl acrylate, ethylene glycol di-methacrylate (a crosslinker) and a thermal initiator. Once swollen, the array is frozen by a thermally initiated reticulation. Here the dried films produced are colorless, but display photonic colors once swollen. Due to its *thermal treatment*, the swollen films are cohesive enough to present mechano-chromic properties.

Similarly, Chen *et al.*[63] modified a crosslinked poly(butyl acrylate) self-assembly through swellings with relatively hydrophobic and hydrophobic

monomers. The hydrophobic one, 2-ethylhexylacetate is firstly introduce to swell the colloidal crystal, then the acrylamide monomers is added in the water dispersion. An *UV curing*, allowed by the presence of benzophenone, produce the formation of poly(acrylamide-2-ethylhexylacetate) chains inside and between the PBA spheres, promoting its cohesion properties. The obtained material display mechano-chromic due to increase of the refractive index difference between the beads, and the surrounding matrix, during the UV curing of the monomers.

- *Hard core@soft-shell self-assemblies*

Such structures are made usually with a hard core presenting a high refractive index and a soft shell with a lower refractive index. Several self-assembly strategies can be explored, depending of the organic or inorganic nature of the cores.

For instance, concerning inorganic cores, Chen *et al.*[129]. conceive a mechano-chromic based on the self-assembly properties of iron oxides, Fe_3O_4 under a magnetic field. The organized array was frozen through the free-radical polymerization of monomers solubilized in the surrounding dimethylformamide. The reaction is thermally initiated at 70°C, to form a copolymeric gel composed of *N*-vinyl caprolactam and *N*-hydroxymethyl acrylamide, encapsulating the magnetically self-assembled Fe_3O_4 array. Kim *et al.*[129–132] proposed a core-shell architecture of silica cores (with an average refractive index of 1.45) with an adsorbed shell of poly(ethylene glycol) phenyl ether acrylate (PEGPEA) (Figure 32). The films are made through the suspension infiltration in a confined space, between two glass layers separated by 50 µm. Then the self-assembled structure is fixed by UV-photopolymerization.

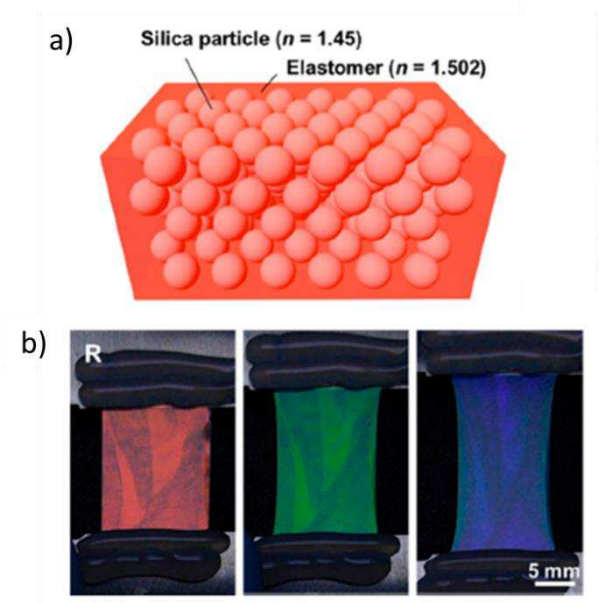

Figure 32. (a)Schematic of mechanochromic photonic films composed of a non-close-packed array of silica particles embedded in an elastomeric matrix. (b) Series of photographs of a photonic film with three different strains taken in reflection. Adapted from Lee et al.[131]*1*

With organic cores, Viel *et al.*[133] conceived a mechano-chromic photonic material. Their colloidal objects are core@interlayer@shell (CIS) system, made of poly(styrene)@poly(methyl methacrylate)@poly(ethyl acrylate). Those CIS objects are made by successive free-radical emulsion polymerization. Then, the dried suspension is mixed with a benzophenone (UV initator) at 120 °C into a micro-extruder to form opalescent films. Those films are finally crosslinked under an UV light.

The production of such responsive photonic crystal involves a strong control on the design parameters of the BBs. Concerning building blocks, the core-shell architecture offers the possibility to set on the same time the refractive index of the scattering beads (core) and its surrounding matrix (shell). As seen earlier, the produced color can then be controlled by the thickness of the grafted shell, according to the core size. The conception of such colloidal object isn't straightforward, and require a careful control of the synthesis process.

2.4. ***Core-shell colloidal design***

Microgels are made with a large variety of polymers, in organic solvent[134] or in water[135–140]. In order to explore different applications possibilities, they can be combined with different materials. They can be noticeably assembled into a

core-shell architecture[141–148,148–159]. Several syntheses have been used in the frame of patented applications. In the next sub-section, a slight description of the synthesis processes usually developed are displayed

Several synthesis ways exist to produce such core-shell colloidal designs. They may be produced through the *self-assemblies' properties of macromolecules*, but most of the time they involved the sequential production of the core, then the organic shell. The targeted cores are then qualified as *seeds* on which the shell would be formed. The shell formation is a critical step, that may require pretreatment steps on the cores 'surface to reduce the *surface tension* differences with the forthcoming shell. Reactive functions may also add on seeds 'surface to make the shell through *condensation reactions*, or *controlled radical polymerizations*. In some cases, polymerizable surface functions may be available directly after the polymerization of the seeds. Consecutively, the shell can be directly synthesized and graft at its surface through *seeded polymerization processes*. The next section describes firstly the general synthetic overview of these synthesis ways.

2.4.1. Core-shell made by self-assembly

Solutions exist to perform the formation of core-shell structures laying on the self-assembly abilities of polymers. The driving forces are usually hydrophilic/hydrophobic interactions from polymerizable block copolymers (BCPs) or the electrostatic interactions from polymers wearing electronic charges.

This solubility difference between hydrophobic/hydrophilic polymers is exploited to force the self-assembly of core-shell structures in water. In a first step, the hydrophilic material is synthesized as seeds. In a second step, the hydrophobic material is synthesized on those seeds. As the two step are done in water, at some point a phase inversion occurs, resulting in a core-shell structure with a hydrophobic core surrounded by a hydrophilic shell[154,156,157,160].

A simpler approach can be performed in a "one-step" process to generate core-shell geometries. In such case, macro-monomers with hydrophilic chains (PEG, PVP) are combined with monomers leading to hydrophobic polymers (PMMA, PS)[153,161,162].

A last synthesis path which use controlled radical polymerization can be exploited. Controlled radical polymerization can be presented as a "living" polymerization: the termination reactions are inhibited to the profit of growth reactions. Three main process are used: Reversible Addition-Fragmentation chain Transfer (RAFT)[163] polymerizations, Atomic Transfer Reaction Polymerization[135] (ATRP) and Nitroxide-Mediated radical Polymerization (NMP) polymerization[164]. Thanks to these processes, it is possible to form block copolymers that self-assemble into core-shell like structures in dispersed state. Such kind of process is also called Polymerization-induce Self-Assembly (PISA). However, these processes might expensive reactants and/or implies several purification steps to get rid of the remaining catalyst for a cosmetic application.

Electrostatic interactions can also be exploited to make multi-layered core-shell structures. In the associate reference[149], the negatively charged polymer (poly(4-styrene sulfonic acid)) is adsorbed on positively chitosan based core. Successive layers are added by alternated addition of positively charged polymer (polyallylamine) and negatively charged polymer. The layer addition is realized with successive dispersions and filtrations.

2.4.2. Condensation reaction

Condensation reaction are also used to make core-shell structures. These reactions result in the formation of an ester or an amide bond. It involves usually carboxylic acid functions and hydroxyl/amines functions to form an ester/amide bond. This path permits to covalently link cores and molecules which present orthogonal reactive functions. These molecules can be unsaturated monomer as pre-made polymers.

In such way, thermo-responsive made core-shell structure can be made. In a first step PNIPAM cores are made by controlled radical polymerization. Then, PEI shell is grafted in a second step[142] with a condensation reaction of acids & amines functions.

An esterification process can also be employed to graft available double bonds on the surface of a core[148]. This process is thus combined with free radical

polymerization to enhance the bonding of the hydrophilic shell on a hydrophobic substrate

2.4.3. Seeded polymerization

The process of seeded polymerization is a powerful tool to control the quantity of particles into the medium. It requires monodispersed particles of controlled size – the seeds. In seeded emulsion polymerization, the main advantage is to limit the nucleation step. At the end of, the number of final particles is equal to number of seeds. For instance, Macchione *et al.*[165] and Ho *et al.*[166] reviewed several grafting methods to form hybrid particles and gathered them in three categories: "grafting-*from*", "grafting-*to*" and "grafting-*through*" (Figure 33).

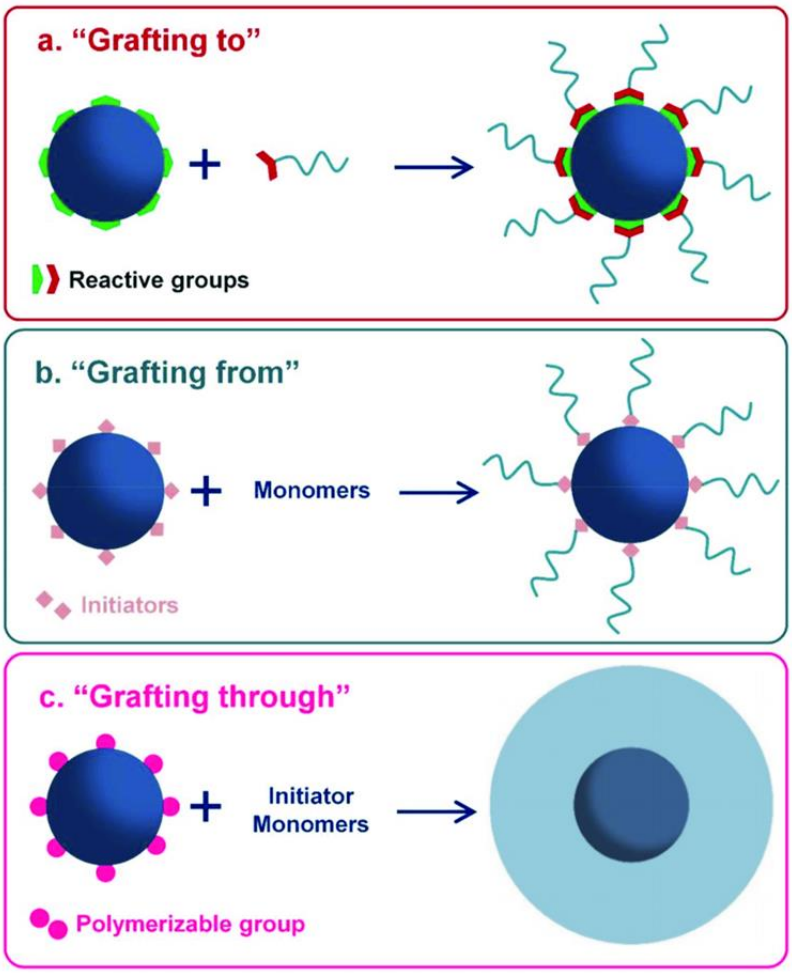

Figure 33. Schematic representations of grafting strategies. Adapted from Macchione et al.[165]

With "*grafting-from*" methods, the surface particle is decorated with initiator sites that can induce the polymerization of a new layer. With "*grafting-to*"

conditions, polymers and particles surfaces possess orthogonal chemical functions able to react with each other, making a covalent bond between the grafted material and the seed. Finally, "*grafting-through"* methods involve the polymerization of surface functions on the seeds taking part into the polymerization process of the shell.

For all the seeded processes involved in the fabrication of photonic materials, the control of the shape and the size in the colloidal scale of the seeds is essential. Nowadays the control of these properties is achievable through well-known emulsion and precipitation polymerization.

Seed synthesis - Emulsion polymerization

Colloidal beads are usually done through several synthesis methods that can be related to classical nucleation and growth theory. Depending on the surfactant quantity, from none with precipitation polymerizations to a high concentration with mini-emulsion polymerizations, the nucleation of the colloids will be altered. It relies on the difference of solubility between the cores

Traditionally, *suspension polymerization*, *dispersion polymerization, emulsion polymerization and precipitation polymerization* are the preferred synthesis procedures for the polymerization of organic beads[167]. Among them, *suspension polymerization* involves a process in which monomers, relatively insoluble in water, are dispersed as liquid droplets with a steric stabilizer through a vigorous stirring. The size dispersion of particle is influenced by the control of dynamic process control (stirring). The achievement of small colloid is achievable, but at the cost of an increase of the size polydispersity, with reactions times up to 24 hours. In *dispersion polymerization*s, the beads formations rely on the solubility difference between the polymers and the monomers. It requires thus organic solvent, leading to the formation of swollen organic beads, sterically stabilized. Indeed, stabilizers such as poly(vinyl pyrrolidone) (PVP) must be utilized to stabilize polymeric particles and prevent particles from coagulation Comparatively, *precipitation polymerization* is based on similar phase segregation of the growing polymer than the *dispersion polymerization*. The peculiarity of the precipitation polymerization comes from the absence of stabilizing agent which is

a key element is dispersion polymerization: the growing oligomers are not swollen with the solvent and truly precipitate.

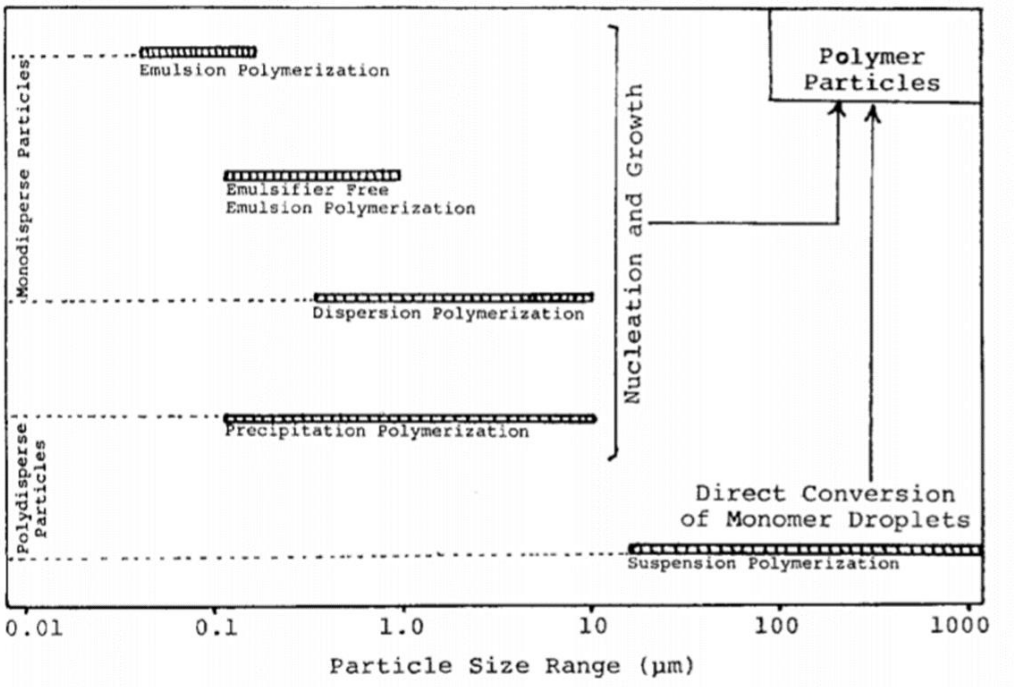

Figure 34. Comparison of several synthesis approaches for the formation of colloidal beads. Adapted from Arshady et al.[167]

Emulsion polymerization allow to achieve easily small colloidal particles with a narrow size distribution (Figure 34). A typic emulsion polymerization requires the dilution of a quantity of surfactant, the surface agents dispersing the monomers into droplets. With this free-radical polymerization process, the polymerization is usually thermally activated thanks to the addition of an initiator into the hot mixture. The emulsion polymerization mechanism is well known[168,169], and is usually described in two steps.

When the initiator is activated, usually through heating, free radicals are formed in the solvent where a slight fraction of the monomer is dissolved. The meeting of both molecules initiates the polymerization in the solvent, it's the *nucleation step*. Following the experimental conditions, several mechanisms happened simultaneously or in different proportions.

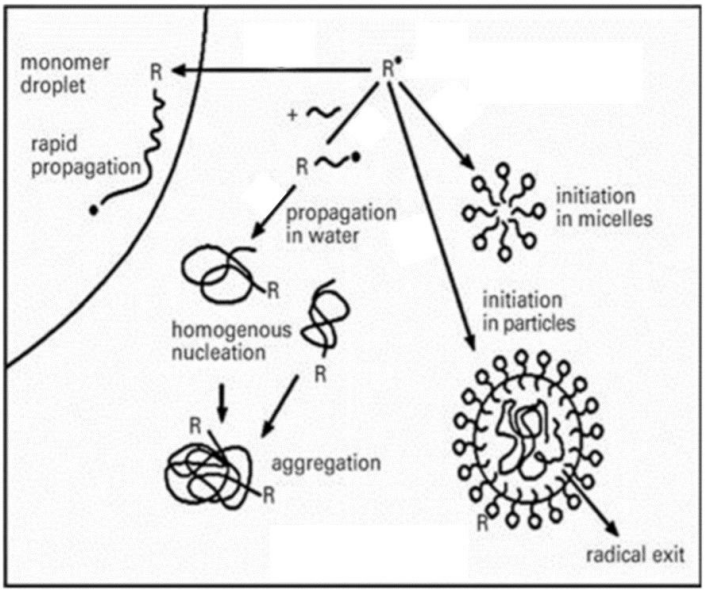

Figure 35. Schematic representation of an emulsion polymerization mechanism. The "R" letters stand for the activated initiators. Three nucleation mechanism are exposed: from a monomer droplet, homogeneous nucleation, and micellar nucleation. The average number of radicals per aggregate is on equilibrium during the growth phase, the entering radicals counterbalancing the exits. Adapted from Distler et al.[169]

Above the CMC, a large number of micelles are formed in the mixture. The small size and the number of the micelles is high against the reservoir droplets. The free radicals and oligo-radicals have statistically more chance to encounter a micelle than a droplet. In this case the nucleation mechanism is *micellar*. Under the CMC, the nucleation is called *homogeneous*. There are no micelles. Oligo-radicals precipitate in solution, stabilized by surfactants, when they achieve a critical size. In both cases, the oligo-radicals growth is fed by the monomers diffusing through the solvent. A third mechanism is possible, when the initiator/oligo-radicals come directly into a monomer reservoir droplet. This droplet nucleation mechanism, is statistically disfavor in classical emulsion polymerization, due to its small number in solution.

This nucleation step, is followed by a growth step. The polymerization continue in the nuclei until no more monomers are available. The control of the nucleation/growth step during the synthesis allow to control the particle size and its distribution.

In the case of a homogeneous nucleation, the concentration of latex particle can be set in function the concentration of surfactant and initiator operating during the nucleation process. Then, according to the Smith-Ewart Theory[168]:

$$\begin{cases} N_p \propto C_{surf}^{0.6} \\ N_p \propto C_{init}^{0.4} \end{cases}$$

Where N_p is the average number of latex particles nucleated per unit of volume of water, C_{surf} and C_{init} are respectively the surfactant concentration and the initiator concentration. In other terms, it allows for a defined quantity of monomer to control the size of the latex particle in function of the number of particles nucleated: the higher the N_P values, the lower the final latex size.

Nevertheless, the chemical affinity between the seeds, the polymer forming the shell and the solvent is crucial to control the design of the final colloidal objects. Indeed, Herrera *et al.*[170] suggested a phase diagram (Figure 36) covering the possible scenarios in function of the surface tension evolution between the seeds (1), the material forming the shell (2) and the solvent (3). Organic seeds can be designed to prevent the phase inversion between the core/shell material. Indeed, the macromolecular chains constituting the seeds can be covalently crosslinker during their synthesis, leading the formation of a three-dimensional mesh with fixed nodes.

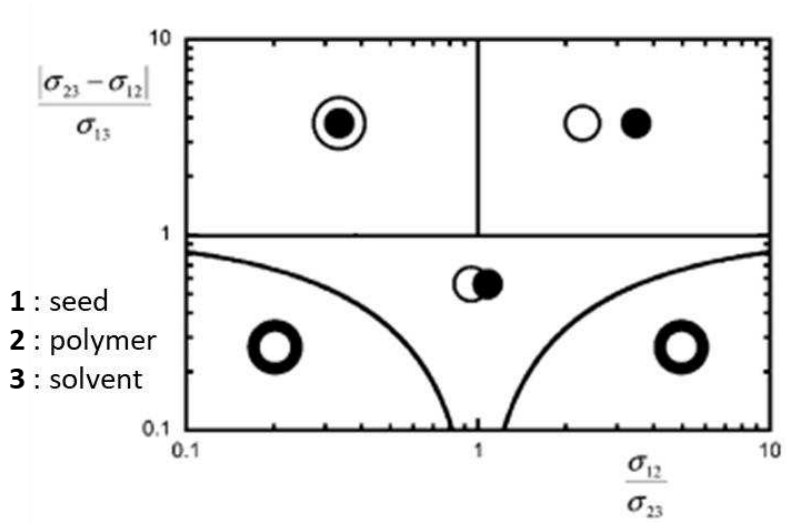

Figure 36. The control of the surface energy between the seeds, the polymer and the solvent can give rise to several molecular self-assembly scenario. Adapted from Herrera et al.[170]

Seeded emulsion polymerization

Core-shell architecture can thus be designed through successive seeded emulsion polymerization. The second emulsion polymerization is performed in presence of already synthesized latex, the seeds. Here again, the seed are introduced to inhibit the nucleation phenomena of the precipitating polymer and promote its the growth on the latex surface. As a usual emulsion polymerization, the process is commonly done in water with the presence of surfactant[139,143,145,150,151,171,172]. The hydrophobic monomers are polymerized under the control of the temperature, the stirring speed, the initiator and surfactant concentrations. The seeds are usually purified by dialysis or centrifugation, before the shell grafting step.

Seeded emulsion polymerization is especially exploited to form hybrid core-shell structures, with an inorganic core. By skipping the polymer nucleation step, the seeded process allow to grow a variety of polymers on organic as inorganic colloidal object, as on carbon quantum dots[144] or on gold nano-rods[146].

Seeded precipitation polymerization

Precipitation polymerization are made from monomers giving rise to macromolecules with a Low Critical Solubility Temperature (LCST). Those polymers have the advantage to switch from hydrophilic to hydrophobic when the temperature reach a specific temperature called the Volume Phase Transition

Temperature (VPTT). Above the VPTT, the polymer/solvent interaction are destabilized by the molecular Brownian motion, promoting the polymer/polymer interactions: the polymer collapse on itself. Below the VPTT, the macromolecules are swollen by the solvent. With free-radical polymerization thermally triggered, it offers the possibility to produce thermo-responsive polymers from a precipitation polymerization. Thermo-responsive microgels can be achieved if crosslinkers are added preventing the dissolution when the temperature decreases above the VPTT. Polymers made with crosslinkers, are usually made of thermo-responsive polymers as Poly(N-isopropylacrylamide) – PNIPAM) – crosslinked with N, N'-Methylene-bis-acrylamide (MBA).

PNIPAM can be used as a core[147] or shell material, depending on the application & the properties aimed. The core-shell structure is usually obtained through a seeded polymerization. In the optic of forming a PNIPAM shell, the seeds are firstly systematically purified[146,155] when a free radical polymerization is involved. Indeed, the presence of residual surfactant is known with PNIPAM to inhibit its growth on seeds[173]. The seeds used can be whether made with a hydrophobic polymeric material[155], or an inorganic material[144,146]. However, seed purification can be avoided in at least two cases. The first one when the core is also made of PNIPAM[147], the shell monomeric material is then added consecutively at the core synthesis. The second one is when polymerizable inorganic carbon quantum dots[144] are used as seeds.

The case of seeded precipitation polymerization of thermo-responsive material appears in the literature. In the work of Anderson *et al,* they used process of seeded precipitation polymerization to graft thermosensitive PNIPAM microgels on a PS particles[174]. They synthetized firstly PS seeds by emulsion polymerization. Then, by adjusting the quantity of latex and PNIPAM microgel precursor, they synthesize particles with several hydrodynamic thickness of PNIPAM shell. In few words, they dissolve NIPAM and MBA (crosslinker) into latex solution, then they inject KPS (initiator) into the mixture at 70°C. Due to its VPTT, the PNIPAM microgel synthesized at this temperature is hydrophobic in an environment made of water and PS particles. It results a promoted aggregation of the PNIPAM microgel nuclei on the PS particle to reduce the surface tensions in the solution.

It seems that the grafting of the PNIPAM on the PS seeds is due mainly to physical properties of the microgel. Once adsorbed at the surface of the PS seed (T°>VPTT), the microgel is kept at the surface due to its high glass transition temperature *Tg* (Tg_{PNIPAM} = 90°C) and the reticulation nodes that maintain the integrity of the shell. As the synthesis is made under a free radical process, some transfer reaction could possibly occur between the core and the seed material and then stabilize the grafting.

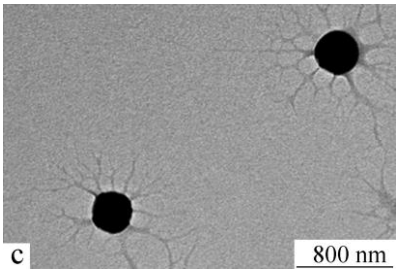

Figure 37. TEM images of PMMA/PNIPAM core-shell particles synthesized by seeded precipitation polymerization, continuous addition at 0.5 mL/min. From Shi et al.[37]

The way to introduce monomers in the mixture as a strong impact on the grafting quality. Shi *et al.*[175] compared the impact of PNIPAM microgels monomers addition conditions, batch wise or continuously, on the PMMA@PNIPAM structure. They obtained particles with an inhomogeneous shell presenting fractal moieties. In this case the KPS is mixed firstly with the PMMA seed dispersion under nitrogen. The PNIPAM microgel monomers are added then continuously at 70°C in the case presented in Figure 37. The first addition of the initiator could favor the transfer reaction between the growing microgel and the PMMA surface. It seems that the seeded precipitation polymerization realized in starved conditions could promote, the transfer reaction between the core and the microgel, but with the apparition of a inhomogeneous shell in the case of the PNIPAM.

Seeded precipitation polymerization are done often from seeds made by emulsion polymerization. In the case where the seed are not purified, the presence of surfactant could interact during the grafting step. Indeed, considering the work of Nguyen[176], the nucleation step of the microgel could be a key parameter to control the particle morphology and the grafting efficiency. In another work of Andersson *et al.*[173], the surfactant concentration appears to stabilize the formation of smaller PNIPAM microgel particles. This involve that the presence of surfactant in a seeded precipitation polymerization could induce the nucleation of more microgels nuclei, with a smaller critical diameter, than in the same conditions without surfactant.

Table 1 Preparation of the Microgel Samples. The Measured Values of Hydrodynamic Radius and the Results of Electrophoretic Measurements, from Andersson et al.[173]

Sample	MBA (mM)	SDS (mM)	R_h (20 °C nm)[a]	R_h (50 °C nm)[a]	μ_e (20 °C × 10^{-8} m^2/Vs)[b]	μ_e (40 °C × 10^{-8} m^2/Vs)[b]	ζ (20 °C mV)[c]	ζ (40 °C mV)[c]
S0.4	1.6	0.4	200	92	−0.18 (±6%)	−4.52 (±4%)	−2.4	−40.7
S1.3	4.2	1.3	97	46	−1.32 (±5%)	−4.61 (±4%)	−16.9	−41.5
S4.0	4.2	4.0	65	29	0.16 (±6%)	−0.34 (±6%)	+2.1	−3.1
S6.7	4.2	6.7	35	19	0.16 (±7%)	−0.09 (±7%)	+2.1	−0.8

In each synthesis batch, the NIPAM concentration was 130 mM, the KPS concentration was 2 mM, and totally 26 mL water was used (20 mL in S0.4).
[a] Hydrodynamic radius (mean, DLS/CONTIN) from the intensity-weighed size distributions in H_2O.
[b] Electrophoretic mobility (mean, six measurements, deviations in brackets) by Zetasizer in H_2O.
[c] Zeta potential (Smoluchovski approximation, mean, six measurements) by Zetasizer in H_2O.

Nevertheless, PNIPAM is characterized by a glass transition temperature (Tg) around 140 °C, meaning at ambient temperature its molecular chains are frozen. This glassy state of the material has strong impact on its mechanical properties, forbidding any structural rearrangement under constrains once dried.

Since the re-highlight in 2008 from Lutz *et al.*[177] about the thermo-responsivity of Poly(oligo(ethylene glycol) methyl ether methacrylate)–(POEGMA)–based polymers, several teams worked on its development. Indeed, due to its ethylene glycol chains, these macromolecules can develop reversible interaction with temperature. The induced VPTT can be set in function of the length and the proportion of oligo(ethylene glycol) chains. Briefly, the longer the ethylene glycol chains, the higher the VPTT.

Boularas *et al.*[178–181] designed POEGMA based microgels by *precipitation polymerization*. The polymeric phase was made of diethylene glycol methyl ether methacrylate (MEO_2MA), oligo ethylene glycol methyl ether methacrylate (OEGMA), methacrylic acid (MAA) and oligo ethylene glycol diacrylate (OEGDA) with a molar composition equal to [MEO2MA:OEGMA:MAA:OEGDA] = [84:9:5:2]. The MEO_2MA/OEGMA ratio was designed to set a VPTT around 32°C, *i.e.* average human skin's temperature, with average molecular masses of 250 $g.mol^{-1}$ and 475 $g.mol^{-1}$ respectively for OEGDA and OEGMA. More, the thermo-responsivity of the material is supported by a pH-responsivity due to the presence of the MAA function on the microgel arrays. Depending on the ionization state of the MAA part, which is pH dependent, the water/polymer solvent can be either reinforced or inhibited. Moreover, they also demonstrated very interesting cohesive and self-supported film-forming

properties by water evaporation[181]. This POEGMA-based microgel offers several advantages to the elaboration of a photonic material: performant self-assembling properties and strong cohesive interaction thanks to chains entanglement (Figure 38).

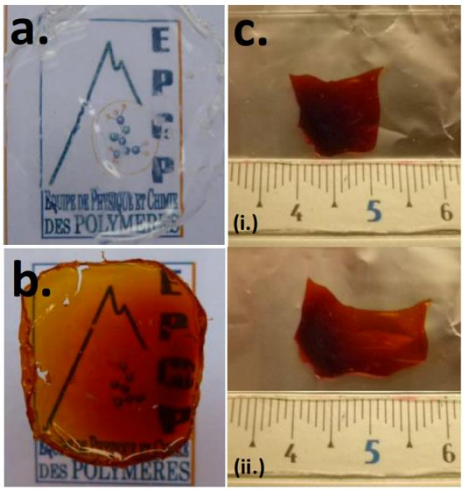

Figure 38. Images of OEG-based microgel films prepared by solvent evaporation of a) P(MEO2MA-co-OEGMA-co-MAA) microgels, b) γ-Fe2O3/P(MEO2MA-co-OEGMA-co-MAA) hybrid microgels with 16 wt-% of γ-Fe2O3, c) Elastic self-assembled γ-Fe2O3/P(MEO2MA-co-OEGMA-co-MAA) hybrid microgels films at the equilibrium state (i) and after elongation (ii). Adapted From Boularas et al.[181]

Throughout the rest of the document, this last multi-responsive microgel will be developed toward the design of hard-core@soft-shell building block, for the elaboration of bio-inspired photonic crystals.

Conclusion

Among the multitude of creatures displaying with iridescent coloration, their ornaments all share a regular organization of the matter which constitute them at the colloidal scale. This regularity is characterized by a periodicity, either in one, two or three dimensions, and by a corresponding alternation of material with different optical properties. This specific organization of the matter at the colloidal scale, *i.e.* between 1 and 1000 nm, is associated with the apparition of iridescent colorations. These structural colorations are even able to be modified depending to the self-assembled structure. The overview about the light-matter interactions exposed the light diffraction phenomenon involved with such colors. The electromagnetic interactions within periodic materials are extremely sensitive to the unit cell design, and the refractive index of the matter which constitute it. The colors are produced because of photonic band-gap, analogue to electronic band gap in dielectric materials, and induce a selective reflection of light wavelength corresponding to the forbidden band-. The position of this photonic band-gap can be easily predicted with a Bragg-Snell equation for crystals made of spherical building blocks.

Artificial Photonic crystals can be made with a large variety of choices, depending of the production conditions. We exposed the advantage of "bottom-up" technics, involving the self-assembly of colloidal building blocks (BBs). One branch of among the tree of possibilities offered by bottom-up technics rely on the evaporation forces during the drying of a dispersion of building blocks. Convective and capillary forces take part in the self-assembly mechanism of the colloidal BBs. The drop-casting/solvent evaporation approach remains one of the most accessible technics to get a fast answer about the optical properties achievable by a BBs' dispersion. For the elaboration of artificial photonic crystal, the design of the colloidal objects remains a key feature to control the optical and mechanical of the final self-assembly. Among the choices of synthesis strategies available, the seeded polymerizations are ways to produce core-shell spherical object, with an efficient control on its dimensions and its properties. The core-shell architecture has been used as a design of choice for the elaboration of responsive self-assembled photonic crystals,

In the next section will be presented the synthesis attempts to form colloidal spheres with a core-shell design with a hard sphere and a soft shell.

References

1. Greenewalt, C. H., Brandt, W. & Friel, D. D. Iridescent Colors of Hummingbird Feathers*. *J. Opt. Soc. Am.* **50**, 1005 (1960).

2. Jones, J. B., Sanders, J. V. & Segnit, E. R. Structure of Opal. *Nature* **204**, 990–991 (1964).

3. Yablonovitch, E. Inhibited Spontaneous Emission in Solid-State Physics and Electronics. *Phys. Rev. Lett.* **58**, 2059–2062 (1987).

4. John, S. Strong localization of photons in certain disordered dielectric superlattices. *Phys. Rev. Lett.* **58**, 2486–2489 (1987).

5. Early lights. *Nature Mater* **11**, 995–995 (2012).

6. Seago, A. E., Brady, P., Vigneron, J.-P. & Schultz, T. D. Gold bugs and beyond: a review of iridescence and structural colour mechanisms in beetles (Coleoptera). *J. R. Soc. Interface* **6**, (2009).

7. Kinoshita, S., Yoshioka, S. & Miyazaki, J. Physics of structural colors. *Reports on Progress in Physics* **71**, 076401 (2008).

8. Kinoshita, S. & Yoshioka, S. Structural Colors in Nature: The Role of Regularity and Irregularity in the Structure. *ChemPhysChem* **6**, 1442–1459 (2005).

9. Sharma, V., Crne, M., Park, J. O. & Srinivasarao, M. Structural Origin of Circularly Polarized Iridescence in Jeweled Beetles. *Science* **325**, 449–451 (2009).

10. Vignolini, S. *et al.* Pointillist structural color in Pollia fruit. *Proceedings of the National Academy of Sciences* **109**, 15712–15715 (2012).

11. Mason, C. W. Structural Colors in Feathers. I. *J. Phys. Chem.* **27**, 201–251 (1923).

12. Medina, J. M., Díaz, J. A. & Vukusic, P. Classification of peacock feather reflectance using principal component analysis similarity factors from multispectral imaging data. *Opt. Express* **23**, 10198 (2015).

13. Vukusic, P. & Sambles, J. R. Photonic structures in biology. *Nature* **424**, 852–855 (2003).

14. Dufresne, E. R. *et al.* Self-assembly of amorphous biophotonic nanostructures by phase separation. *Soft Matter* **5**, 1792 (2009).

15. Saito, A. Material design and structural color inspired by biomimetic approach. *Science and Technology of Advanced Materials* **12**, 064709 (2011).

16. Kinoshita, S., Yoshioka, S. & Kawagoe, K. Mechanisms of structural colour in the Morpho butterfly: cooperation of regularity and irregularity in an iridescent scale. *Proceedings of the Royal Society of London B: Biological Sciences* **269**, 1417–1421 (2002).

17. Prum, R. O. Anatomically diverse butterfly scales all produce structural colours by coherent scattering. *Journal of Experimental Biology* **209**, 748–765 (2006).

18. Vukusic, P., Sambles, J. R., Lawrence, C. R. & Wootton, R. J. Quantified interference and diffraction in single Morpho butterfly scales. *Proc. R. Soc. Lond. B* **266**, 1403–1411 (1999).

19. Saenko, S. V., Teyssier, J., van der Marel, D. & Milinkovitch, M. C. Precise colocalization of interacting structural and pigmentary elements generates extensive color pattern variation in Phelsuma lizards. *BMC Biol* **11**, 105 (2013).

20. Teyssier, J., Saenko, S. V., van der Marel, D. & Milinkovitch, M. C. Photonic crystals cause active colour change in chameleons. *Nat Commun* **6**, 6368 (2015).

21. Kragh, H. Max Planck: the reluctant revolutionary. *Phys. World* **13**, 31–36 (2000).

22. Purcell, E. M. *Electricity and magnetism*. (Cambridge University Press, 2013).

23. Fleisch, D. *A Student's Guide to Maxwell's Equations*. (Cambridge University Press, 2008). doi:10.1017/CBO9780511984624.

24. Cohen-Tannoudji, C. & Guéry-Odelin, D. *Advances in Atomic Physics: An Overview*. (WORLD SCIENTIFIC, 2011). doi:10.1142/6631.

25. Landau, L. D. & E. M. Lifshitz. *Quantum Mechanics.* (Elsevier Science, 1981).

26. Wiester, J. B. Investigating the Similarities and Differences among UV/Vis, Infrared, Fluorescence, and Raman Spectroscopies through Discussion of Light–Matter Interactions. in *ACS Symposium Series* (ed. Sonntag, M. D.) vol. 1305 13–33 (American Chemical Society, 2018).

27. *Encyclopedia of Color Science and Technology*. (Springer New York, 2016). doi:10.1007/978-1-4419-8071-7.

28. Cox, A. J., DeWeerd, A. J. & Linden, J. An experiment to measure Mie and Rayleigh total scattering cross sections. *American Journal of Physics* **70**, 620–625 (2002).

29. *Photonic crystals: molding the flow of light*. (Princeton University Press, 2008).

30. Yu, P. Y. & Cardona, M. *Fundamentals of semiconductors: physics and materials properties*. (Springer, 2010).

31. Yablonovitch, E. & Gmitter, T. J. Photonic band structure: The face-centered-cubic case. *Phys. Rev. Lett.* **63**, 1950–1953 (1989).

32. *Nanomaterials and Nanoarchitectures: A Complex Review of Current Hot Topics and their Applications*. (Springer Netherlands, 2015). doi:10.1007/978-94-017-9921-8.

33. Merbs, S. L. & Nathans, J. Absorption spectra of human cone pigments. *Nature* **356**, 433–435 (1992).

34. *The science of color*. (Elsevier ; Optical Society of America, 2003).

35. Kumar, K. *et al.* Printing colour at the optical diffraction limit. *Nature Nanotech* **7**, 557–561 (2012).

36. Ródenas, A. *et al.* Three-dimensional femtosecond laser nanolithography of crystals. *Nature Photon* **13**, 105–109 (2019).

37. Romanato, F. *et al.* Fabrication by means of x-ray lithography of two-dimensional GaAs/AlGaAs photonic crystals with an unconventional unit cell. *Nanotechnology* **13**, 644–652 (2002).

38. Suzuki, K., Kitano, K., Ishizaki, K. & Noda, S. Three-dimensional photonic crystals created by single-step multi-directional plasma etching. *Opt. Express* **22**, 17099 (2014).

39. Takahashi, S. *et al.* Direct creation of three-dimensional photonic crystals by a top-down approach. *Nature Mater* **8**, 721–725 (2009).

40. Liu, Y. *et al.* Structural color three-dimensional printing by shrinking photonic crystals. *Nat Commun* **10**, 4340 (2019).

41. Hamley, I. W. *The physics of block copolymers*. (Oxford University Press, 1998).

42. Zhang, H., Hong, K. & Mays, J. W. Synthesis of Block Copolymers of Styrene and Methyl Methacrylate by Conventional Free Radical Polymerization in Room Temperature Ionic Liquids. *Macromolecules* **35**, 5738–5741 (2002).

43. Uhrig, D. & Mays, J. W. Experimental techniques in high-vacuum anionic polymerization. *J. Polym. Sci. A Polym. Chem.* **43**, 6179–6222 (2005).

44. Hong, K., Uhrig, D. & Mays, J. W. Living anionic polymerization. *Current Opinion in Solid State and Materials Science* **4**, 531–538 (1999).

45. Hadjichristidis, N., Iatrou, H., Pitsikalis, M. & Mays, J. Macromolecular architectures by living and controlled/living polymerizations. *Progress in Polymer Science* **31**, 1068–1132 (2006).

46. Matsen, M. W. & Bates, F. S. Origins of Complex Self-Assembly in Block Copolymers. *Macromolecules* **29**, 7641–7644 (1996).

47. Lennon, E. M., Katsov, K. & Fredrickson, G. H. Free Energy Evaluation in Field-Theoretic Polymer Simulations. *Phys. Rev. Lett.* **101**, 138302 (2008).

48. Kang, Y., Walish, J. J., Gorishnyy, T. & Thomas, E. L. Broad-wavelength-range chemically tunable block-copolymer photonic gels. *Nature Mater* **6**, 957–960 (2007).

49. Lim, H. S., Lee, J.-H., Walish, J. J. & Thomas, E. L. Dynamic Swelling of Tunable Full-Color Block Copolymer Photonic Gels *via* Counterion Exchange. *ACS Nano* **6**, 8933–8939 (2012).

50. Wang, X. *et al.* [INVITED] Hyperbolic-by-design self-assembled metamaterial based on block copolymers lamellar phases. *Optics & Laser Technology* **88**, 85–95 (2017).

51. Deng, T., Chen, C., Honeker, C. & Thomas, E. L. Two-dimensional block copolymer photonic crystals. *Polymer* **44**, 6549–6553 (2003).

52. Hirao, A., Goseki, R. & Ishizone, T. Advances in Living Anionic Polymerization: From Functional Monomers, Polymerization Systems, to Macromolecular Architectures. *Macromolecules* **47**, 1883–1905 (2014).

53. Xie, Y. *et al.* Liquid crystal self-assembly of upconversion nanorods enriched by depletion forces for mesostructured material preparation. *Nanoscale* **10**, 4218–4227 (2018).

54. Seelig, E. W., Tang, B., Yamilov, A., Cao, H. & Chang, R. P. H. Self-assembled 3D photonic crystals from ZnO colloidal spheres. *Materials Chemistry and Physics* **80**, 257–263 (2003).

55. Kim, B. G. *et al.* Optical characteristics of SiO2 photonic band-gap crystal with ferroelectric perovskite oxide. *Appl. Phys. Lett.* **81**, 4440–4442 (2002).

56. Ge, J., Hu, Y. & Yin, Y. Highly Tunable Superparamagnetic Colloidal Photonic Crystals. *Angew. Chem. Int. Ed.* **46**, 7428–7431 (2007).

57. Lagerwall, J. P. F. *et al.* Cellulose nanocrystal-based materials: from liquid crystal self-assembly and glass formation to multifunctional thin films. *NPG Asia Mater* **6**, e80–e80 (2014).

58. Parker, R. M. *et al.* The Self-Assembly of Cellulose Nanocrystals: Hierarchical Design of Visual Appearance. *Adv. Mater.* **30**, 1704477 (2018).

59. Frka-Petesic, B., Guidetti, G., Kamita, G. & Vignolini, S. Controlling the Photonic Properties of Cholesteric Cellulose Nanocrystal Films with Magnets. *Adv. Mater.* **29**, 1701469 (2017).

60. Waterhouse, G. I. N. & Waterland, M. R. Opal and inverse opal photonic crystals: Fabrication and characterization. *Polyhedron* **26**, 356–368 (2007).

61. Zhang, Y., Fu, Q. & Ge, J. Photonic sensing of organic solvents through geometric study of dynamic reflection spectrum. *Nat Commun* **6**, 7510 (2015).

62. Ito, T., Katsura, C., Sugimoto, H., Nakanishi, E. & Inomata, K. Strain-Responsive Structural Colored Elastomers by Fixing Colloidal Crystal Assembly. *Langmuir* **29**, 13951–13957 (2013).

63. Chen, J. *et al.* Highly Stretchable Photonic Crystal Hydrogels for a Sensitive Mechanochromic Sensor and Direct Ink Writing. *Chem. Mater.* **31**, 8918–8926 (2019).

64. Yan, D., Qiu, L., Xue, M., Meng, Z. & Wang, Y. A flexible surface-enhanced Raman substrates based on cellulose photonic crystal/Ag-nanoparticles composite. *Materials & Design* **165**, 107601 (2019).

65. Kassim, S., Padmanabhan, S., McGrath, J. & Pemble, M. E. Preparation and Properties of Silica Inverse Opal *via* Self-Assembly. *AMM* **699**, 318–324 (2014).

66. Zhao, H. *et al.* Chemically Responsive Polymer Inverse-Opal Photonic Crystal Films Created by a Self-Assembly Method. *J. Phys. Chem. C* **120**, 11938–11946 (2016).

67. H. Ng, E. C., K., Y. & C., C. Colloidal Crystals. in *Modern Aspects of Bulk Crystal and Thin Film Preparation* (ed. Kolesnikov, N.) (InTech, 2012).

68. van Dommelen, R., Fanzio, P. & Sasso, L. Surface self-assembly of colloidal crystals for micro- and nano-patterning. *Advances in Colloid and Interface Science* **251**, 97–114 (2018).

69. Li, Q., Jonas, U., Zhao, X. S. & Kappl, M. The forces at work in colloidal self-assembly: a review on fundamental interactions between colloidal particles. *Asia-Pacific Jrnl of Chem. Eng* **3**, 255–268 (2008).

70. Xu, P., Mujumdar, A. S. & Yu, B. Drying-Induced Cracks in Thin Film Fabricated from Colloidal Dispersions. *Drying Technology* **27**, 636–652 (2009).

71. Park, S.-J. & Seo, M.-K. Intermolecular Force. in *Interface Science and Technology* vol. 18 1–57 (Elsevier, 2011).

72. Derjaguin, B. V., Churaev, N. V. & Muller, V. M. The Derjaguin—Landau—Verwey—Overbeek (DLVO) Theory of Stability of Lyophobic Colloids. in *Surface Forces* 293–310 (Springer US, 1987). doi:10.1007/978-1-4757-6639-4_8.

73. Steric Stabilization. in *Encyclopedia of Colloid and Interface Science* (ed. Tadros, T.) 1048–1049 (Springer Berlin Heidelberg, 2013). doi:10.1007/978-3-642-20665-8.

74. Romero-Cano, M. S., Martín-Rodríguez, A., Chauveteau, G. & de las Nieves, F. J. Colloidal Stabilization of Polystyrene Particles by Adsorption of Nonionic Surfactant. *Journal of Colloid and Interface Science* **198**, 273–281 (1998).

75. González García, Á., Nagelkerke, M. M. B., Tuinier, R. & Vis, M. Polymer-mediated colloidal stability: on the transition between adsorption and depletion. *Advances in Colloid and Interface Science* **275**, 102077 (2020).

76. Ueno, K., Inaba, A., Kondoh, M. & Watanabe, M. Colloidal Stability of Bare and Polymer-Grafted Silica Nanoparticles in Ionic Liquids. *Langmuir* **24**, 5253–5259 (2008).

77. Parfitt, G. D. & Barnes, H. A. The dispersion of fine particles in liquid media. in *Mixing in the Process Industries* 99–117 (Elsevier, 1992). doi:10.1016/B978-075063760-2/50027-5.

78. Napper, D. H. Steric stabilization. *Journal of Colloid and Interface Science* **58**, 390–407 (1977).

79. Lazarov, G. S., Denkov, N. D., Velev, O. D., Kralchevsky, P. A. & Nagayama, K. Formation of two-dimensional structures from colloidal particles on fluorinated oil substrate. *Faraday Trans.* **90**, 2077 (1994).

80. Davis, S. H. Moving contact lines and rivulet instabilities. Part 1. The static rivulet. *J. Fluid Mech.* **98**, 225–242 (1980).

81. Troian, S. M., Herbolzheimer, E., Safran, S. A. & Joanny, J. F. Fingering Instabilities of Driven Spreading Films. *Europhys. Lett.* **10**, 25–30 (1989).

82. Holgado, M. *et al.* Electrophoretic Deposition To Control Artificial Opal Growth. *Langmuir* **15**, 4701–4704 (1999).

83. Prieve, D. C., Sides, P. J. & Wirth, C. L. 2-D assembly of colloidal particles on a planar electrode. *Current Opinion in Colloid & Interface Science* **15**, 160–174 (2010).

84. Yethiraj, A. & van Blaaderen, A. A colloidal model system with an interaction tunable from hard sphere to soft and dipolar. **421**, 5 (2003).

85. Zhang, K.-Q. & Liu, X. Y. In situ observation of colloidal monolayer nucleation driven by an alternating electric field. *Nature* **429**, 739–743 (2004).

86. Jiang, P. & McFarland, M. J. Large-Scale Fabrication of Wafer-Size Colloidal Crystals, Macroporous Polymers and Nanocomposites by Spin-Coating. *J. Am. Chem. Soc.* **126**, 13778–13786 (2004).

87. Padding, J. T. & Louis, A. A. The interplay between hydrodynamic and Brownian fluctuations in sedimenting colloidal suspensions. *Phys. Rev. E* **77**, 011402 (2008).

88. Park, S. H., Gates, B. & Xia, Y. A Three-Dimensional Photonic Crystal Operating in the Visible Region. *Advanced Materials* **11**, 462–466 (1999).

89. Velev, O. D. & Lenhoff, A. M. Colloidal crystals as templates for porous materials. *Current Opinion in Colloid & Interface Science* **5**, 56–63 (2000).

90. Pusey, P. N. *et al.* Structure of crystals of hard colloidal spheres. *Phys. Rev. Lett.* **63**, 2753–2756 (1989).

91. Deegan, R. D. *et al.* Capillary flow as the cause of ring stains from dried liquid drops. *Nature* **389**, 827–829 (1997).

92. Dushkin, C. D., Yoshimura, H. & Nagayama, K. Nucleation and growth of two-dimensional colloidal crystals. *Chemical Physics Letters* **204**, 455–460 (1993).

93. Denkov, N. *et al.* Mechanism of formation of two-dimensional crystals from latex particles on substrates. *Langmuir* **8**, 3183–3190 (1992).

94. Bhardwaj, R., Fang, X., Somasundaran, P. & Attinger, D. Self-Assembly of Colloidal Particles from Evaporating Droplets: Role of DLVO Interactions and Proposition of a Phase Diagram. *Langmuir* **26**, 7833–7842 (2010).

95. Lee, S. Y., Kim, H., Kim, S.-H. & Stone, H. A. Uniform Coating of Self-Assembled Noniridescent Colloidal Nanostructures using the Marangoni Effect and Polymers. *Phys. Rev. Applied* **10**, 054003 (2018).

96. *Sol-Gel Science*. (Elsevier, 1990). doi:10.1016/C2009-0-22386-5.

97. Scherer, G. W. Theory of Drying. *J American Ceramic Society* **73**, 3–14 (1990).

98. Wedin, P., Martinez, C. J., Lewis, J. A., Daicic, J. & Bergström, L. Stress development during drying of calcium carbonate suspensions containing carboxymethylcellulose and latex particles. *Journal of Colloid and Interface Science* **272**, 1–9 (2004).

99. Film Formation in Coatings. Mechanisms, Properties, and Morphology Edited by Theodore Provder (Polymer and Coatings Consultants) and Marek W. Urban (University of Southern Mississippi). American Chemical Society: Washington, DC (Distributed by Oxford University). viii + 304 pp. $130.00. ISBN: 0-8412-3712-3. *J. Am. Chem. Soc.* **124**, 3799–3799 (2002).

100. Kiennemann, J. *et al.* Drying mechanisms and stress development in aqueous alumina tape casting. *Journal of the European Ceramic Society* **25**, 1551–1564 (2005).

101. Brown, L. A., Zukoski, C. F. & White, L. R. Consolidation during drying of aggregated suspensions. *AIChE J.* **48**, 492–502 (2002).

102. Jiang, P., Bertone, J. F., Hwang, K. S. & Colvin, V. L. Single-Crystal Colloidal Multilayers of Controlled Thickness. *Chem. Mater.* **11**, 2132–2140 (1999).

103. Petty, M. C. *Langmuir-Blodgett Films: An Introduction*. (Cambridge University Press, 1996). doi:10.1017/CBO9780511622519.

104. Reculusa, S. & Ravaine, S. Synthesis of Colloidal Crystals of Controllable Thickness through the Langmuir−Blodgett Technique. *Chem. Mater.* **15**, 598–605 (2003).

105. Parchine, M., McGrath, J., Bardosova, M. & Pemble, M. E. Large Area 2D and 3D Colloidal Photonic Crystals Fabricated by a Roll-to-Roll Langmuir–Blodgett Method. *Langmuir* **32**, 5862–5869 (2016).

106. Kohoutek, T., Parchine, M., Bardosova, M. & Pemble, M. E. Controlled self-assembly of Langmuir-Blodgett colloidal crystal films of monodispersed silica particles on non-planar substrates. *Colloids and Surfaces A: Physicochemical and Engineering Aspects* **593**, 124625 (2020).

107. Wong, S., Kitaev, V. & Ozin, G. A. Colloidal Crystal Films: Advances in Universality and Perfection. *J. Am. Chem. Soc.* **125**, 15589–15598 (2003).

108. Dimitrov, A. S. & Nagayama, K. Continuous Convective Assembling of Fine Particles into Two-Dimensional Arrays on Solid Surfaces. *Langmuir* **12**, 1303–1311 (1996).

109. Gu, Z.-Z., Fujishima, A. & Sato, O. Fabrication of High-Quality Opal Films with Controllable Thickness. *Chem. Mater.* **14**, 760–765 (2002).

110. Deleuze, C. *et al.* Photonic properties of hybrid colloidal crystals fabricated by a rapid dip-coating process. *Phys. Chem. Chem. Phys.* **13**, 10681 (2011).

111. Prevo, B. G. & Velev, O. D. Controlled, Rapid Deposition of Structured Coatings from Micro- and Nanoparticle Suspensions. *Langmuir* **20**, 2099–2107 (2004).

112. Yang, H. & Jiang, P. Large-Scale Colloidal Self-Assembly by Doctor Blade Coating. *Langmuir* **26**, 13173–13182 (2010).

113. Jones, S. F., Evans, G. M. & Galvin, K. P. Bubble nucleation from gas cavities — a review. *Advances in Colloid and Interface Science* **80**, 27–50 (1999).

114. Coquerel, G. Crystallization of molecular systems from solution: phase diagrams, supersaturation and other basic concepts. *Chem. Soc. Rev.* **43**, 2286–2300 (2014).

115. Pruppacher, H. R., Klett, J. D. & Wang, P. K. Microphysics of Clouds and Precipitation. *Aerosol Science and Technology* **28**, 381–382 (1998).

116. Palberg, T. Colloidal crystallization dynamics. *Current Opinion in Colloid & Interface Science* **2**, 607–614 (1997).

117. The Stokes-Einstein law for diffusion in solution. *Proc. R. Soc. Lond. A* **106**, 724–749 (1924).

118. Gasser, U. Real-Space Imaging of Nucleation and Growth in Colloidal Crystallization. *Science* **292**, 258–262 (2001).

119. Karthika, S., Radhakrishnan, T. K. & Kalaichelvi, P. A Review of Classical and Nonclassical Nucleation Theories. *Crystal Growth & Design* **16**, 6663–6681 (2016).

120. Sandomirski, K., Allahyarov, E., Löwen, H. & Egelhaaf, S. U. Heterogeneous crystallization of hard-sphere colloids near a wall. *Soft Matter* **7**, 8050 (2011).

121. C. W. Lan, W. C. Yu & W. C. Hsu. Bulk, Single Crystal Growth. in *Encyclopedia of Surface and Colloid Science - Volume II* 1075–1078 (Taylor & Francis, 2002).

122. Nozawa, J. *et al.* Step Kinetics Dependent on the Kink Generation Mechanism in Colloidal Crystal Growth. *Crystal Growth & Design* **18**, 2948–2955 (2018).

123. Park, J.-G. *et al.* Photonic-crystal hydrogels with a rapidly tunable stop band and high reflectivity across the visible. *Optical Materials Express* **7**, 253 (2017).

124. Fudouzi, H. & Xia, Y. Colloidal Crystals with Tunable Colors and Their Use as Photonic Papers. *Langmuir* **19**, 9653–9660 (2003).

125. Shen, Z., Shi, L., You, B., Wu, L. & Zhao, D. Large-scale fabrication of three-dimensional ordered polymer films with strong structure colors and robust mechanical properties. *J. Mater. Chem.* **22**, 8069 (2012).

126. Duan, L., You, B., Wu, L. & Chen, M. Facile fabrication of mechanochromic-responsive colloidal crystal films. *Journal of Colloid and Interface Science* **353**, 163–168 (2011).

127. Chen, L. *et al.* The toxicity of silica nanoparticles to the immune system. *Nanomedicine* **13**, 1939–1962 (2018).

128. Foulger, S. H. *et al.* Photonic Crystal Composites with Reversible High-Frequency Stop Band Shifts. *Adv. Mater.* **15**, 685–689 (2003).

129. Hong, R. *et al.* Highly sensitive mechanochromic photonic gel towards fast-responsive fingerprinting. *RSC Adv.* **7**, 33258–33262 (2017).

130. Lee, G. H. *et al.* Colloidal Photonic Inks for Mechanochromic Films and Patterns with Structural Colors of High Saturation. *Chem. Mater.* **31**, 8154–8162 (2019).

131. Lee, G. H. *et al.* Chameleon-Inspired Mechanochromic Photonic Films Composed of Non-Close-Packed Colloidal Arrays. *ACS Nano* **11**, 11350–11357 (2017).

132. Lee, G. H. *et al.* Elastic Photonic Microbeads as Building Blocks for Mechanochromic Materials. *ACS Appl. Polym. Mater.* **2**, 706–714 (2020).

133. Viel, B., Ruhl, T. & Hellmann, G. P. Reversible Deformation of Opal Elastomers. *Chemistry of Materials* **19**, 5673–5679 (2007).

134. Yang-Bae, K., Chan-Ho, P. & Jin-Who, H. Electrically conductive microgel and method for preparing the same. (2002).

135. Berge, T. *et al.* Microgels and Process for Their Preparation. (2004).

136. Kurauchi, T., Ishii, K., Yamada, A. & Nozue, J. Topcoating Composition. (1986).

137. Kurauchi, T., Ishii, K., Ishikura, S. & Nozue, J. Clear Coating Composition for Top Coat. (1985).

138. Kurauchi, T., Ishii, K., Yamada, A. & Nozue, J. Top Coat Composition Containing Microgel Particles. (1985).

139. Wright, H. J., Leonard, D. P. & Etzell, R. A. Colouring composition containing an acrylic microgel resin. (1983).

140. Hu, Z., Cai, T., Chi, C. & Marquez, M. Monodisperse Thermo-Responsive Microgels of Poly(ethylene Glycol) Analogue-Based Biopolymers, Their Manufacture, and Their Applications. (2010).

141. Han, Z., Luo, J. & Yuan, G. Core-shell microgel and its application in improvement of properties of colloidal material. (2018).

142. Xu, S., Lei, B., Shen, N., Wang, Y. & Liu, H. Temperature-sensitive tri-block polymer, reduction and ultrasonic-sensitive core-shell structural microgel with same and application of reduction and ultrasonic-sensitive core-shell structural microgel. (2017).

143. Tie, L. *et al.* Method for improving polymer flooding effect, and polymer flooding composition and application thereof. (2017).

144. Sun, W. & Wu, P. Core halo/core-shell halo structure fluorescent microgel having double responsiveness and preparation method thereof. (2015).

145. Shen, Y. *et al.* Preparation method of core-shell type cationic microgel-nano noble metal composite material. (2015).

146. Zha, L. & Li, S. Light/temperature double responsiveness hybrid microgel of silver-loaded nanoparticles and preparation method thereof. (2015).

147. He, X. *et al.* Core-shell-type microgel and preparation method thereof. (2015).

148. Moon, T. K., Lee, J. T., Lee, H. S., Park, J. Y. & Ko, K. H. Microgel and Method for Preparing Same, and Water-Soluble Paint Composition. (2012).

149. Yanqiang, Z. *et al.* Self-expandable microgel pulse preparation with layer-by-layer assembled polyelectrolytes and preparation method thereof. (2011).

150. Mengquan, S., Feipeng, W., Yunlong, Z. & Yuxi, Z. Emulsion deep profile/displacement control agent and preparation method of emulsion deep profile/displacement control agent containing gel microspheres of core shell structure. (2012).

151. Ko, K. H., Park, J. Y., Baek, K. H., Kim, W. J. & Kim, S. K. Multi-Layered Microgel for Automotive Paint Composition. (2011).

152. Hong, L. *et al.* Method for preparing nucleocapsid type microgel composite microsphere using polymeric surfactant. (2008).

153. Xiaonong, C. *et al.* Hydrophobic polymer material surface hydrophilicity improving method. (2009).

154. Hyun, S. W. *et al.* Inverted Core-Shell Type Microgel Polymer Containing Urethane. (2007).

155. Richtering, W. & Berndt, I. Core-shell microgels, for use as catalyst supports, comprise a microparticle core and at least one polymeric shell comprising at least

two different thermosensitive polymers having different switch temperatures. (2004).

156. Bae, T. Y., Hong, S. M. & Park, J. M. Method for Producing Reverse-Phase Core/Shell Microgel, and Aqueous Paint Composition Comprising the Same. (2003).

157. Chi, C. H., Oh, J. K., Lee, H. K., Park, J. M. & Hong, S. M. Method for Preparation of Phase Reversing Core/Shell Type Microgel. (2000).

158. Hong, S. M., Park, J. M. & Kim, Y. B. Core/shell type microgel comprising alkylene monoisocyanate/poly(ethylene oxide)monoalcohol monomer and having excellent water resistance, anti-fouling property and adhesion, and coating composition comprising the same. (2005).

159. Tanaka, K. & Kojima, A. Painting Method. (1987).

160. Kim, S. H. & Chi, M. K. Micorgel Water-Soluble Paint Composition Containing Acryl Core-Shell Emulsification Polymer. (2000).

161. Sugiyama, Y., Shirakami, H. & Miyazawa, K. Starting Material for Cosmetics. (2017).

162. Sugiyama, Y., Sato, T. & Shoji, K. Core-Corona Type Microgel Emulsifier, and Oil-in-Water Emulsion Composition. (2014).

163. Hatton, F. L., Lovett, J. R. & Armes, S. P. Synthesis of well-defined epoxy-functional spherical nanoparticles by RAFT aqueous emulsion polymerization. *Polym. Chem.* **8**, 4856–4868 (2017).

164. Qiao, X. G., Dugas, P.-Y., Charleux, B., Lansalot, M. & Bourgeat-Lami, E. Synthesis of Multipod-like Silica/Polymer Latex Particles *via* Nitroxide-Mediated Polymerization-Induced Self-Assembly of Amphiphilic Block Copolymers. *Macromolecules* **48**, 545–556 (2015).

165. Macchione, M., Biglione, C. & Strumia, M. Design, Synthesis and Architectures of Hybrid Nanomaterials for Therapy and Diagnosis Applications. *Polymers* **10**, 527 (2018).

166. Ho, K. M., Li, W. Y., Wong, C. H. & Li, P. Amphiphilic polymeric particles with core–shell nanostructures: emulsion-based syntheses and potential applications. *Colloid and Polymer Science* **288**, 1503–1523 (2010).

167. Arshady, R. Suspension, emulsion, and dispersion polymerization: A methodological survey. *Colloid & Polymer Science* **270**, 717–732 (1992).

168. Chern, C. S. Emulsion polymerization mechanisms and kinetics. *Progress in Polymer Science* **31**, 443–486 (2006).

169. Distler, D., Neto, W. S. & Machado, F. Emulsion Polymerization. in *Reference Module in Materials Science and Materials Engineering* B9780128035818037000 (Elsevier, 2017). doi:10.1016/B978-0-12-803581-8.03746-2.

170. Herrera, V., Pirri, R., Leiza, J. R. & Asua, J. M. Effect of in-Situ-Produced Block Copolymer on Latex Particle Morphology. *Macromolecules* **39**, 6969–6974 (2006).

171. Howard, J. W., David, P. L. & Roger, A. E. Acrylic microgel resin for use in paint - prepd. by incorporating crosslinked aq. acrylic microgel emulsion into acrylic resin prepd. by soln. polymerisation. (1981).

172. Lindner, C. D. C. D., Liebig, L. D. C. D. & Ott, K.-H. D. C. D. Dispersions of crosslinked diene rubber and process for preparing them. (1980).

173. Andersson, M. & Maunu, S. L. Structural studies of poly(N-isopropylacrylamide) microgels: Effect of SDS surfactant concentration in the microgel synthesis. *Journal of Polymer Science Part B: Polymer Physics* **44**, 3305–3314 (2006).

174. Andersson, M., Hietala, S., Tenhu, H. & Maunu, S. L. Polystyrene latex particles coated with crosslinked poly(N-isopropylacrylamide). *Colloid and Polymer Science* **284**, 1255–1263 (2006).

175. Shi, S. *et al.* Poly(methyl methacrylate)/poly(N-isopropylacrylamide) core-shell particles prepared by seeded precipitation polymerization: Unusual morphology and thermo-sensitivity of zeta potential. *Chinese Journal of Polymer Science* **32**, 524–530 (2014).

176. Nguyen, D. Etude de la nucléation contrôlée de latex polymère à la surface de nanoparticules d'oxyde pour l'élaboration de colloïdes hybrides structurés. (Université Sciences et Technologies-Bordeaux I, 2008).

177. Lutz, J.-F. Polymerization of oligo(ethylene glycol) (meth)acrylates: Toward new generations of smart biocompatible materials. *J. Polym. Sci. A Polym. Chem.* **46**, 3459–3470 (2008).

178. Boularas, M. Synthèse de microgels hybrides, biocompatibles et stimulables pour des applications cosmétiques. (Université de Pau et des Pays de l'Adour, 2015).

179. Boularas, M., Gombart, E., Tranchant, J.-F., Billon, L. & Save, M. Design of Smart Oligo(ethylene glycol)-Based Biocompatible Hybrid Microgels Loaded with Magnetic Nanoparticles. *Macromolecular Rapid Communications* **36**, 79–83 (2015).

180. Boularas, M. *et al.* Dual stimuli-responsive oligo(ethylene glycol)-based microgels: insight into the role of internal structure in volume phase transitions and loading of magnetic nanoparticles to design stable thermoresponsive hybrid microgels. *Polym. Chem.* **7**, 350–363 (2016).

181. Boularas, M. *et al.* Functional film by trigger-free self-assembly of adhesive soft microgels at skin temperature. *Materials & Design* **147**, 19–27 (2018).

Chapter II: Colloidal object synthesis: seeded precipitation polymerization

Introduction

Colloidal crystals are materials presenting a periodic arrangement at the colloidal scale. When the adequate conditions are reunited, as described in the previous chapter, the light wavelength can be selectively diffracted and produce colors in the visible range: the material is thus considered as a photonic crystal. The utilization of viscoelastic polymer allows to develop switchable colors, such as mechanochromism [1–5]. The elaboration of such responsive & bio-inspired colors is achievable through the self-assembly of core-shell colloidal spheres[6–8]. Seeded emulsion and precipitation polymerization are two promising approaches to conceive these multilayered architectures. Here, we investigated the conception of hard core with high refractive index surrounded by soft materials with lower refractive index. The main purpose was to integrate a multi-responsive microgel made of POEGMA onto polystyrene cores to develop color switchable materials. The Bragg-Snell coloration being expected in reasons of the performant self-assembly properties of the POEGMA-based microgel (MG), and the refractive index difference between the core ($n_{PS} \approx 1.59$), and the surrounding matrix ($n_{POEGMA} \approx 1.47$) in the dried films. Nevertheless, the synthesis and the characterization of such objects are not straightforward. A peculiar attention was brought on the effective grafting of the MG shell to promote the self-assembly of regular arrangements. In this context, two different colloidal designs were explored, core-interlayer-shell (CIS)[9] and core-shell (CS)[10] particles. The CIS design was firstly explored with the expectation that an adhesive interlayer may promote the effective grafting of the shell. An interlayer of poly(*n*-butyl acrylate) was chosen due to its adhesive properties associated with its low Tg ($Tg_{PBA} \approx$ - 49 °C) but also to its refractive index close to the POEGMA shell ($n_{ABu} \approx 1.46$).

1. Core-interlayer-shell: adhesion on interlayer

1.1. *Synthesis protocol*

The synthesis of the core-interlayer-shell rely on three successive steps of polymerization. The core is obtained through the polymerization of Styrene S and a crosslinker, the divinylbenzene (DVB) in dispersed media (emulsion). The interlayer is made from *n*-butyl acrylate (BA) and diethylene glycol methacrylate (EGDMA) from PS seeded polymerization and form a core@shell PS@PBA colloid. Finally, the responsive POEGMA-based shell is synthesized through a seeded precipitation polymerization, thanks to the raw PS@PBA seeds' dispersion previously obtained.

Polystyrene beads (core)

Materials: Styrene (S – from Sigma-Aldrich); divinylbenzene (DVB – from Sigma-Aldrich); Sodium Dodecylsulfate (SDS – from ABCD); potassium persulfate (KPS – from Sigma-Aldrich).

The PS cores are produced from the emulsion polymerization of the St with DVB. The total amount of DVB, the crosslinker, is calculated to keep a molar ratio o$\frac{n_{DVB}}{n_{St}+n_{DVB}} = 5\%$. The surfactant (SDS) concentration is controlled, according to the core size targeted (Appendix 1, p. 211). The final solid content targeted - SC_{th}, considering a conversion rate of 100%, is adjusted with water to keep $SC_{th} = 6.0 \pm 0.5\ wt\%$.

For instance, in 1.5 liter 3-neck rounded bottom beaker set up with a thermostat and a mechanical stirrer, 650 g of MiliQ water and a mass $\boldsymbol{m_{SDS}}$ *of sodium dodecylsulfate were mixed. Successively, the mix of* 42.636 *g (0.409 mol) of styrene and of* 2.647 g *(0.020 mol) of DVB were added into the reactor. The mixture was then stirred at 300 rpm for 45 min under bubbling nitrogen gas while the temperature was increased to 70 °C. After 45 min and once the set temperature was reached, a degassed aqueous solution of KPS (0.193 g (0.7 mmol) /10 mL) was injected into the reactor.*

After 3 hours, of reaction, a sample was withdrawn for analysis right before the successive synthesis of the poly(*n*-butyl acrylate) layer (PBA) reticulated with EGDMA.

PBA interlayer

Materials: *n*-butyl acrylate (BA – from Sigma-Aldrich); ethylene glycol dimethyl acrylate (EGDMA – from Sigma-Aldrich); Sodium Dodecylsulfate (SDS – from ABCR), potassium persulfate (KPS – from Sigma-Aldrich).

The PBA interlayer is produced from a seeded emulsion polymerization with the previously made PS dispersion. The total amount of EGDMA, the crosslinker, is calculated to keep a molar ratio of $\frac{n_{EGDMA}}{n_{BA}+n_{EGDMA}} = 5$ mol%. The total amount of BA and EGDMA introduced are calculated to keep a mass ratio of $\frac{m_{St}+m_{DVB}}{m_{BA}+m_{EGDMA}} = 50\ wt\%$. The final solid content targeted - SC_{th}, considering a conversion rate of 100%, is adjusted with water to keep $SC_{th}=11.3 \pm 0.5$ wt%.

In 1.5 liter 3-neck rounded bottom beaker containing the degassed and heated raw dispersion of raw seeds under N_2, an aqueous solution of SDS (0.081g / 5 mL) was added to the solution. A degassed mix of BA (42 g – 0.327 mol) and EGDMA (3.248 g – 0.16 mol) were introduced in the reactor and stirred for 15 minutes. Then, an aqueous KPS solution (0.1575 g (0.6 mmol) / 10 mL) previously degassed was introduced in the mixture. The reaction was let for 3 hours. The reaction was stopped by reducing the system temperature to ambient temperature and by opening the reactor to air.

POEGMA microgel shell

Materials: diethylene glycol methyl ether methacrylate (MEO2MA), oligo ethylene glycol methyl ether methacrylate (OEGMA – $M_w = 475\ g.mol^{-1}$), methacrylic acid (MAA); oligo ethylene glycol diacrylate (OEGDA – $M_w = 250\ g.mol^{-1}$) and potassium persulfate (KPS). All the materials are provided by Sigma-Aldrich.

The following protocol theoretically lead to a solid rate of 8.5 ± 0.5 wt%. The theoretical shell as the same composition than the Boularas microgel, with a OEGMA/MEO2MA ratio of 10 mol%, a MAA/(OEGMA + MEO2MA) ratio of 5 mol%,

a crosslinker/monomers ratio of 1.92 mol% and a initiator/vinylic molecules ratio of 0.86 mol%. The quantity of microgels precursor and seed dispersions is adjusted in function of the wanted balance between thermosensitive shell and the core of the particle. For instance, to achieve at 25 wt% of shell material against the theoretical final solid content, the following protocol is used with PS@PBA seeds.

Firstly, MEO2MA (14.0466 g – 74.7 mmol), OEGMA (3.9420 g – 8.3 mmol) and crosslinker (0.4160 g – 1.7 mmol) were dilute into the seed dispersion (20 g – 0.111 g/mL) and mixed with a magnetic stirrer. This solution and a complement of seed dispersion (460 g – 0.111 g/mL) were introduced into a 1.5 liter 3-neck rounded bottom beaker equipped with a mechanical stirrer (set at 300 rpm). The reactor was purged with nitrogen for 45 min at room temperature to remove oxygen. When the purge is over, a mix of dissolved MAA (0.3726 g – 4.4 mmol) into seed dispersion (20 g – 0.111 g/mL) was introduced in the reactor. The system was heated up to 70 °C for 30 min, then an aqueous solution of KPS (0.2071 g (0.8 mmol) / 20 mL) was introduced in the reactor. Finally, the reaction was let for 6 hours, then stopped by cooling the mixture and by opening the reactor to the air

1.2. ***Size distribution and morphology (AFM/TEM and DLS)***

The colloidal objects were firstly analyzed to evaluate the shell grafting step on the overall size dispersion and on the morphology of the spheres. The size dispersion was evaluated by Dynamic Light Scattering (DLS), whereas the morphology of the particles was probed by Atomic Force Microscopy (AFM). Figure 1a shows the size evolution of the colloidal particles after the successive grafting step.

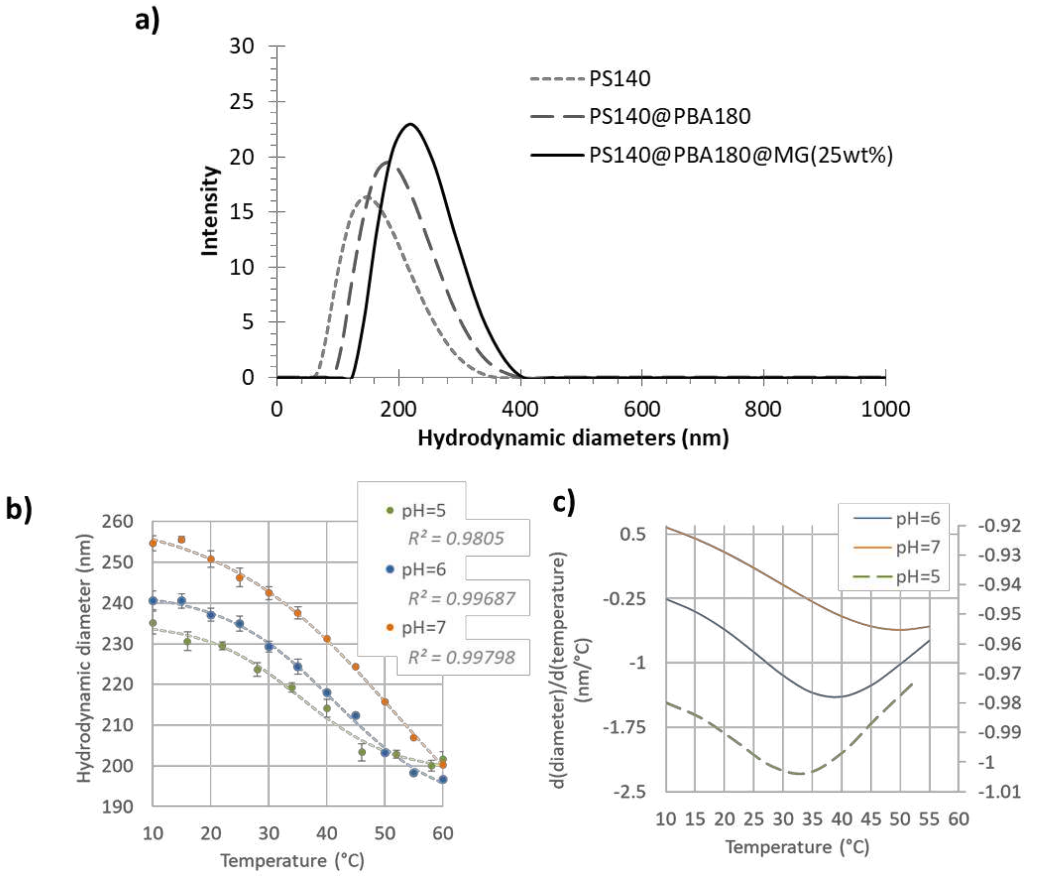

Figure 1. (a) Evolution of the hydrodynamic diameters (Dh) distribution of suspended objects from raw dispersions of PS spheres (average Dh = 140 nm), PS@PBA spheres (average Dh = 180 nm) and PS@PBA@MG made with 25 wt% of POEGMA-based microgel in the solid content (average Dh = 214 nm at 60 °C). (b) Evolution of the Dh values of PS140@PBA180@MG(25wt%) spheres according to the suspension temperature and pH. The data is fitted with a decreasing sigmoid function, correspondent regression coefficient (r^2) are noted. (c) The corresponding derivative of the sigmoid regressions with respect to the temperature. The minimum of each curve indicates the VPTT of the suspended object, at the set pH.

Figure 1 displays the size of PS spheres, with an average size of 140 nm, named PS140. Then after a grafting of a PBA layer, a core@layer object is achieved, named PS140@PBA180 with an average hydrodynamic diameter of 180 nm, corresponding to a PBA layer with a thickness of 20 nm. Finally, the grafting of the microgel shell give rise to the formation of core@interlayer@shell objects (CIS), named PS140@PBA180@MG(25wt%) with a size around of 214 nm at 60 °C (collapsed state) . Indeed, the CIS spheres displays an analog temperature and pH responsive behavior due to the microgel shell than microgel particles[11]. The pH was set with a citrate-phosphate buffer[12], made from solutions of citric acid and Na_2HPO_4 respectively at 0.01 and 0.02 mol/L. Below its Volume Phase Transition Temperature (VPTT), the shell@microgel is swollen by the solvent due to H-

bonding between the polymer and water. Above the VPTT, the polymer/solvent interactions are destabilized, reinforcing the polymer/polymer interactions: the shell@microgel collapse, with a volume decrease (Figure 1*b*). Due to the presence of methacrylic acid, the polarity of the microgel chains can be tuned according to the pH of the solvent. The more ionized the carboxylic acid, the stronger the water/polymer interactions. That's why a shift of the VPTT occurs when the solvent become more basic – pH increase (Figure 1*c*).

The morphology of the objects after these two successive grafting is observed through AFM (Figure 2).

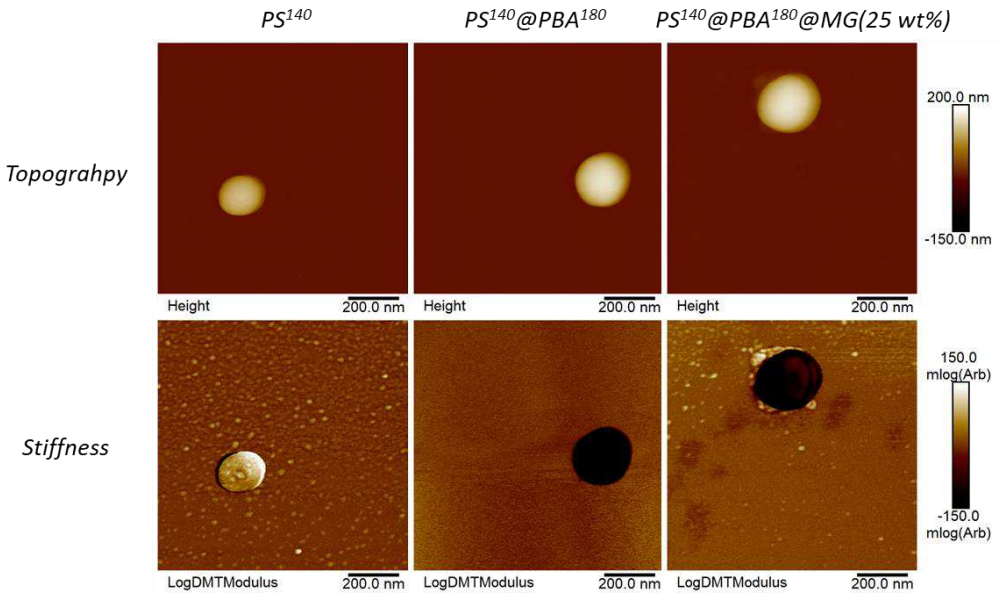

Figure 2 Atomic Force Microscopy (AFM) pictures of isolated colloidal beads. The images of the first line are display with a contrast in function of the surface relief whereas the pictures from the second line shows the same area, but with a contrast depending of the rigidity of the surface – the whiter are the pixel, the stiffer is the surface.

The objects appear spherical, with a significant modification of the size and the mechanical properties of their surface. The AFM in PeakForce mode allows to gather information about how the tip of the apparatus, probing the surface, adhere to the surface. From this information is extracted an evaluation of the stiffness of the surface. After the grafting steps, the particles appear softer than the initial PS seeds. This mechanical modification relies on the viscoelastic properties of PBA and PEGMA material characterized by a negative glass transition temperature. In other terms, the polymeric chains of the layer/shell are flexible and develop weak Van der Waals interactions with the tip, typical of rubbery materials.

Those CIS material were then self-assembled into film by solvent evaporation. Briefly, the raw CIS suspension was let drying on a polystyrene petri dish mounted on a heating plate set at 40 °C, above the shell VPTT. The UV-visible spectrum was then acquired by transmission photospectrometry, in the visible range. It must be mentioned these substrates absorb strongly light in the range below 300 nm due to aromatic chemical function of PS material (Figure 3).

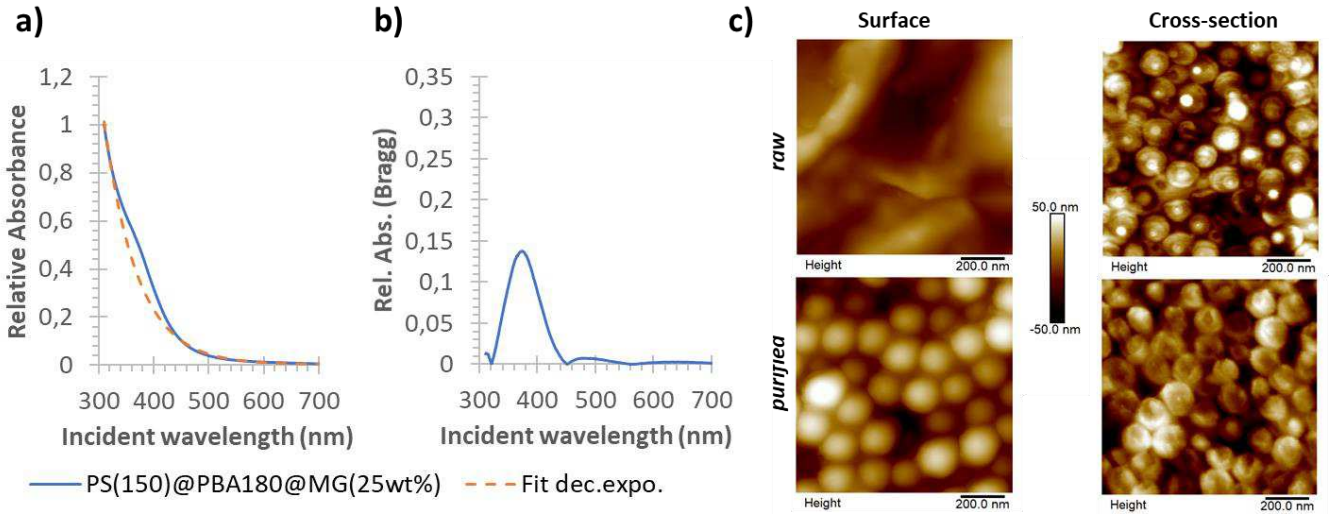

Figure 3 (a) UV-visible spectrum of a film made from a raw suspension of PS140@PBA180@MG(25wt%). The curve with the dashed line displays the baseline considered to isolate the diffraction peak. The baseline is traced from a partial fit on the experimental data from decreasing exponential function describe below. (b) Difference between experimental data and the fitted baseline. (c) AFM pictures of the surface and the cross-section of films made from raw and purified suspensions.

The spectrum registered in the extended visible range (300 – 700 nm) was considered valid, as at least 60 % of the light is not absorbed by the support. Therefore, the support contribution to the gathered signal is removed thanks to a blank with a petri dish support before each analysis. The spectra obtained are then normalized with respect to their maximum intensity to further comparisons. Figure 3*a* displays a spectrum with a distinctive scattering behavior associated to an increase of the apparent absorbance in the wavelength range of 300-500 nm. This absorbance increase is assumed to be cause by a selective reflection due to the scattering and diffraction of colloidal objects. Indeed, the films don't show any iridescent coloration, and trend to produce a blueish coloration independent of the observation angle (Figure 3*a*). However, a slight scattering peaks may be identified

at a wavelength coherent with the PS@PBA size, according to the Bragg-Snell equation (*Figure 3b*).

The AFM observation of the film surface made from raw suspension displays an apparent "skin" hiding the colloidal arrangement (*Figure 3c*). The same film was then prepared to observe its cross-section by cryo-ultramicrotome. To do so, the films were firstly frozen at -120 °C with liquid nitrogen, then the section was sized to form a pyramid of which the top surface was surfaced at the controlled speed of 10 µm/s. The sample was then let at ambient temperature in a close flask with desiccants to limit the frost formation. The surface of the truncated pyramids was then observed by AFM. The cross-section displays a disordered arrangement of colloidal beads but with the presence of smaller particles, with diameters around 50 nm (Figure 3*c* – *raw*). The same suspensions were then purified through 5 centrifugation/redispersion cycles in MiliQ water at 10.000 rpm, for 30 minutes. The films made from those purified suspensions gave rise to surface without "skin", but still with disorganized arrangement, even with cross-section pictures. Those smaller particles were not observed with films made from purified suspensions (Figure 3*c* – *purified*).

1.3. ***Impact on the self-assembly (UV-vis. & AFM)***

A comparable study was then performed on a CIS system made with a bigger PS with an average hydrodynamic diameter of 190 nm. In the same way, a PBA layer was grafted on those PS seeds, giving rise to beads with an average hydrodynamic diameter of 250 nm, before the grafting of a microgel shell. Here, a higher amount of microgel was introduced, with a mass ratio of 50 wt% of microgel monomers against the targeted total solid content. As previously, the grafting steps induce also a softening of the colloidal surface – darkening of the particle with stiffness contrast – coherent with the viscoelastic properties of the material (Figure 4). Nevertheless, the observation of raw CIS beads shows clearly the presence of soft and spread residue after the microgel grafting step. The more the quantity of microgel monomers, the larger is the size of these residues.

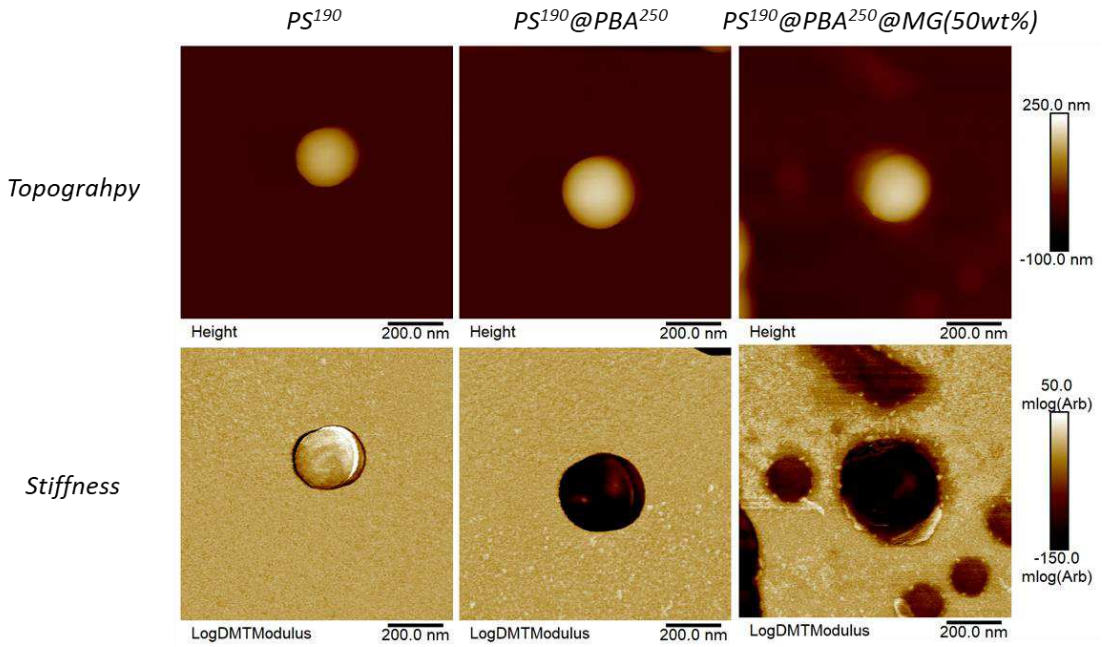

Figure 4 Atomic Force Microscopy (AFM) pictures of isolated colloidal beads. The images of the first line are display with a contrast in function of the surface relief whereas the pictures from the second line shows the same area, but with a contrast depending of the rigidity of the surface – the whiter are the pixel, the stiffer is the surface.

Moreover, these residues show a significant impact on the self-assembly properties. Indeed, Figure 5 shows the organized patterns produced by the self-assembly of the cores and the core@layer beads made by ambient solvent evaporation. The arrangement is regular, crystalline, in comparison with the films made from raw CIS particles at 40 °C, where non-order is discernable. No impact of the temperature on the beads ordering was identified. It appears thus this microgel shell grafting step is identified as causing a loss of the arrangement's periodicity.

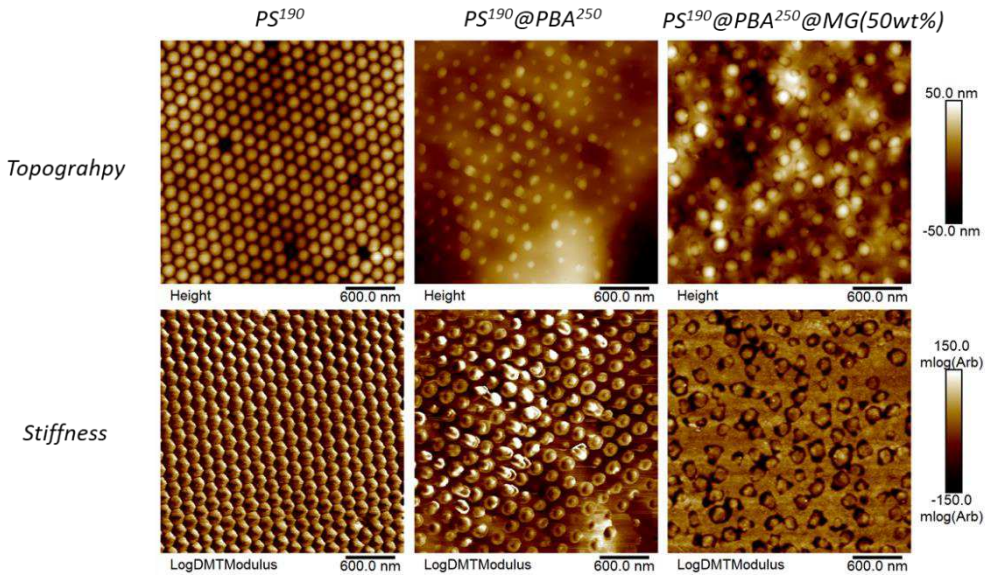

Figure 5 Atomic Force Microscopy (AFM) pictures of films surfaces made from the solvent evaporation of raw particles suspensions. The images of the first line are display with a contrast in function of the surface relief whereas the pictures from the second line shows the same area, but with a contrast depending of the rigidity of the surface – the whiter are the pixel, the stiffer is the surface.

Figure 6 relates the loss of the arrangement with the loss of the optical properties. The samples made from PS@PBA display a significant Bragg diffraction peak around 490 nm, with a relative contribution to the spectrum of 0.3. The impact of the shell grafting step was investigated through the grafting of different shell ratios, 25 and 50 wt% with respect to the solid content. It appears clearly the diffracted intensity decrease quickly with the proportion of shell material incorporated. A slight shift of the diffraction peak from films with the highest amount of shell fraction is however perceptible, possibly due to a weak modification of the interparticle distances, according to Bragg-Snell theory.

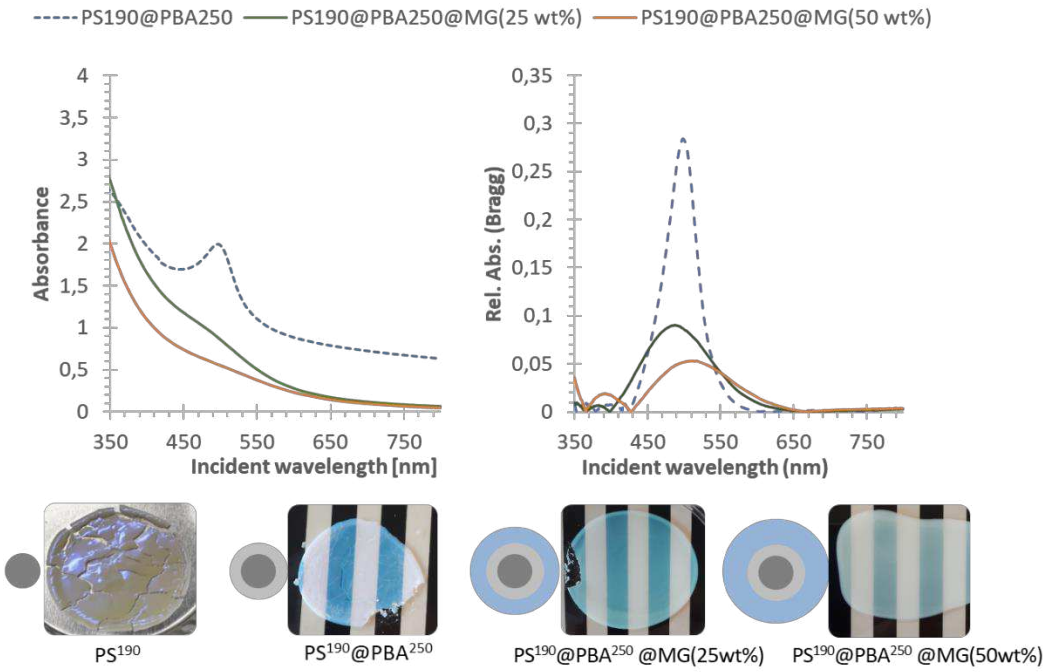

Figure 6 Left – Raw spectra of films from solvent evaporation of suspensions of PS190@PBA250 and PS190@PBA250@MG(25wt%) and PS190@PBA250@MG(50wt%). Right – Identified Bragg peak from the difference of the experimental data and the fitted baseline. Bottom – Schematic of suspended particles with pictures of films made from corresponding raw suspensions.

This first approach to graft this thermo-responsive microgel shell shows significant secondary nucleation can happens. This secondary nucleation induces the formation of free polymeric material, swollen in the suspension. These small objects appear then invisible to DLS analysis, the refractive index between these particles and the solvent being too weak to induce a measurable signal. However, they were found, by AFM, to be the cause of disorder after the self-assembly process. In order to effectively graft this microgel shell, a simplified approach is discussed in the next section of this chapter.

2. Core-shell systems

The synthesis of core-interlayer-shell material implies several uncertainties about the role of the interlayer, especially its implication during the microgel nucleation and growth. The architecture of a simpler core-shell system has the advantage to reduce the synthesis steps and focus on the fundamental properties of the targeted beads: a hard core, a soft shell and a significant refractive index

difference. In this context, this section focuses on the conception of core-shell beads (CS) made of PS core, with a shell of microgel.

Firstly, core-shell beads were made with the previously described PS beads cross-linked by DVB. Obviously, the grafting step of the PBA layer was skipped, and the core-shell was synthesized with the raw PS-DVB seed dispersion. A mass fraction of microgel of 50 wt% was aimed, giving rise to PS-DVB@MG(50 wt%).

Figure 7*a* shows the films after the solvent evaporation of raw CS suspension. Small beads are distinguishable as traces of secondary nucleation occurring during the shell grafting. The study of isolated particles (Figure 7 *b* & *c*) shows a large number of spread nanoparticles. The shape of these small objects, with a width higher than their height attest of their soft viscoelastic properties attributed to microgels secondary nucleation. More, the "core-shell" objects containing a PS core present heterogenous morphologies (Figure 7*a*), surely troublesome for the self-assembly of photonic crystals.

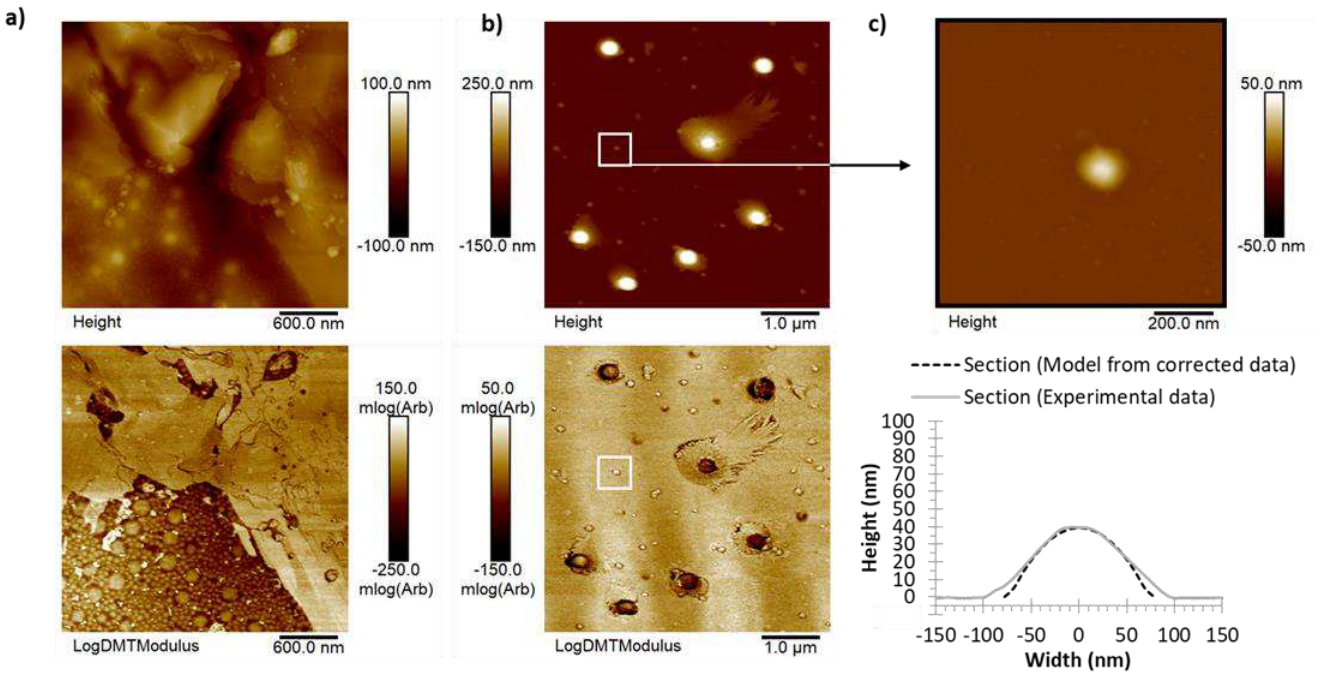

Figure 7 AFM pictures from raw PS-DVB@MG films (a) and beads (b). The images of the first line are display with a contrast in function of the surface relief whereas the pictures from the second line shows the same area, but with a contrast depending of the rigidity of the surface – the whiter are the pixel, the stiffer is the surface. (c) Zoom on a smaller particle, with a section analysis showing its spreading (grey line). In dashed line is represented a reconstruction integrating the tip-correction on the diameter.

From previous experiment, it appears the microgel grafting step is a critical issue to the formation of colloidal photonic crystals. Herein, we targeted the chemical modification of the hard cores as a simplified experimental approach to produce colloidal crystals.

In consequence, two different kinds of PS core were synthesized. The main difference lay in the crosslinker used for their conceptions. On one hand, divinyl benzene (DVB), with a chemical structure close to the PS beads, on the other hand, ethylene glycol dimethacrylate (EGDMA), closer to the POEGMA-based microgel from a chemical point of view. The shell grafting step was investigated through a semi-batch process in order to limit the risk of secondary nucleation.

2.1. *Synthesis protocol*

Two kind of PS cores were thus made with different crosslinkers. The amount of crosslinker, DVB or EGDMA, was fixed at 5 mol% with respect to styrene monomer. The shell material was grafted upon the raw seed suspension through a semi-batch process. with different experimental conditions.

Polystyrene beads (core) – chemical modification

Materials: Styrene (S – from Sigma-Aldrich); divinylbenzene (DVB – from Sigma-Aldrich); Sodium Dodecylsulfate (SDS – from ABCR); ethylene glycol dimethyl acrylate (EGDMA – from Sigma-Aldrich); potassium persulfate (KPS – from Sigma-Aldrich).

The PS cores are produced from the emulsion polymerization of the St with DVB/EGDMA. Before use, the inhibitors contained in the all commercial monomers are removed through mixing with an adapted inhibitor remover provided by Sigma-Aldrich, and filtering. The total amount of crosslinker is calculated to keep a molar ratio of $\frac{n_{crossl}}{n_{St}+n_{crossl}} = 5\ mol\%$. The surfactant (SDS) concentration is controlled, according to the core size targeted, here between 150 – 200 nm (Appendix 1, p.211). The final solid content targeted - SC_{th}, considering a conversion rate of 100%, is adjusted with water to keep $SC_{th} = 6.0 \pm 0.5\ wt\%$.

Here, in 1.5 liter 3-neck rounded bottom beaker set up with a thermostat and a mechanical stirrer, 650 g of MiliQ water and 0.426 g of SDS were mixed. Successively, 42.636 g of styrene with the corresponding amount of crosslinker were added into the reactor, that is 2.665 g of DVB or 4.057 g of EGDMA. *The mixture was then stirred at 300 rpm for 45 min under bubbling nitrogen gas while the temperature was increased to 70 °C. After 45 min and once the set temperature was reached, a degassed aqueous solution of KPS (0.1930 g/10 mL) was injected into the reactor. The reaction was stopped after 4 hours by opening the reactor to air and cooling the mixture to ambient temperature.*

POEGMA microgel shell

Materials: diethylene glycol methyl ether methacrylate (MEO2MA), oligo ethylene glycol methyl ether methacrylate (OEGMA – $M_w = 475\ g.mol^{-1}$), methacrylic acid (MAA); oligo ethylene glycol diacrylate (OEGDA – $M_w = 250\ g.mol^{-1}$) and potassium persulfate (KPS). All the materials are provided by Sigma-Aldrich.

The grafting step of the POEGMA shell is then performed on the obtained raw seeds. As raised in the introduction of this section, a semi-batch approach is

investigated for this grafting step, in parallel of the crosslinker modifications. In our case, it involves the continuous injection of the monomers and the initiator solution in the raw dispersion of the seeds. According to the work of Shi *et al.*[13] where similar semi-batch technic was employed, it may promote the growth of shell by seeded precipitation polymerizations. Briefly, the slow addition of monomers set the polymerization in "starved" conditions, where the growth of the polymeric chains depends on the "feeding" speed, *e.g.* the monomer injection speed. The purpose here is the inhibition of the risks of secondary nucleation, and then promote the growth of the shell. To do so, the initiator is injected in concomitantly, to progressively initiate the POEGMA polymerization.

The following protocol theoretically leads to a dispersion with a final solid rate of 8.9 ± 0.3 wt%. The monomers are prepared to keep a OEGMA/MEO2MA ratio of 10 mol%, a MAA/(OEGMA + MEO2MA) ratio of 5 mol%, a crosslinker/monomers ratio of 1.92 mol% and a initiator/vinylic molecules ratio of 0.86 mol%. Three different injections speeds are explored thanks to an automated push-syringe: 120, 6 and 1 mL/h. The volume of each syringe is adjusted with water to be similar. The shell to material ratio is set at 50 wt%.

In 1.5 liter 3-neck rounded bottom beaker set up with a thermostat and a mechanical stirrer, 132.256 g or 139.707 g of raw PS-EGDMA or PS-DVB seeds' dispersion – initial solid content of 5.7 and 6.0 respectively – was degassed under nitrogen gas, stirred at 300 rpm and heated up to 70 °C. In parallel, two mixtures were prepared. The first one, the monomer aqueous dispersion, made with 0.150 g of MAA, 8.000 g of MiliQ water, 6.000 g of MEO_2MA, 1.515 g of OEGMA and 0.183 g of OEGDA. The second mixture was an aqueous solution of KPS (0.0874 g/ 20 mL). Both were degassed for at least 15 minutes. Once the reactor was at the right temperature and after at least 45 minutes of nitrogen bubbling, the reactants were injected with a controlled injection speed thanks to an automated push-syringe, at 120, 6 or 1 ml/h. Once the injection was done, the seeded polymerization was let to occur for 6 hours, then stopped by cooling the mixture and by opening the reactor to the air.

2.2. ***Impact on the size and the morphology***

The hydrodynamic diameters of the core-shell (CS) particles at 60 °C was compared to the one of the PS seeds used. Each DLS measurement is an average of

at least 50 acquisitions, with for all a monodisperse size distribution characterized by a polydispersity index (PDI) below 0.1 (*Figure* 8).

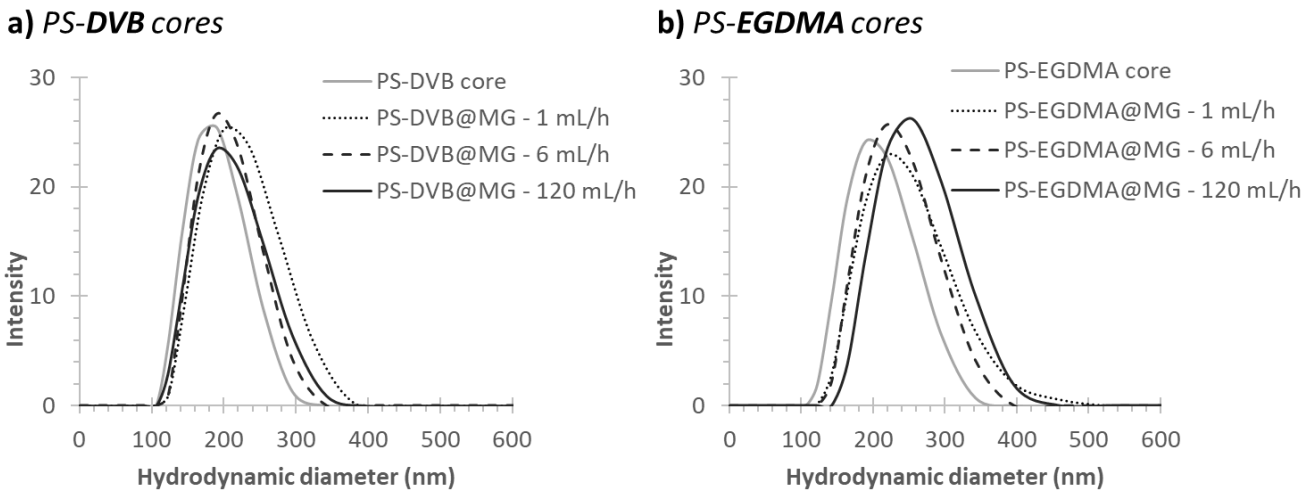

Figure 8. Hydrodynamic diameters distribution of PS seed and the corresponding purified suspensions of core-shell particles made at different injection speed. (a) Samples series with seeds crosslinked with DVB. (b) Samples series with seeds crosslinked with EGDMA.

A slight shift is observable from the results of CS made with PS-DVB cores, whatever the injection speed considered. From PS-DVB cores with an average size of 179 ± 27 nm, CS made with 120 and 6 mL/h have similar average sizes with 193 ± 33 and 195 ± 21nm, respectively. The maximum collapsed hydrodynamic diameter is reached with the slowest injection speed, with an average size of 219 ± 35 nm. Nevertheless, in the case of PS-EGDMA cores, the opposite trend is observed. With initial seeds of 179 ± 27 nm, the two slowest injection speed gives CS particles of 225 ± 49 and 221 ± 22 nm. Surprisingly, with the highest injection speed, at 120 mL/h, the tallest objects are measured around 244 ± 29 nm.

The particles morphology of purified suspensions (5 centrifugation/redispersion cycles at 10k rpm) was then compared thanks to Atomic Force Microscopy (AFM). Briefly, the dispersions were diluted to approximatively 1 mg /mL and then drop-casted on cleaned silicon wafers. The silicon wafers were cleaned by several washing with absolute ethanol and MilliQ water. The samples were let drying overnight before the AFM observations.

Figure 9 displays pictures of isolated beads corresponding to seeds used as core and their respective CS particles made at several injection speed.

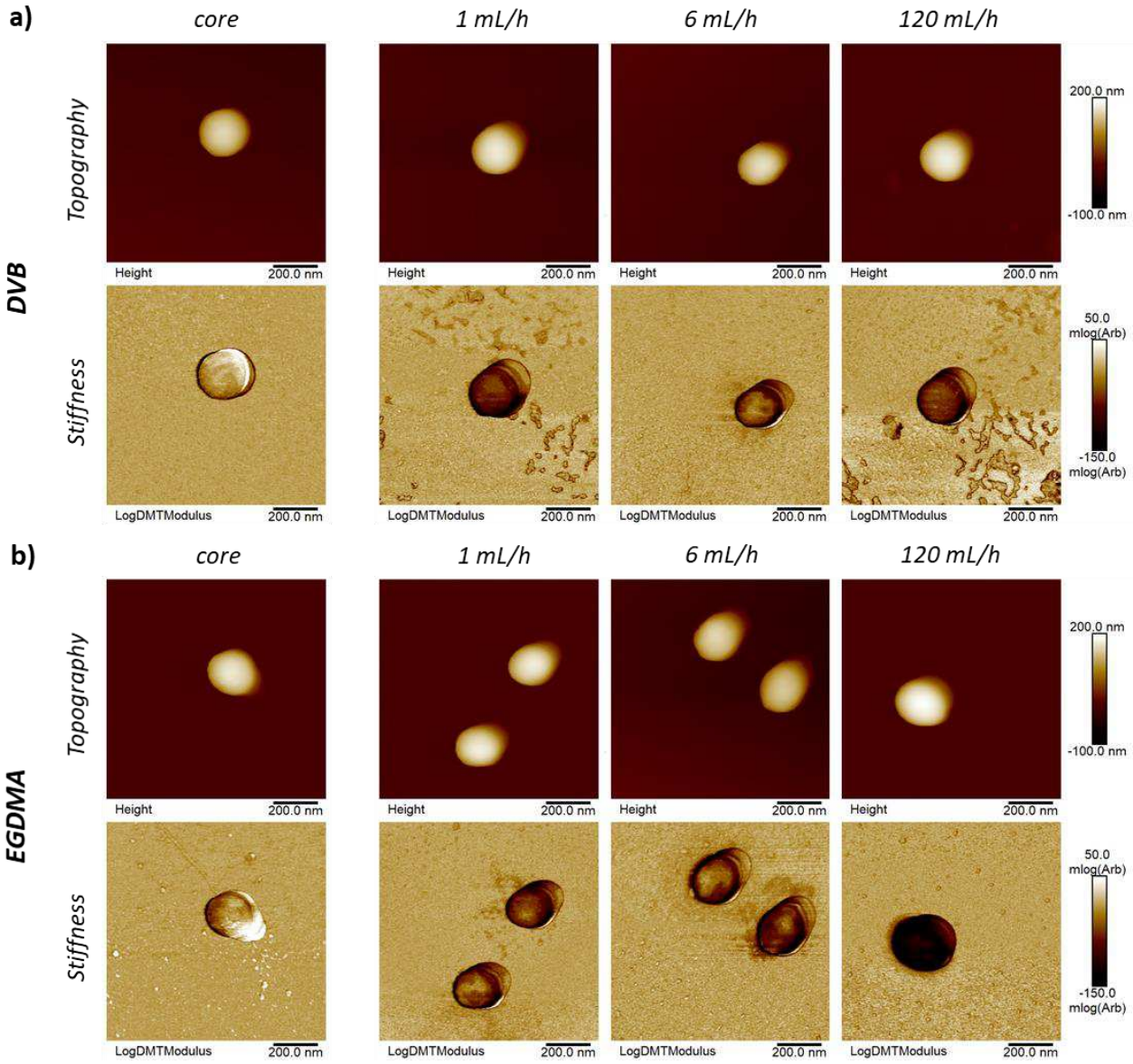

Figure 9 Atomic Force Microscopy (AFM) pictures of isolated colloidal beads. The images of the first line are display with a contrast in function of the surface relief whereas the pictures from the second line shows the same area, but with a contrast depending of the rigidity of the surface – the whiter are the pixel, the stiffer is the surface. (a) Samples series with seeds crosslinked with DVB. (b) Samples series with seeds crosslinked with EGDMA.

Whatever the sample, spheres with homogeneous shapes can be guessed, with average diameters close to the measured heights. AFM analysis allows to perceive a surface according to its contrast of mechanical properties. For each set of pictures, is displayed representation of the same area, either in function of its topography, or its stiffness. The stiffness is measured according to the measurement of the Derjaguin, Muller, Toropov, or DMT modulus, giving an approximation of the Young's modulus of the surface. In brief, the whiter the area, the stiffer the surface.

Due to the size dispersion of the colloidal object, no reliable information about the impact of the process on the size evolution can be done. However, it clearly appears that all the protocols considered lead to a darkening of the beads' surfaces, with respect to the silicon, compared to the initial PS beads. The softening of beads can be related here also to an effective grafting of the microgel shell.

The comparison of the particles spreading on the surface may give also information about the relative efficiency of each grafting protocol. Indeed, due to the viscoelastic properties of POEGMA material, the thicker is the shell, the more spread the CS particles on the wafer surface. However, AFM tip trends to slightly oversize the measured diameter, due to its geometry. The geometrical characteristic of the tips can be integrated simply in a relation described in the work of Canet-Ferrer *et al.*[14] to correct the diameter (width) measurements.

Figure 10 displays for PS-DVB@MG or PS-EGDMA@MG particles, a comparison of AFM measurement realized on at least 3 particles and hydrodynamic diameter measured with DLS. For core-shell particles, it appears systematically than the corrected width measured by AFM are higher than the measured height, testifying of the particles spreading

- The particles' heights of the dried core-shell particles are correlated to the hydrodynamic diameters of the seeds used. The grafted shell spread on the silicon wafer, and the tip probe essentially the diameter of the PS core.
- The particles' widths of the dried CS beads are related to the hydrodynamic diameters of the collapsed core-shell particles at 60 °C. The Standard deviation overlaps nonetheless the average value measured by DLS is often superior to the AFM measurements as expected. With DLS measurement, the shell's particle may remain swollen, even if the temperature is above its VPTT. Moreover, the light scattering gives access to the hydrodynamic diameter, which over evaluates the size of suspended object since it considers the solvation sphere surrounding the particles.
- The width/height ratios measured by AFM give access to a relative evaluation of the shell quantity grafted on the seed surface. With such consideration, the particle the more spread is the CS particle with a PS-EGDMA core and a high injection speed (120 mL/h)

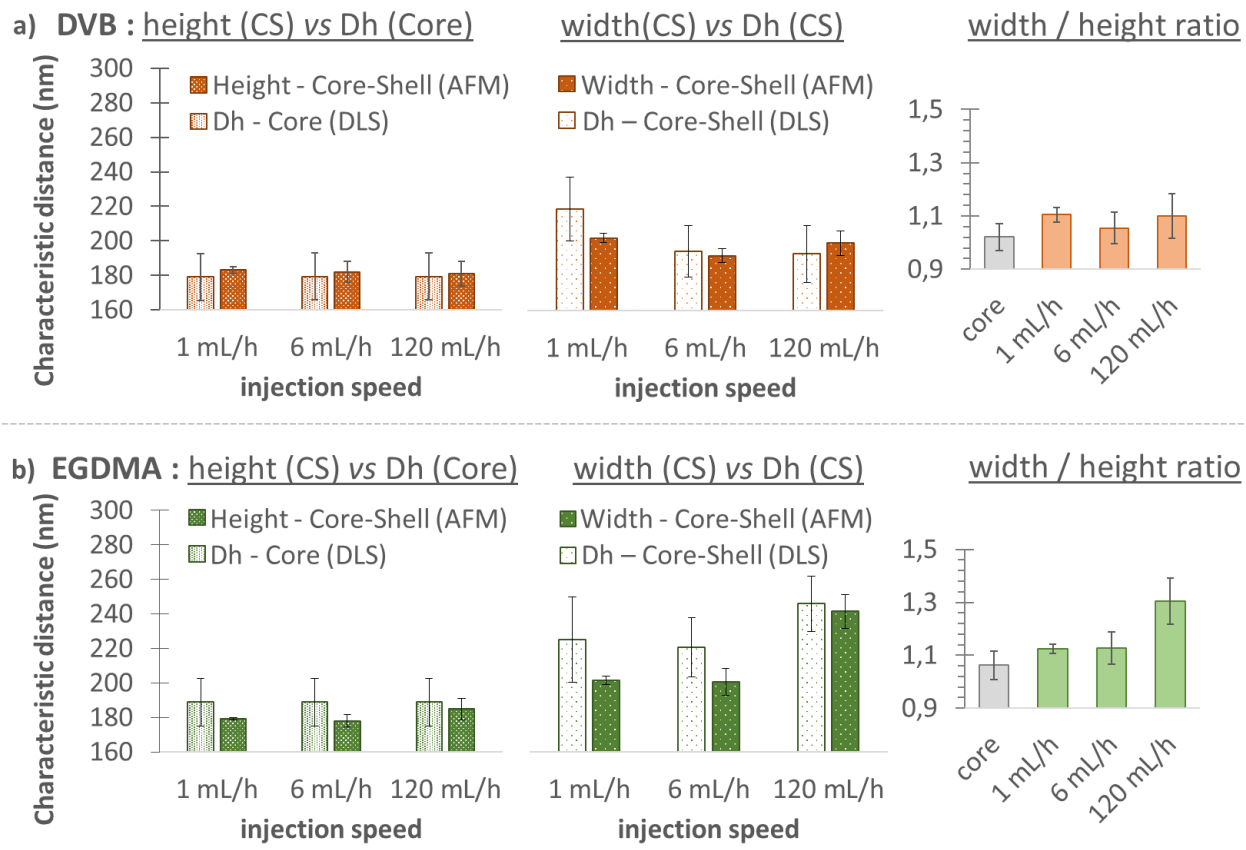

Figure 10 Comparison of hydrodynamic diameters (Dh) of purified suspensions of core-shell spheres and the corresponding seeds (DLS), with the average's measures of height and corrected width from core-shell colloids by AFM. On the right, an evaluation of the object spreading thanks to the comparison of the width/height ratios. (a) Samples series with seeds crosslinked with DVB. (b) Samples series with seeds crosslinked with EGDMA.

The size measurement by DLS and the morphological shape by AFM give similar results, both indicating a preferred grafting step. Indeed, PS cores crosslinked with EGDMA lead to the formation of the most important proportion of POEGMA shell. But this evaluation remains relative, only by comparison to the other protocol studied. A deeper investigation on the shell grafting rate is accessible through several approach.

2.3. *Grafting rate evaluation*

The evaluation of the grafting efficiency can be done in three different ways. The first one consists in the evaluation of the diameter of purified core-shell particles and compare this diameter to a theoretical one. The theoretical diameter is calculated considering some assumption on the particle density, and the absence of secondary nucleation during the grafting step. In this case, the diameters ratio

(experimental/theoretical) gives a first consideration of the grafting efficiency. The experimental methods involved are DLS (hydrodynamic diameters), and microscopy technics (AFM, TEM). Nevertheless, light scattering technics has the advantage to quickly gives an average value on a large population, at the opposite of visualization technics. That's why DLS is preferred in the rest of the manuscript for grafting rate evaluation. In such case, the grafting rate is expressed as:

$$\gamma_{Graft}^{Size} = \frac{D^{exp\,3} - {D_c}^3}{D^{max\,3} - {D_c}^3} \qquad \& \qquad D_{max} = \sqrt[3]{\frac{-(D_c)^3}{f_{MG}^m - 1}}$$

With D_{max} the theoretical diameter of the core-shell particle, considering that the density of the shell and core are equal, no secondary nucleation occurs, and the particle are spherical. D_c is the core diameter, f_{MG}^m is the theoretical mass fraction of microgel in the solid content and D^{exp} is the experimental diameter measured by DLS or microscopy.

Briefly, the raw suspensions are diluted roughly to 1 mg/mL with MilliQ water, then analysis with a Malvern ZetaSizer Nano Dynamic apparatus.

The second way to evaluate the grafting efficiency consider the chemical nature difference between raw dispersion and purified dispersions. Indeed, after purification, the suspension is free of un-grafted microgel whereas the proportion of grafted microgel on PS seed should remain the same. The comparison of the relative quantity of MG/PS remaining in the dispersion after purification with respect to the raw dispersion gives an evaluation of the grafting efficiency. The ratio of microgel/polystyrene in the dispersion was probed by ThermoGravimetric Analysis (TGA) & Fourier Transform InfraRed spectroscopy of Attenuated Total Reflectance (FTIR-ATR). The mass grafting rate is thus expressed as:

$$\gamma_{Graft}^{Compo} = \frac{{r_{MG/PS}}^{pure}}{{r_{MG/PS}}^{raw}}$$

With ${r_{MG/PS}}^{raw}$, the mass ratio of MG/PS in a film made from a purified dispersion & ${r_{MG/PS}}^{pure}$, the mass ratio of MG/PS in a film made from a raw dispersion.

For both TGA and FTIR-ATR, the films are prepared from suspensions dried under ambient conditions for at least 1 day and put in the oven for 6 hours under vacuum at 70 °C, just before TGA analysis.

With TGA, the data is gathered with an Q50 TA instrument apparatus. To do so, the films were heated from ambient temperature to 550 °C at the rate of 10 °C/min under nitrogen flux. The values of $r_{MG/PS}$ are extrapolated from the MG/PS intensities ratio of the weight derivative curve with respect to temperature. The two peaks used are located at 360~380 °C and 410~440 °C, for respectively the MG and the PS phases (Figure 11).

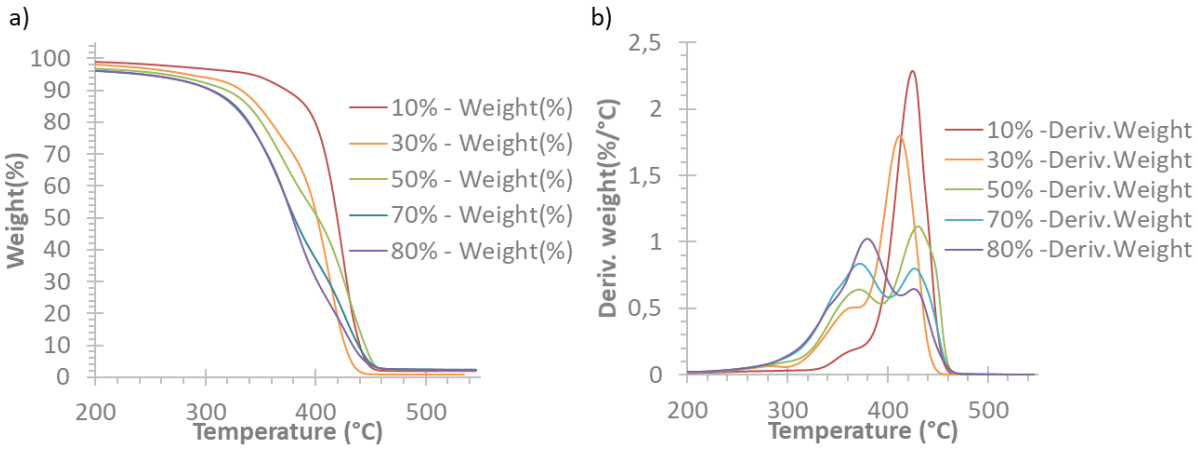

Figure 11 Thermogravimetric analysis (TGA) of dried residue made from POEGMA microgel and PS mixture. (a) Thermograms displaying the weight according to the temperature. (b) Variation of the weight derivative according to the temperature.

With FTIR-ATR, the apparatus used was a Nicolet iS50 FT-IR™ from Thermo Fisher Scientific. Each FTIR-ATR spectrum was made consecutively to a background acquisition of the ambient atmosphere. In such case, the values of $r_{MG/PS}$ are taken from MG/PS absorptions ratio (Figure 12). The two absorption peaks considered are located around 690 cm^{-1} and around 1110 cm^{-1}, corresponding respectively to the C-H deformation vibration of the PS phase and to the C-O elongation vibration of the POEGMA phase.

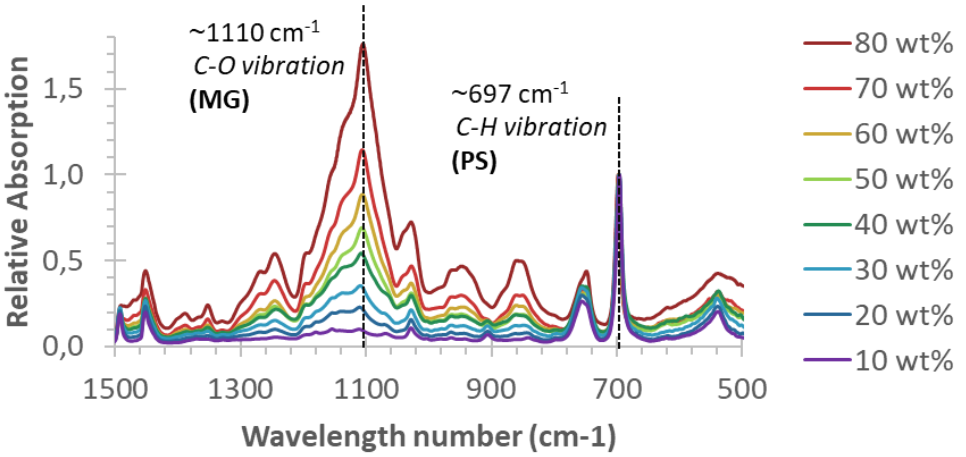

Figure 12. FTIR-ATR absorption spectrum of films made from the solvent evaporation of MG/PS mixtures. The mass percentage is related to the proportion of POEGMA microgel (MG) in the solid content.

The data were systematically treated with an automated baseline correction. More, as the ATR spectroscopy trends to overestimate the intensities of signals with low wavelength number, an automated ATR correction provided by the apparatus software was also performed. This correction considers, the crystal nature of the ATR set-up, here a diamond, the incidence angle, here 45° and the refractive index of the sample averaged at 1.50.

It is worth noting that the FTIR-ATR analysis was performed from the reflection of a light beam that penetrate evanescently inside the sample before being reflected up to the detector. The depth penetration of the incident IR beam must be superior than at least a row of CS particles (~0.5 µm) to get chemical information on the shell/core composition. Table 1 presents the evaluation of the depth penetration of the incident beam, according to our experimental set-up. Here, the refractive index of the sample is taken between two extremums constituting the suspensions, corresponding to the water and the poly(styrene). In those conditions, the depth probed by ATR is sufficient to go through at least one monolayer of CS particles, in wavenumber range of 500 – 4000 cm^{-1}.

Table 1. Variation of the depth penetration of the incident IR light in a sample in function of the wavenumber.

dp = depth penetration of the incident infrared light in the sample.
λ_1= wavelenght in the crystal of the infrared light
λ = wavelenght of the incident infrared light
n_1= refractive index of the crystal = 2.41
n_2= refractive index of the sample = [1.33 - 1.6]
θ = angle of incidence of the infrared light = 45°

$$dp = \frac{\lambda_1}{2\pi\sqrt{sin^2\theta - (n_2/n_1)^2}}$$

$$\lambda_1 = n_1 \times \lambda$$

σ	dp
500 cm-1	14.3 - 11.8 µm
1000 cm-1	7.1 - 5.9 µm
1500 cm-1	4.8 - 3.9 µm
2000 cm-1	3.6 - 3.0 µm
2500 cm-1	2.9 - 2.4 µm
3000 cm-1	2.4 - 2.0 µm
3500 cm-1	2.0 - 1.7 µm
4000 cm-1	1.8 - 1.5 µm

The viability of both procedures, TGA and FTIR-ATR, were confirmed with the characterization of films with a known MG/PS ratio, leading for each technic, to the corresponding calibration curves (*Figure* 13). The masses ratios are traced in function of the TGA intensities ratios or the FTIR-ATR absorbance ratios. For each experiment, it appears a linear relation between the masses' ratio and the experimental data. More information about the relative quantification approach is available in appendix 3, p.216.

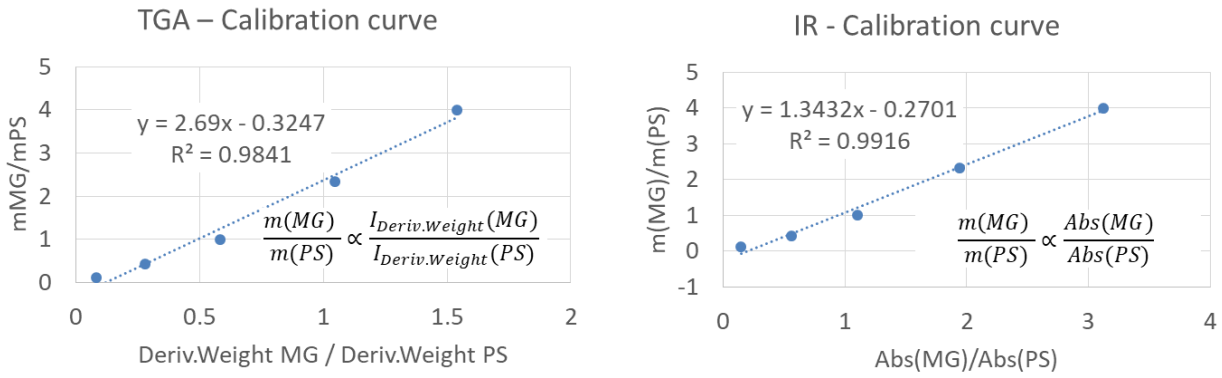

Figure 13. Calibration curves for TGA and IR relative quantification analysis. The $I_{Deriv.Weight}$ is the intensity of the weight derivative with respect to temperature (%/°C) extracted from the TGA thermograms.

The existence of a linear relation between the absorbances ratio and masses ratio has serious advantages for the evaluation of the shell grafting rate. Indeed, in case of seeded precipitation polymerization, the shell formation may induce the formation of free objects. This un-grafted material, possibly a mix between water

soluble polymers and nano/microgels, can be removed through several centrifugation/redispersion cycles of the raw suspension (Figure 14).

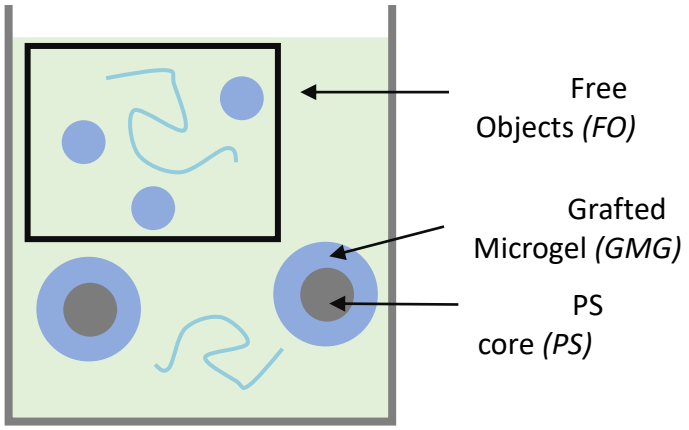

Figure 14 Schematic representation of the potential population suspended in the colloidal dispersion after the shell grafting step.

For instance, with FTIR-ATR data, before purification, the relation between the absorbances and the masses of polystyrene (PS) cores and POEGMA microgel (MG) material can be express as:

$$r_{MG/PS}^{raw} = \frac{Abs(MG)^{raw}}{Abs(PS)^{raw}} = K_{MG/PS}^{raw} \frac{m(GMG) + m(FO)}{m(PS)}$$
$$= K_{MG/PS}^{raw} \frac{Abs(GMG) + Abs(FO)}{Abs(PS)}$$

Where GMG represent the grafted microgel and FO the un-grafted free objects. After purification the relation should evolve as:

$$r_{MG/PS}^{pure} = \frac{Abs(MG)^{pure}}{Abs(PS)^{pure}} = K_{MG/PS}^{pure} \frac{m(GMG) + m(FO)}{m(PS)} = K_{MG/PS}^{pure} \frac{Abs(GMG)}{Abs(PS)}$$

Consecutively, the existence of linear relation between the absorbance ratio and the masses ratio implies that $K_{MG/PS}^{raw} \approx K_{MG/PS}^{pure}$. The comparison of the $r_{MG/PS}$ ratios allows thus an evaluation of the POEGMA shell grafting rate, with respect to the overall MG material in the suspension. This grafting rate is expressed as:

$$\frac{r_{MG/PS}^{pure}}{r_{MG/PS}^{raw}} = \frac{m(GMG)}{m(GMG) + m(FO)}$$

An analog reasoning is applicable for TGA experiences, where the corresponding absorbances are replaced by the intensities' ratio of the weight

derivative curves with respect to the temperature ($I_{deriv.weight}$). Instead of $\frac{Abs(MG)}{Abs(PS)}$ is thus considered $\frac{I_{Deriv.weight}(MG)}{I_{Deriv.weight}(PS)}$.

Those three methods (DLS, TGA and FTIR-ATR) brought coherent results with the grafting rate evaluation of PS-EGDMA@MG and PS-DVB@MG core-shell particles (Figure 15).

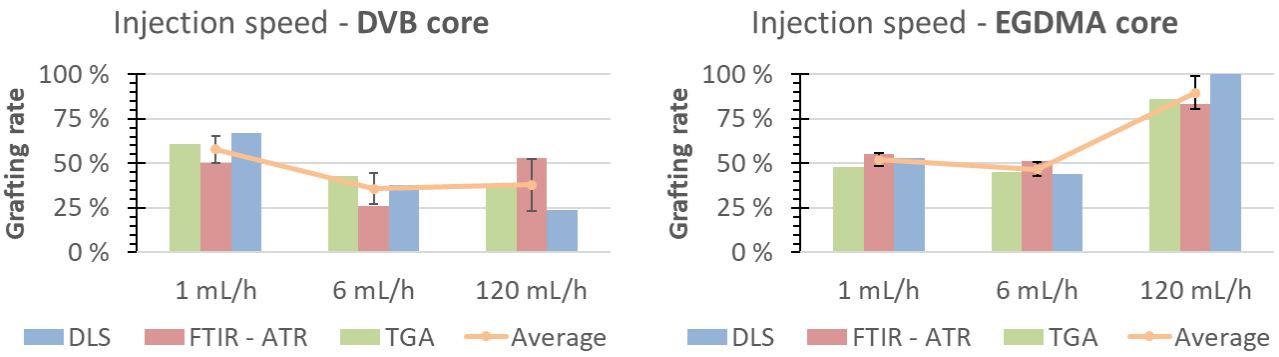

Figure 15 Summary of the grafting rate evaluation of the POEGMA-base microgel shell on the PS seeds, according to the seeds' crosslinker and the injection speed investigated.

From these three different approaches, an average value of the grafting rate is calculated for each injection speed. The *Figure* 15 confirms the trend identified previously. With CS made from DVB crosslinked cores, the highest grafting rates are effectively obtained with the slowest injection speed with an average value of 58 ± 8 wt%. The two highest injection speed, 6 & 120 mL/h, are associated with a decrease of the grafting rates, with respectively 36 ± 9 and 38 ± 15 wt%. With PS-EGDMA seeds, outstanding grafting rates are achieved with the highest injection speed, with an average value of 90 ± 9 wt%. For the 6 mL/h and 1 mL/h injection speeds, lower values are reached with average values of 47 ± 4 and 52 ± 4 wt%.

The PS-DVB series shows that a slight improvement of the grafting rate may be effectively achievable through the utilization of a semi-batch process with starved condition. Nonetheless, the utilization of a different crosslinker, here EGDMA improves significantly the probability of an efficient grafting. In this case, the grafting rate skyrockets when the monomers/initiators preparations are rapidly injected in the seed suspension.

2.4. ***Impact on the self-assembly***

The impact on the grafting rate on the self-assembly was focused on seeded EGDMA CS beads. The surface of films from raw and purified suspension were observed by AFM after solvent evaporation on a heating plate at 40°C. Surface images brought information on the self-assembly ability on the suspension, depending on the shell grafting rate. The samples' images are thus films from *raw* with ungrafted material and *purified* dispersions. Organization of particles presenting a grafting rate of around 90% and 50% are then compared (Figure 16).

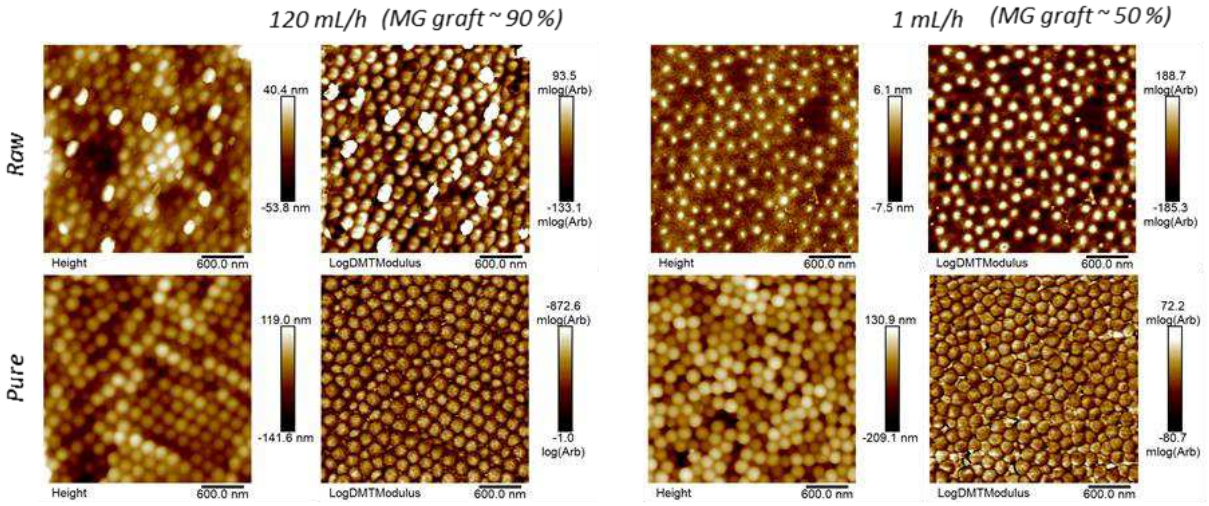

Figure 16. AFM pictures of films made from dispersion synthesized with an injection speed of 120 mL/h and 1 mL/h. PS core are crosslinked with EGDMA. Purified films are made from centrifuged dispersions. For each injection speed, the contrast in either displayed in function of the surface topography (left) or stiffness (right).

It appears firstly than higher is the grafting efficiency, higher is the particle organization on the film surface. The improvement of the surface organization is especially noticeable with purified dispersion. About raw films, no nanogels are observable for both dispersions. However, in the case of the slow injection speed (1mL/h), the presence of a slight "skin" seems cover the surface.

A decreased injection speed seems impact the microgel nucleation, limiting the formation of nanogels, however the presence of WSP still perturbs the particle organization. With the highest injection speed comes the raise of grafting rate. This process allows the particle to form a more regular array. This phenomenon can be associated with the strong abilities of microgel particles self-assembly.

As seen above, the highest injection speeds for the synthesis of PS-EGDMA@MG particles lead to an improvement of the particle organization, but what consequence does-it have on the film's optical properties? The Bragg diffraction phenomenon result from the interaction of the light with a well-ordered array. However, in our case, because of the size of the particle, Mie scattering phenomenon occurs simultaneously in the same spectral area. In order to evaluate the impact of the structural coloration on the Bragg diffraction intensity, it's required to separate the Bragg contribution from the spectrum. The isolated scattering spectrum is simulated by a function which is a combination of a classical exponential decrease and a power law. The UV – visible transmission spectra were obtained in a range of 300 nm and 800 nm, with a step of 1 nm. The apparatus was an UV-2450 spectrometer from SHIMADZU. The films were drop casted on a PS support relatively transparent in UV-visible.

With λ, the incident wavelength and k_0, τ, σ, c as fitting parameters, the equation is fitted on the experimental spectrum truncated from around 400 nm to 550 nm, corresponding to the area where the Bragg diffraction occurs. This empirical equation allows the reconstruction of a reliable baseline ($r^2 > 0.999$) of the scattering spectrum for each sample, without any diffraction phenomenon. The intensity difference between the experimental and the fitted baseline gives an evaluation of the Bragg contribution intensity in the experimental spectrum. It is then possible to compare the samples spectrum and observe how the synthesis process impact the Bragg diffraction (Figure 17).

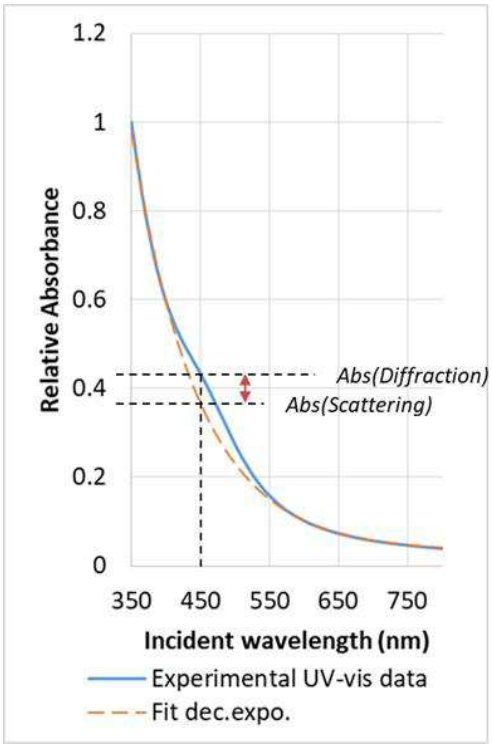

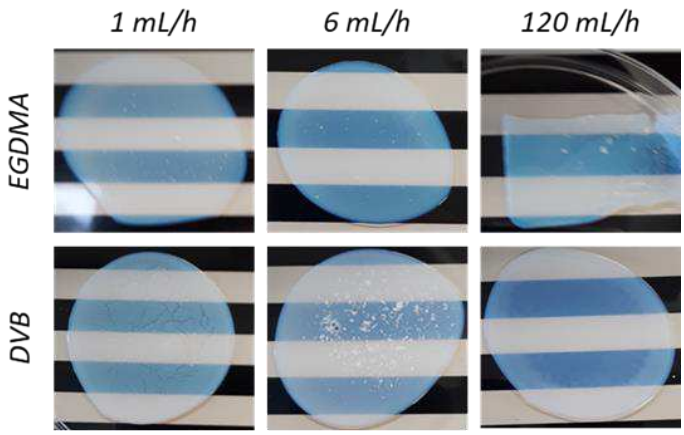

$$Abs = k_0 \times e^{-\tau \times \lambda} \times \lambda^{-\sigma} + c$$

Figure 17. Macroscopic images of films made from PS@MG dispersions synthesized with different injection speeds. The graph represents the evolution of an experimental spectrum and its modeled scattering baseline. The Bragg contribution is obtained from the subtraction.

This empirical approach was applied to all dry films of PS@MG. A slight decrease of the Bragg contribution is observable for core-shell particles from PS-DVB seeds, following the drop of the MG grafting rate (*Figure* 18).

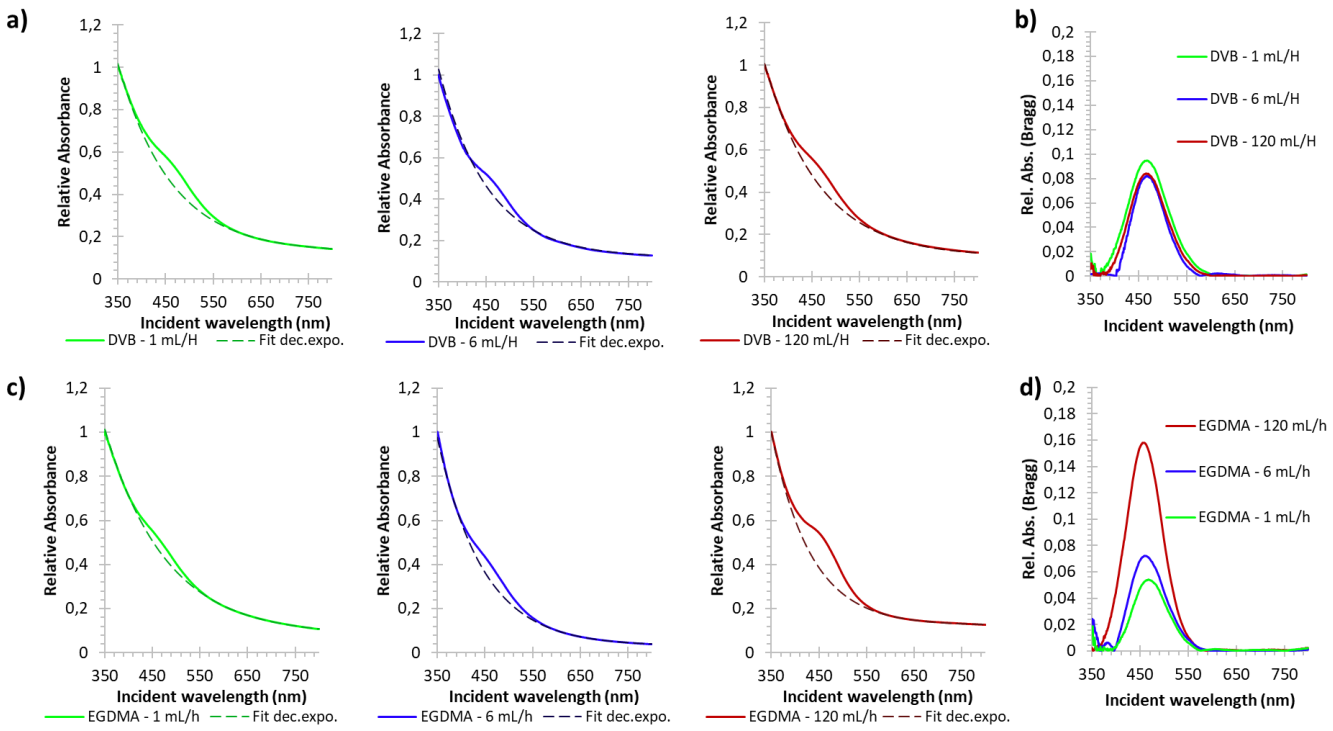

Figure 18 (a) & (c) UV-visible spectrum of a film made from a raw suspension of PS@MG(50wt%). The curve with the dashed line displays the baseline considered to isolate the diffraction peak. The baseline is traced from a partial fit on the experimental data from decreasing exponential function describe above. (b) & (d) Difference between experimental data and the fitted baseline. (a) & (b) Samples series with seeds crosslinked with DVB. (c) & (d) Samples series with seeds crosslinked with EGDMA.

However, for PS-EGDMA systems, the Bragg contribution raise significantly with the augmentation of the grafting rate. Globally, the intensity of the Bragg contribution raises with the grafting efficiency of the microgel phase. This result appears coherent with the improvement of surface organization observed with the AFM.

Conclusion

Core-shell like colloidal beads offers the possibility to conceive responsive photonic crystals. The elaboration of colloidal spheres made with a hard core of PS and a soft shell of POEGMA has been investigated. The purpose of such architecture is to control the shell thickness of the POEGMA layer and then control the parameter of unit lattice characterizing the crystalline arrangement.

The use of an adhesive interlayer of PBA has been firstly investigated through a batch process, with the direct mixing of the POEGMA monomers and the PS@PBA seeds. The observation *via* atomic force microscopy of films and isolated colloids highlighted POEGMA grafting issues. The outer shell synthesis leads to the formation of free POEGMA microgel particles due to secondary nucleation phenomenon. It has for consequence an inhibition of the self-assembly ability of the core-interlayer-shell CIS particles with respect to their seeds. A simplification of the colloidal design was then performed to focus on the POEGMA grafting on PS as core-shell CS particles, with less time and steps-consuming.

Core-shell CS architectures made of POEGMA-based microgel around crosslinked PS spheres was thus aimed. Two series of cores were compared, one cross-linked with DVB, with a similar chemical structure to PS, the other with EGDMA displaying chemical similarities with the POEGMA-based microgel (MG). In addition, a semi-batch synthesis protocol was tested, with a continuous introduction both of the monomers and the crosslinker in the seed dispersion. Several injection speeds were probed. The grafting rate of the POEGMA shell was evaluated from several characterization approaches to identify an effective synthesis pathway for the elaboration of PS@MG particles. The semi-batch protocol with a high injection speed involving the use of PS sphere crosslinked with EGDMA gives rise to the highest grafting rate, with an average grafting up to an average value around 90 ± 9 wt%. The improvement of the grafting rate is correlated with the formation of more organized self-assembled films, giving more intense structural colors.

To conclude this section, we have presented a way to make core-shell particles through two successive steps. We have managed the synthesis to overcome the requirement of intermediary purification with seeded precipitation polymerization[10,13,15,16]*. The copolymeric POEGMA shell offers a tunable VPTT*[17] *in contrast with classical acrylamide-based materials*[18]*. Moreover, the biocompatibility of the shell*[19,20] *give rise to interesting development, especially for skincare applications.*

References

1. Shen, Z., Shi, L., You, B., Wu, L. & Zhao, D. Large-scale fabrication of three-dimensional ordered polymer films with strong structure colors and robust mechanical properties. *J. Mater. Chem.* **22**, 8069 (2012).

2. Duan, L., You, B., Wu, L. & Chen, M. Facile fabrication of mechanochromic-responsive colloidal crystal films. *Journal of Colloid and Interface Science* **353**, 163–168 (2011).

3. Foulger, S. H. *et al.* Photonic Crystal Composites with Reversible High-Frequency Stop Band Shifts. *Adv. Mater.* **15**, 685–689 (2003).

4. Ito, T., Katsura, C., Sugimoto, H., Nakanishi, E. & Inomata, K. Strain-Responsive Structural Colored Elastomers by Fixing Colloidal Crystal Assembly. *Langmuir* **29**, 13951–13957 (2013).

5. Chen, J. *et al.* Highly Stretchable Photonic Crystal Hydrogels for a Sensitive Mechanochromic Sensor and Direct Ink Writing. *Chem. Mater.* **31**, 8918–8926 (2019).

6. Hong, R. *et al.* Highly sensitive mechanochromic photonic gel towards fast-responsive fingerprinting. *RSC Adv.* **7**, 33258–33262 (2017).

7. Lee, G. H. *et al.* Chameleon-Inspired Mechanochromic Photonic Films Composed of Non-Close-Packed Colloidal Arrays. *ACS Nano* **11**, 11350–11357 (2017).

8. Lee, G. H. *et al.* Elastic Photonic Microbeads as Building Blocks for Mechanochromic Materials. *ACS Appl. Polym. Mater.* **2**, 706–714 (2020).

9. Viel, B., Ruhl, T. & Hellmann, G. P. Reversible Deformation of Opal Elastomers. *Chemistry of Materials* **19**, 5673–5679 (2007).

10. Andersson, M., Hietala, S., Tenhu, H. & Maunu, S. L. Polystyrene latex particles coated with crosslinked poly(N-isopropylacrylamide). *Colloid and Polymer Science* **284**, 1255–1263 (2006).

11. Boularas, M. *et al.* Dual stimuli-responsive oligo(ethylene glycol)-based microgels: insight into the role of internal structure in volume phase transitions and loading of magnetic nanoparticles to design stable thermoresponsive hybrid microgels. *Polym. Chem.* **7**, 350–363 (2016).

12. McIlvaine, T. C. A buffer solution for colorimetric comparison. *JOURNAL OF BIOLOGICAL CHEMISTRY* 183–186.

13. Shi, S. *et al.* Poly(methyl methacrylate)/poly(N-isopropylacrylamide) core-shell particles prepared by seeded precipitation polymerization: Unusual morphology and thermo-sensitivity of zeta potential. *Chinese Journal of Polymer Science* **32**, 524–530 (2014).

14. Canet-Ferrer, J., Coronado, E., Forment-Aliaga, A. & Pinilla-Cienfuegos, E. Correction of the tip convolution effects in the imaging of nanostructures studied through scanning force microscopy. *Nanotechnology* **25**, 395703 (2014).

15. Park, J.-G. *et al.* Photonic-crystal hydrogels with a rapidly tunable stop band and high reflectivity across the visible. *Optical Materials Express* **7**, 253 (2017).

16. Yuan, S., Ge, F., Yang, X. & Guang, S. Self-Assembly of Colloidal Photonic Crystals of PS@PNIPAM Nanoparticles and Temperature-Responsive Tunable Fluorescence. *Journal of Fluorescence* **26**, 2303–2310 (2016).

17. Lutz, J.-F. Thermo-Switchable Materials Prepared Using the OEGMA-Platform. *Adv. Mater.* **23**, 2237–2243 (2011).

18. Islam, M., Ahiabu, A., Li, X. & Serpe, M. Poly (N-isopropylacrylamide) Microgel-Based Optical Devices for Sensing and Biosensing. *Sensors* **14**, 8984–8995 (2014).

19. Lutz, J.-F. Polymerization of oligo(ethylene glycol) (meth)acrylates: Toward new generations of smart biocompatible materials. *J. Polym. Sci. A Polym. Chem.* **46**, 3459–3470 (2008).

20. Cooperstein, M. A. & Canavan, H. E. Assessment of cytotoxicity of (*N* -isopropyl acrylamide) and Poly(*N* -isopropyl acrylamide)-coated surfaces. *Biointerphases* **8**, 19 (2013).

Chapter III: Colloidal self-assembly: film characterization

Introduction

In the previous chapter, several technological limitations were identified for the elaboration of core-shell beads without the utilization of intermediary purification steps. Fortunately, a synthesis method has been identified for the grafting of a thermo-responsive POEGMA-based microgel on PS spheres. In this chapter, we expose the design of several core-shell particles, with different thickness of shell producing films with tunable colorations. At this end, the architecture/composition of the beads were followed by AFM, TEM, DLS and FTIR-ATR spectroscopy, similarly to the previous chapter. The self-assembled photonic crystals were then characterized by AFM/SEM microscopy and by UV-visible photo spectroscopy to identify the crystalline lattices formed, and their spontaneous mechano-chromic responsiveness. Finally, a focus on the copolymer composition that constitute the shell is presented, aiming the promotion of the self-assembly properties of raw suspensions. The impact of the core size on the self-assembled structure is also discussed.

1. Tunable coloration

1.1. *Experimental Method:*

Polystyrene beads (core) – chemical modification

Materials: Styrene (S– from Sigma-Aldrich); divinylbenzene (DVB – from Sigma-Aldrich); Sodium Dodecylsulfate (SDS – from ABCR); ethylene glycol dimethyl acrylate (EGDMA – from Sigma-Aldrich); potassium persulfate (KPS – from Sigma-Aldrich).

The PS cores are produced from the emulsion polymerization of the St with DVB/EGDMA. Before use, the inhibitors contained in the all commercial monomers are removed through mixing with an adapted inhibitor remover provided by Sigma-Aldrich, and filtering. The total amount of crosslinker is calculated to keep a molar ratio of $\frac{n_{crossl}}{n_{St}+n_{crossl}} = 5\ mol\%$. The surfactant (SDS) concentration is controlled, according to the core size targeted, here between 150 – 200 nm (Appendix 1). The final solid content targeted - SC_{th}, considering a conversion rate of 100%, is adjusted with water to keep $SC_{th} = 6.0 \pm 0.5\ wt\%$.

Here, in 1.5 liters 3-neck rounded bottom beaker set up with a thermostat and a mechanical stirrer, 650 g of MiliQ water and 0.426 g (1.5 mmol) of SDS were mixed. Successively, 42.636 g (0.409 mol) of styrene with the corresponding amount of crosslinker (0.020 mol) were added into the reactor, that is 2.665 g of DVB or 4.057 g of EGDMA. *The mixture was then stirred at 300 rpm for 45 min under bubbling nitrogen gas while the temperature was increased to 70 °C. After 45 min and once the set temperature was reached, a degassed aqueous solution of KPS (0.1930 g (0.7 mmol) /10 mL) was injected into the reactor. The reaction was stopped after 4 hours by opening the reactor to air and cooling the mixture to ambient temperature.*

POEGMA microgel shell

Materials: diethylene glycol methyl ether methacrylate (MEO2MA), oligo ethylene glycol methyl ether methacrylate (OEGMA – $M_w = 475\ g.mol^{-1}$), methacrylic acid (MAA); oligo ethylene glycol diacrylate (OEGDA – $M_w = 250\ g.mol^{-1}$) and potassium persulfate (KPS). All the materials are provided by Sigma-Aldrich.

The grafting step of the POEGMA shell is then performed on the obtained raw seeds, according to the protocol identified in the previous chapter.

The following protocol theoretically lead to a dispersion with a final solid rate of 8.9 ± 0.3 wt%. The monomers are prepared to keep a OEGMA/MEO2MA ratio of 10 mol%, a MAA/(OEGMA + MEO2MA) ratio of 5 mol%, a crosslinker/monomers ratio of 1.92 mol% and a initiator/vinylic molecules ratio of 0.86 mol%. The shell proportion is adjusted with the seed dispersion quantity, for a fixed masses of shell monomers. Consecutively, core-shell particles with expected proportion of 67, 75, 80 and 85 wt% of shell material in the solid content (f_{MG}) are produced.

In 1.5 liter 3-neck rounded bottom beaker set up with a thermostat and a mechanical stirrer a controlled mass, $m_{seeds,}$ of raw PS-EGDMA seeds' dispersion (Table 1)– initial solid content of 5.31 respectively – was degassed under nitrogen gas, stirred at 300 rpm and heated up to 70 °C. In parallel, two mixtures were prepared. The first one, the monomer aqueous dispersion, made with 0.150 g (1.8 mmol) of MAA, 8.000 g of MiliQ water, 6.000 g (31.9 mmol) of MEO₂MA, 1.515 g

(3.2 mmol) of OEGMA and 0.183 g (0.7 mmol) of OEGDA. The second mixture was an aqueous solution of KPS (0.0874 g (0.3 mmol) / 20 mL). Both were degassed for at least 15 minutes. Once the reactor was at the right temperature and after at least 45 minutes of nitrogen bubbling, the reactants were injected with a controlled injection speed thanks to an automated push-syringe, at 120 ml/h. Once the injection was done, the seeded polymerization was let to occur for 6 hours, then stopped by cooling the mixture and by opening the reactor to the air.

Table 1.

f_{MG}	67 wt%	75 wt%	80 wt%	85 wt%
m_{seeds}	74.692 g	49.795 g	37.346 g	26.362 g

1.2. ***Impact of the shell thickness on optical properties***

The hydrodynamic diameters of the core-shell spheres were evaluated by DLS. The samples were prepared from raw suspensions diluted to roughly 1mg/mL. The Figure 1 shows the evolution of the size distribution, according to the expected proportion of shell material in the solid content.

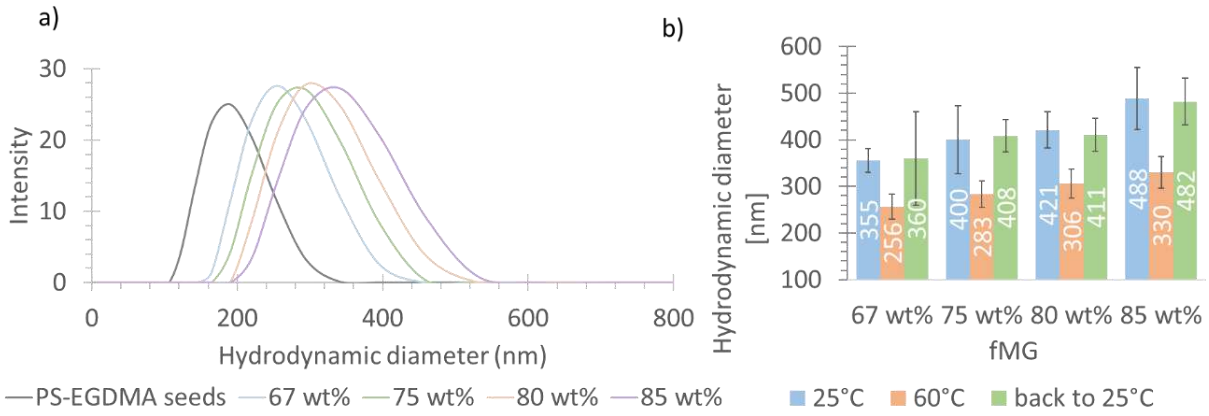

Figure 1 (a) Hydrodynamic diameter distribution of particles, from raw seeds suspensions at 25 °C to purified core-shell particles dispersions at 60 °C. (b)The average hydrodynamic diameters of purified core-shell suspensions undergoing several temperatures: at 25 °C then after 10 minutes at 60 °C and finally cooled to 25 °C, stabilized during 10 minutes before the acquisitions.

The average hydrodynamic diameters of collapsed particles grow with the expected amount of POEGMA-based microgel in the solid content (f_{MG}). As all the core-shell dispersions were made from the same seed dispersions, with an initial

average diameter of 185 ± 19 nm, an increase of the shell thickness is observed. For suspensions with targeted microgels content of 67, 75, 80 or 85 wt% in the solid content of raw suspensions, average diameters of 256 ± 27 nm, 283 ± 28 nm, 306 ± 32 nm and 230 ± 33 nm are respectively obtained at 60°C. The suspensions obtained are associated with polydispersity indexes (*PDI*) below 0.05 whatever the experimental conditions probed corresponding to a narrow size distribution of the microgels. The conservation of the thermo-responsivity of the particle, associated with the coherent increase of the hydrodynamic diameters indicate the protocol synthesis seems to operate, with a gradual increase of the shell thickness according to f_{MG}. To push forward the investigation on the grafting rate of the shell material, similar approach as in the chapter 2, can confirm the robustness of the synthesis method.

Grafting rates particles. Isolated particles were studied by AFM from samples prepared through the solvent evaporation of purified suspension (5 centrifugation/re-dispersion cycles) diluted at 1 mg/mL on cleaned silicon wafers (Figure 2*a*).

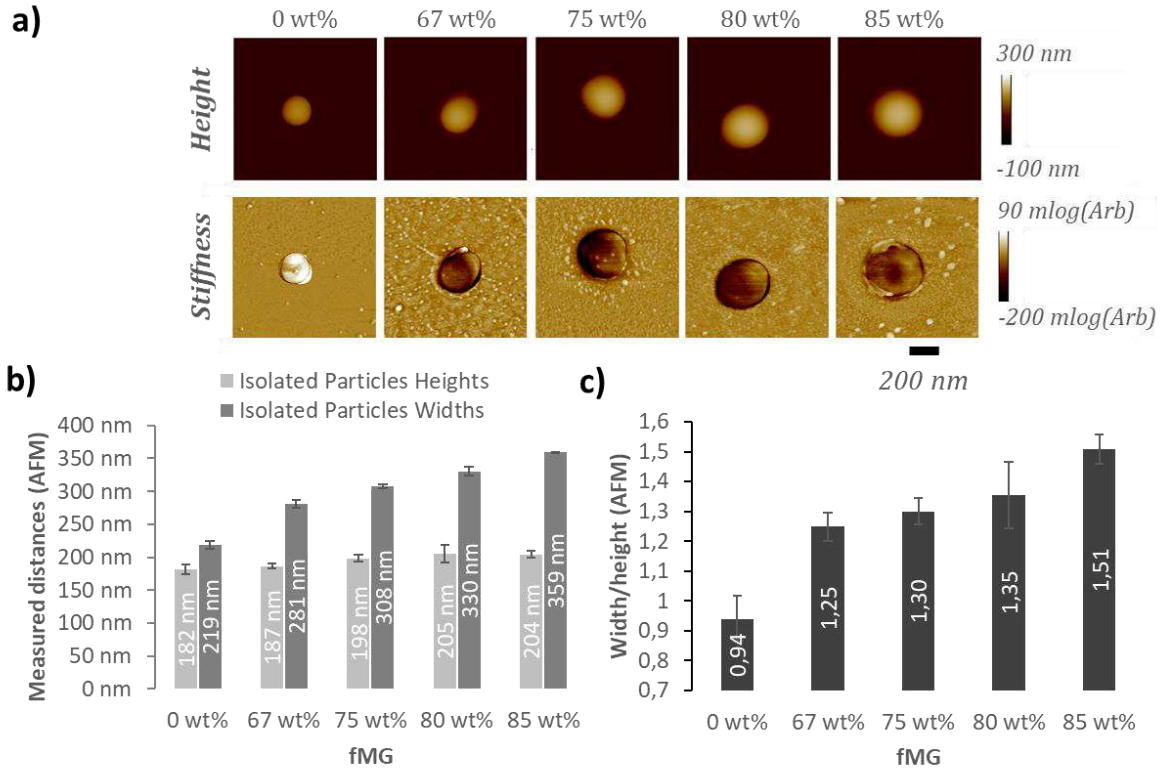

Figure 2. (a) AFM pictures of isolated particles from purified dispersions with contrast depending of the surface topography or stiffness. (b) Comparison between the measured heights & widths of these particles(c) Evaluation of the average width/height ratios for each group of particles. At least two different particles are considered each time

Homogeneous spheres in size and shape were observed. The enlarging of the soft-shell thickness is related to an increase of spheres' spreading on the substrate. Indeed, the comparison of the corrected width measured by AFM, with respect to the measured heights gives an appreciation of the object's spreading on the substrate (Figure 2*b*). As in the previous study presented in chapter 2, the measured heights give values similar to raw core measurement, marked by a slight increase with the microgel percentage. At the opposite, the corrected width increases significantly with the rise of MG material. Consecutively, the width/height ratio increase with the MG proportion, testifying of the particle spreading (Figure 2*c*). POEGMA/PEGMA materials are known for their visco-elastic

properties due to their negative glass transition temperature: the polymeric chains are mobile at ambient temperature and interact with their surrounding and spread on the silicon. Moreover, a strong adhesion of the isolated microgels with silicon surface was already observed by AFM[1]. It worth noting that the stiffness is coherently impacted by the MG grafting step: the particle becoming darker than the initial PS seeds, with respect to the substrate.

As described in the previous chapter, a deep analysis of the shell grafting rate was performed. Briefly, the grafting rate presents the amount of MG effectively grafted on seeds, compared to the total amount of MG material in the suspension. Evolutions of the size and the chemical composition were realized by DLS and FTIR-ATR, respectively (Figure 3).

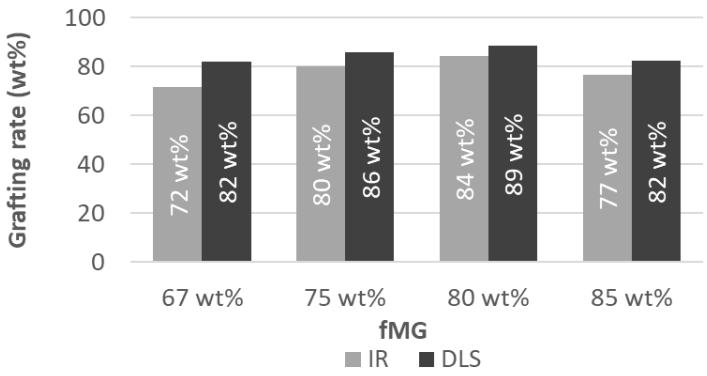

Figure 3. FTIR-ATR & DLS microgel (MG) grating rate evaluation on PS-EGDMA seeds.

The analysis of the MG grafting rate by DLS & FTIR-ATR shows similar results with an average microgel grafting rate around 81 ± 5 wt%, whatever the f_{MG} proportion. In other words, around 20 wt% of the microgel precursors as led to objects still free in the solution. However, the pure microgel synthesis is known to form also free-water soluble polymer with around 25 ± 5 wt% of the final solid content of microgel. The apparent constancy of the grafting rate values could be explained as an intrinsic limitation inherent to the microgel formation mechanism.

Coloration. The macroscopic observation of the films obtained from the dispersions synthesized shows the formation of iridescent layers from f_{MG} = 66.7 wt to higher fraction (Figure 4). The films were prepared by solvent evaporation of corresponding dispersions on PS substrates set on a heating plate at 40 °C.

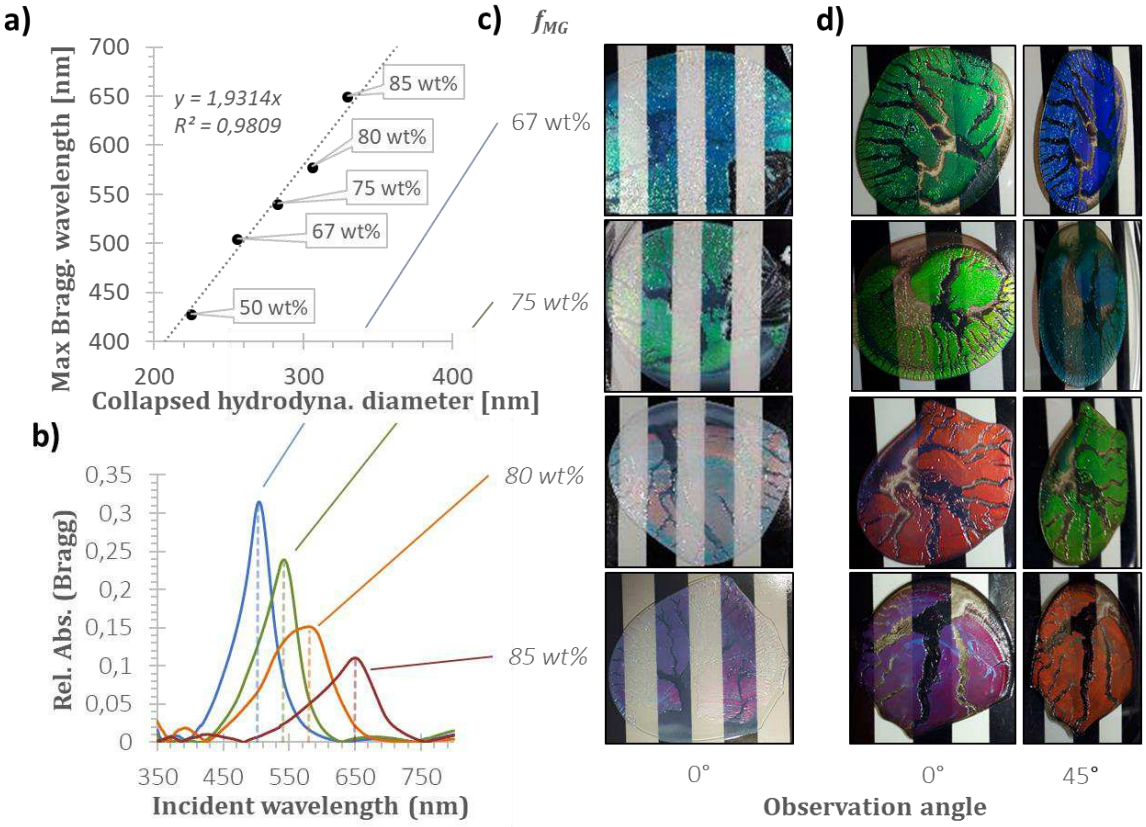

Figure 4. Macroscopic pictures of PS/MG films with transmission spectroscopy analysis. (a) Maximum intensity of the Bragg contribution in function the size of the CS particles. (b) Contribution of the Bragg diffraction in the normalized transmission spectrum of films made from raw suspensions by solvent evaporation at 40 °C. (c) Corresponding films photographed with an incidence angle of 0° with respect to the surface normal. (d) Films made in the same conditions and from the same dispersion with the addition of 0.0075 wt% of carbon black nanotubes in the dispersions. The photography was taken with the same lighting, from observation angle of roughly 0° and 45° with the surface normal.

The more the microgel fraction increase, the more the color is red-shifted, with a decrease of the evaluated Bragg contribution intensity. The color shift follows effectively a linear relation with the particle sizes, coherent with the Bragg-Snell equation. The intensity decrease appears here as a consequence, of the scattering dependence of the diffraction phenomena, in relation to the incident wavelength in this size range. However, the films are crackled. During the drying, a macroscopically observable iridescent layer is formed at the surface of the wet film.

This photonic layer is fractured during the drying process, and finally is "frozen" progressively as the water evaporates, letting an iridescent film on the substrate.

Sphere interpenetration Colloidal lattices are observable on the films' surfaces by AFM (Figure 5).

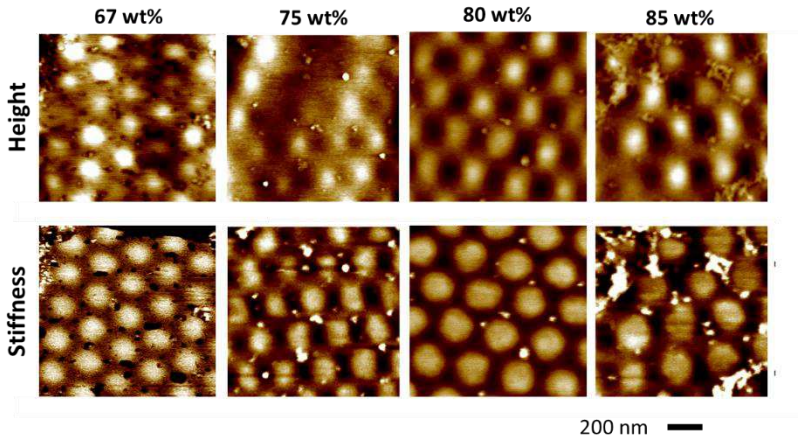

Figure 5. Picture from AFM of film's surfaces made with raw suspensions of CS particles. The amount of microgel material in the solid content is displayed above. The contrast is either displayed in function of the surface topography – the whiter the pixel, the higher the surface (top) or its rigidity – the whiter the pixel, the harder the surface. (bottom).

Most of the time, hexagonal patterns are observed but depending the area probed, cubic lattices may appear. However, the inter-particle distances measures are the same for given systems, whatever the surface square/hexagonal array. Such characteristics may be coherent with (100)/(111) crystalline plans of classical face-centered cubic lattice. The complementary observation of isolated CS particles by TEM can demonstrate an interpenetration of the shell in the films as the inter-distance is lower than the dimeter of individual particle.

At this end, TEM images were performed by drying of suspensions roughly diluted to 1 mg/mL on TEM grids in environmental conditions. The visualization of the particles by TEM allows to distinguish the grafted PEGMA shell (Figure 6*b)*.

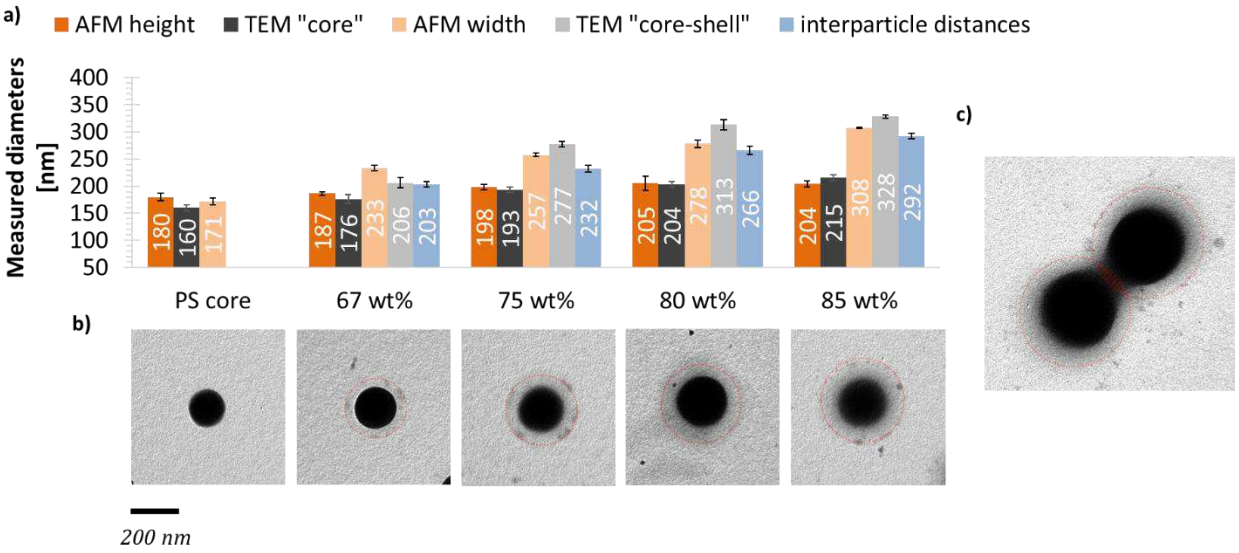

Figure 6 (a) Evolution of the measured particles dimensions by microscopy. The "core" measurement by TEM designed the darker are of the particles whereas the "core-shell" stands for the diameter of the outer limitation revealed by the dust, highlight here with red circles made of a dashed line.

Indeed, a dense core is observed and surrounded by a light halo: the more the thickness of microgel increases, the more the halo circumference raises. The MG shell is composed of a loose network of deformable PEGMA-like chains which can flow at room temperature (a glass transition temperature *Tg* was measured by DSC to be around Tg ~ -35°C).[19] On the opposite, the core is made of a thermoplastic polymer as a frozen network of PS chains. Here, we supposed that the looseness of the PEGMA network associated to its spreading on the support doesn't allow to get enough contrast to be perceived directly by TEM. However, the circumference of the core@soft shell building blocks is revealed thanks to some dust adsorbed at their surfaces. The dark region of the particles displayed by TEM, the "cores", present similar dimensions with the heights measured by AFM, and confirm the presence of more compact cores in the center of the particles (*Figure 6a*). In addition, the diameters of the halo observed by TEM ("core-shell" diameters) have values close to the widths measured by AFM and confirm the perception of the shell by TEM. More interestingly, the interparticle distances measured by AFM on the films surfaces appears systematically lower than the CS widths measurement, whatever the imaging technic used. This difference is explained by the intertwinement of the particles in the self-assembled structures. Indeed, the corresponding interpenetration of the shells is thus possible due to the

loose and flexible network of the MG layer. This interpenetration is observable in Figure 6*c*, where this phenomenon is associated to a darkening of the mixed shell. Nonetheless, this observed darkening here may be also due to an overlapping of the shell: only the compared particle measurements give the certitude of this interpenetration.

1.3. *Self-assembly mechanism*

Convection driven self-assembly. The self-organization of colloidal systems is depending of entropic forces and particles visco-elastic behavior during the dispersion drying process[2–4]. In order to explore the impact of the temperature, the same dispersion of PS-EGDMA@MG(75 wt%) were dropped on PS substrates. As the CS particles demonstrated to be thermo-responsive, similar behavior was probed on films. To do so, PS substrates were put on a heating plate set at 30 °C & 60 °C and compared with a film made at ambient temperature. The corresponding macroscopic pictures of the films are presented in Figure *7*.

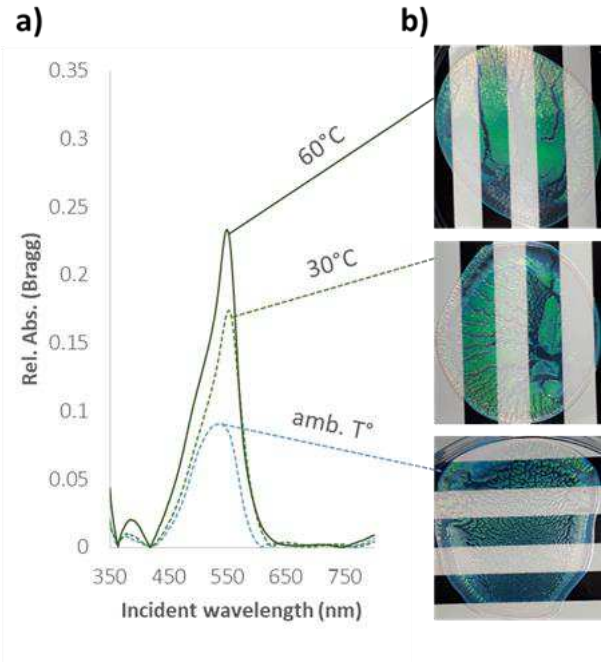

Figure 7. Macroscopic pictures of films made at on substrate at different temperatures and their respective

It can be observed an expansion of the colloidal crystal surface with the increase of the substrate's temperature. At ambient temperature, the film presents a transparent, glassy aspect. A slight coloration is still noticeable, but less to what is currently observed with films made on hot substrates.

A temperature close or above the VPTT (27°C for raw suspensions) seems to improve the surface organization. When the temperature increase, the particles dispersed switch from a soft and swollen state to a harder and collapsed state. The colloidal system get similarity with systems known to form well-designed self-assembled arrays, like PS particles[5,6]. With heat, the particles surfaces become more hydrophobic and the shells collapse.

Heterogeneous arrangement. The macroscopic aspect of the films presents on surface a colorful iridescent layer, but fractured. Beneath this layer, the film seems to present a glassy aspect. The hypothesis proposed is the core-shell particles self-organized only on the top of the wet film during its drying. This behavior would be comparable to self-assembly mechanism proposed in the literature for hard spheres[5,6].

To confirm the existence of this localized iridescent layer, a dispersion of PS-EGDMA@MG (75 wt %) with 0.0075 wt% of CNT was let drying on thermo-plastic poly-urethane (TPU). The film was then characterized by reflectance spectroscopy. The TPU support was firstly characterized by transmission spectroscopy to confirm its transparency in the visible range. Then the TPU supported films of CS particles were characterized by reflectance spectroscopy on each face (up and down). The total reflectance (*Rt*) and the diffuse reflectance (*Rd*) spectra are both collected for the TPU support and the TPU support + film (Figure 8).

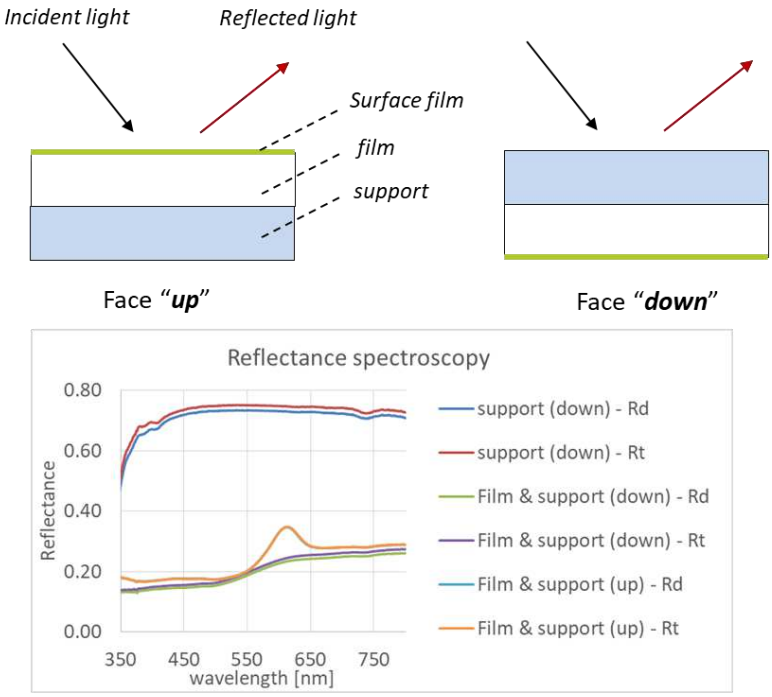

Figure 8. Schema of the faces of the films probed by reflectance spectroscopy. The TPU support is non-absorbing in the visible spectrum. Corresponding spectra are displayed below.

Figure 8 shows no differences between Rd & Rt. The TPU support displays no significant reflectance signal by comparison with the ones with the sample. Indeed, the spectra of films face "up" show a peak related to diffraction signals identified for usual CS films. However, with films face "down", the diffraction signal totally disappears due to the formation of a colloidal glass. If the colloidal crystal were formed both on bottom and the top of the film, a diffraction signal should be present for face "down" samples, too.

With a colloidal glass beneath the colloidal crystal layer, the carbon nanotubes would absorb the incident light, forbidding the acquisition of any diffraction signal for face "down" samples. With face "up" films, the selective reflection of wavelength corresponding to the Bragg wavelength is allowed, and a diffraction signal is perceived. The comparison of the reflection spectra from film's surfaces at the former air/water (top) and water/substrate (bottom) dispersion interfaces indicate the diffraction is thus localized only at the former air/water top interface.

At this interface, significant colloidal organization's differences appear by SEM observations depending of the film areas. Where iridescent colorations are

perceived, mono-crystalline surfaces with length up to 20 µm are observed. On more transparent areas, the colloidal organization is completely disordered (Figure 9).

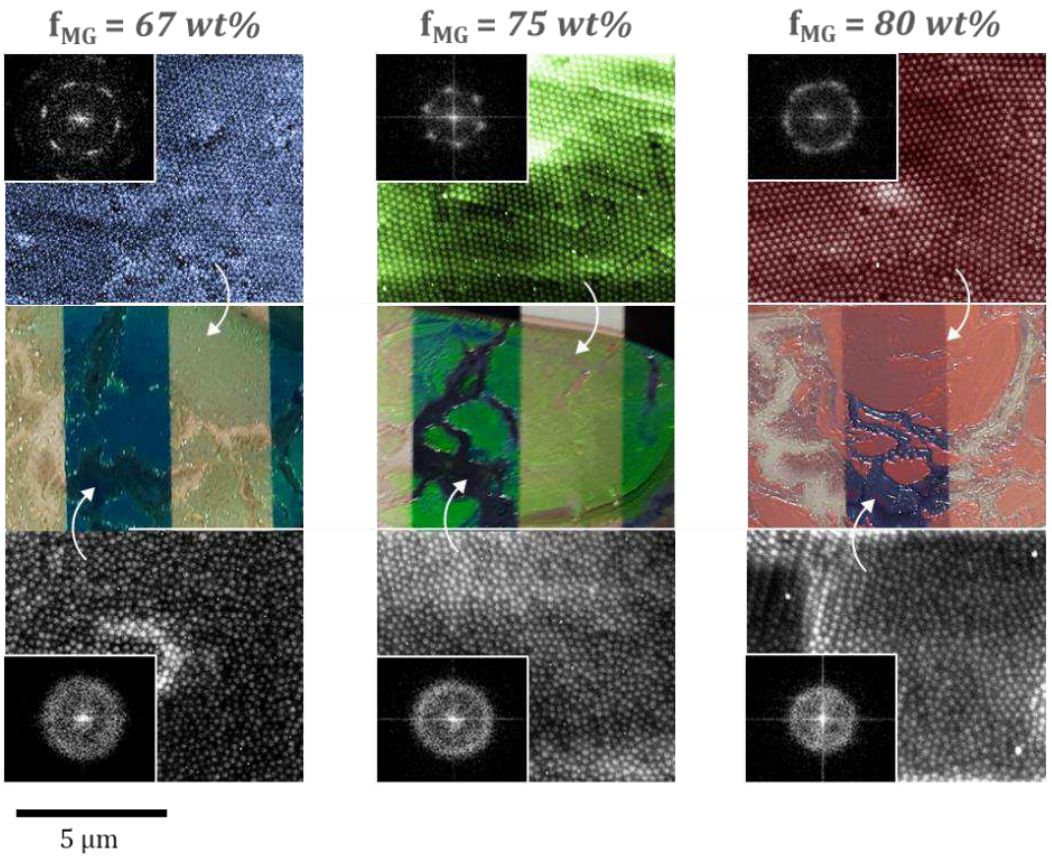

Figure 9. Pictures from TEM of films made from raw suspensions of CS particles with different proportion of MG material in the dried residue. The TEM pictures have been taken from different macroscopic areas on the films. Corresponding Fourier transformation of the TEM picture is represent each time in the corner of the associated image. The TEM picture at the top are artificially colored.

It comforts the previous experimental observations where a slight iridescent layer was macroscopically observed on the top surface of drying films. The self-assembled layer during the solvent evaporation breaks and reveals the amorphous arrangement below. Indeed, this self-assembly heterogeneity should also be observed in the depth of the film.

The in-depth organization analysis was performed from sample to be cut by cryo-ultramicrotomy, before AFM imaging. To do so, a dispersion of PS-EGDMA@MG (75 wt %) was let drying on a Thermanox™ plastic support at ambient temperature overnight. Then, the film was frozen at -120°C in the cryo-

ultramicrotome chamber. The sample was trimmed to form a truncated pyramid on the film cross-section (*Figure 10*).

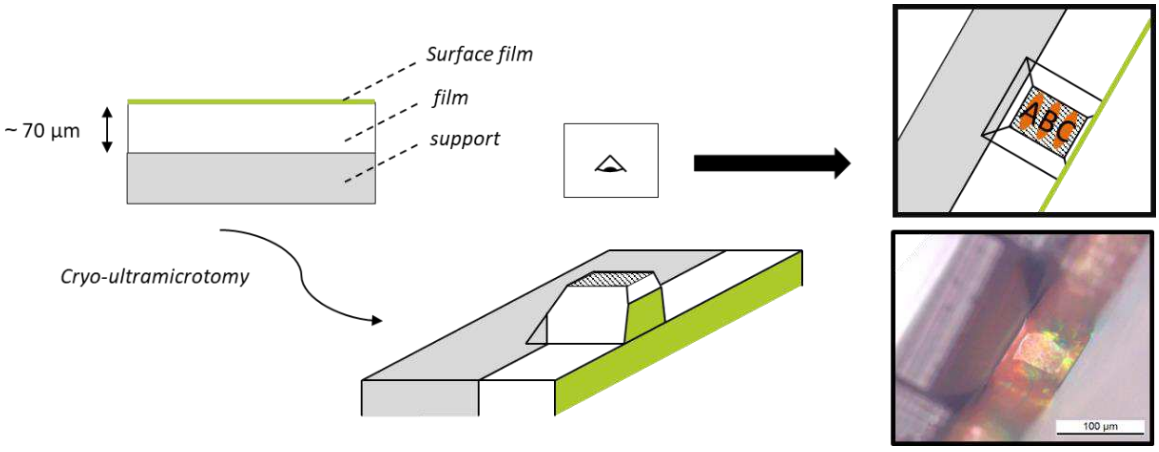

Figure 10. Schema of the surface preparation done with cryo-ultramicrotome (microscopy picture in the corner right – x20)

The top of the pyramid forms a rectangle of around 40x60 μm^2 which was probed by AFM. This surface covers roughly an area from the bottom to the top of the film thickness. A color difference seems noticeable between areas close to the support (A), slightly red, then those close to the surface of the film (C).

Several areas were investigated by AFM to observe the consequences on the colloidal organization. Figure 11 shows that the particle organization is more and more defined as areas close to the surface are probed.

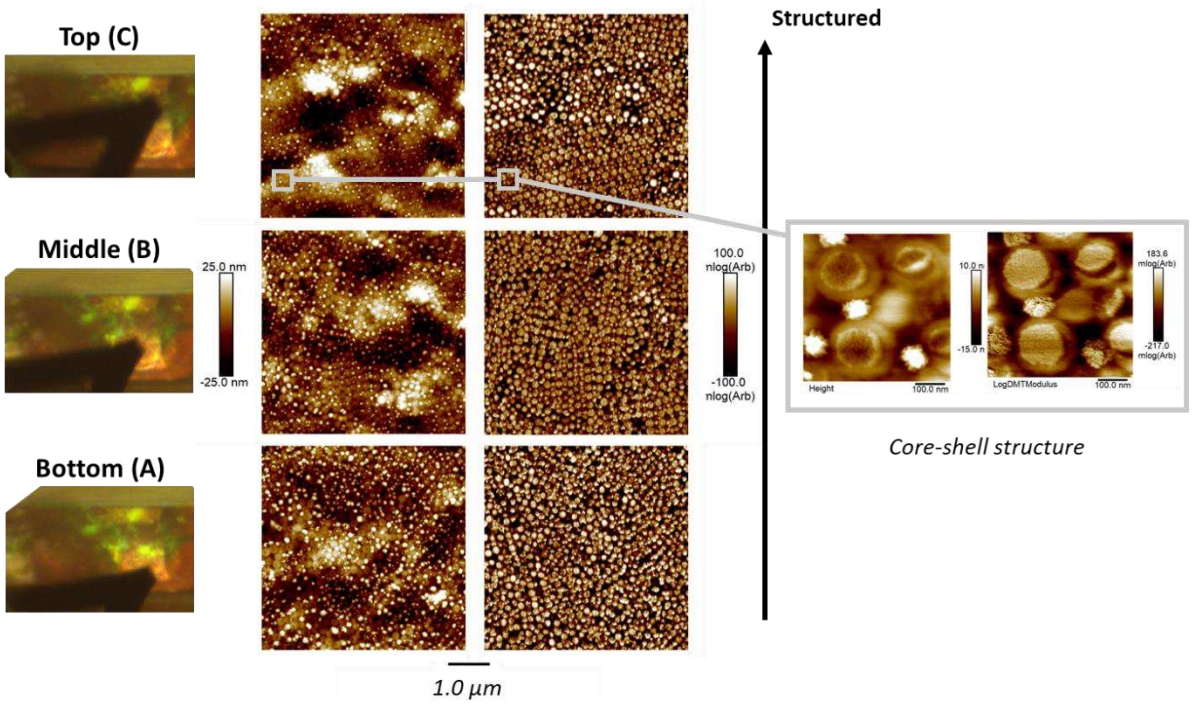

Figure 11. AFM pictures with height (left) and stiffness (right)contrast of area close to the support (A), in between (B) and close to the surface (C). The corresponding camera captures of the areas probed are displayed above. A zoom showing the core-shell architecture of the particles is displayed on the right.

The area close to the substrate (A) seems to be mostly disorganized, even if some grains are noticeable. The intermediate picture (B) seems to be slightly more organized. Finally, close to the air interface (C), the particles are strongly organized forming apparent layers. The current observation seems to suggest that the redder areas correspond here mostly to disorganized packing whereas the greener areas are associated with the most organized area.

The combination of reflectance spectroscopy and cross-section AFM confirm the presence of a colloidal crystal layer above a disorganized bed. Considering the previous identification of the organized/disorganized areas in function of the sample color, a quick measurement with optical microscopy would suggest a crystal layer between 30 and 50 µm. The cross-section visualization by AFM of such samples shows that the self-assembled organization is preferentially localized at the surface of the material and bring a visual confirmation of the core-shell architecture of the building blocks (Figure 11). This "surface localized" organization is coherent with the literature[5] about the self-assembly of hard-spheres. Nevertheless, it is worth noting that our BBs are composed by a soft and

sticky PEGMA-like shell[1] which should limit the self-assembly ability to form a periodic organized structure[7].

Addition of a filmogenic agent. Whatever the current control on the coloration of the films, the surface remains heterogeneous. Park *et al*[8] displayed the impact of depletion forces to maintain the stability of colloidal crystal independently of the temperature. They used macromolecules too large to enter the hydrogel mesh and then increase the osmotic pressure. In their case, concentrations above 4.7 g/L showed best results to stabilize hydrogels arrays in a swollen state.

Carboxymethylcellulose (CMC) is known to be a good water soluble filmogenic agent and a good candidate to mimic previous results in order to promote the colloidal self-assembly. A formulation trial was explored with a CMC of 60,000 g/mol, with concentration considered with respect to the proportion of CMC in the final solid content.

It appears that if the increase of CMC concentration in the system, macroscopically improves the filmogenic properties of the films. Such behavior is associated with a degradation of the optical properties (*Figure 12*).

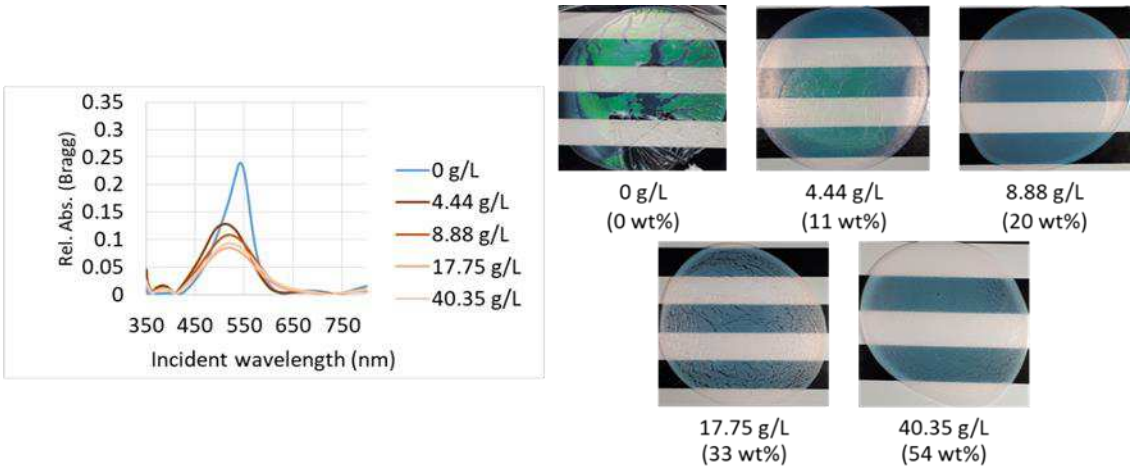

Figure 12 Macroscopic pictures of films made from dispersions with several concentration of carboxymethylcellulose (CMC). Between brackets are showed the percentage of glycerol in the final solid content. The corresponding treated relative absorption spectra are displayed on the left.

From the conditions, the results don't show any significant improvement of the colloidal organization. Carboxymethyl cellulose of different masses could be

considered, at lower concentrations. The impact of others filmogenic agent as hyaluronic acid or chitosan should be also investigated.

2. Stimulable coloration

1.1. Crystalline structure evaluation

We experimentally observed a variation of the diffracted wavelength in function of the shell thickness of the core-shell colloids. The Snell-Bragg law allows to associate a diffracted wavelength, the "Bragg wavelength", with several experimental parameters, as it is display below (*Equation 1*). In order to identify the possible 3D crystalline structure produced experimentally, we compared the variation of the diffracted wavelength with theoretical values obtained from a

Equation 1 Snell-Bragg equation

$$\lambda_{Bragg} = 2 \times d_{hkl} \times (n^2_{mat(core)} \times f_{mat(core)} + n^2_{mat(shell)} \times f_{mat(shell)})^{1/2}$$

λ_{Bragg} = maximum wavelength of the diffracted light
d_{hkl} = inter-reticular distance between (hkl) plans family
$n_{mat(core)}$ = refractive index of the core material, in our case, PS (1.59)
$n_{mat(shell)}$ = refractive index of the shell material, in our case, PEGMA (1.47)
$f_{mat(core)}$ = volume fraction of the core material in the considered lattice
$f_{mat(shell)}$ = volume fraction of the shell material in the considered lattice

developed version of the Snell-Bragg equation.

The shell/core ratios inside the colloidal crystal are function of two parameters. Firstly, the compacity of the array (C) and secondly the quantity of core/shell material effectively incorporated inside the cell lattice. To this end, we distinguish here the shell material effectively grafted to the core ($f_{mat(shell)}$), considering the whole shell material inside the system ($f_{mat(shell)-tot}$) and the percentage grafted at the surface of PS cores (γ_{graft}), as presented below (*Equation 2*). It has to be noticed that we assume for the organic matter a similar value of the volume fraction and the mass fraction. Indeed, the densities of the poly(styrene)

(PS) and the poly(ethylene glycol methacrylate) –(PEGMA) are both close to 1, with

Equation 2. Consideration of the compacity & the shell material grafting rate into the Snell-Bragg equation

$$f_{mat(core)} = C \times (1 - \frac{f_{mat(shell)-tot}}{100} \times \frac{\gamma_{graft}}{100})$$

$$f_{mat(shell)} = C \times \left(\frac{f_{mat(shell)-tot}}{100} \times \frac{\gamma_{graft}}{100}\right) + (1 - C)$$

γ_{graft} = weight proportion of the shell material effectively grafted on the core with respect to the total mass of colloidal object

$f_{mat(shell)}$ = weight proportion of the shell material with respect to the total mass of core and shell material

C = compacity of the considered lattice

respectively d_{PS} ~ 1.04 and d_{PEGMA} ~ 1.10.

The nature of crystalline structure contributes to the Snell-Bragg equation thanks through the intervention of the reticular distance (d_{hkl}) term. In the case of the systems considered, this d_{hkl} is related to the crystalline array by a unique lattice parameter, *a*. This last parameter can be considered as a function of the core-shell spheres diameters, as "$a = D_{CS} \times \tau$", where τ represents a "geometric" term specific to each crystalline structure and related to the tangency of the spheres for each lattice. However, the core-shell diameter (D_{CS}) is linked to the shell material percentage grafted at its surface ($f_{mat(shell)}$).

Considering the *Equation 4* and *Equation 3,* the diameter D_{CS} can be expressed as a function of $f_{mat(shell)-tot}$ (Equation 5*)* to get an expression of the diffracted wavelength in function of $f_{mat(shell)-tot}$.

Equation 4 $$f_{mat(shell)} = \frac{m_{mat(shell)} \times \gamma_{\text{graft}}}{m_{mat(shell)} \times \gamma_{\text{graft}} + m_{mat(core)}}$$

Equation 3 $$f_{mat(shell)-tot} = \frac{m_{mat(shell)}}{m_{mat(shell)} + m_{mat(core)}}$$

Here, the D_{core} values is taken from the average hydrodynamic diameters values at 25 °C and the grafting rate (γ_{graft}) is fixed at 81 wt% which is the average value experimentally observed. Finally, the percentage of shell material used to make the colloids ($f_{mat(shell)-tot}$) is taken from the mass experimentally used during the synthesis.

Equation 5

$$D_{CS} = D_{core} \times \left(1 - \left(1 + \frac{100}{\gamma_{graft}} \times \left(\frac{100}{f_{mat(shell)-tot}} - 1\right)\right)^{-1}\right)^{-\frac{1}{3}}$$

Four different lattices are considered (Figure 13*a*). According to the theoretical crystalline structure, the expression of d_{hkl} in function of the cell parameter "a" is adapted. Figure 13*b* displays the expression of d_{hkl} and the values of τ considered for each lattice.

a)

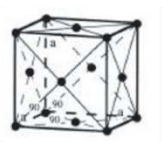

Face Centered Cubic - FFC (Fm3m)

Body-Centered Cubic – BCC (Im3m)

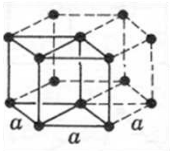

Hexagonal – Hexa. (P6/mmm)

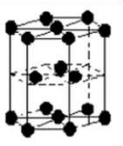

Hexagonal Compact – Hexa. ($P6_3/mmc$)

b)

Name	Symmetry group	d_{hkl} equation	τ	Reflection condition	Fitted (h k l) plan
FCC lattice	Im3m	$d_{hkl} = \frac{a}{h^2 + k^2 + l^2}$	$\sqrt{2}$	h, k, l = 2n or h, k, l = 2n+1	(2 0 1)
BCC lattice	Fm3m		$2/\sqrt{3}$	h + k + l = 2n	(1 1 1)
Hexa. lattice [1]	P6/mmm	$d_{hkl} = \frac{1}{\sqrt{\frac{4}{3 \times a^2} \times (h^2 + k^2 + h \times k) + \frac{l^2}{c^2}}}$	1	no extra conditons	(1 0 1)
HC lattice [2]	$P6_3/mmc$				(1 0 2)

$1 : c = a$ $\quad 2 : c = \sqrt{\frac{8}{3}} \times a$ $\quad \boxed{a = D_{cs} \times \tau}$

c)

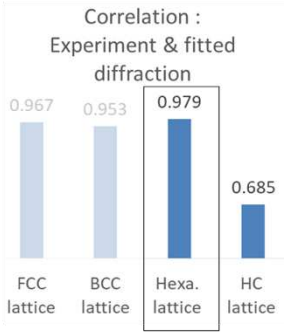

Figure 13. a) Schematic representation of several crystalline arrays. Their corresponding group space is indicated between brackets. b) For each packing presented is indicated its corresponding d_{hkl} equation, τ value, reflection conditions and the fitted (h k l) plans which are obtained. c) The values of the regression parameters in each case are represented in this histogram. FCC and BCC lattice results doesn't satisfy the reflection conditions of the lattice.

However, the diffracted wavelengths are also specific to a *(h k l)* plan family. The identification of the right crystalline structure operates mainly in the following step. Firstly, the variation of the theoretical λ_{Bragg} is expressed in function of $f_{mat(shell)}$. The *h, k, l* values are free fitting parameters with the constraint to be non-decimal and positive values. Then, the theoretical variation of the diffracted wavelength in function of the shell material are fitted to the experimental variation of λ_{Bragg}. Finally, the fitted *(h k l)* plans for each theoretical identified crystalline

structure are compared against their physical reflection conditions found in the literature[9,10]. In our case, even if FCC and BCC lattices present satisfying regression coefficient, the fitted plans don't correspond to the well-known reflection conditions for these structures. Finally, a non-compact hexagonal array seems to be acceptable as it presents the best results through this method (Figure 13*c*).

In that study, we developed a versatile approach to consider easily several crystalline structures. The type of crystalline array is integrated into the Snell-Bragg equation by the mean of its compacity, the relation between the core-shell tangency, the cell parameters. In few words, the theoretical wavelength positions evolution, in function of the shell thickness, is compared with those measured by spectrophotometry in order to identify a coherent crystalline structure.

This identification is performed into two steps. The first one consists to fit the theoretical wavelength evolution with the shell thickness for several crystalline structures. The fitting parameters are here the Miller indices to identify diffractions plans that fit with experimental observations. In a second step, the diffraction selection rules associated with each crystalline structure are applied on identified plans to segregate only physical plausible structures.

In literature[11], hard colloidal spheres tend to be organized into Face Centered Cubic (FCC) – space group Fm2m. The Hexagonal Compact (HC) array – space group P6/mmm – is another classical compact organization considered as suitable for hard spheres with surface hexagonal arrangement. However, in our system, the experimental evolution of the Bragg wavelengths doesn't fit with any of these compact arrangements (Figure 14*a*).

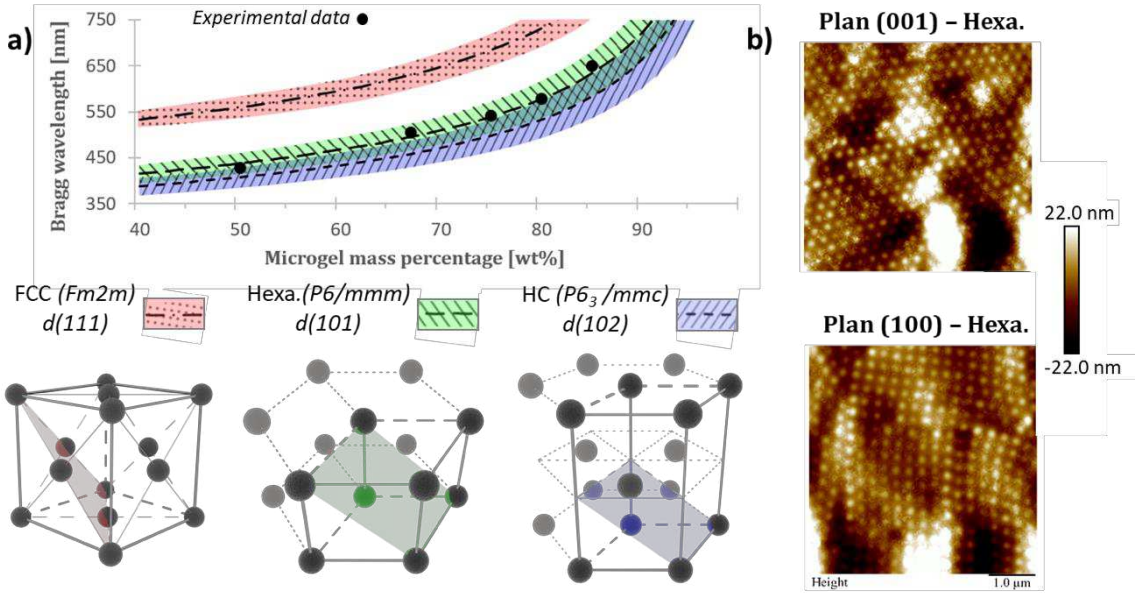

Figure 14. (a) Comparison between theoretical variations of the diffracted wavelength, for a selection of reticular plan from wisely chosen crystalline structures and the experimental variation of the diffracted wavelength measured by spectrophotometry. The variation of the diffracted wavelength is in function of the shell material mass percentage in the dried system. (b) Pictures of a film surface from AFM presenting at same time a hexagonal and a square 2D arrangement, respectively identified as (001) and (100) plans of a non-compact 3D hexagonal array.

Nonetheless, a satisfying fit is obtained with a hexagonal non-compact array – space group $P6_3/mmc$. In addition of this analytical identification, the observation of the same surface sample can present simultaneously square and hexagonal surface arrangements. Those two surface organizations are both characterized by the same center-to-center distances. In the case of a non-compact hexagonal structure, these observations can be respectfully attributed to (100) or (001) plans (Figure 14*b*). If these microscopic observations aren't sufficient alone though they support the analytical identification presented earlier.

2.1. ***Thermo-responsiveness***

A thermal stimulation test was done to probe the thermo-responsiveness of the film. Three dispersions samples were dried on PS substrate at ambient temperature. The first one was heated 30 minutes on at heating plate set at 60 °C, whereas the second one was cold in a fridge at 4 °C for the same amount of time. The third one was kept as reference. UV-visible transmission spectra were performed before and just after the thermal treatment (Figure 15).

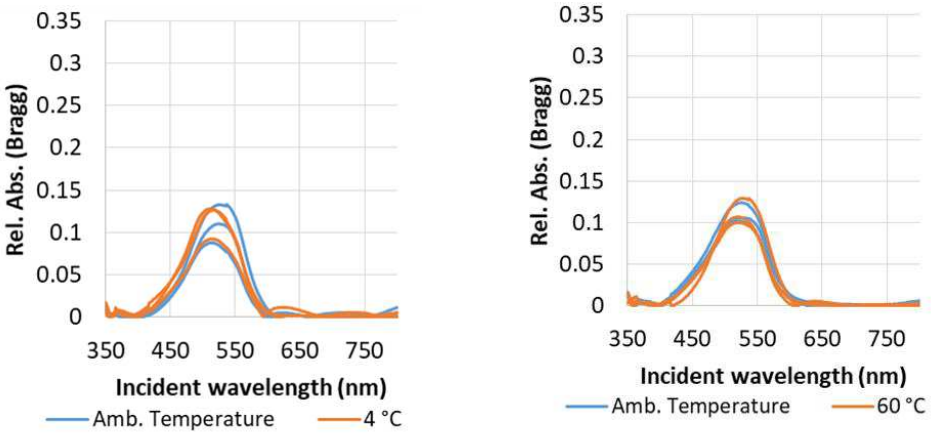

Figure 15. Treated relative absorption spectrum to compare Bragg diffraction signals before and after thermal treatments.

It turns out neither heating nor cooling as any significant effect on the Bragg contributions and its corresponding relative absorbance spectra.

With photonic crystals, the diffracted wavelength is correlated to the inter-particle distance. These core-shell particles are known to be thermo-responsive in solution. To get a thermo-responsive behavior with film, the shell must be sufficiently swollen to collapsed as a function of the temperature in a dried state to impact the inter-distance particle. Nevertheless, the LCST behavior is intrinsically due to a modification of polymer solubility with the solvent, due to a destabilization of the solvent-polymer interactions. In the absence of any solvent, the polymer constituting the shell undergoes only the polymer-polymer interactions: no thermo-responsivity is then induced at the dried state.

1.2. Mechanical responsiveness analysis

We discuss in this part the mechanical responsivity of the film's colors. Firstly, the mechanical sensitivity of the color shift is evaluated by a homemade colorimetric tension test which associate the samples relative deformations to their dominant wavelength (Figure 16).

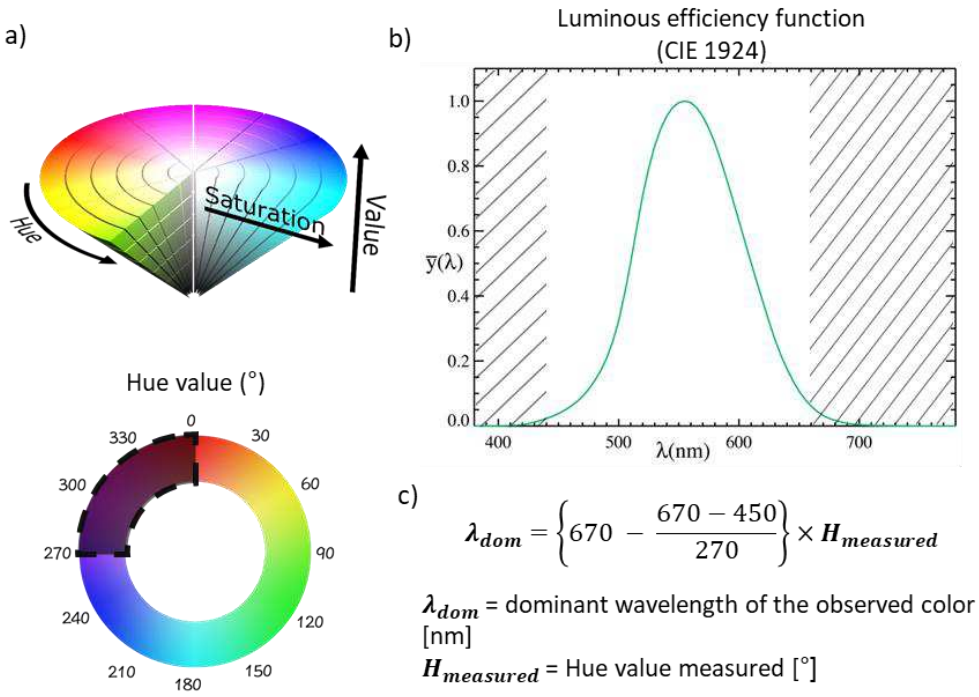

Figure 16 (a) Three-dimensional representation of the color in a Hue, Saturation and Value space (HSV). The hue control essentially the essence of the perceived color and is express in degree, from 0° to 360°.In this HSV space, only the colors contained between the 0°-270° range corresponds to physical monochromatic wavelength. (b) Representation of the human eye sensibility in function of the monochromatic wavelength. Below is expressed the equation used to calculated the dominant wavelength from digital pictures, according to the average hue measured.

In a second time, the macroscopic deformation is correlated to microscopic ones by AFM. Finally, we develop argues that could explain the observed cohesion based on compared DLS and AFM analysis.

The mechanical responsiveness on the films colors was evaluated after casting on a thermoplastic polyurethane (tPU). The deformation of such films leads systematically to a hue shifting, as the evolution of the films dominant wavelength shows it (Figure 17*a*).

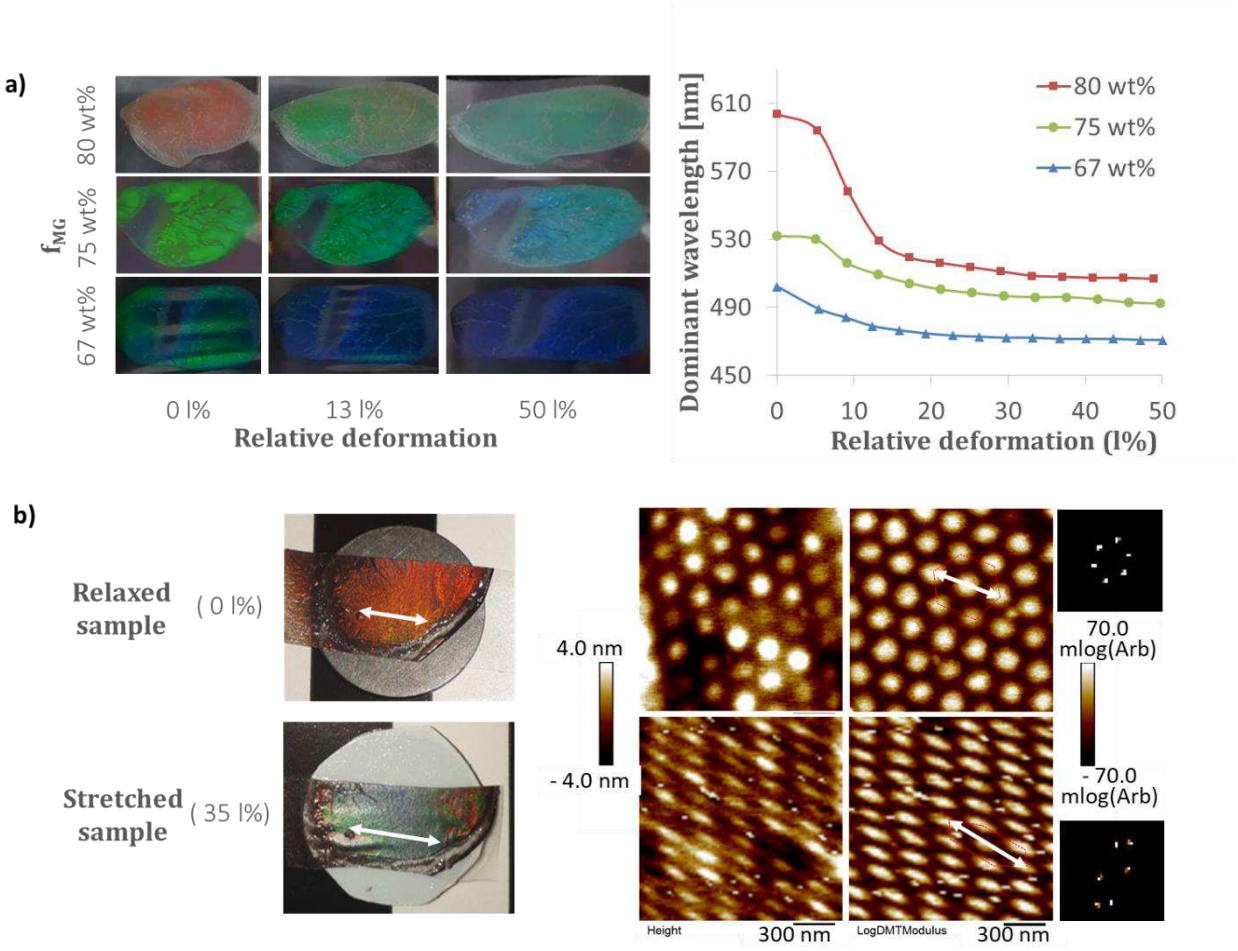

Figure 17. a) Macroscopic pictures of films stretched at different relative deformation rates under controlled tensile tests. On the right is represented the evolution of their dominant wavelength in function of the relative deformation.

b) Macroscopic pictures of the same film before and after its fixation at a measured relative deformation. On the right is displayed the corresponding AFM pictures. The images are displayed in function of the topographic and mechanical modulus contrasts. Corresponding Fourier transformations of these pictures are coupled next to them.

A significant color modification is systematically obtained with a relative elongation between 10 & 15 l%. Factually, the more the film is stretched, the more the hue is shifted toward low wavelength. Moreover, this color shift is totally reversible, without any macroscopic degradation of the self-assembled film for deformation up to 50 l%. The photonic crystal recovers its initial coloration immediately after the end of its mechanical solicitation. According the classical Snell-Bragg theory, a blue-shift of the diffraction wavelength is associated with a decrease of the cell lattice parameter for a fixed crystalline structure and refractive index difference between the core and the shell.

Microscopic observations reveal these that these macroscopic elongations are correlated with a colloidal crystalline deformation. Indeed, when a controlled solicitation of 30 l% is macroscopically applied, the surface hexagonal arrangement is elongated with the same elongation rate (Figure 17*b*). However, the surface arrangement presents also a significant compression upon the perpendicular axe. This alteration of the crystalline structure inducing a compression of the lattice upon a direction appears as coherent with the tendency described by the Snell-Bragg equation. A more complete investigation through numerical simulation may bring useful information.

Complementary to these color shifts, the crystalline structure conserve macroscopically and microscopically its cohesion under mechanical stress. The hydrodynamic diameters in the collapsed state and their corresponding dried diameters are compared to the inter-particles distance measure on films surfaces. Systematically, the center-to-center distances between spheres for each system are lower than isolated dried particles diameters or their corresponding hydrodynamic diameters in the collapsed state. It implies that parts of the shell intertwine during the CPC formation and contribute to maintain its cohesion when a mechanical stress is applied. Indeed, the PEGMA-based shell is a soft material characterized by a Tg around -35 °C offering enough molecular mobility at ambient temperature to adapt its conformation and support the constrain. Moreover, all the films discussed are made from raw suspensions, meaning that a part of free water-soluble polymer (WSP) may develop inter and intra shell interactions to reinforce the film cohesion. This last element may be responsible of the material color switchable properties without further photochemical crosslinking.

3. Core/shell alteration & optical properties

In this section we point out the modification of shell composition and the core size deviation and define the consequence on the optical properties of the films produced. Each film was made from raw suspensions casted on PS substrates set on a heating plate at 40 °C. Each time, the chemical modification was performed, keeping all the experimental conditions even, at the exception of the adjusted ratios. The grafting rates was probed by dynamic light scattering (DLS) and

InfraRed spectroscopy (IR) and the impact on the optical properties was evaluated from transmission photo-spectrometry.

3.1. *Crosslinker rate variation*

The crosslinker rate was modified to investigate the possibility of promoting either "hard sphere" (higher crosslink rate) or the intertwinement of the shells during the film self-assembly to reduce the surface self-assembly heterogeneity (lower crosslink rate). Suspensions with 0.1 and 2 mol% of OEGDA with respect to shell monomers were thus synthesized to evaluate the impact of the decrease of the crosslinker rate. In parallel, suspensions with 2 and 10 mol% of OEGDA with respect to shell monomers were produced to probe the consequence of a rise of the crosslinker rate in the shell. The decrease or the increase of the crosslinker ratio is here observed thanks to the comparison of respectively samples with f_{MG} = 75 wt% or f_{MG} = 80 wt% (Figure 18).

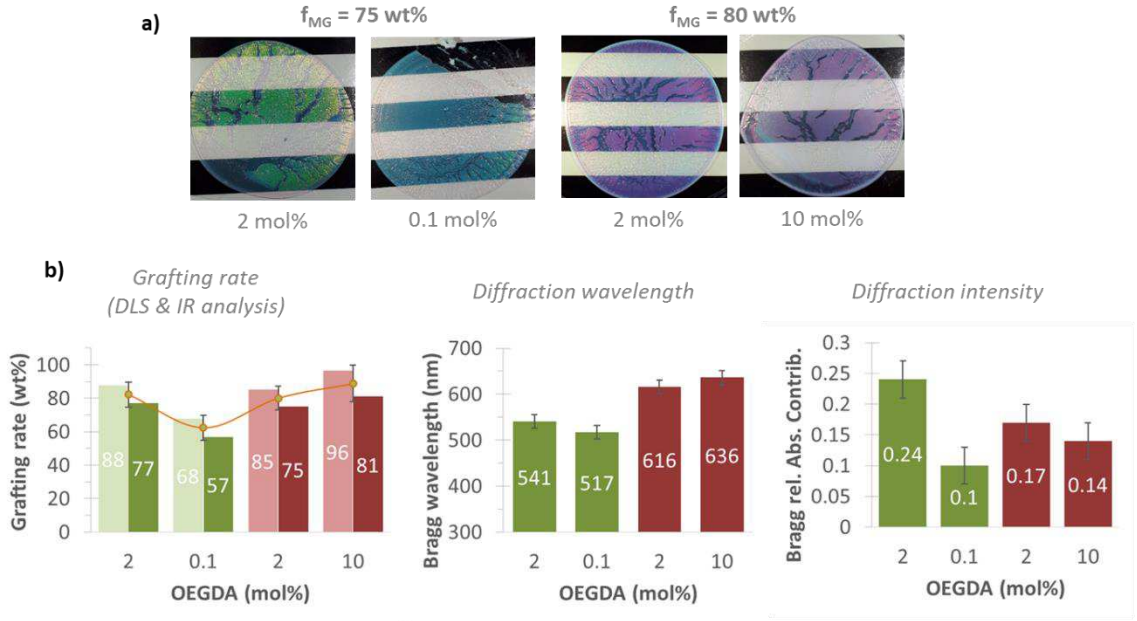

Figure 18(a) Macroscopic pictures of films with different molar proportion of OEGDA again the total amount of monomers. The corresponding microgel percentages are displayed each time. (b) A comparison of the average grafting rates, diffraction wavelength and intensity for each MG percentages and OEGDA proportions.

Macroscopically, the decrease of the crosslinker rate lead to a perceptible loss of the color intensity. Nevertheless, the diffraction wavelength is not significantly altered. According to the related grafting rate loss, it can be supposed the free un-grafted material perturb the ordering of the suspended CS particles

during the solvent evaporation. However, the free POEGMA contribute to maintain the distances between the cores, preserving the diffracted wavelength compared to the reference sample. The increase of the OEGDA ratio for the shell synthesis doesn't have a so dramatic effect on the obtained material (f_{MG} = 80 wt%). Indeed, the reddish diffracted color is still perceptible macroscopically, with a conservation of the grafting rate, measured Bragg wavelength and relative intensity with respect to the reference (2 mol%). Even if there is no apparent improvement of the photonic crystal produced, the surface sample with the highest amount of crosslinker appears slightly less sticky than the reference. We evaluated then by AFM the consequences of the shell modification on the mechanical properties of the produced shells

Indeed, the AFM technic allows to probe the interactions between the tip which classically used to realize surface pictures of material surfaces[12,13]. In our case it's possible to evaluate the impact of the shell grafting on the surface properties of the PS seeds, as presented previously (Section 1.2, p.116). More interestingly, the adjustment of the crosslinker proportion into the shell may altered the surface properties. Force spectroscopy by AFM focuses on the adhesion forces occurring between a surface and AFM tip, bringing critical information about the mechanical evolution of the surface. Several purified CS particles suspensions were thus prepared in order to probe the mechanical modulus of the CS beads and their adhesion energy with the tip. Briefly, the raw CS suspensions were firstly centrifuged and re-dispersed 5 times in MiliQ water (10k rpm, 30 min), and diluted to roughly 1 mg/mL. The diluted suspension was the drop-casted on cleaned silicon shards. From the acquisition of at least 20 approach/retract, averaged force curves were then produced for PS-EGDMA beads and CS particles with a crosslinker rate of 2 mol% and 10 mol%. Without surprises and corresponding to their respective glass transition temperatures, the mechanical modulus of the PS core appears significantly higher than those grafted with the PEGMA shell (Figure 19*a*).

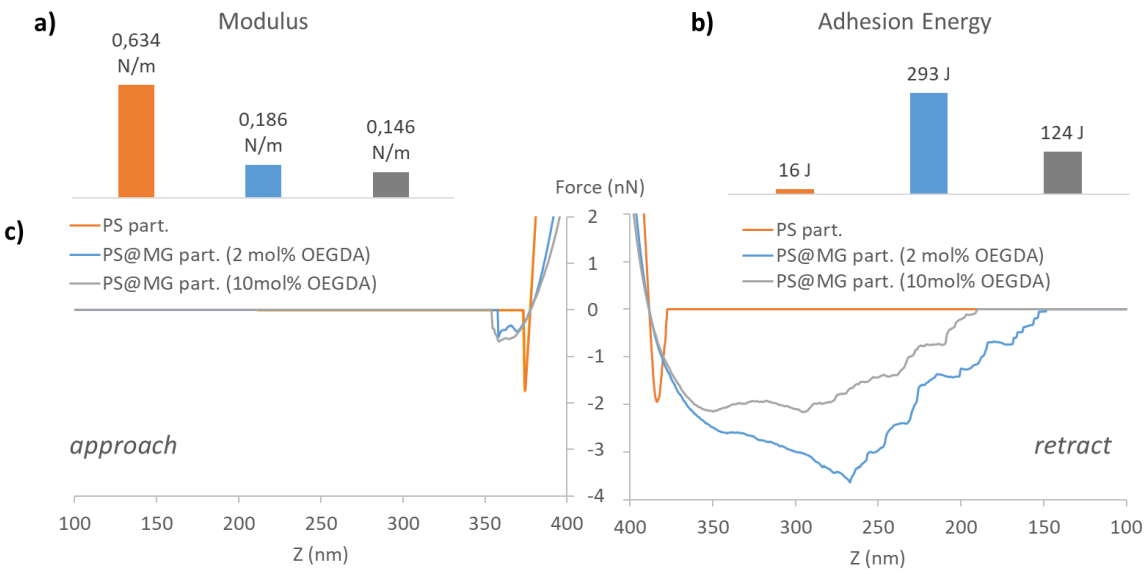

Figure 19. (a) Evolution of the mechanical modulus measured during the tip approach on isolated particles. (b) Evolution of the adhesion energy measured during the tip retraction. (c) Evolution of the force curves during the approach and the retraction.

In the same way, the adhesion energy of the core-shell particles is significantly increased. However, an increase of the crosslinker rate lead to a drop of the adhesion energy (Figure 19*b*). The adhesion comes from weak interactions between the tip and the mobile chains at the surface of particle. When the tip is withdrawn, those interaction persist and are continuously broken as long as the tip is retracted (Figure 19*c*). In the case of an increase of the crosslinker rate, the length of the chain able to develop these interactions is reduced, leading to a decrease of the adhesion energy.

3.2. ***MAA ratio***

The MAA ratio was also adjusted to probe the consequence of a modification of shell ionization on the optical properties. To do so, suspensions of CS particles were made from the same core but with different molar proportions of MAA/(OEGMA+MEO_2MA) ratios for the synthesis of the shell. Consecutively, it was then expected to produce MG shells with MAA ratio of 0, 5 and 15 mol%, with 5 mol% as our reference composition. The raw suspension was then dried on PS support set on a heating plate at 40 °C before further analysis. The grafting rate was evaluated here only according to DLS data, due to the strong correlation observed between IR and DLS data until here (Figure 20).

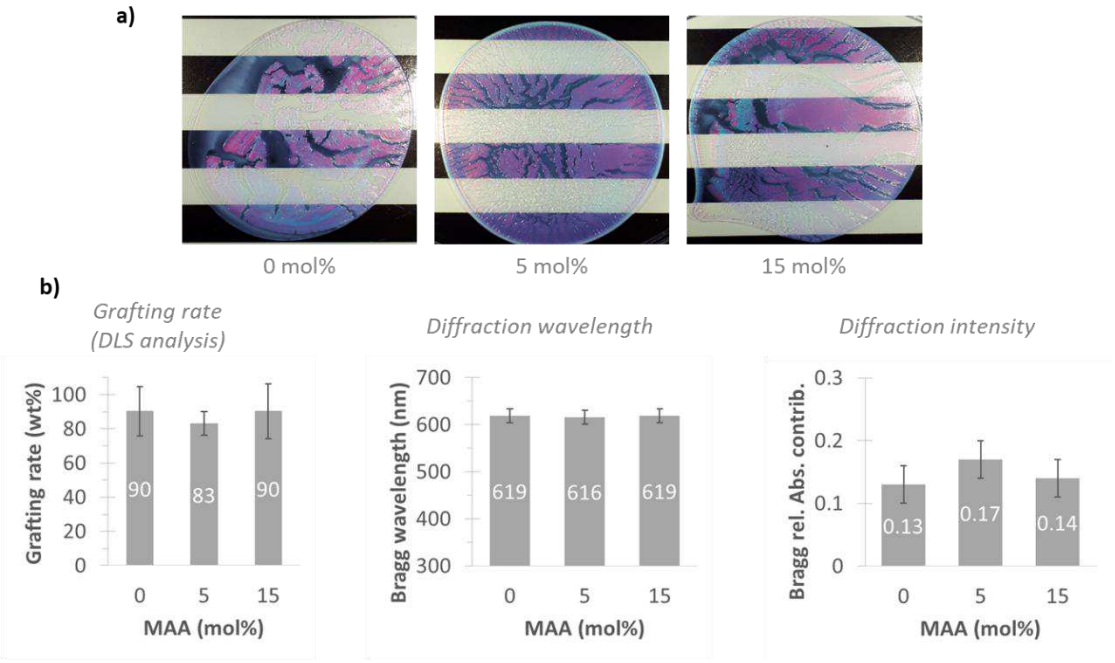

Figure 20 (a) Macroscopic pictures of films with different molar proportion of MAA/(OEGMA + MEO_2MA). The films were made with a constant MG percentage of 85 wt%. (b) A comparison of the average grafting rates, diffraction wavelength and intensity for each MAA proportions.

The macroscopic films obtained doesn't show significant differences between each other. The diffracted wavelength and its relative intensity appear even, with no alteration of the measured grafting rate. If the electrostatic interactions, promoted by the presences of ionic force are well known to operate in the colloidal stability, here, the modification of the ionizable functions doesn't lead to any self-assembly alteration.

3.3. ***OEGMA/MEO_2MA ratio***

The OEGMA/MEO_2MA ratio is known to set the volume phase transition temperature (VPTT) of the microgel. The higher the molar ratio, the higher the VPTT. The reference molar sample, made from CS particles with 80 wt% of MG, and 10 mol% of OEGMA/MEO_2MA was compared to similar suspensions but with respectively 5 and 25 mol%. All the suspensions were made from the same seeds' suspension. Coherently with literature, a higher molar ratio induces effectively an apparent shift of the VPTT[14,15] (Figure 21).

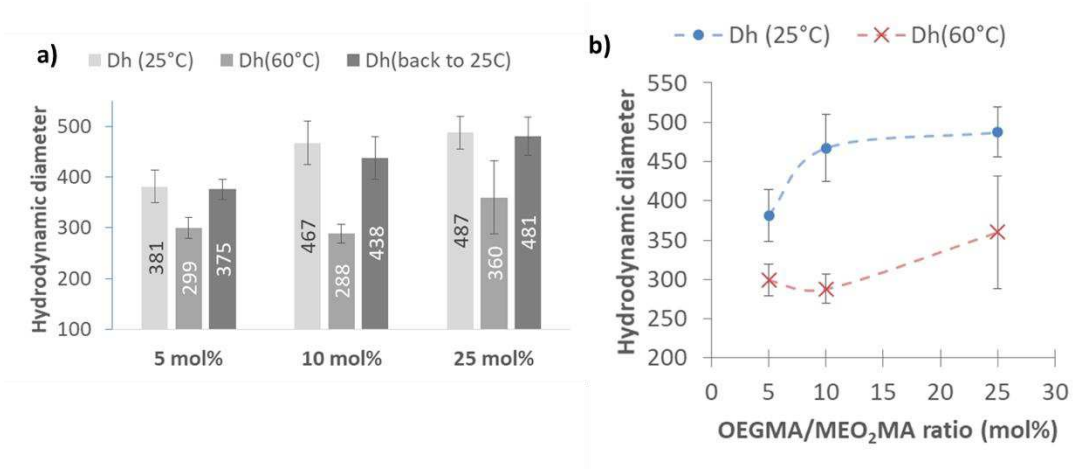

Figure 21 (a) Evolution in function of the temperature of the hydrodynamic diameters (Dh) for CS particles made from PS-EGDMA core with an average Dh of 178 nm and shell with variable proportions of OEGMA/MEO₂MA molar percentages. (b) Hydrodynamic diameters in function of the OEGMA/MEO₂MA ratios

Indeed, the particle stay swollen at higher temperature due to a reinforcement of the polymer-solvent interaction brought by the higher proportion of oligo ethylene glycol chains. At the opposite, a decrease of the OEGMA/MEO_2MA ratio for the shell synthesis leads to CS particles almost collapsed at 25°C, that shrink a bit more at higher temperature, but much less than with the reference composition (10 mol%).

For all these compositions, the grafting rate remains roughly unchanged with an average value around 80 wt% (Figure 22*a*).

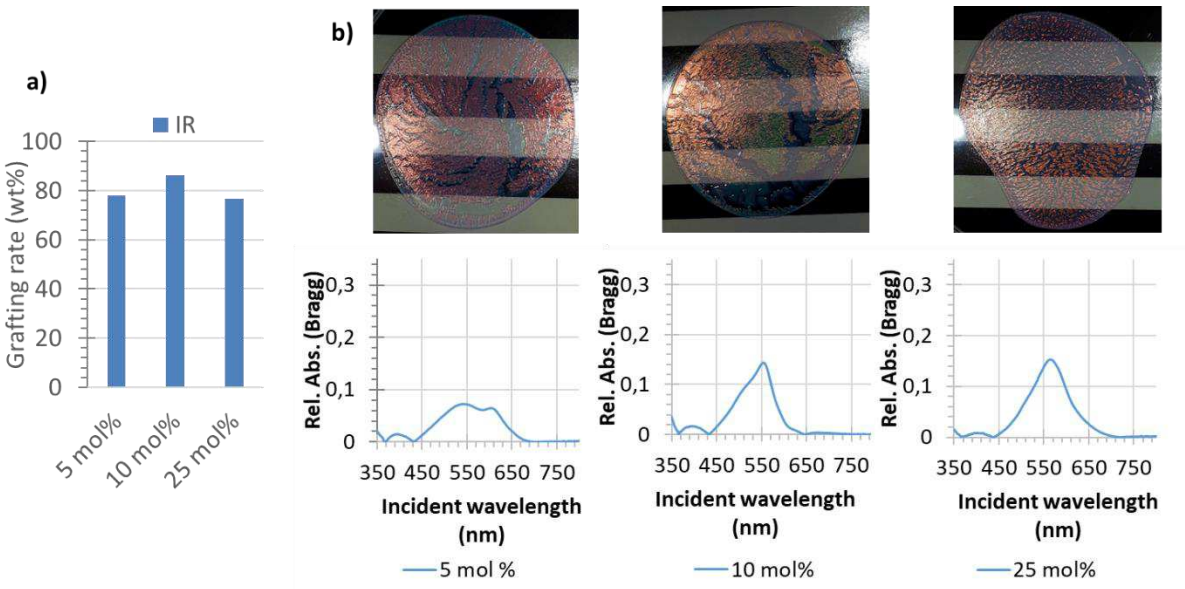

Figure 22 (a) Macroscopic pictures of films with different molar proportion of OEGMA/MEO₂MA ratios. The films were made with a constant MG percentage of 80 wt%. (b) A comparison of Bragg contribution for each ratio

The macroscopic observation of the film shows the persistence of a similar iridescent coloration, whatever the molar proportion of OEGMA/MEO₂MA (Figure 22*b*). The Bragg's contributions to the transmission spectra show peaks roughly at the same positions. A slight intensity decrease with the lower molar ratio is observable, but is considered as mainly due to the heterogeneity of the film's surface.

3.4. ***Core size***

Finally, two different CS suspensions were prepared with the same reference composition for the MG shell, but with variable seed sizes and MG proportions. The target was to evaluate the impact of the core size on the optical properties of similar photonic crystals, with similar interparticle distances. To do so, the shell thickness was adjusted, considering an expected grafting rate of 80 wt%, to produce CS particles with a collapsed hydrodynamic diameter of 285 nm. The seeds used as core have diameters of 141 and 190 nm, and were then used respectively with grafting protocol involving respectively 91 & 75 wt% of microgel material.

The films produced display macroscopically similar hues, but with a less intense diffracted coloration, as confirmed by the UV-Visible spectroscopy (Figure 23).

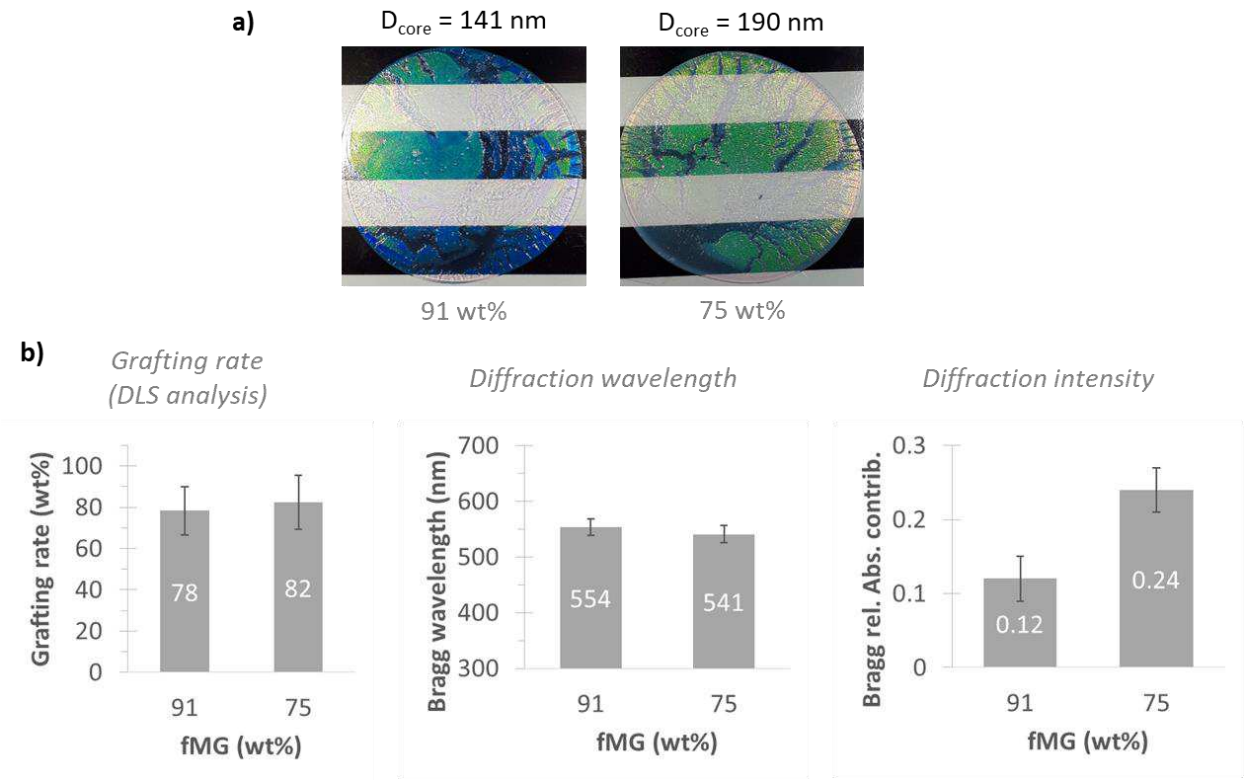

Figure 23(a) Macroscopic pictures of films made from different core-shell suspensions. The difference relies on the size of the core, either with a hydrodynamic diameter of 141 nm or 190 nm. The proportion of POEGMA microgel (fMG) is adjusted to get particles with similar collapsed size, around 285 nm.

The grafting rate remain roughly the same. The loss of the diffracted relative intensity may be thus associated to two phenomena. The first is related to the absolute increase of the free un-grafted POEGMA in a film presenting a set thickness, for f_{MG}=91 wt%, compared to the reference system. Indeed, as we seen previously, the presence of free WSP as serious consequences on the self-assembly abilities of the dispersed particles. However, one preferred explanation highlights the dependence of the scattering intensity to beads sizes. Indeed, with such a system, the coloration is mainly produced by the resonant scattering of the PS beads embedded in the soft POEGMA matrix. Lower the core size, lower the scattering intensity, and so the diffracted wavelength. At the opposite, an increase of the PS beads over 200 nm induces an increase of the scattering intensity all over the visible range, leading to a whitening of self-assembled films.

Conclusion

In this chapter, we developed the synthesis method to produce core-shell particles with a well-controlled design. The shell thickness was adjusted experimentally to the shell/core weight ratio in a controlled way thanks to a robust synthesis process, characterized by a constant grafting rate of the POEGMA-based microgel. The films show a heterogeneous organization due to the solvent evaporation method. The colloidal particles are mainly disorganized in the lower part of the films close to the substrate, whereas the upper part, closer to the former air/water interface, is highly ordered. This surface photonic crystal is then at the origin of the iridescent coloration. These colors are thus tunable, according to the experimental methods but especially mechano-responsive. Due to the identified intertwinement of the shell, the self-assembled photonic crystals display a spontaneous tenacity to deformation: the lattice obtained by solvent evaporation is deformed with the elongation of the film, and induce a color shifting. This macroscopic deformation of the film, correlated to microscopic deformation, cause an overall increase of the interparticle distances in the direction perpendicular to the deformation, producing a color change coherent with the Bragg-Snell theory.

The initial purpose with this core-shell design is the elaboration of responsive films for a cosmetic application. The transfer of the developed CS technology to a potential marketable product require the development of a convenient formulation. Moreover, the self-assembled structure must be produced during a skin application, on time largely shorter. The next chapter approaches those problematics and develops the investigated solutions.

To conclude this chapter, we have presented the spontaneous self-assembly properties of the core-shell particle under solvent evaporation conditions. The films present mechanochromic properties on clear support without any post (photo-)chemical treatment by contrast with analog core-shell material[16–23]. This cohesion is assured by the lower Tg of the POEGMA shell by comparison with others acrylamides materials[24,25]. The shell contraction assures a self-assembly related to similar self-assembly through solvent evaporation[26–31].

References

1. Boularas, M. *et al.* Functional film by trigger-free self-assembly of adhesive soft microgels at skin temperature. *Materials & Design* **147**, 19–27 (2018).

2. Gasser, U. Real-Space Imaging of Nucleation and Growth in Colloidal Crystallization. *Science* **292**, 258–262 (2001).

3. Sandomirski, K., Allahyarov, E., Löwen, H. & Egelhaaf, S. U. Heterogeneous crystallization of hard-sphere colloids near a wall. *Soft Matter* **7**, 8050 (2011).

4. Dinsmore, A. D., Crocker, J. C. & Yodh, A. G. Self-assembly of colloidal crystals. *Current Opinion in Colloid & Interface Science* **3**, 5–11 (1998).

5. Xu, P., Mujumdar, A. S. & Yu, B. Drying-Induced Cracks in Thin Film Fabricated from Colloidal Dispersions. *Drying Technology* **27**, 636–652 (2009).

6. Yan, Q., Zhou, Z. & Zhao, X. S. Inward-Growing Self-Assembly of Colloidal Crystal Films on Horizontal Substrates. *Langmuir* **21**, 3158–3164 (2005).

7. Sowade, E., Blaudeck, T. & Baumann, R. R. Inkjet Printing of Colloidal Nanospheres: Engineering the Evaporation-Driven Self-Assembly Process to Form Defined Layer Morphologies. *Nanoscale Research Letters* **10**, (2015).

8. Park, J.-G. *et al.* Photonic-crystal hydrogels with a rapidly tunable stop band and high reflectivity across the visible. *Optical Materials Express* **7**, 253 (2017).

9. Pecharsky, V. K. & Zavalij, P. Y. *Fundamentals of powder diffraction and structural characterization of materials*. (Springer, 2009).

10. Perez-Mato, J. M. *et al.* Symmetry-Based Computational Tools for Magnetic Crystallography. *Annual Review of Materials Research* **45**, 217–248 (2015).

11. Hales, T. C. Sphere packings, I. 51.

12. Horecha, M. *et al.* Ordered surface structures from PNIPAM-based loosely packed microgel particles. *Soft Matter* **6**, 5980 (2010).

13. Sommer, F., Duc, T. M., Pirri, R., Meunier, G. & Quet, C. Surface Morphology of Poly(butyl acrylate)/Poly(methyl methacrylate) Core Shell Latex by Atomic Force Microscopy. *Langmuir* **11**, 440–448 (1995).

14. Lutz, J.-F. Thermo-Switchable Materials Prepared Using the OEGMA-Platform. *Adv. Mater.* **23**, 2237–2243 (2011).

15. Hu, Z., Cai, T. & Chi, C. Thermoresponsive oligo(ethylene glycol)-methacrylate- based polymers and microgels. *Soft Matter* **6**, 2115 (2010).

16. Foulger, S. H. *et al.* Photonic Crystal Composites with Reversible High-Frequency Stop Band Shifts. *Adv. Mater.* **15**, 685–689 (2003).

17. Ito, T., Katsura, C., Sugimoto, H., Nakanishi, E. & Inomata, K. Strain-Responsive Structural Colored Elastomers by Fixing Colloidal Crystal Assembly. *Langmuir* **29**, 13951–13957 (2013).

18. Chen, J. *et al.* Highly Stretchable Photonic Crystal Hydrogels for a Sensitive Mechanochromic Sensor and Direct Ink Writing. *Chem. Mater.* **31**, 8918–8926 (2019).

19. Hong, R. *et al.* Highly sensitive mechanochromic photonic gel towards fast-responsive fingerprinting. *RSC Adv.* **7**, 33258–33262 (2017).

20. Viel, B., Ruhl, T. & Hellmann, G. P. Reversible Deformation of Opal Elastomers. *Chemistry of Materials* **19**, 5673–5679 (2007).

21. Lee, G. H. *et al.* Colloidal Photonic Inks for Mechanochromic Films and Patterns with Structural Colors of High Saturation. *Chem. Mater.* **31**, 8154–8162 (2019).

22. Lee, G. H. *et al.* Chameleon-Inspired Mechanochromic Photonic Films Composed of Non-Close-Packed Colloidal Arrays. *ACS Nano* **11**, 11350–11357 (2017).

23. Lee, G. H. *et al.* Elastic Photonic Microbeads as Building Blocks for Mechanochromic Materials. *ACS Appl. Polym. Mater.* **2**, 706–714 (2020).

24. Biswas, C. S. *et al.* Effects of Tacticity and Molecular Weight of Poly(*N* -isopropylacrylamide) on Its Glass Transition Temperature. *Macromolecules* **44**, 5822–5824 (2011).

25. Stetsyshyn, Y. *et al.* Temperature and pH dual-responsive POEGMA-based coatings for protein adsorption. *Journal of Colloid and Interface Science* **411**, 247–256 (2013).

26. *Sol-Gel Science*. (Elsevier, 1990). doi:10.1016/C2009-0-22386-5.

27. Scherer, G. W. Theory of Drying. *J American Ceramic Society* **73**, 3–14 (1990).

28. Wedin, P., Martinez, C. J., Lewis, J. A., Daicic, J. & Bergström, L. Stress development during drying of calcium carbonate suspensions containing carboxymethylcellulose and latex particles. *Journal of Colloid and Interface Science* **272**, 1–9 (2004).

29. Film Formation in Coatings. Mechanisms, Properties, and Morphology Edited by Theodore Provder (Polymer and Coatings Consultants) and Marek W. Urban (University of Southern Mississippi). American Chemical Society: Washington, DC (Distributed by Oxford University). viii + 304 pp. $130.00. ISBN: 0-8412-3712-3. *J. Am. Chem. Soc.* **124**, 3799–3799 (2002).

30. Kiennemann, J. *et al.* Drying mechanisms and stress development in aqueous alumina tape casting. *Journal of the European Ceramic Society* **25**, 1551–1564 (2005).

31. Brown, L. A., Zukoski, C. F. & White, L. R. Consolidation during drying of aggregated suspensions. *AIChE J.* **48**, 492–502 (2002).

Chapter IV: Cosmetic formulation

Introduction

The works in the previous chapters described the elaboration of a new technology to produce tunable and responsive colors from a POEGMA-based microgel. At this end, suspensions of core-shell (CS) particles were prepared thanks to a robust synthesis method, leading after water evaporation to films with intense colors. The current chapter focuses on the transfer of this technology into a skincare product.

The development of a skincare product involves the use of several key compounds. These essential additives can be gathered into three distinct family, each assuming an essential role of the cosmetic formulation. The first one is the bactericide, acting as a preservative and preventing the expiration of the product. The second family regroups the emollients, which are able to form a protect layer on the skin and limit the skin dehydration during the day. Finally, the last family is composed of the fragrances which has, with the color, an essential contribution in the perception of the final product. It is worth mentioning that the color produced from the suspensions are obtained thanks to a self-assembly mechanism identified during the solvent evaporation. Moreover, this color is exalted with the utilization of nanoparticles of carbon blacks (10-15 nm) whatever the color of the substrates. The transfer to a skincare application requires thus the replacement of those hazardous nanoparticles by safe absorbing additives and the evaluation of the self-assembly ability of the suspensions by casting conditions more representatives of a skincare utilization.

1. Impact of cosmetic additives on coloration

All the films presented in this section were prepared from solvent evaporation of raw suspension with variable proportion of additives. The suspensions were let drying on PS supports set on a heating plate at 35°C. The absorption spectra of the films were obtained from transmission photo-spectrometry.

1.1. *Bactericide*

The preservatives are known as fundamental part of the composition of a skincare product, insuring an extension of its lifespan. Its role is essentially to

inhibit the development of bacteria which could alter the properties of the product and being dangerous for the consumer.

The photonic crystals formation can be extremely sensitive to the presence of additives which could destabilized the interparticle interactions and then their self-assembly dynamic. Considering the potential sensibility of the colloidal crystallization two different kinds of bactericide were evaluated at several concentrations.

The main difference between both is their state under environmental conditions as sodium benzoate is a crystalline powder and phenoxyethanol a liquid. In both cases, the proportions of preservative were evaluated at 0.1, 0.5 and 1 wt% of bactericide in raw suspensions with concentrations of CS colloid of 4 wt%. With sodium benzoate, the addition of the slightest amount of bactericide has a serious impact on the optical properties. Macroscopically, the film produced loss its iridescent green color and trend to an angle-independent blueish color, sign of a degradation of the self-assembly quality with respect to the reference (0wt%). For higher amount a whitening of the material is observed, due to the uncoherent scattering happening in the disordered material. Indeed, the characterization of this color degradation by UV-visible photospectrometry shows effectively a fall of the Bragg diffraction contribution in the optical spectrum related to a perturbation of the spheres ordering (Figure 1).

Motions in the CS beads suspension are constrained by the crystallization of the sodium benzoate during the solvent evaporation. Moreover, the crystals limit the accessible position of the colloids which trend to be more disorganized. In other terms, 2.5 wt% of solid additive with respect to the mass of CS spheres induce a significant decrease of the perceived coloration. With percentages above 12.5 wt%, the diffracted colors are strongly attenuated and inhibited.

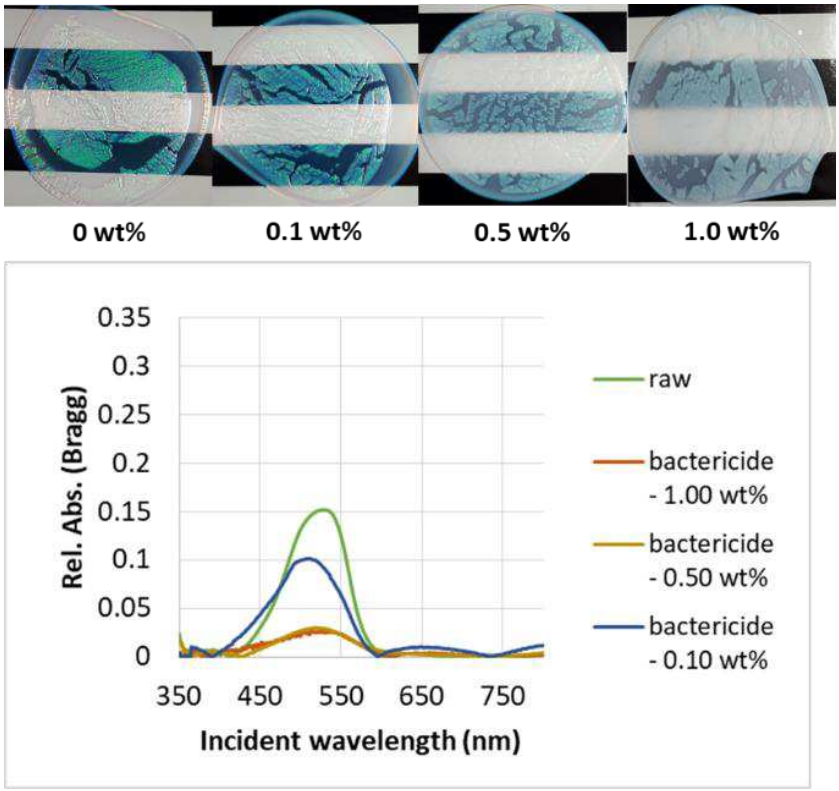

Figure 1. Macroscopic pictures of films made from dispersions with several concentration of sodium benzoate. The corresponding treated relative absorption spectra are displayed below.

At the opposite, the use of liquid preservative as phenoxyethanol leaded to promising results. The films obtained display iridescent colorations, with solid content of bactericide in the suspensions up to 1.0 wt%. The corresponding UV-visible spectra shows analogous Bragg contributions related to the iridescent colors (Figure 2). The color trends to loss of its intensity with the highest amount correlated with a slight increase of the diffracted wavelength. Indeed, the more preservative in the suspension, the higher diffraction wavelength. On one hand, the phenoxyethanol is miscible in water and in simple polyol compounds as glycerol. On the other hand, the POEGMA-based microgel used as shell is well-known for its strong encapsulating property, able to encapsulate in solution additives up to 100wt% of its mass[1]. Therefore, in dried films this liquid preservative has all its chances to swell the MG matrix, altering slightly the inter-particles distances inducing a shift of the resulting Bragg wavelength. Moreover, with a refractive index of 1.51 for the phenoxyethanol, 1.0 wt% of bactericide corresponds to 30 wt% of the MG material in the film and simultaneously increases also the average

refractive index of POEGMA matrix, contribution to the wavelength and intensity alteration of the diffracted light.

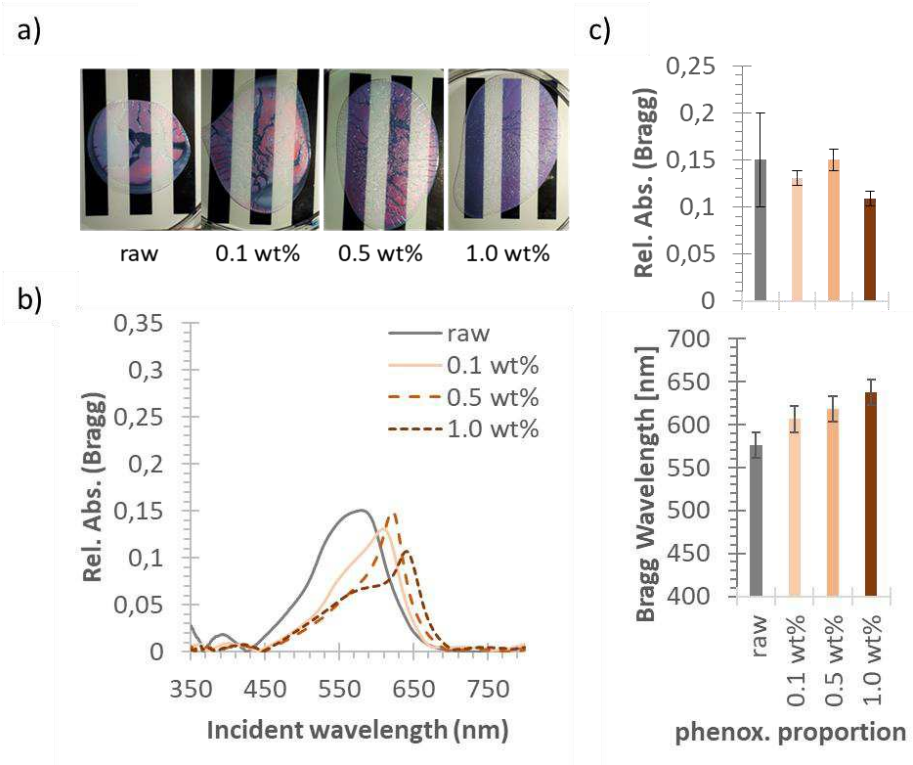

Figure 2.Macroscopic pictures of films from raw dispersions with several concentration of phenoxyethanol(a). The corresponding Bragg contribution in the relative absorbance spectra (UV-vis transmission) are displayed below (b). Finally, the average positions & intensities of the peaks observed are represented (c).

1.2. ***Fragrance***

The fragrance is one of the essential compounds that gives its uniqueness to a skincare. The consequence of its implementation on the film coloration was evaluated by the controlled addition of market-ready perfumed oil in raw suspensions.

To do so, dispersions were prepared with concentrations of 0.1, 0.5 and 1.0 wt% of dried oil of fragrance "J'adore" in raw suspensions (4 wt% of CS beads). The suspensions of CS spheres were used as-made, with a POEGMA-based microgel ratio of 75 wt% in the dried residue. Surface layer on the films with a stronger Bragg coloration seems to appear as the concentration of dried oil increase. The maximum diffraction intensity is captured on the strongly colored area observable at 0.5 wt%. This intensity rise can be associated with a modification of the flow inside the drying suspension. The presence of the oil can modify the gradient

tension and promote the Marangoni effect. According to Bhardwaj *et al.*[2] it can alter the self-assembly dynamic and explain the formation of a photonic layer in the central zone of the dried film. The increase of the diffracted Bragg contribution could thus be explained by an enhancement of the photonic crystal homogeneity/thickness in the measured area, due to this self-assembly alteration. However, it is worth noting that all the films still present a heterogeneous aspect (Figure 3).

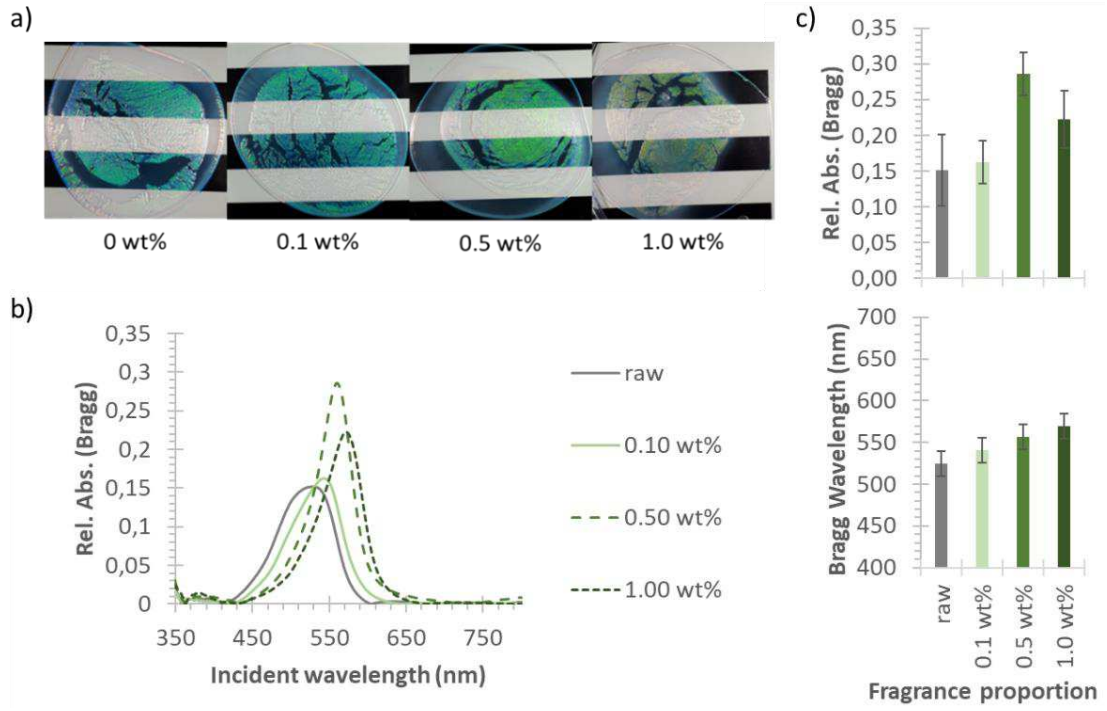

Figure 3. Macroscopic pictures of films made from dispersions with several concentration of fragrance. The corresponding treated relative absorption spectra are displayed below.

The swelling of the microgel phase with the perfumed oil can contribute to the modification of the film coloration, increasing the interparticle distances. Complementary to this diffracted color, raw oil has itself a yellowish color, associated to a dominant wavelength of around 570 - 590 nm. The increase of the oil amount in the dried film can intrinsically modify the color of the film, shifting the absorption peak attributed to higher wavelength. In other words, the addition of this light absorbing oil into the dried film can alter the expected coloration due to the light absorbing properties of the fragrance, but also due to a possible shift of the diffracted light caused by an increase of the interparticle distances due to MG swelling.

1.3. ***Emollient***

The emollients are used as a key compound to insure the moisturizing functions of skincare products. The purpose is to cover the skin with a protective layer, preventing its dehydration. For instance, glycerol is commonly used as an emollient thanks to its high viscosity associated with its low-pressure vapor – low volatility, its biocompatibility and its olfactory neutrality.

That's why the consequence of an emollient on the optical properties was studied with the addition of vegetal glycerol. Several concentrations were tuned to control the amount of glycerol in the final solid content, varying from 5 wt% *(concentration of 0.19 wt% in the dispersion)*, to 30 wt% *(concentration of 1.53 wt% in the dispersion)* (Figure 4).

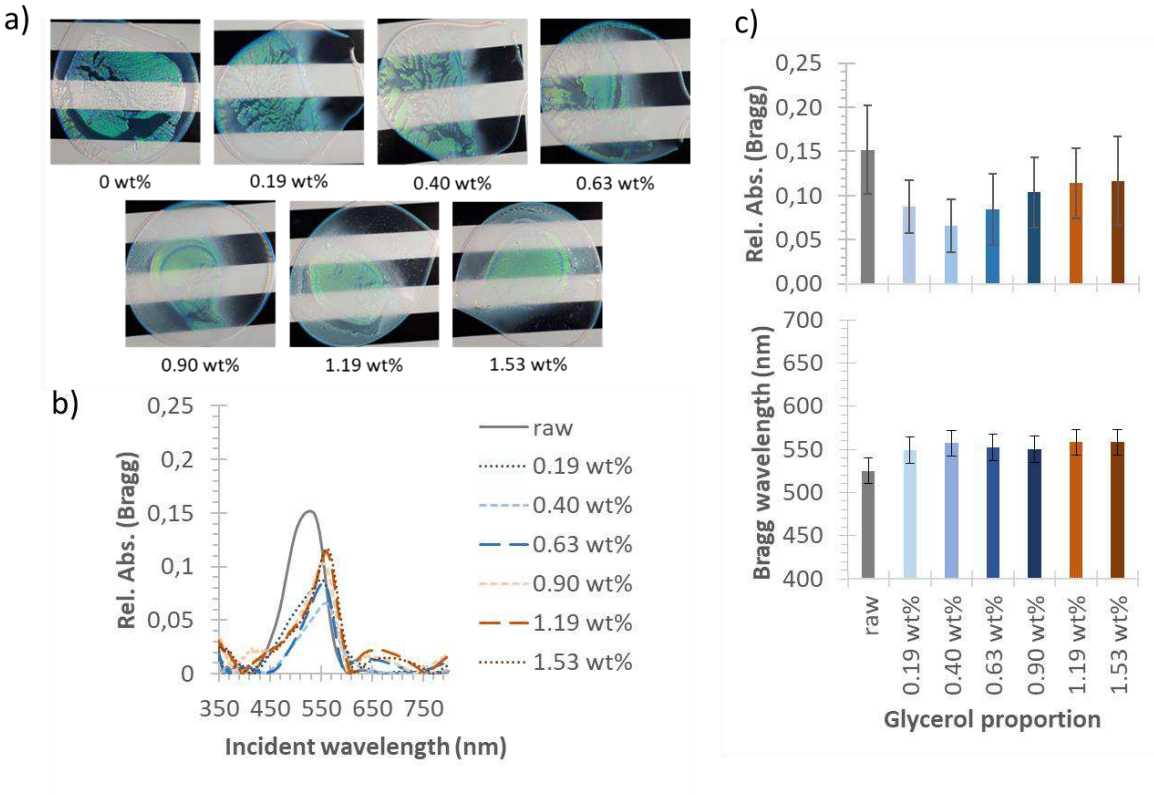

Figure 4. (a) Macroscopic pictures of films made from dispersions with several concentration of glycerol. (b) Corresponding treated relative absorption spectra. (c) Representations of the relative Bragg contribution to the normalized spectra variation, with the associated wavelength shift, according to the glycerol proportion in the suspension.

Macroscopically, all the films obtained display a similar iridescent green layer, testifying of the photonic crystal formation. Similarly, to what observed with the perfumed oil, an alteration of the self-assembly dynamic appears with the

increase of the glycerol ratio. Nevertheless, the dried films cannot support too high proportions of glycerol: above 0.90 wt% of glycerol in the suspension, droplets of emollient are identified, sweating out of the film surface. This proportion of glycerol is associated with 23 wt% of emollient against the CS spheres. The photonic crystal cannot be swollen above this proportion. Indeed, according to the photospectrometry spectra, the addition of the glycerol induces a slight shift of the contribution of the Bragg diffraction. Glycerol shares almost the same refractive index than the POEGMA-based microgel, and is transparent in the visible range. That's why this shift can be reasonable attributed to an effective alteration diffracted wavelength, by opposition to the previous fragrance analysis.

1.4. ***pH***

The pH of the raw suspension is relatively acid, around 3.5 ± 0.5. The pH of the skin being around 5-6, a pH adjustment may be required to produce skincare application. The pH of raw suspension was thus adjusted with a citrate-phosphate buffer[3], made from solutions of citric acid and Na_2HPO_4 respectively at 0.01 and 0.02 mol/L (Figure 5).

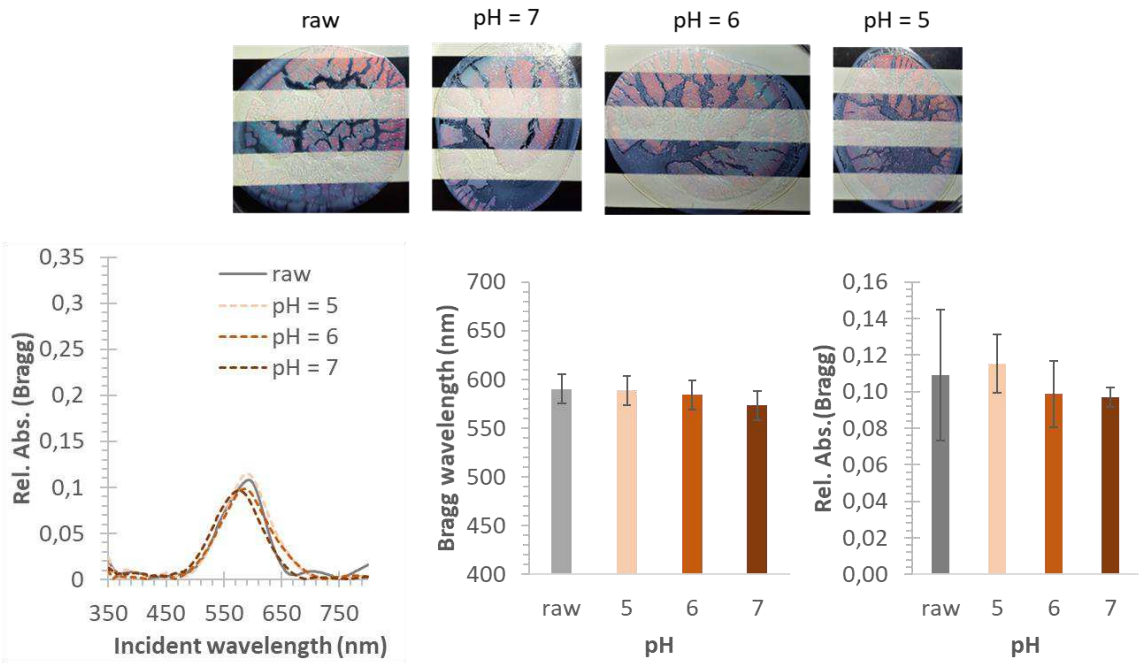

Figure 5 Macroscopic pictures of films made from dispersion buffered at several pH in comparison with a film from a raw dispersion. All the films are made on a hot plate set at 35°C. The corresponding average peaks positions and relative intensities (after baseline subtraction) from relative UV-vis absorbance are displayed below.

The films colorations with buffered dispersion are very similar to film based on raw dispersion. Moreover, the spectroscopic analysis doesn't show a significant analysis of the Bragg peak positions & intensities, whatever the pH of the dispersion. In other terms, the electrostatic changes induced by pH don't alter the self-assembly dynamic neither its corresponding coloration, apparently.

1.5. ***Complete formulation***

Up to this point, the influence of the additives has been evaluated separately. The addition of a crystalline compound has showed its dramatic effects on the optical properties but promising results has been identified with the utilization of other liquid additives. Even if photonic layers were producible with varied proportion of additives, the self-assembly mechanism and the colors induced are largely impacted by the proportion of additives in the final dried film. In a final product, the controlled amounts of emollient, fragrance and preservative are obviously integrated together into the final formulation. As synergetic effects may appear, the investigation of the additives blends appears thus as essential.

Consecutively, the several suspensions were produced with controlled amount of glycerol (emollient), phenoxy ethanol (preservative), "J'adore" dried oil (fragrance) and raw CS suspensions at 3.6 wt%. The fragrance and phenoxy ethanol proportions were kept constant at respectively 0.2 wt% for each additive with respect to the final suspensions. The proportions of glycerol were variable, from 0 to 3.1 wt% with respect to the final suspensions. Those experimental conditions, with the amounts described in the Table 1 allow to produce formulated suspensions with a total mass of additives corresponding of a range between 10 to 50 wt% of the final dried residue. Each formulation trial was prepared through the successive addition of the correct amount of glycerol, phenoxy ethanol, fragrance and raw suspensions. The mix was stirred with a magnetic stirrer for at least 24 hours, until the suspensions appeared homogeneously white (Table 1).

Table 1. Quantity of additives used with the corresponding amount of raw suspension with an initial solid content of 3.6 wt% to prepare several suspensions, with different global proportions of additives in the final solid content.

add./dried residue [wt%]	**glycerol [g]**	**phenox. [g]**	**fragrance [g]**	**raw susp. [g]**
10	*0.0000*	*0.0400*	*0.0400*	*19.9200*
15	*0.0470*	*0.0400*	*0.0400*	*19.8730*
20	*0.0994*	*0.0400*	*0.0400*	*19.8206*
30	*0.2255*	*0.0400*	*0.0400*	*19.6945*
40	*0.3913*	*0.0400*	*0.0400*	*19.5287*
50	*0.6187*	*0.0400*	*0.0400*	*19.3013*

The corresponding films were produced by solvent evaporation on PS substrate set on a heating plate at 35 °C for 1 night. The dried films were successively characterized by UV-visible photo-spectrometry. The rise of the additives proportion doesn't show significant impact on the Bragg wavelength, as observed with previous analysis, with roughly the same Bragg wavelength. However, the evaluated diffraction intensity in the absorption spectra is more affected. Up to 15 wt% of additives, the Bragg contribution intensity is preserved,

but a brutal loss of the diffraction signal is observed for higher amount of additives in the final film (Figure 6).

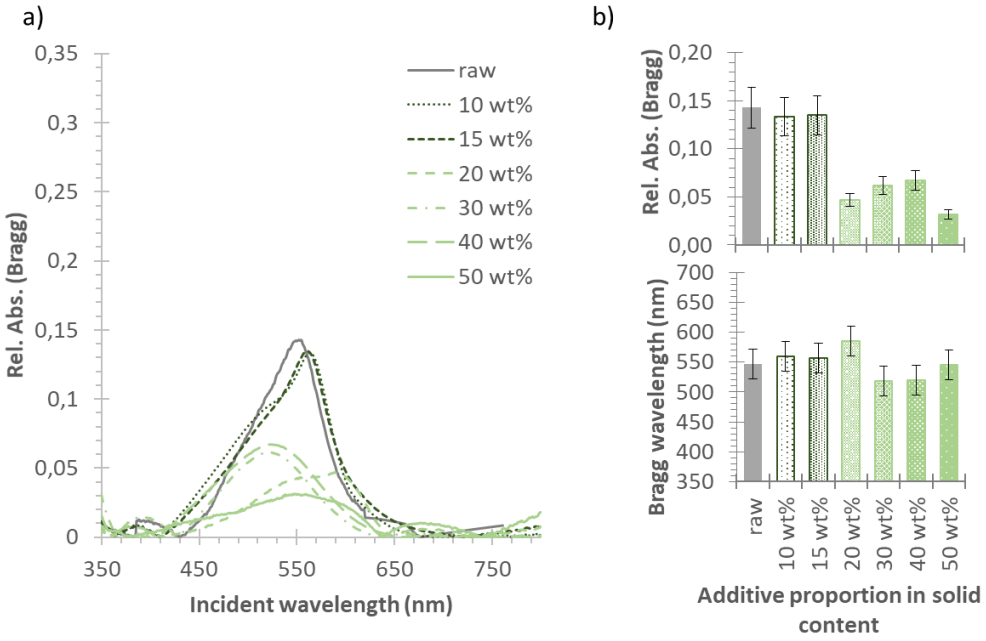

Figure 6 (a) Absorption spectra of films made with variable calculated amounts of additives in the dried films. (b) Corresponding Bragg contribution to the relative absorption spectra and Bragg wavelength positions in function of amounts of additives.

The data appear as coherent with the previous evaluation on the addition of several proportion of emollient, and allow to conclude that whatever the additives incorporated into the CS suspensions, the critical parameter is effectively the proportion of additives. The understanding of the formulation limitations opens the transferability of the core-shell produced toward the elaboration of skincare applications. Nevertheless, it has been displayed the colors produced require a light scattering additive in order to reduce the uncoherent light scatterings that parasite the color perception. The next section presents the efforts developed in this direction.

2. Replacement of carbon nanoparticles by iron oxides

The substitution of carbon black (nano) is necessary in order to consider the moving legislation around the nano-materials (1-100 nm) for skincare products. This substitution is essential concerning carbon nanotubes which are known now for their toxicity[4,5]. An interesting substitute is the black iron oxide (II, III). It is referenced as “Sunpuro” and “Sympholight”. The first one is made of

cuboid particles between 50 – 150 nm whereas the second one is made of spherical particles between 100 -300 nm (Figure 7). According to the Stokes-Einstein equation, the sedimentation speed of particles can be estimated according to their average radius (r), the gravity acceleration (g), the density difference between the solvent and the particle(Δ(ρ)) and the dynamic viscosity of the suspension (μ). For instance, those Fe_3O_4 oxides are associated with an average density of 5240 $kg.m^{-3}$, around fifth times higher than polymeric material. Consecutively, the sedimentation of such colloidal particle in water-like fluid ($\mu \sim 10^{-3}$ Pa.s) is inevitable.

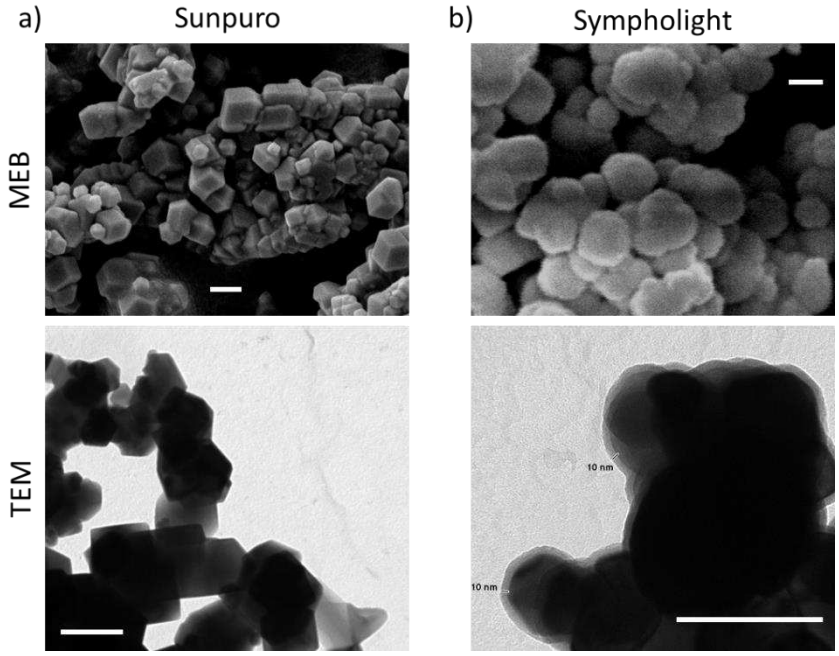

Figure 7 MEB and TEM images of the iron oxides referenced as (a) Sunpuro (provided by SunChemical) and (b) Sympholight (provided by Kowa Europe GmbH). Scale bars represent 200 nm.

The main solution to achieve a dynamic stabilization of such colloidal oxide particle is through the increase of the dynamic viscosity of the suspension. As discussed in the previous section, the total amount of additive, comprising thickening agents as glycerol, must be controlled according to the total amount of suspended CS particles, otherwise a degradation of the optical properties must be expected. In other terms, the rise of the suspensions' viscosity can only be envisaged thanks to the increase of the CS particle concentration in the suspension to preserve the structural coloration intensity. Depending on the dynamic viscosity

reached, the travelled distance of the colloidal oxides can be thus evaluated, according to the time period[6] (Figure 8).

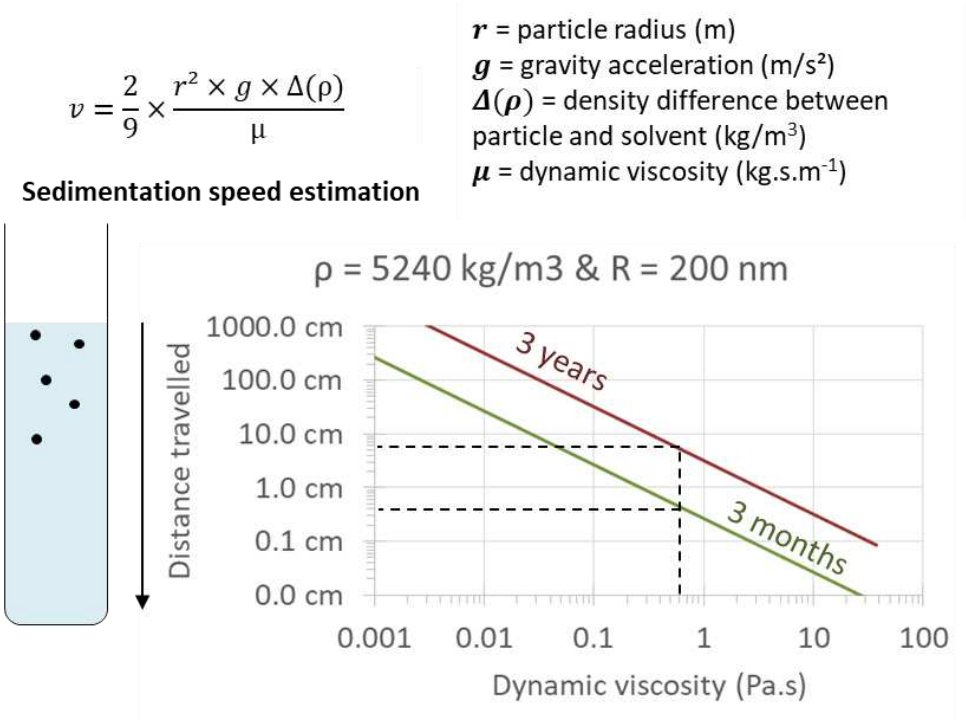

Figure 8. Stokes-Einstein equation used to estimate the sedimentation celerity. An estimation of the distance travelled by the oxides in the dispersion is plotted below, after 3 month & 3 years of aging.

It's a reason why cosmetic products present usually a controlled and a relatively high viscosity with respect to water. However, the produced raw core-shell suspensions have solid content of roughly 4 wt%, with a water-like viscosity, and any increase of the solid content above 8 wt% had dramatic consequences on the colloidal stability during the shell formation. The grafting was no more controlled, with the production of large and precipitating aggregates. In the context of the development of a skincare product, the rheological properties of the fluid must be controllable, without deteriorating the optical properties of the film produced. More, the application conditions of cosmetic products impose usually the formation of dry films with a controlled thickness around 30 µm, from wet films not thicker than 100 µm. Roughly, suspensions with a solid content around 30 wt% would offers the corresponding conditions to the production of such films. The rise of the solid content appears thus as the next step toward the development of a viable skincare application.

At this end, several approaches were probed to increase the solid content of the suspensions and preserve the self-assembly properties of the colloids. Two industrially transferable strategies were investigated. The first one consisted to gently heat the dispersion under a slow stirring to evaporate the excess of water. The heating was controlled between 40 and 60 °C to avoid the degradation of the polymeric chains and follow more easily the solvent evaporation. This soft solvent evaporation was controlled on relatively long period up to 3 days. The solid content was followed as a function of the mass loss of the dispersion. It appeared the solid content was hard to control with the thickening of the suspension, leading to the irreversible aggregation of particles on the border of the drying suspension. This process allowed only the rise of the solid content up to 19 wt%.

With the second strategy, aqueous colloidal dispersions were concentrated by a drying/re-dispersion process. The former dispersion was firstly completely dried by freeze-drying then the residue was re-dispersed with the addition of a controlled amount of water. The freeze-drying process rely on the water sublimation at low-pressure and low-temperature conditions. The dispersion was firstly frozen in liquid nitrogen, put in a freeze-dryer where the pressure was decreased. The residue dryness was checked by TGA. It was then re-dispersed with a controlled amount of MilliQ water in function of the solid content aimed. The redispersion was assured by a mechanical stirring, thanks to a stirring anchor set on a stirring motor. The stirring was let for 2 days at ambient temperature, with a rotation speed of 60 rpm. Dispersions of 10, 20, 30 and 40 wt% of core-shell solid content were then produced.

Thin films are made with a doctor blade device from raw dispersions and concentrated dispersions (40 wt% of core-shell).

2.1. *Elaboration of concentrated suspensions*

A completely dried core-shell residue is obtained by the freeze-dried process and presents some re-dispersibility abilities. A milky white dispersion is obtained after 2 days of stirring with a magnetic stirrer at ambient temperature for all solid contents. However, some aggregates are not re-dispersed throughout the stirring process (Figure 9).

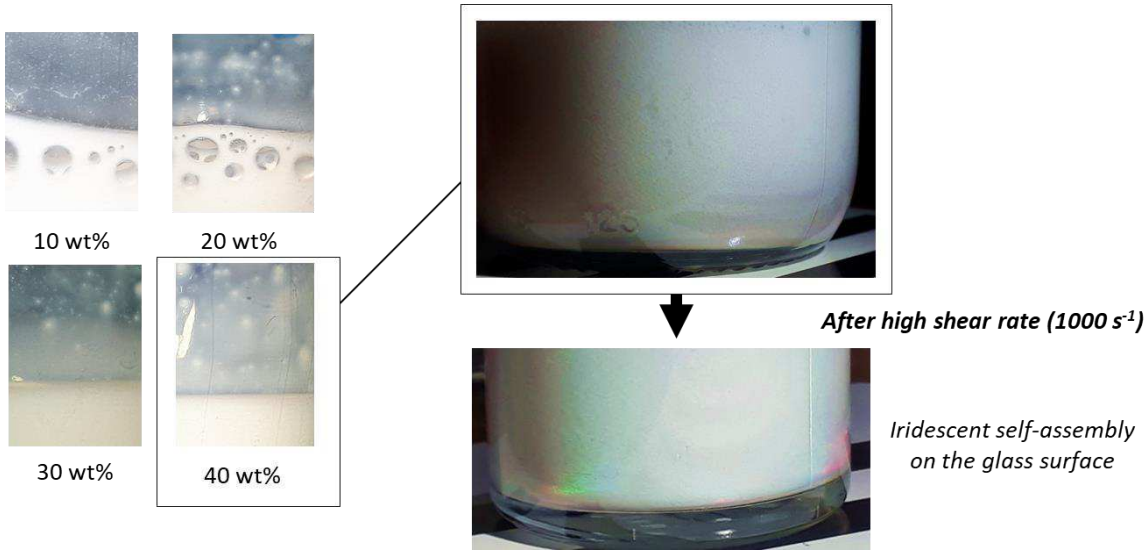

Figure 9. Macroscopic pictures of concentrated dispersions obtained from freeze-dried residues. An iridescent layer is spontaneously generated at the interface water/glass with the highly sheared dispersions.

This result could be expected due to the filmogenic properties of the core-shell particles presenting a shell interpenetration. Then to apply a higher mechanical energy, each dispersion was thus stirred in a Couette geometry with a rheometer, allowing also the measurement of the dynamic viscosity.

The suspensions were sheared during 30 minutes progressively with shear rate from 1 to 1000 s^{-1}, each time after a pre-shear at 200 s^{-1} for 10 minutes to limit as much as possible the presence of bubble during the viscosity measurement. This shearing treatment gives first clues of an improvement of the particles' dispersion after one day of rest. Indeed, it appears that the highest concentration (40 wt%) of core-shell displayed the formation of an iridescent layer at the interface water/glass after this shearing treatment (Figure 9). This phenomenon appears spontaneously when the dispersion is let at rest, and surprisingly only after this treatment. This stirring process allowed some aggregates to be re-dispersed but not fully, as aggregates remain visible at the surface of the glassware.

The impact of the remaining aggregates on the size dispersion was probed thanks to Dynamic Light Scattering (DLS) size measurements. The analyses were performed on dilution at 1 mg/mL from raw and sheared suspension. Figure 10 shows that either at 25 °C or 60 °C, the size distribution of concentrated suspension

spread slightly towards the larger sizes. This size spreading is related to the presence of some aggregates, enlarging the size distribution after the concentration protocol of the suspension. The role of the un-grafted shell material on this aggregation was evaluated thanks to the analysis of concentrated suspensions originating from purified dispersions. Surprisingly, the widening of the size distribution doesn't appear in such case. The size distribution resulting of the concentrated purified suspensions is roughly superimposable to the ones arising from the raw suspensions (Figure 10), whatever the temperature. The presence of the free un-grafted material would limit the re-dispersibility of the concentrated suspensions, producing a "cement" between particles, probably.

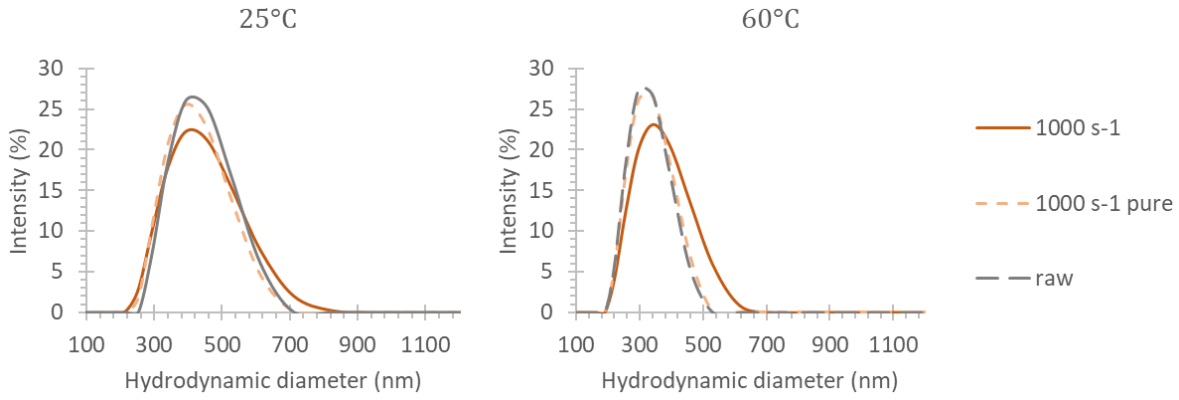

Figure 10. DLS hydrodynamic diameters size distribution of raw dispersion and re-dispersed core-shell at the same concentration.

Fortunately, the residual aggregates may not disturb the colloidal self-assembly process controlled by solvent evaporation. Indeed, the comparison of films made from raw and reformulated dispersions at the same solid content of 3.5 wt%, didn't show a significant difference of coloration. The suspensions were separately treated at shear rates of 500, 1000 and 1500 s^{-1}, probing the consequences on the self-assembly properties of the films. Moreover, films made from freeze-dried residues re-dispersed only with the softer magnetic stirring were also compared. The corresponding films were consecutively analyzed by transmission UV-visible spectroscopy (Figure 11).

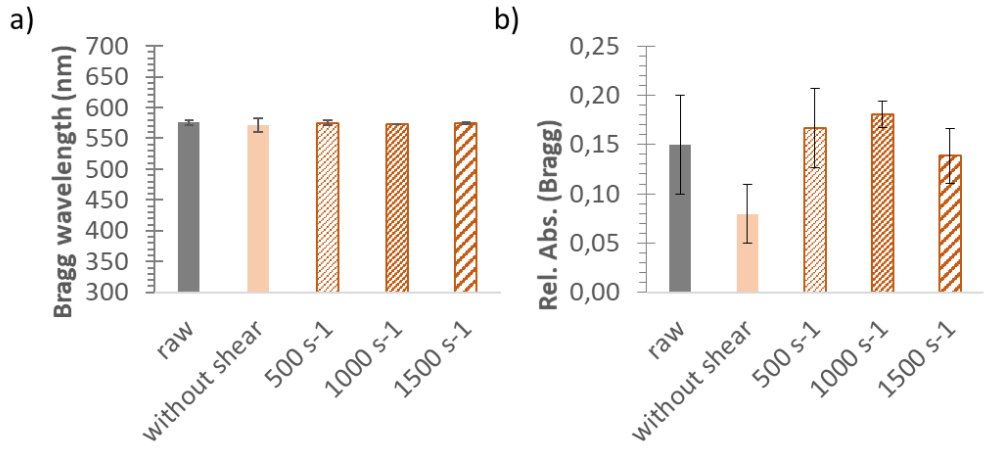

Figure 11 (a) Representation of the measured Bragg wavelength maximum and (b) its related contribution to the normalized absorption spectra produced by solvent evaporation. At the exception of the film made from raw suspensions (3.5wt%), the others were casted from suspensions at 40 wt% sheared or not and rediluted to 3.5 wt%. The shear rate is indicated, between 500 and 1500 s^{-1}.

Whatever the films, the measured Bragg wavelength corresponding to the diffraction peak position are not affected by the concentration process. The interpretation of the measured diffraction intensity is less obvious. Due to the already discussed surface heterogeneity, the Bragg contribution to the normalized spectra is associated with a relatively large standard deviation. All the samples present roughly the same diffraction intensity, at the exception of the film originating from the un-sheared suspension. The shearing control appears thus as critical to regenerate the self-assembly ability of the CS suspensions during the evaporation of diluted suspension.

Surprisingly, the different intensities of color between films cannot be associated to a significant difference of surface film organization (Figure 12).

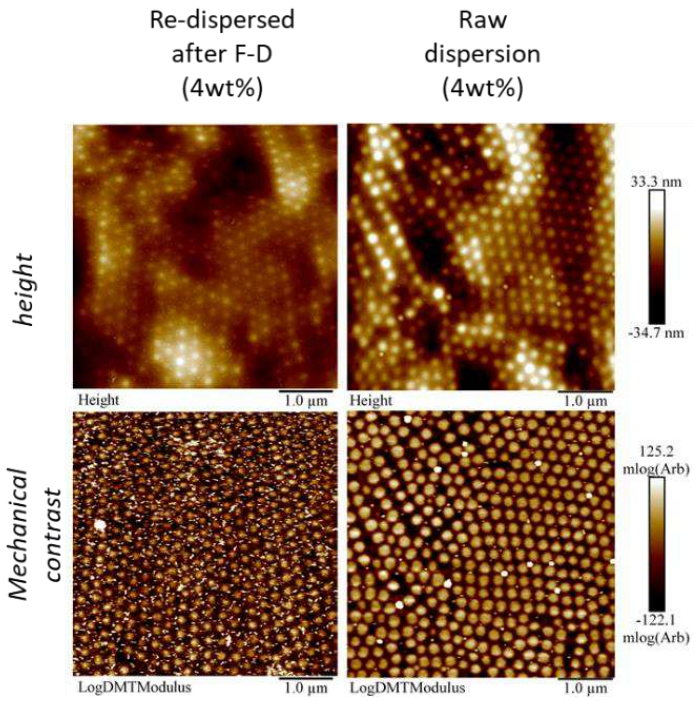

Figure 12. AFM pictures in peak force mode with contrast set on height or mechanical modulus contrast. The films were made from raw dispersion or un-sheared concentrated suspensions diluted afterward to the same solid content than raw dispersions.

Indeed, a similar surface organization is observed which is coherent with the same diffraction peak wavelengths. Additionally, it involves that the identified decreasing of the peak maximum could be related with in-depth organization differences.

2.2. ***Black iron oxides in viscous suspensions & thin films***

As discussed previously, the dynamic stabilization of denser and bigger light absorbing colloidal particles, replacing the nanosized carbon black particles, require the rise of the dynamic viscosity of the suspensions. The undertook concentration procedures allow the production of thicker suspensions, with apparently no significant impact on the self-assembly properties of the particles (Figure 11 & Figure 12).

As previously, the suspensions were sheared 30 minutes progressively with shear rate from 1 to 1000 s^{-1}, each time after a pre-shear at 200 s^{-1} for 10 minutes limiting as much as possible the presence of bubble during the viscosity measurement, succeeded with pause of 1 minute. The average dynamic viscosity increases effectively with the concentration, achieving a viscosity 1,000 times

higher than the lowest concentration, with 5.1×10^{-1} Pa.s^{-1} for the highest concentration (Figure 13).

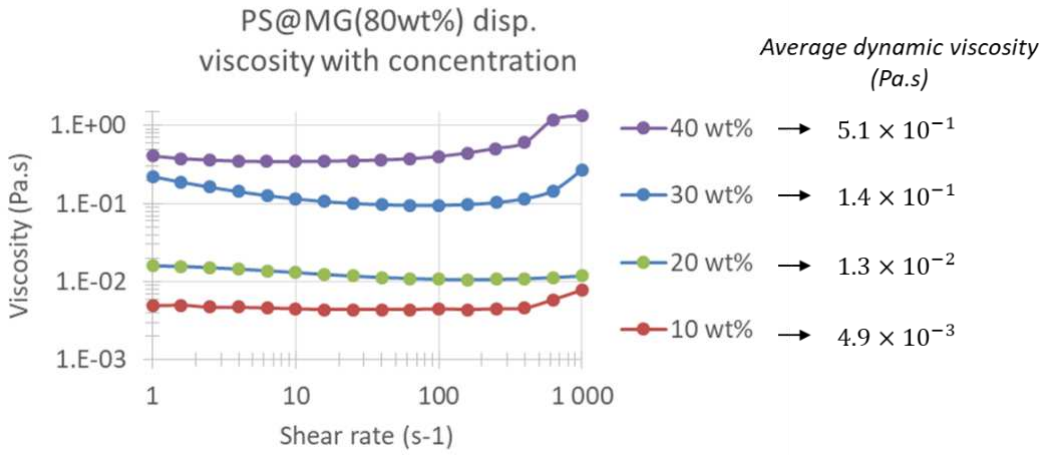

Figure 13. Viscosity evolution in function of the shear rate of a core-shell dispersion from 10 to 40 wt%. The average dynamic viscosity is displayed next to each concentration. Each point of the graphs was captured after a stabilizing time of 10 s at the indicated shear rate.

For each sheared suspension, the same amount of black iron oxide was dispersed to evaluate its dynamic stability. First, the adequate amount of iron oxide was firstly wet with 0.1 mL of the suspension, and stirred manually to promote the formation of solvent/oxide interfaces instead of air/oxide interfaces. Consecutively the dispersion was completed with the adequate amount of concentrated and sheared suspensions to adjust the final concentration from 10 to 40 wt%. In a next step, the suspensions were stirred then sonicated for 10 minutes respectively. It is worth noting that the final amount of iron oxide is around 1.8×10^{-2} wt%, higher than nanosized carbon black used before (around 0.1×10^{-2} wt%). This value is mainly due to the difference of density and respective extinction coefficient to achieve a comparable darkening between both light absorbers in the visible range. Figure 14 shows the obtained suspensions after 24h of rest.

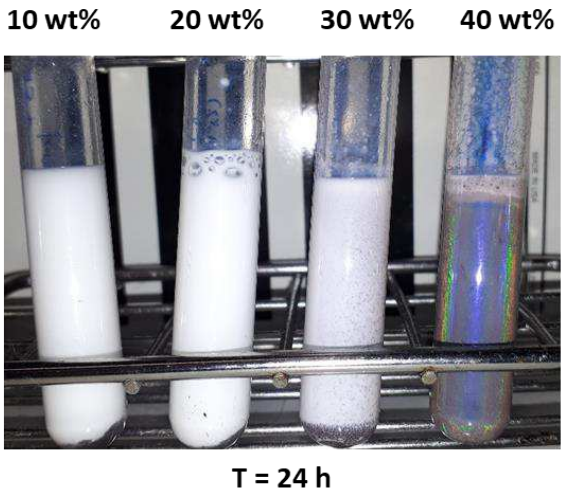

Figure 14. Macroscopic pictures of dispersions at several concentration mixed with cuboid iron oxides.

The suspensions are homogeneously gray, with the same apparent color. After 24 hours, the oxides fall completely on the bottom of the glassware for suspension with CS particles concentration between 10 and 30 wt%. According to the Stokes-Einstein theory, the more viscous suspensions (40 wt%) offer the more stable oxides suspensions. Moreover, the rest of the CS spheres self-assemble at the suspension/glassware interface, forming iridescent photonic crystals with a color perception effectively enhanced by the presence of iron oxides. This encouraging observation about the self-assembly ability of such viscous suspensions with bigger iron oxide particles lead to next concern: the elaboration of thinner films from those suspensions.

The sheared mixtures were thus casted with a doctor blade at several wet film thicknesses on PVC support. The supports were installed in an oven heated set at 40 °C during all the casting procedure. The several castings were attempted, from wet films of 100 and 200 µm. The films were casted from raw suspensions of core shell particles with core of 180 nm with a proportion of shell material of 80 wt% that gave rise to iridescent reddish coloration in previous solvent evaporation casting. Here, the doctor blade casting was performed from original raw suspensions, with a solid content around 4wt% and compared with its concentrated and sheared analogues, with a solid content of CS particles around 40 wt% and the impact of iron oxide was evaluated (Figure 15).

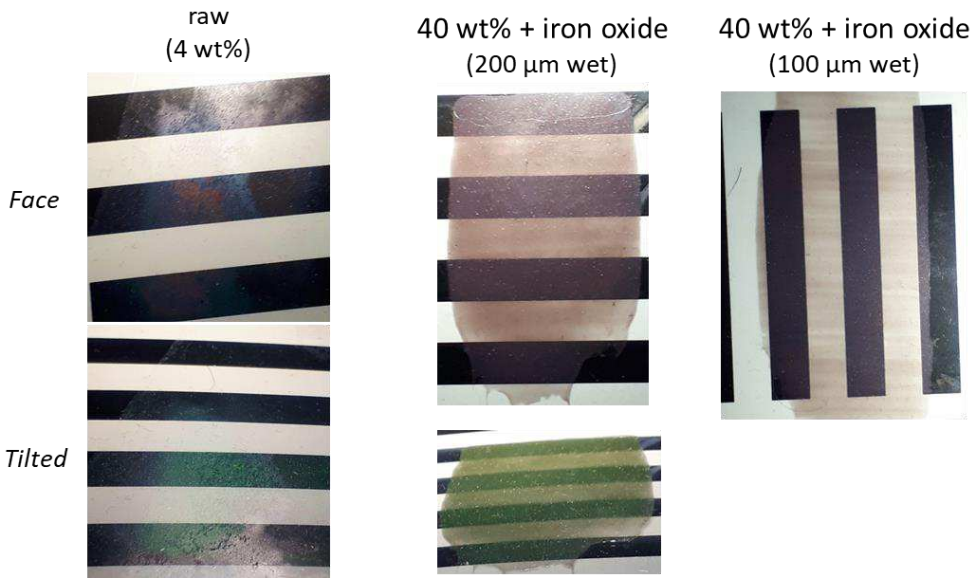

Figure 15. Macroscopic pictures of thin films made with a doctor blade from dispersions with different core-shell solid content and iron oxides particles at the same concnetration of 1.8×10^{-2} *wt%. The films are made on transparent PVC supports at 35°C.*

The casting of water-like suspension at 4 wt% lead to heterogeneous films, with variable thicknesses as it appears macroscopically (Figure 15 *left*). This heterogeneity caused by the dewetting of the substrate leading to several ponds instead of a homogeneous wet film of 100 µm. Nonetheless, a slight coloration remains perceptible on the center of the filmed formed, presumably due to the slow solvent evaporation and the higher colloidal particle mobility in more fluid suspensions. The thickness of the colored area was measured with a digital micrometer screw gauge. The corresponding thickness was around 23 ± 5µm, proving that perceptible structural and iridescent colors may effectively formed from such thin film. The films made with the same wet film thickness of 100 µm (39 ± 3µm once dried), but with a higher concentration doesn't lead to highly perceptible colors, even with light absorbing materials. A slight coloration starts being perceptible only from thicker films, made from 200 µm wet films (72 ± 6µm once dried).

Figure 16 displays macroscopic and microscopic pictures of analogue films.

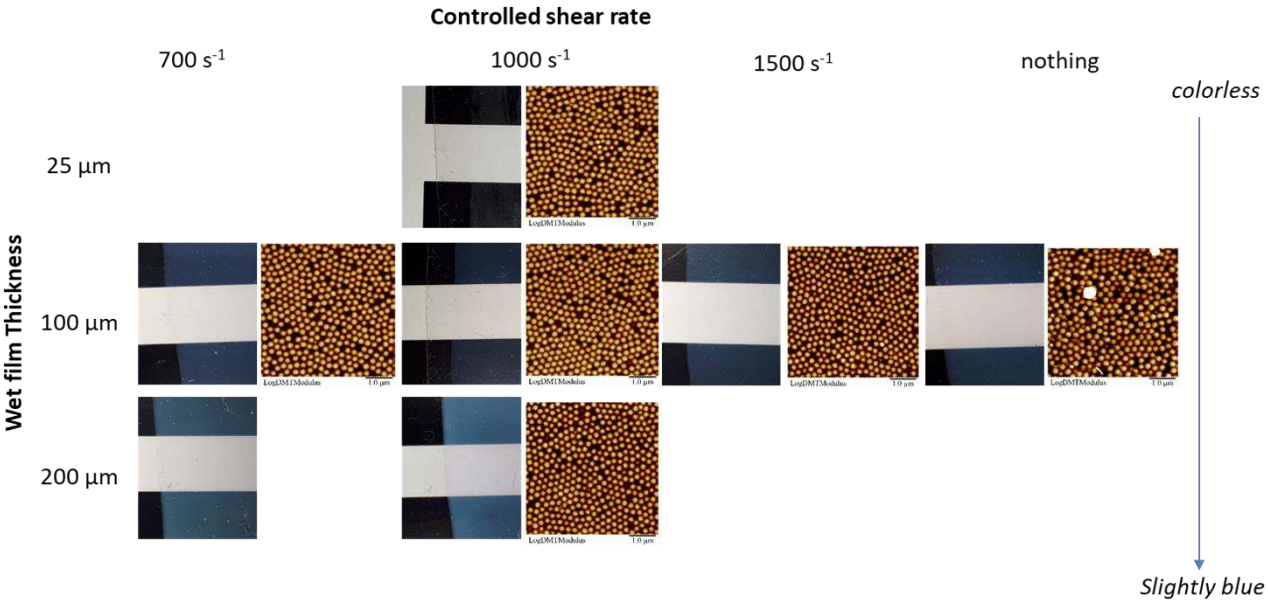

Figure 16. Macroscopic picture of thin films prepared with a doctor blade. The thickness of the wet film is indicated on the left. The shear rate used to mix the concentrated suspension is mentioned on the top. Corresponding AFM surface pictures are displayed next to some macroscopic pictures. Suspensions concentration is each time 40 wt%

For comparison, without light absorber, the films are transparent or blueish, in function of their thicknesses. In each case, AFM pictures show the surface is mostly disorganized, whatever the wet film thickness or the shearing rate used for the stirring treatment of the concentrated suspensions. In other words, the surface of the obtained films shows no trace of large photonic crystals: the disorder of the colloidal arrangement being associated thus to photonic glass.

Few usual skincare additives were also added in the concentrated suspensions that could act as a plasticizer and may improve the colloidal organization. The addition of hydrophilic (*glycerol*) or hydrophobic (*caprylate/caprate oil*) emollient doesn't lead to any perceptible optical improvement and the addition of light absorbing particles doesn't reveal any iridescent coloration, as the system remains disorganized (Figure 16). Our hypothesis is the drying process is too fast, considering the colloidal mobility in these concentrated suspensions: again, only photonic glasses are obtained.

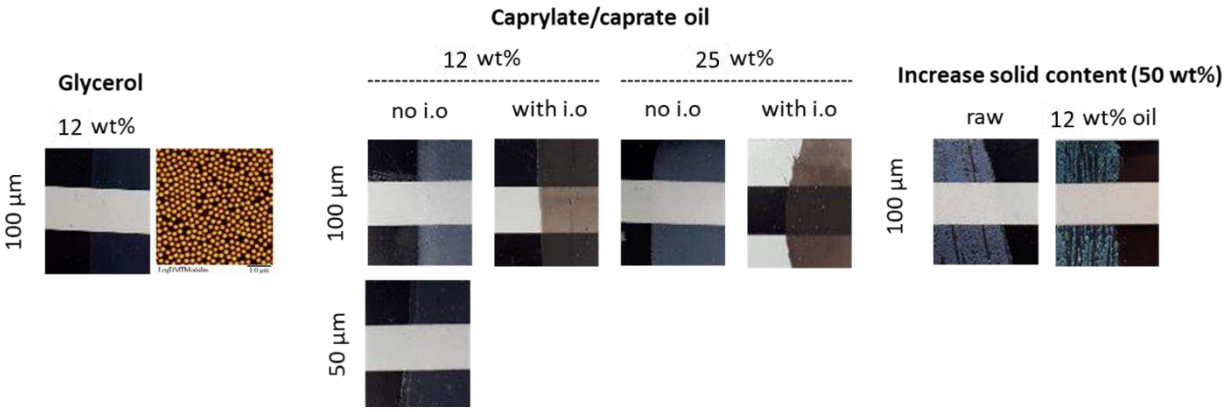

Figure 17 Macroscopic picture of thin films prepared with a doctor blade, with or without iron oxides (i.o.), and with several fraction of hydrophilic or hydrophobic emollient, respectively glycerol and caprylate/caprate oil. The solid content of the CS particles was kept constant at 40 wt%, except when notified.

Indeed, due to a too fast drying process and considering the colloidal mobility in these concentrated suspensions, only photonic glasses seem to be achievable.

Conclusion

In this section, three compounds' families that are essential for the development of a usual skincare application have been analyzed. The control of the solid/liquid state of the additive considered at ambient conditions show critical impact on the optical properties of the films produced by solvent evaporation. Hopefully, the film forming properties (Chapter 3) are conserved with liquid additives, paving the way to formulation trials. Nevertheless, the proportion of additives with respect to the core-shell particles must be controlled, leading otherwise to a degradation of the intensity of the structural/iridescent coloration.

The elaboration of a skincare product requires a peculiar attention on the additives used. At this end, the replacement of nanosized carbon particles by larger iron oxides has been investigated. The stabilization of these heavier particles required the increase of the suspension viscosity through a raise of the CS particle concentration. Consecutively, a way to concentrate and homogeneously redisperse the particles has been presented. The successive freeze-drying and controlled redispersion of the dried residue allow the formation of concentrated suspension up to 40 wt%, without altering the self-assembly ability of the core shell particles. A specific attention has been brought on the shearing protocol of the concentrated particles. A sufficiently strong shear rate is indispensable to the maintain of the organized self-assembly ability of the particles after drying.

Nevertheless, the self-assembly was evaluated only with diluted suspension through the solvent evaporation process analyzed in the chapter 3. This film formation mechanism led to dried films with thicknesses up to 200 µm. However, in the context of a skincare/cosmetic application, the dried film must have an around 6-7 times lower thickness. The evaluation of the optical properties was performed from concentrated suspensions casted through doctor blade casting. Films with a thickness between 20-40 µm thick were successfully produced. However, the confinement of the particle in such concentrate particles combined with the faster drying of the thin wet film lead systematically to photonic glasses. The particles don't have enough mobility nor time to self-assemble during the drying film and form a well-organized top surface layer. The liquid flow, has been identified as the motor of the self-assembly phenomenon and is significantly

reduced by the viscosity raise. Without other assembling forces, the suspended particles are frozen during the film drying leading ineluctably to the formation of photonic glasses. From our point of view, the casting conditions of a commercial application are thus inextricably related to the formation of disorganized arrangement of colloids. The next chapter present the perspectives toward the possible elaboration of color tunable photonic glasses with an innovative colloidal design involving this multi-responsive POEGMA-based microgel.

To conclude this chapter, we have presented the limitations of solvent-evaporation for colloidal self-assembly purposes. The increase of the suspension viscosity induces a loss of the colloids 'mobility[7], inhibiting the colloidal crystallization. Additives perturbate the self-assembly dynamic leading to a loss of the diffracted intensity with an additive proportion higher than 20-25 wt%.

References

1. Aguirre, G. *et al.* Versatile oligo(ethylene glycol)-based biocompatible microgels for loading/release of active bio(macro)molecules. *Colloids and Surfaces B: Biointerfaces* **175**, 445–453 (2019).

2. Bhardwaj, R., Fang, X., Somasundaran, P. & Attinger, D. Self-Assembly of Colloidal Particles from Evaporating Droplets: Role of DLVO Interactions and Proposition of a Phase Diagram. *Langmuir* **26**, 7833–7842 (2010).

3. McIlvaine, T. C. A BUFFER SOLUTION FOR COLORIMETRIC COMPARISON. *Journal of Biological Chemistry* **49**, 183–186 (1921).

4. Karakoti, A. S., Hench, L. L. & Seal, S. The potential toxicity of nanomaterials—The role of surfaces. *JOM* **58**, 77–82 (2006).

5. Sharma, M. Understanding the mechanism of toxicity of carbon nanoparticles in humans in the new millennium: A systemic review. *Indian J Occup Environ Med* **14**, 3 (2010).

6. The Stokes-Einstein law for diffusion in solution. *Proc. R. Soc. Lond. A* **106**, 724–749 (1924).

7. Würger, A. Thermal non-equilibrium transport in colloids. *Rep. Prog. Phys.* **73**, 126601 (2010).

Chapter V: Perspectives – Elaboration of Photonic glasses

Introduction

The previous chapter described the effort for making a film with responsive structural colors from self-assembled photonic crystals. Hard-core@soft-shell particles were successfully made, producing actually self-assembled films with responsive colorations through a process driven by convection forces. The transfer of this technology into a skincare application allowed to highlight the formulation limits associated with the development of a marketable product. More, the casting conditions of a skin care applications were identified as limiting the self-assembly ability of the core-shell particles, giving rise only to disordered patterns at the microscopic scale: colloidal glasses. This chapter presents a preliminary approach toward the conception of photonic glasses displaying colors suitable in peculiar for a cosmetic application, with reddish hues.

1. Red Photonic Glasses

Colloidal glasses refer to materials where the colloidal objects are arranged in a disorganized way. The arrangement of the particles is *amorphous* by analogy with inorganic glasses where the properties are due to similar atomic organizations. In the literature, such colloidal glasses can produce specific structural colors. Those colors have the peculiarity to present hues independent to the observation angle, by contrast with iridescent photonic crystals.

However, the colorations obtained by photonic glasses made from spheres suspensions are usually associated with blueish/white colors, caused by a predominant behavior of the particles Mie scattering. According to the size of the particles, the blueish/white coloration would be caused by the dependency of light scattered intensity in function of the incident wavelength.

Kim *et al.*[1] produced successfully photonic glasses with an apparently perceptible reddish coloration. To do so, they firstly synthesized hollow silica spheres (HSS) embedded in a matrix of trimethylolpropane ethoxylate triacrylate (TMPEOTA). The TMPEOTA was photopolymerized to form a matrix with roughly the same refractive index than the silica. The formation of such colloidal glass made of air beads incorporated into a matrix with a higher refractive index appears an appealing design for making red photonic glasses (*Figure* 1).

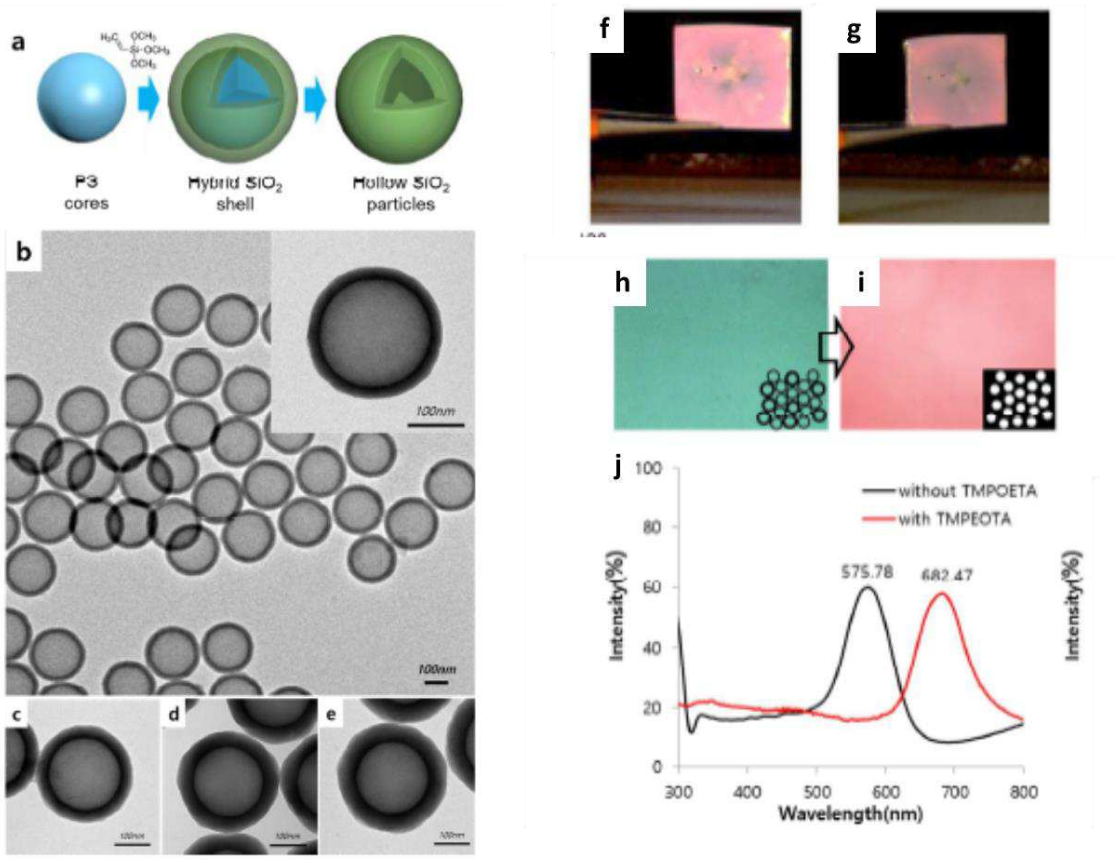

Figure 1 (a) Schematic representation of the conception of hollow silica spheres (HSS) from PS template. (b) Overview of produced spheres (c – e) HSS with controlled silica thicknesses. (f – g) Films of disordered HSS spheres infiltered with trimethylolpropane ethoxylate triacrylate (TMPEOTA) at different angle of observation. (h – i). Films with before (h) and after (i) the infiltration. (j) Compared reflectance spectra of films without or with TMPEOTA.

The wavelength of the color produced (λ_{PhG}) can be considered as analog to the Bragg-Snell description, usually used for the description of photonic crystals. Indeed, the amorphous arrangement induces no ordering, by definition. This overall disorder is however associated with an averaged spatial periodicity, where the distance between each particle in the three space directions is the same. This averaged distance, controlled by the sphere diameters (D_{sphere}) can be integrated into the Bragg-Snell equation. The Bragg-Snell diffraction is then considered at normal incidence, as if it could be considered the incident light can interact with the same virtual reticular plans in any direction due to the amorphous arrangement.

$$\lambda_{PhG} \approx 2 \times n_{aver.material} \times D_{sphere}$$

The average refractive index of the material ($n_{aver.material}$) is evaluated in similar manner as in the chapter 3.

$$n_{aver.\ material}=(1-\phi_p)\times n_{matrix}+\phi_p\times\left\{\frac{D^3_{sphere}-D^3_{HSS}}{D^3_{sphere}}\times n_{MG}+\frac{D^3_{HSS}-D^3_{Core}}{D^3_{sphere}}\times n_{glass}+\frac{D^3_{core}}{D^3_{sphere}}\times n_{air}\right\}$$

Where n_{matrix}, n_{MG}, n_{glass} and n_{air} are respectively the refractive indexes of the matrix surrounding the particles, the POEGMA-based microgel and the air. The measures of D_{sphere}, D_{HSS} and D_{core} are the diameters of the hollow silica sphere (HSS) with a MG layer grafted, the diameter of the HSS alone, and the diameter of the air core inside the HSS, respectively. The packing parameter Φ_p is taken at 0.64, corresponding to randomly close packed spheres according to Scott *et al.*[2]

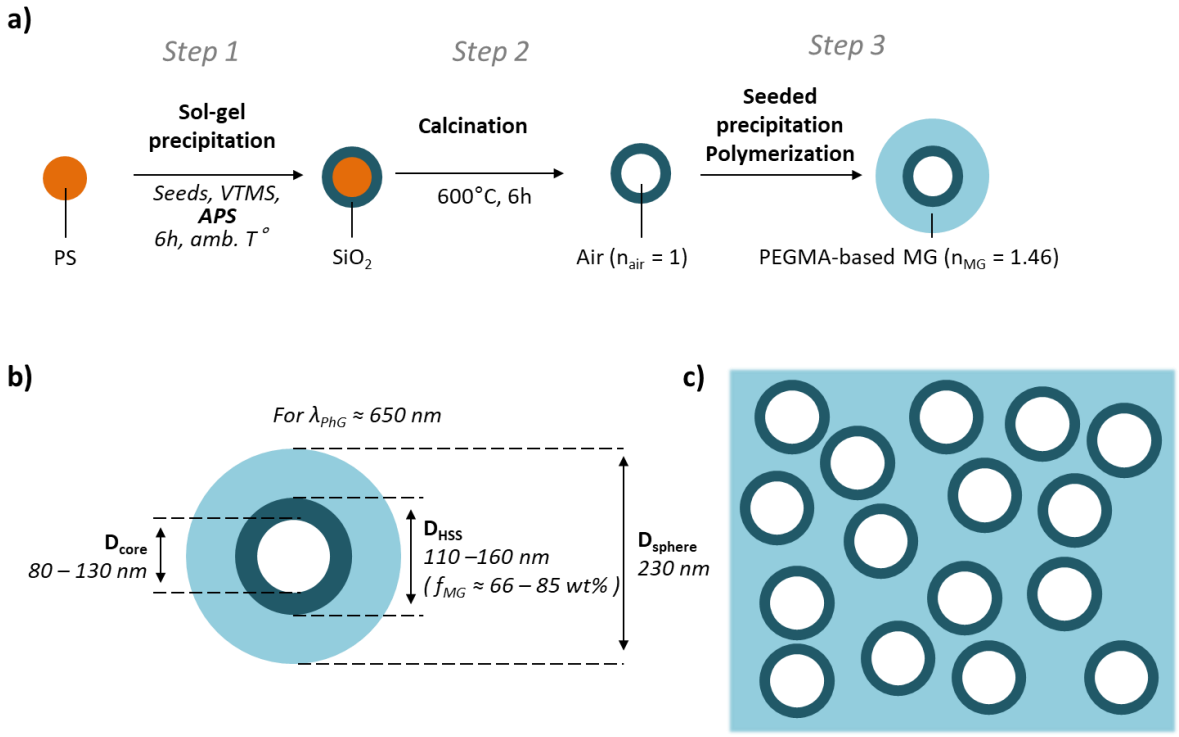

Figure 2 (a) Synthesis plan for the elaboration of HSS with a POEGMA-based shell. (b) Design aimed according, to the work of Kim et al to get a photonic glass with associated with a wavelength of around 650 nm.

According to the equations developed above, a design of photonic glass can be achieved integrating the multi-responsive POEGMA-based microgel (MG). The corresponding colloidal object targeted are HSSs, with controlled silica thicknesses and core diameters, surrounded by a MG layer with controlled thicknesses at the collapsed state. Such objects were aimed through a synthesis protocol involving

three critical steps. The first one is the actual grafting of a SiO_2 layer on PS spheres, with a precise control on the silica thicknesses. The second step rely on the effective formation of hollow silica spheres, thanks to a controlled calcination of the PS@SiO_2 spheres to remove the PS templates, without degrading the SiO_2 shell. Finally, the third step consists in the grafting of the MG layer. Each of these steps are critical in the sense they can dramatically impact the size polydispersity value of the colloid. Even if Kim *et al.*[1] showed that a control of the dispersity promotes the formation of the photonic glasses, a too high size dispersion could inhibit the production of coherent scattering, and so reduce the structural color intensity.

The next section focuses on the production of hollow silica sphere suitable for the elaboration of the targeted colloidal design.

2. Hollow Silica Spheres

The two first and critical synthesis steps are studied through the production of two series of samples, with different sizes of PS templates and expected thickness of silica. The synthesis methods of these objects are described in the following lines.

Polystyrene beads (core)

Materials: Styrene (S – from Sigma-Aldrich); Sodium Dodecylsulfate (SDS – from ABCR); ethylene glycol dimethyl acrylate (EGDMA – from Sigma-Aldrich); potassium persulfate (KPS – from Sigma-Aldrich).

The PS cores are produced from the emulsion polymerization of S with EGDMA, similarly to the protocol exposed in previous chapters. Before use, the inhibitors contained in the all commercial monomers are removed through mixing with an adapted inhibitor remover provided by Sigma-Aldrich, and filtering. The total amount of crosslinker is calculated to keep a molar ratio of $\frac{n_{EGDMA}}{n_S+n_{EGDMA}} = 5\ mol\%$. The surfactant (SDS) concentration is controlled, according to the targeted core size, here between 100 – 200 nm (Appendix 1). The final solid content - SC_{th}, considering a conversion rate of 100%, is adjusted with water to keep $SC_{th} = 6.0 \pm 0.5\ wt\%$.

Here, in 1.5 liter 3-neck rounded bottom beaker set up with a thermostat and a mechanical stirrer, 650 g of MiliQ water and 0.426 g (1.5 mmol) or 1.163 g (4.0 mmol) of SDS were mixed, according to the aimed size. Successively, 42.636 g of styrene (409.3 mmol) with 4.057 g of EGDMA (20.4 mmol) were added into the reactor. The mixture was then stirred at 300 rpm for 45 min under bubbling nitrogen gas while the temperature was increased to 70 °C. After 45 min and once the set temperature was reached, a degassed aqueous solution of KPS (0.1930 g (0.7 mmol) / 10 mL) was injected into the reactor. The reaction was stopped after 4 hours by opening the reactor to air and cooling the mixture to ambient temperature.

PS cores surrounded by a SiO_2 layer (PS@SiO_2)

Material: vinyl trimethoxysilane (VTMS- from Sigma-Aldrich), aqueous solution of NH_3 at 28 wt% (Sigma-Aldrich)

The mass of VTMS is adjusted according to the mass ratio of aimed shell material with respect to the mass of core-shell material (f_{shell}^{mass}). This mass ratio is controlled with the corresponding volume ratio of shell against the core-shell volume (f_{shell}^{volume}).

Equation 1

$$f_{shell}^{mass} = \frac{m_{shell}}{m_{core} + m_{shell}}$$

$$f_{shell}^{vol} = \left(1 + \frac{d_{shell}(1 - f_{shell}^{mass})}{f_{shell}^{mass} \times d_{core}}\right)^{-1}$$

Equation 3

This volume fraction of shell material is used as an experimental tool, targeting a theoretical diameter D^{th} for the produced core-shell particles.

$$D^{th} = \frac{D_{seed}}{\left(1 - f_{shell}^{vol}\right)^{\frac{1}{3}}}$$

Equation 2

Where D_{seed} is the seeds' diameter approximated for convenience as the measured hydrodynamic diameters by DLS, m_{shell} is approximated as the mass of VTMS and m_{core} is the mass of dried seeds. The densities d_{shell} and d_{core} corresponds respectively to the glass (2.2 g/cm^3) and PS (1 g/cm^3).

From the PS cores, core-shell particles with a theoretical size of 328 nm and 182 nm are aimed. The seed concentration is kept constant at 1 wt% in the reactor. The protocol is inspired from Kim *et al.*[1]

Briefly, in a rounded flask of 250 mL, 16 g of raw PS suspension are diluted with the corresponding $m_{water-1}$ mass of water and m_{ammon} mass of ammonia solution at 28 wt% are stirred at 300 rpm. In parallel, the adapted mass of VTMS, m_{VTMS} and mass of water $m_{water-2}$ are vigorously mixed for at least 30 minutes or until the mixture become completely homogeneous. The hydrolyzed VTMS aqueous solution is then injected quickly in the seeds' suspension and let under stirring for at least 12 hours.

Table 1 Proportion of material used, according to the seeds and the mass fraction of shell material aimed

Dh (seeds) (nm)	f_{shell}^{mass} **(wt%)**	$m_{water-1}$ **(g)**	m_{ammon} **(g)**	m_{VTMS} **(g)**	$M_{water-2}$ **(g)**
178	89	86.468	10.906	8.291	62.179
109	80	66.064	10.178	7.685	57.638

2.1. ***Polystyrene@Silica spheres***

The distribution of the hydrodynamic diameters corresponding to the obtained particles were analyzed by Dynamic Light Scattering (DLS).

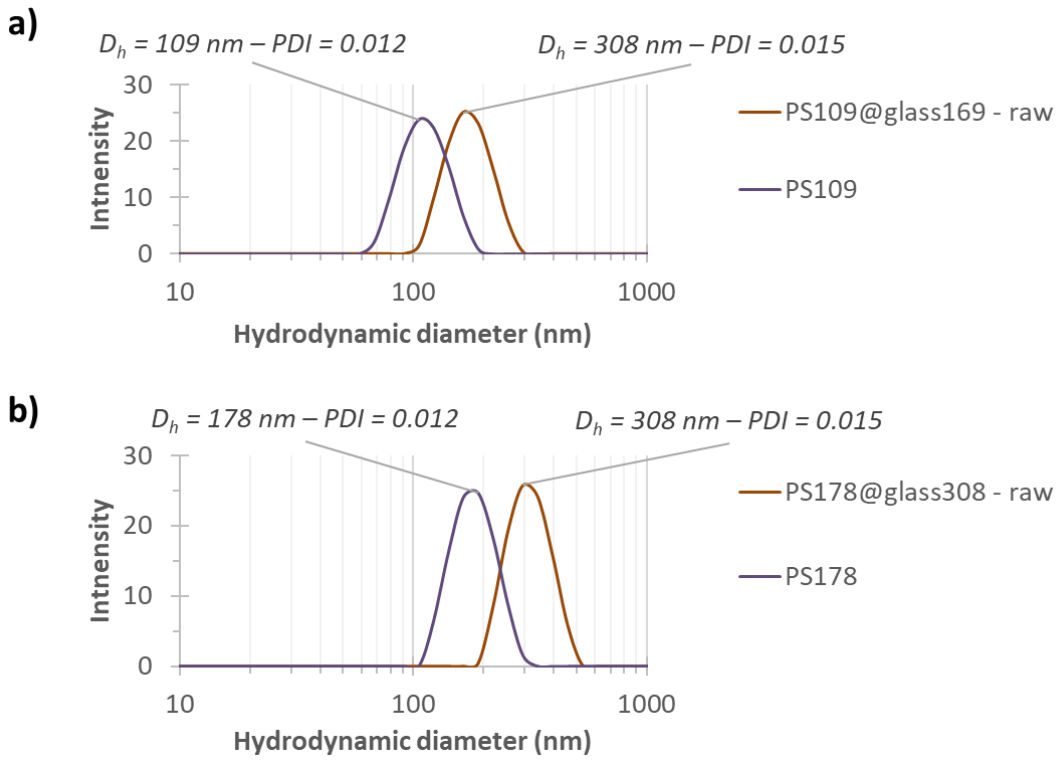

Figure 3 Hydrodynamic diameters distribution before and after the grafting step of a silica layer on PS beads. (a) and (b) referring two different series of PS templates

Whatever the samples analyzed, the grafting step induce an increase of the hydrodynamic diameters. The size dispersions, evaluated by the corresponding polydispersity indexes (PDI), are not affected by the synthesis of the silica shell. The colloids are monodispersed, with no significant evidences of secondary nucleation of silica beads. Even if the grafting step seems satisfactory, the microscopic observation of the objects can confirm the effective achievement of core-shell particles.

The Transmission Electron Microscopy (TEM) images of isolated particles give a direct observation of the core-shell structure. The samples were prepared from raw suspensions diluted roughly to 1 mg/mL, drop casted on TEM grids and let drying for at least 6 hours. The PS particles are compared to their corresponding PS@SiO_2 particles.

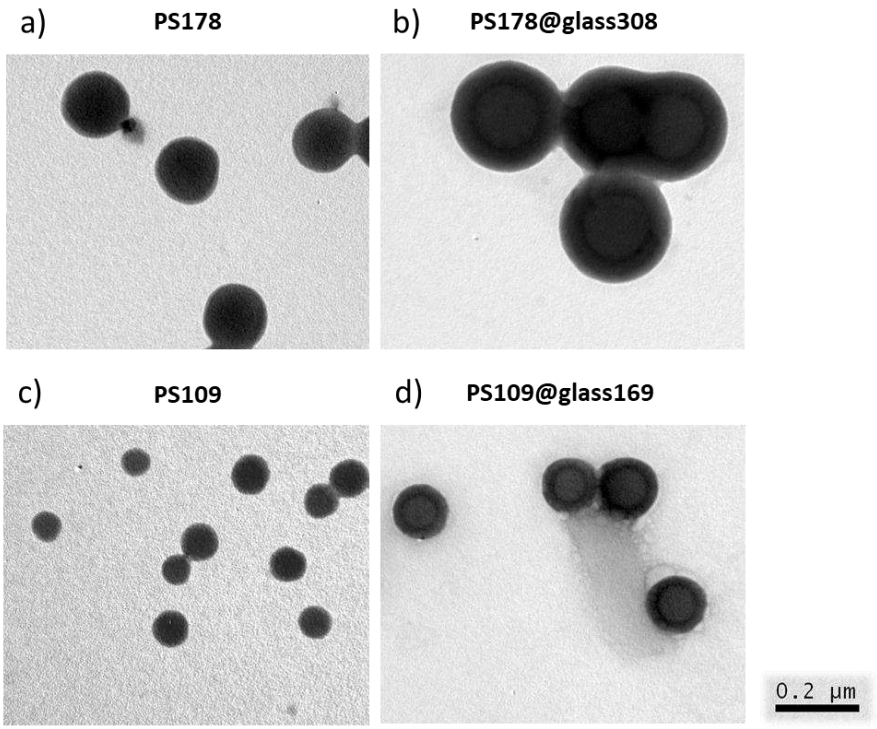

Figure 4 Images from Transmission Electronic Microscopy of PS (a & c) and PS@SiO_2 (b & d) spheres. The digits indicate the hydrodynamic diameter of the corresponding PS or PS@SiO_2 spheres.

Similarly, with DLS results, the both PS@SiO_2 particles show a significant size increase from 156 ± 4 and 90 ± 11 nm for their PS seed homologues to 270 ± 6 and 153 ± 7 nm, respectively. As the silicon atoms have a higher number of electrons than carbon ones, the silica glass highly absorbs the electron beam and appears darker on the images (Figure 4*d*). In consequence, the shell appears darker than the PS cores, confirming the effective conception of core-shell particles. The grafting rate of the silica is a critical parameter to control the architecture of the final particles. Several methods are used to evaluate this grafting rate. The first one considers the final dimensions of the particles by comparison with the expected size.

According to the Equation 2, the theoretical shell thickness can be estimated from the hydrodynamic diameter of the seeds used and the mass proportion of shell against the core used experimentally. This theoretical shell thickness is related as the ideal case where 100% of the hydrolyzed VTMS is effectively condensed at the surface of PS particles. The shell thickness thus is evaluated as

the $t_{shell} = \frac{1}{2}(D_{core-shell} - D_{core})$; where $D_{\text{core-shell}}$ is the averaged hydrodynamic diameter of PS@SiO_2 particles. The SiO_2 thicknesses are also measured from TEM images (Figure 5*a*). The measured shell thickness is finally compared to theoretical diameters with theoretical mass grafting rate of 100 wt% and 75 wt%

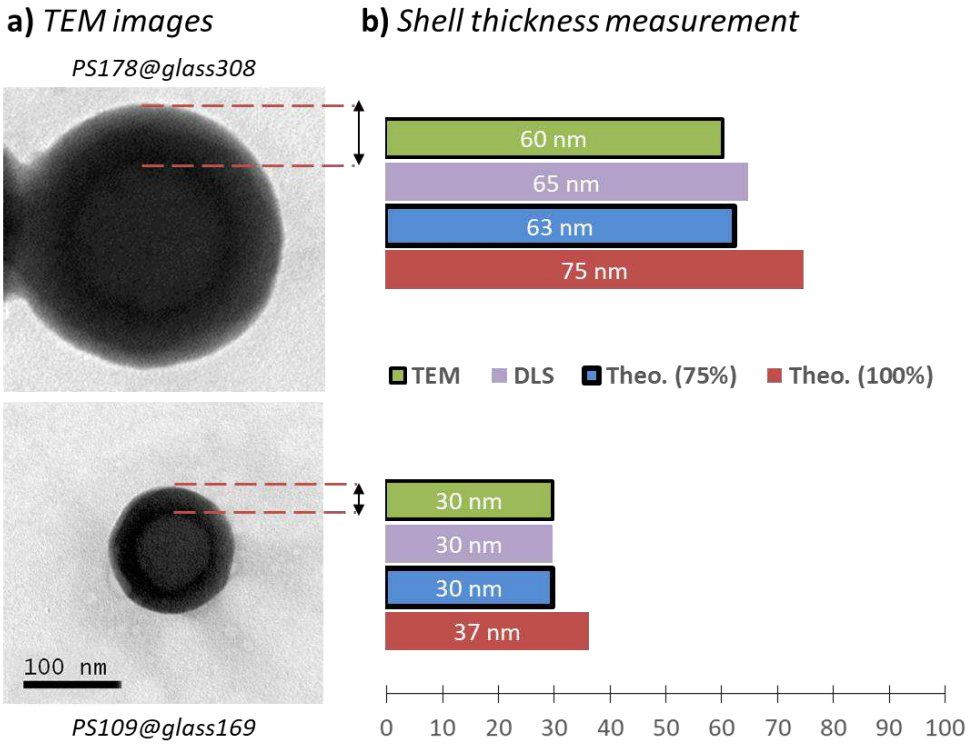

Figure 5 (a) Zoom on TEM image of two different series of PS spheres with a shell of SiO_2 (PS@glass). (b) Shell thickness measurement according to TEM and DLS technics, compared to theoretical grafting rate at 75 wt% and at 100 wt%.

The shell thickness measurements by TEM agree with the DLS ones. The shell thickness is systematically below the theoretical thickness for 100 wt% of shell grafting. However, comparable theoretical thicknesses are found with a theoretical grafting rate of around 75 wt%.

Nevertheless, the TEM images confirm the effective grafting of a silica shell, with a thickness close to an apparent grafting rate around 75 wt%. According to the DLS results, the colloidal particles are roughly monodispersed and open the way to the next critical step: the removal of the PS template.

2.2. Calcination: Hollow Silica Spheres formation

The PS template aimed for the design of the targeted colloids is made through an emulsion polymerization. It is used without purification for the synthesis of PS@SiO_2 particles., meaning surfactants are still present in the core-shell suspensions. The removal of the core through successive solvent wash thus isn't a realizable solution. The solvent carrying the template polymer would not be separable from the HSSs[3]. In this context, another solution consists in eliminating the organic template by calcination.

The calcination is usually developed in the literature at this end, taking advantage of the thermal stability of the shell formed by sol-gel precipitation against the organic template. One way to produce such hollow silica spheres from suspensions require firstly the solvent elimination by freeze-drying[4]. The purpose of freeze_drying is to inhibit the close interaction of suspended silica colloids that could otherwise continue to condense on each other, especially with centrifugation or classical solvent evaporation methods. This first freeze-drying step was performed with raw suspensions firstly degassed at 250 mBar for 48 hours at 40 °C to promote the NH_3 evaporation. The degassed suspensions were controlled by DLS to insure the absence of aggregate formation during the degassing process, in the opposite of the centrifugation/redispersion method in the conditions explored (Figure 6)

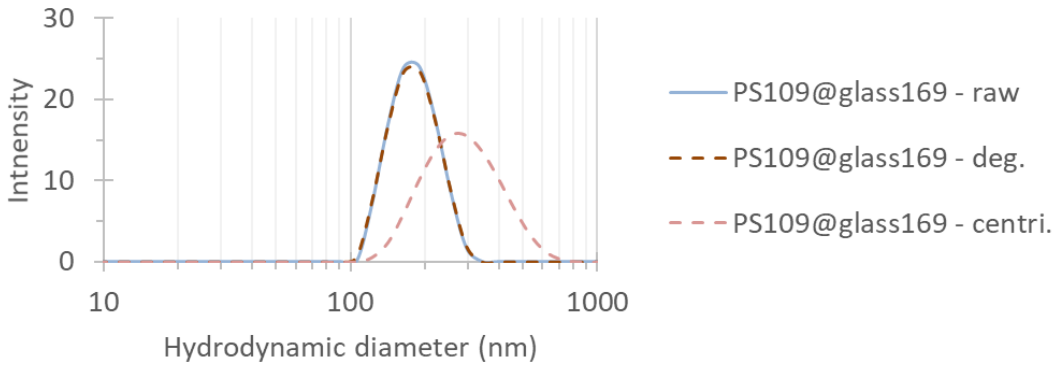

Figure 6 Evolution of the hydrodynamic diameters' distribution of PS@SiO_2 spheres from raw suspensions, degassed suspensions at 250 mbar for 48 hours at 40 °C, and purified PS@SiO_2 by three centrifugation/re-dispersion cycles at 10k rpm for 5 minutes.

The degassed suspensions were then plunged in liquid nitrogen until complete freezing, A successive freeze-drying was performed for 4 to 5 days, until complete drying of the material. The powder obtained was successively heated at 1 °C/min to 600°C for 6 hours and was let cooling overnight. The control of the heating rate is fundamental because a fast heating of the colloidal particle leads systematically to rupture of the shell and heterogeneous silica residue.

The HSSs were dispersed in absolute EtOH and were sonicated for 10 minutes. Samples for TEM observations were prepared from those suspensions diluted roughly to 1 mg/mL. The suspensions were then drop-casted on TEM grids and dried in ambient conditions for at least 4 hours (Figure 7).

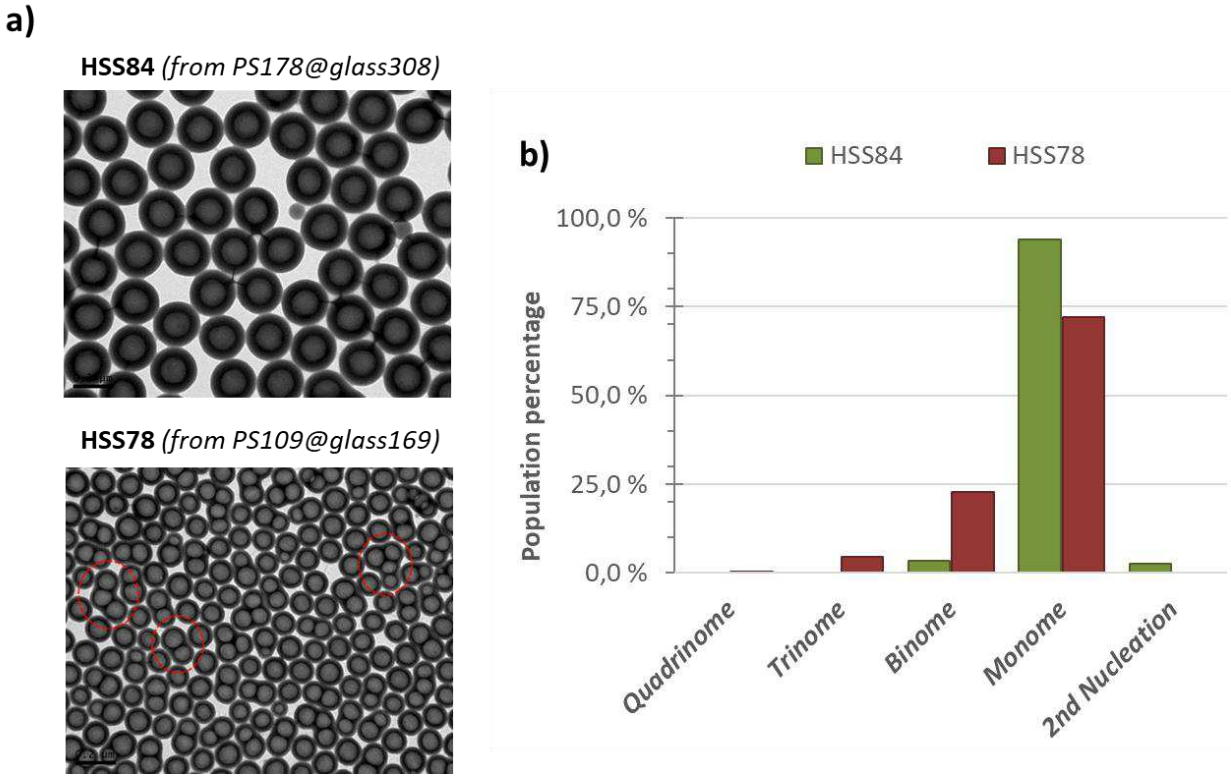

Figure 7 (a) TEM images of produced HSS spheres from the two series of PS@SiO_2 spheres. (b) Evolution of the number of cores by particle One, two, three, four cores by particles being here called monomes, binomes, trinomes or quadrinomes and are shown with red circles. The particles without cores are designed as providing from a 2nd nucleation. The evaluation of the population distribution was done on at least 100 particles for each set of particles.

The TEM images show the effective elaboration of hollow silica spheres (Figure 7*a*). The silica layer appears darker and contrast with the lighted air core for both particles' series. Some smaller particles are identified as traces of secondary nucleation of silica during the previous sol-gel precipitation. Moreover, traces of particles with more than one cavity are identified with both series of HSSs (Figure 7*a* – *see HSS78 for illustration*).

A higher sol-gel condensation of the silica can be achieved at high temperature. This phenomenon occurring between 200 and 800 °C can promote the covalent bonding of the annealed particles and merging them into bigger particles/aggregates. This phenomenon can contribute to the formation of colloidal objects where more than one cavity may exist. These particles are noted as "binomes"," trinomes" or" quadrinomes" according to the number of cavity existing, respectively 2, 3 or 4 and are opposed to "monomes" with only one cavity

per particles[5]. An estimation of their distributions was evaluated from a population of at least 100 particles and approximatively 94 % and 72 % of monomes were calculated for PS178@glass308 and PS109@glass169, respectively (Figure 7*b*).

The distinction of the core/cavities against the silica shell offers the opportunity to correlate the measured dimensions at each step of the HSS elaboration, and highlight the sizes evolution, step by step.

The comparison of the core and core-shell diameters by TEM confirms firstly the current correlation between the size of the PS template and the cores diameters of the PS@SiO_2 particles for both series. However, the cavities and core-shell diameters of HSSs endure an apparent contraction (Figure 8).

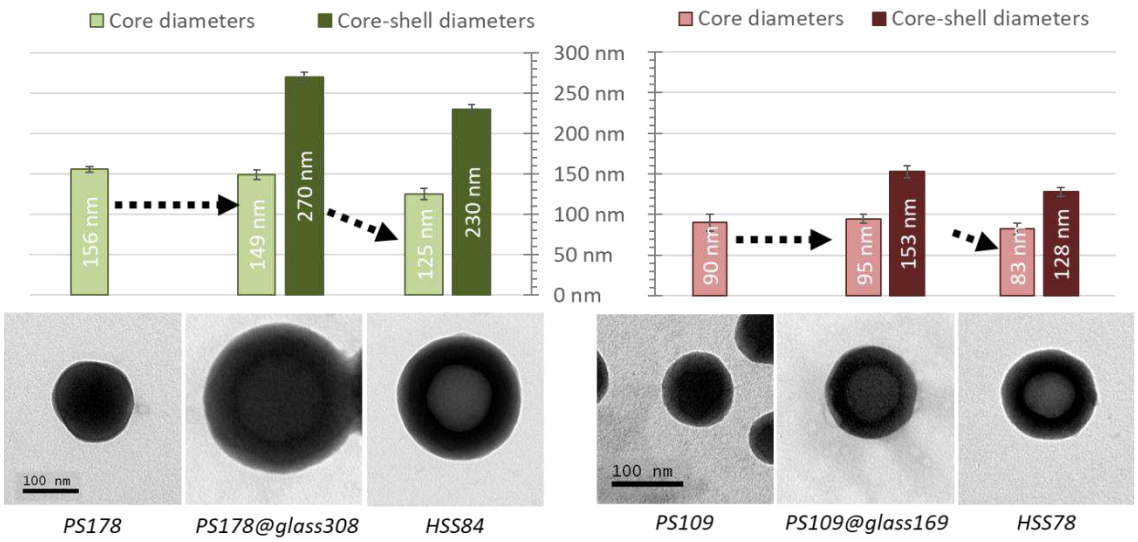

Figure 8 Measurement from TEM images of core diameters and core-shell diameters for each PS, PS@SiO_2 and HSS corresponding to each set of samples.

The core-shell particles diameters decrease from 270 nm to 230 nm and 153 nm to 128 nm after calcination. Their cores turn into cavities with smaller dimensions, from 149 nm to 125 nm and from 95 nm to 83 nm, respectively. The condensation of the silica at high temperature include a water loss that could induce a volume loss of the particle after annealing. A peculiar attention is brought on the evolution of the measured core diameters, core-shell diameters, and shell

thickness on particles before and after annealing. The purpose is to fully evaluate the impact of the annealing treatment on final particles (Figure 9*a*).

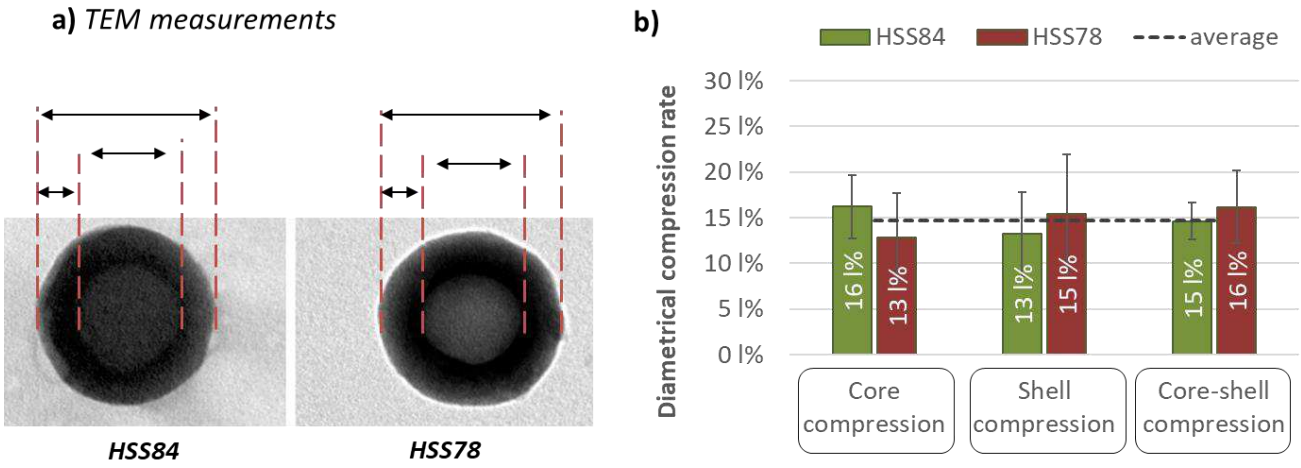

Figure 9 (a) Zoom on HSS images displaying the measurement of a core diameter, an overall core-shell diameter and the silica thickness. (b) Comparison of compression rate with respect to the measurement of PS@$_{SiO2}$ for each set of particles.

The comparison of the measured dimensions before and after annealing display a homogenous compression of the evaluated distances with respect to their initial size. The compression of approximatively 15 l% is common for both series.

The dimensions by TEM are finally coherent with those obtained by DLS. However, the agreement of both measurements is apparent only with size distribution normalized in function of the number of particles. As a reminder, scattering intensity of particles is proportional to D_h^6, where the hydrodynamic diameter of the particle is noted D_h. In other terms, the average size is significantly impacted by the increase of polydispersity index, shifting artificially the peaks toward higher sizes. Figure 10 displays the hydrodynamic evolution of the HSS78 series, made from the small PS templates (PS109).

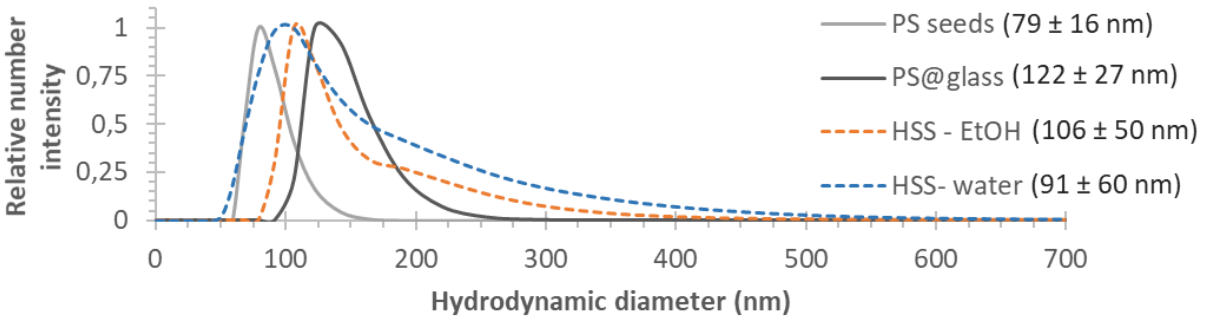

Figure 10 DLS measurement of hydrodynamic diameters of the colloids produced from the PS109 series. The signal is normalized

The evolution of the size distribution stays coherent with the previous analysis, with firstly a shift toward higher D_h values after the silica grafting step, then a contraction of the hydrodynamic diameter after the annealing. The sizes indicated correspond to the maximum of the number intensity, the standard deviation is taken as the half of the full width at half maximum.

A significant widening of size distribution is observed for HSS spheres. This widening remains coherent with the formation of aggregates during the calcination step, due to the condensation between silica spheres. The redispersion of the calcinated particles in EtOH or water leads to similar size distribution, even if the size distribution appears weaker with EtOH. This difference doesn't appear significant by comparison with the overall size distributions.

3. Microgel grafting on silica surface

The next step exposed in the global strategy to achieve HSS surrounded by POEGMA-based microgels is the effective grafting of this last layer on the silica surface. The grafting step is evaluated by convenience on full silica spheres made by classical Stöber sol-gel condensation.

First of all, the synthesis of silica spheres with sizes close to the HSS spheres are produced. According to the Bragg-Snell equation a hypothetical diffraction wavelength of 600 nm can be produced from ordered particles of SiO_2 spheres with a diameter close to 170 nm and a volume percentage of microgel of 75% in the core-shell particles (Figure 11). It is worth noting that the arrangement considered

is here by default a classical FCC structure, with a diffracted wavelength induced by (111) reticular plans.

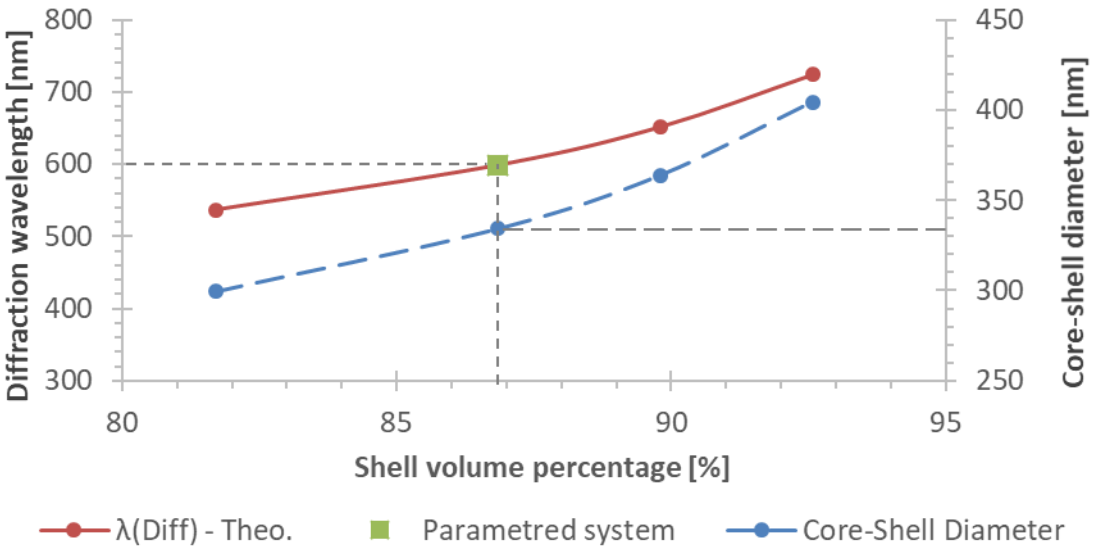

Figure 11 Evolution of the estimated core-shell diameter with 75 wt% of grafting rate, and the associated wavelength of (111) plans in the case of a FCC crystalline lattice, according to the Bragg-Snell equation.

Consecutively, the synthesis of SiO_2 spheres surrounded by 75% in volume of POEGMA material may lead to colloids with an estimated diameter around 334 nm. The self-assembly of these objects into a photonic crystal may theoretically give rise to a diffraction wavelength at 600 nm.

The synthesis of such structure was thus attempted to evaluate simultaneously two distinct phenomena: firstly, evaluate the grafting of MG on silica surface with the minimum of synthesis steps and confirm the impact of a low refractive index differences between the core and shell materials in photonic crystals. Indeed, according to the Mie theory, the scattering intensity depends on the refractive index difference between the scattering colloids (core) and its environment (matrix made from the shell). An absence of refractive index difference should induce an absence of scattering and so no perceptible diffracted wavelength.

3.1. ***Silica size control***

The first step of this study consists in the formation of Silica beads with a controlled diameter. According to the work of Greasley *and al.*[6], the size of the

particles made from a Stöber sol-gel condensation follows a linear relation with the ammonia concentration and the concentration of ethanol (EtOH), water and tetraethoxysilane (TEOS) in the reactive media (Figure 12*a*). This linear relation between the ammonia and the particle size was experimentally demonstrated in the concentration range among 0 and 0.5 mol/L of ammonia.

Two first attempts with ammonia concentrations of 0.109 and 0.245 mol/L were made to trace the linear relation corresponding to our experimental set-up and determine thus the concentration needed for a targeted diameter between 160-190 nm. The concentrations of EtOH, water and TEOS are fixed at 16.295 ± 0.094, 1.022 ± 0.099 and 0.129 ± 0.001 mol/L, respectively. Figure 12*b* represents the corresponding calibration curve integrating the third attempt, with an ammonia concentration of 0.183 mol/L giving rise to SiO_2 particles with an average hydrodynamic diameter of 174 nm. The hydrodynamic diameters distribution of each synthesis is associated with a polydispersity index below 0.04, testifying of monodisperse suspensions.

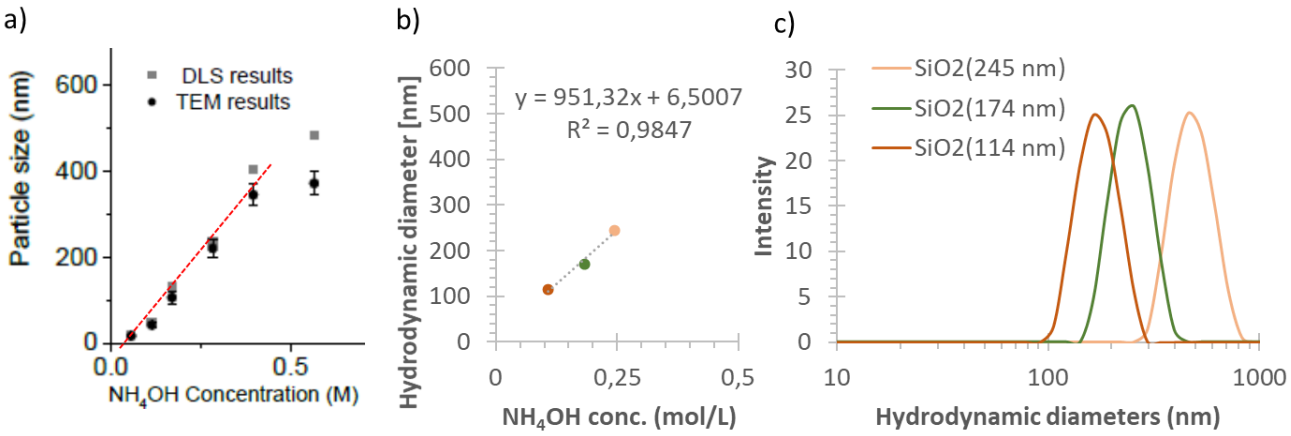

Figure 12 (a) Evolution of the SiO_2 spheres sizes in function of the ammonia concentration, with fixed proportion of EtOH, water and TEOS during the sol-gel condensation. Adapted from Greasley and al.[6] (b) Experimental variation of the SiO_2 spheres with molar concentration of EtOH, water and TEOS respectively of 16.295 ± 0.094, 1.022 ± 0.099 and 0.129 ± 0.001 mol/L.

The produced silica spheres with an average D_h of 171 ± 4 nm, used as experimental model for the grafting step of the POEGMA-based layer on silica can be described briefly as follow:

Material: tetraethoxysilane (TEOS – Sigma-Aldrich), ammonia aqueous solution at 28 wt% (Sigma-Aldrich)

In a 1 L rounded bottom beaker, 558.4 g of ethanol were firstly mixed with 16.43 g of aqueous solution of ammonia at 28 wt% and 0.849 g of water for at least 10 minutes under vigorous stirring performed here by a magnetic stirrer at 300 rpm, at ambient temperature. Successively, 20 g of TEOS was quickly injected in the mixture, and let under stirring for at least 6 hours.

The produced silica beads were then successively used for a first grafting attempt, without any surface modification, counting on the hypothetical reactivity of the silanol surface function possibly activated in presence of radicals[7]. The produced silica sphere was used after 3 centrifugation/redispersion in MiliQ water at 10k rpm for 5 minutes. Each redispersion was carried with vigorous agitation and sonication for at least 10 minutes each. The tested POEGMA-based microgel grafting step can be described as follow:

This protocol theoretically leads to a dispersion with a final solid content of 4.0 ± 0.3 wt%. The monomers are prepared to keep a OEGMA/MEO_2MA ratio of 10 mol%, a MAA/(OEGMA + MEO_2MA) ratio of 5 mol%, a crosslinker/monomers ratio of 1.92 mol% and a initiator/vinylic molecules ratio of 0.86 mol%. The shell proportion is adjusted with the seed dispersion quantity, for a fixed masses of shell monomers. Consecutively, core-shell particles with expected proportion of 75 wt% of shell material in the solid content (f_{MG}) are produced.

Material: diethylene glycol methyl ether methacrylate (MEO_2MA), oligo ethylene glycol methyl ether methacrylate (OEGMA – $M_w = 475\ g.mol^{-1}$), methacrylic acid (MAA); oligo ethylene glycol diacrylate (OEGDA – $M_w = 250\ g.mol^{-1}$) and potassium persulfate (KPS). All the materials are provided by Sigma-Aldrich.

In 250 milliliter 3-neck rounded bottom beaker set up with a thermostat and a mechanical stirrer a controlled 34.175, of purified seeds' dispersion – initial solid content of 1.7 wt% – was degassed under nitrogen gas, stirred at 300 rpm and heated up to 70 °C. In parallel, two mixtures were prepared. The first one, the monomer

aqueous dispersion, made with 0.100 g (0.1 mmol) of MAA, 5.000 g of MiliQ water, 4.000 g (21.3 mmol) of MEO_2MA, 1.010 g (2.1 mmol) of OEGMA and 0.122 g (0.5 mmol) of OEGDA. The second mixture was an aqueous solution of KPS (0.0583 g (0.2 mmol)/ 5 mL). Both were degassed for at least 15 minutes. Once the reactor was at the right temperature and after at least 45 minutes of nitrogen bubbling, the reactants were injected with a controlled injection speed thanks to an automated push-syringe, at 120 ml/h. Once the injection was completed, the seeded polymerization was let to occur for 6 hours, then stopped by cooling the mixture and by opening the reactor to the air.

The suspensions lead to unstable particle dispersion segregating quickly in the bottom of a vial (Figure 13*a*). In other terms, the grafting process leads to the formation of heavy aggregates that can be caused by a predominant phenomenon of secondary nucleation or/and by the formation of a colloidal network during the POEGMA polymerization.

The strategy set up to answer this identified graft issue was to promote the bonding of the MG on the silica through the introduction of polymerizable functions. As it appears in Figure 13*b*, the suspensions obtained through the same grafting protocol gives apparently more stable suspensions at identical solid content.

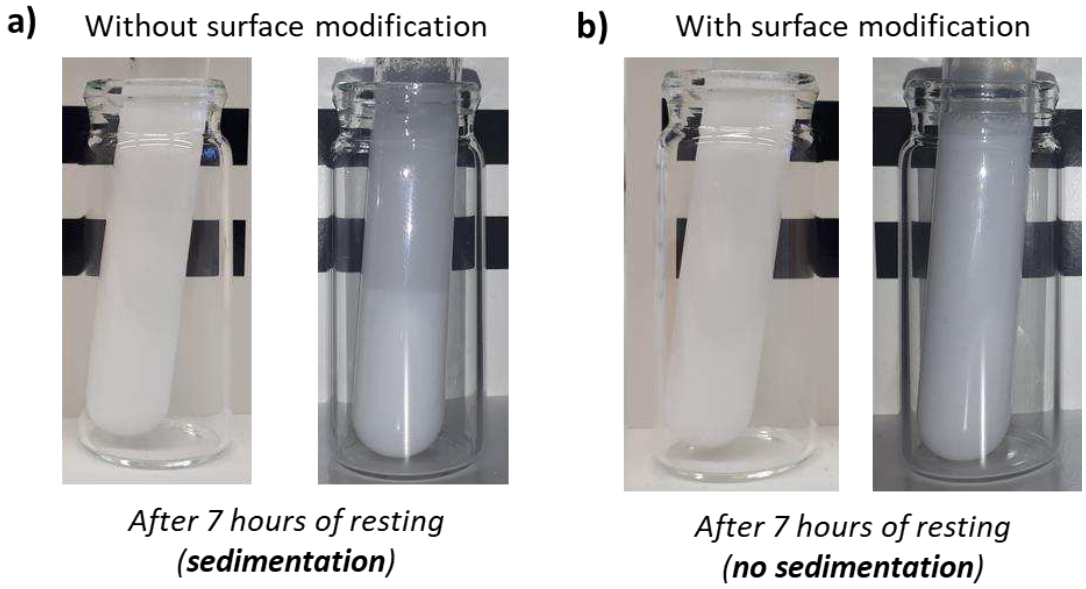

Figure 13. Macroscopic evaluation of the suspensions stability of silica spheres treated after a grafting step of POEGMA-based microgel. The silica spheres were treated without (a) or with (b) a surface modification step.

The next sections develop the studies to control the silica surface modification, then detail the colloids after the MG grafting step from surface modified silica.

3.2. ***Silica surface modification***

The target was to assure the surface modification of the silica sphere with a controllable surface density to allow further experiments. The surface modification of silica sphere was inspired from Inoubli *et al.*[8] who used 3-methacryloxypropyltrimethoxysilane (MPS) to introduced polymerizable vinylic function on the beads surfaces. The surface modification was performed consecutively to the synthesis of the silica beads. The mass of MPS was controlled to keep a mass ratio with respect to the dried mass of silica beads around 3/1.

The hydrodynamic diameters of the surface particles are compared to their corresponding bare silica beads (Figure 14*a*). A slight increase of the averaged D_h is observed for surface modified particles, from 176 ± 22 nm (PDI = 0.015) to 181 ± 36 nm (PDI = 0.04). In spite of this apparent average difference, the standard deviation remains too high to proof itself the actual presence of MPS particles at the surface of the colloidal particles. The spreading of the size distribution toward

the larger sizes can indicate the formation of some aggregates formed during the surface treatment. Indeed, the presence of three silanol functions in the MPS molecule allow the crosslinking of the particles, even if those events may remain disadvantaged because of the low concentration of particles during the MPS grafting, around 1 wt%.

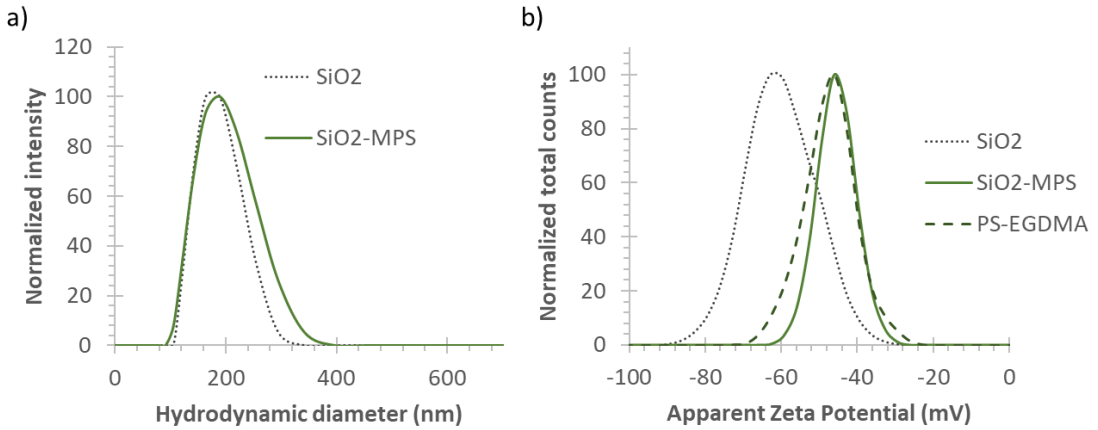

Figure 14 (a) Hydrodynamic diameter distribution of silica and corresponding surface modified spheres. (b)Evolution of the apparent Zeta potential extrapolated from the measurement of the electrophoresis mobility by DLS.

In contrast, the evaluation of the apparent zeta potential by DLS display a significant shift of the charge surface on colloids (Figure 14*b*). The zeta potential was performed from raw suspensions, diluted to approximatively 1 mg/mL. In this context, the charge surface on raw silica colloidal spheres and modified silica are compared with PS-EGDMA spheres. The apparent zeta potential appears lower than its organic analogs, with -63 ± 13 and -46 ± 7 mV, respectively. This difference appears coherent with literature[9]: the maximal charge surface density for silica spheres is around 5 charges/nm^2, according to the measured surface density of silanol functions. In contrast, the charges of our PS beads are considered as brought mainly from the ionic initiator used during the emulsion polymerization. The maximal charge surface density of PS particles (d_c^{PS})can thus be calculated from the particles concentrations (N_{part}):

$$N_{part} = \frac{SC \times 6}{\pi \times d_{PS} \times D_h^3}$$

$$d_c^{PS} = \frac{C_{KPS} \times 2 \times N_a}{4\pi \times \left(\frac{D_h}{2}\right)^2 \times N_{part}}$$

Where SC is the particle solid content (kg/L), d_{PS} is the PS density (kg/L), D_h is the hydrodynamic diameter (m), C_{KPS} is the concentration of KPS used for the particle polymerization and N_a is the Avogadro number (mol^{-1}). According to this equation, the maximal charge surface density for our organic particles is approximatively four time lower than SiO_2 particles, with a density among [0.8 – 1.0] charges/nm^2. Surface modification of the silica beads shift the apparent Zeta potential to a similar value, testifying of a modification of the particles' surfaces.

Thermogravimetric analyses offer a more accurate evaluation the surface modification achievement, with a quantitative evaluation of the molecular surface density (Figure 15). At this end, the suspensions were purified by 3 centrifugation/redispersion cycles before being analyzed.

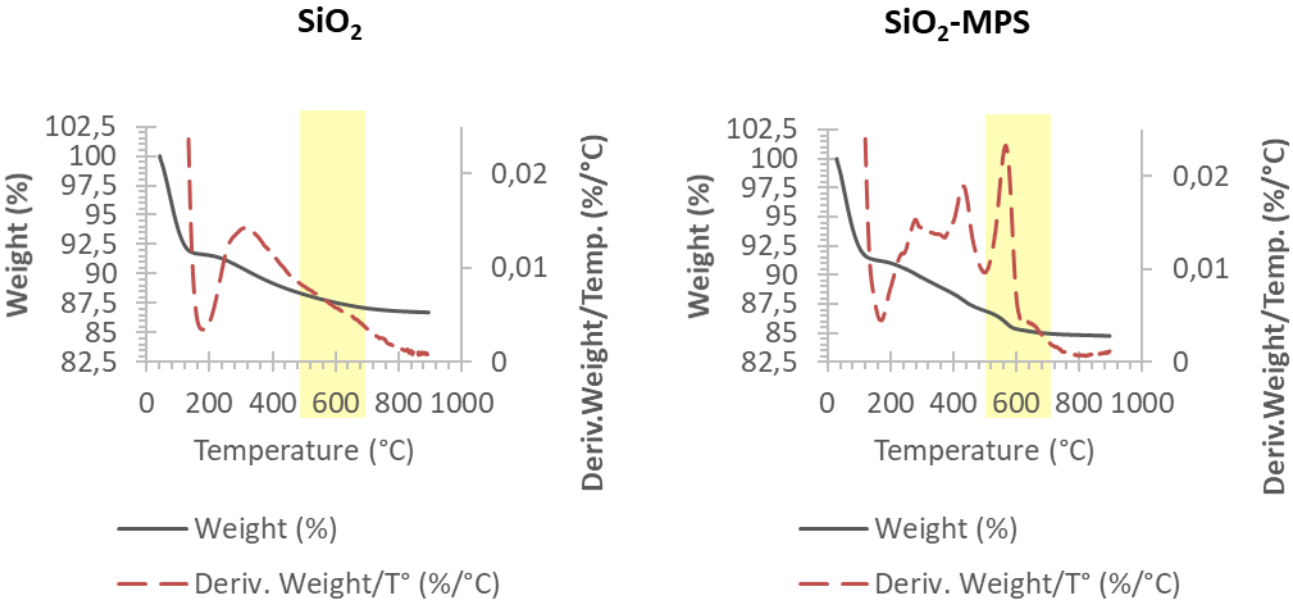

Figure 15 Thermograms from TGA of purified spheres of SiO_2 and surface modified SiO_2 spheres with 3-(Trimethoxysilyl)propyl methacrylate (MPS). The surface density of MPS aimed is indicated between brackets, accordingly to the proportion of MPS used during the surface modification protocol.

Indeed, according to the thermograms obtained from the calcination of dried suspensions, the surface modified particles shows a degradation peak related

to the degradation of grafted MPS molecules in the 450-650 °C range[10]. Both samples were heated at the same heating rate (10°C/min) to 1000 °C to assure a complete degradation of the organic molecules, and a complete condensation of the silica. The identification of the MPS degradation gives rise to the following analysis for the MPS quantitative evaluation.

The MPS surface density (σ) is here expressed in function of the number of particles calcinated:

$$\sigma = \frac{n_{MPS} \times N_a}{\pi \times D_{seed}^2 \times N_{part}} \qquad N_{part} = \frac{m_{SiO_2} \times 6}{\rho_{SiO_2} \times \pi \times D_{seed}^3}$$

Where n_{MPS} is the molecular quantity of calcinated MPS (mol), D_{seeds} is the diameter of the silica beads(m), ρ_{SiO_2} is the density of the silica(g/cm^3) and m_{SiO_2} is the mass of calcinated silica beads (g).

The molecular surface density of MPS can thus be expressed as:

$$\sigma = \frac{m_{MPS}}{m_{SiO_2}} \times \frac{\rho_{SiO_2} \times N_a \times D_{seed}}{M_{MPS} \times 6} \qquad \begin{cases} m_{MPS} = m_{tot} \times wt_{MPS} \\ m_{SiO_2} = m_{tot} \times wt_{SiO_2} \end{cases}$$

Where M_{MPS} is the molecular weight of fully hydrolyzed MPS (206.35 g/mol), m_{MPS} is the mass of hydrolyzed MPS calcinated, m_{tot} is the total calcinated mass (g), wt_{MPS} and wt_{SiO_2} are respectively the mass fraction of MPS and silica respectively

$$\sigma = \frac{\boldsymbol{wt_{MPS}}}{\boldsymbol{wt_{SiO_2}}} \times \frac{\rho_{SiO_2} \times N_a \times D_{seed}}{M_{MPS} \times 6} \times 10^{-14}$$

initially calcinated. It gives rise to the following equation, expressing the molecular surface density in molecules/nm^2

The surface density depends thus essentially of the $\mathbf{wt_{MPS}/wt_{SiO_2}}$ ratio, measurable by TGA. Figure 16 presents the analysis of the thermograms of silica and surface modified silica beads to get these values.

The inconvenient of the MPS degradation/weight loss is that it happens simultaneously with the water loss due to the condensation of the silica at high temperature, producing a a unique readable weight loss (wt_{loss}). The reading of the weight fraction of silica is thus encrypted: the proportion of water loss during the

silica condensation must be known (wt_c) to identify proportions of $\mathbf{wt_{SiO_2}}$ and $\mathbf{wt_{MPS}}$.

At this end, the thermogram of a bare silica beads allow to identify wt_c in function of the mass of fully condensed silica (wt_{SiO_2-c}). It is assumed here that for a population of monodispersed particles with a defined size, $wt_c/wt_{SiO_{2-c}}$ is constant. This constant is then used to estimate the proportion of masse loss due to the degradation of MPS (wt_{MPS}) against the proportion of initial silica (wt_{SiO_2}).

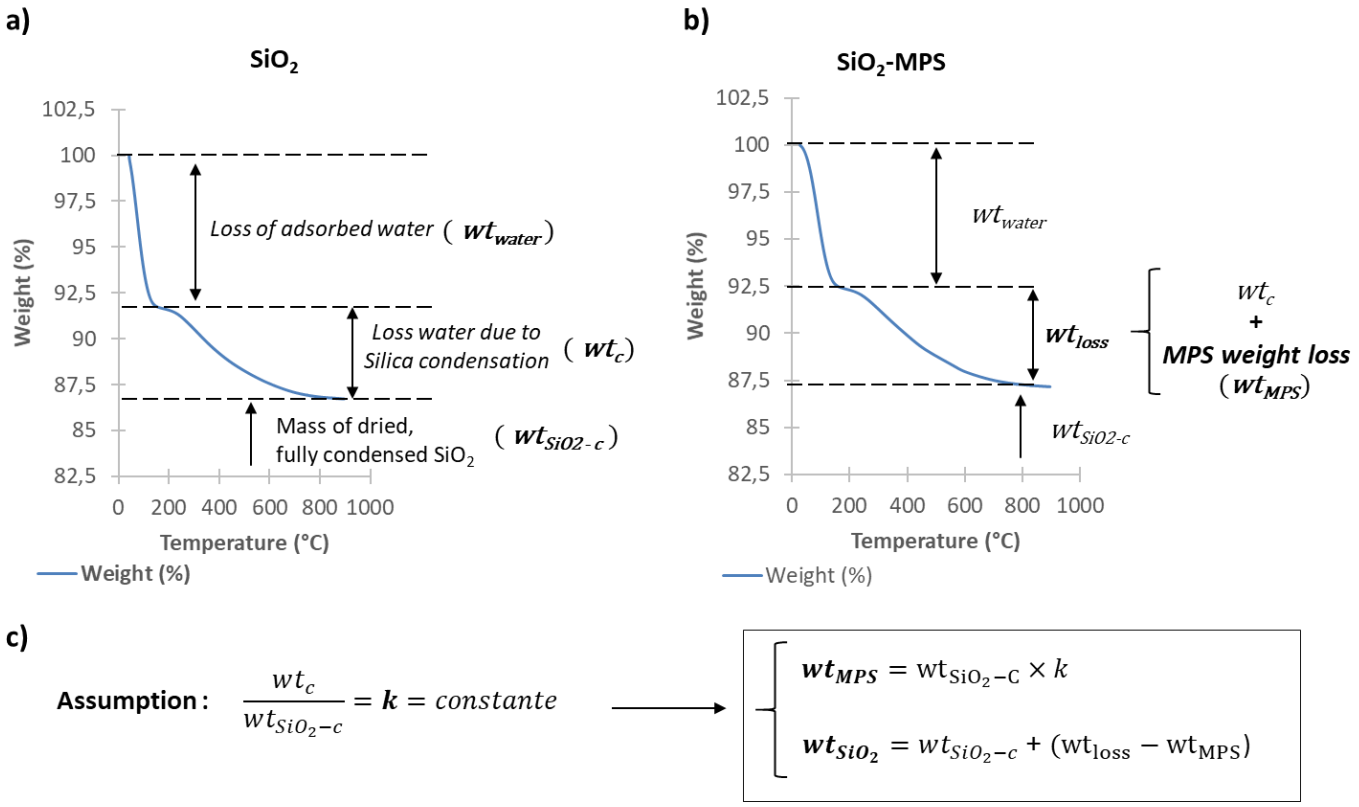

Figure 16 Analysis of thermograms from TGA, identifying the loss of waster adsorbed or due to silica condensation and the residual mass of condensed silica (a) of pure silica spheres, compared to purified functionalized SiO_2 spheres with MPS (b). (c) The normalization of the water loss due to silica condensation allow the identification of mass loss corresponding to the MPS degradation and to uncondensed silica spheres.

This analysis offers a quantitative estimation of the molecular MPS surface density, with a value approximatively to 3.1 molecules/nm^2. However, due to the three silanol functions of MPS monomers, there is a non-negligible probability that the molecules grafted on the surface can be organized into patches, or thin layer.

Nonetheless, the evidences of surface modification brought by Zeta potential evaluation and TGA measurement comforted the decision to attempt a MG grafting attempt on these model colloids.

3.3. *Microgel shell grafting attempt on surface modified particles.*

The MG grafting attempt was performed according to the protocol described p.197, where the bare silica seeds were replaced by the modified particles. The apparent improved colloidal stability of the suspensions indicates the production of at least less aggregates: indeed, a sedimentation is still observed after 24 hours. Moreover, the DLS measurement performed led to correlograms indicating large settling particles. However, the supernatant after 24 hours of rest remains still trouble, indicating the presence of smaller particles, more stable in suspensions, and presenting a refractive index difference with the solvent to scatter light, but here again no reliable size distribution was achievable.

However, the particles in the supernatant were observed by AFM, to determine if at least some core-shell particle were formed during this grafting step. In this context, the supernatant was gathered and let to dry on PS substrate set on heating plates at 40 °C to form dried films. In parallel, the suspensions were diluted to approximately 1 mg/mL and drop-casted on cleaned silicon wafers to visualize isolated particles.

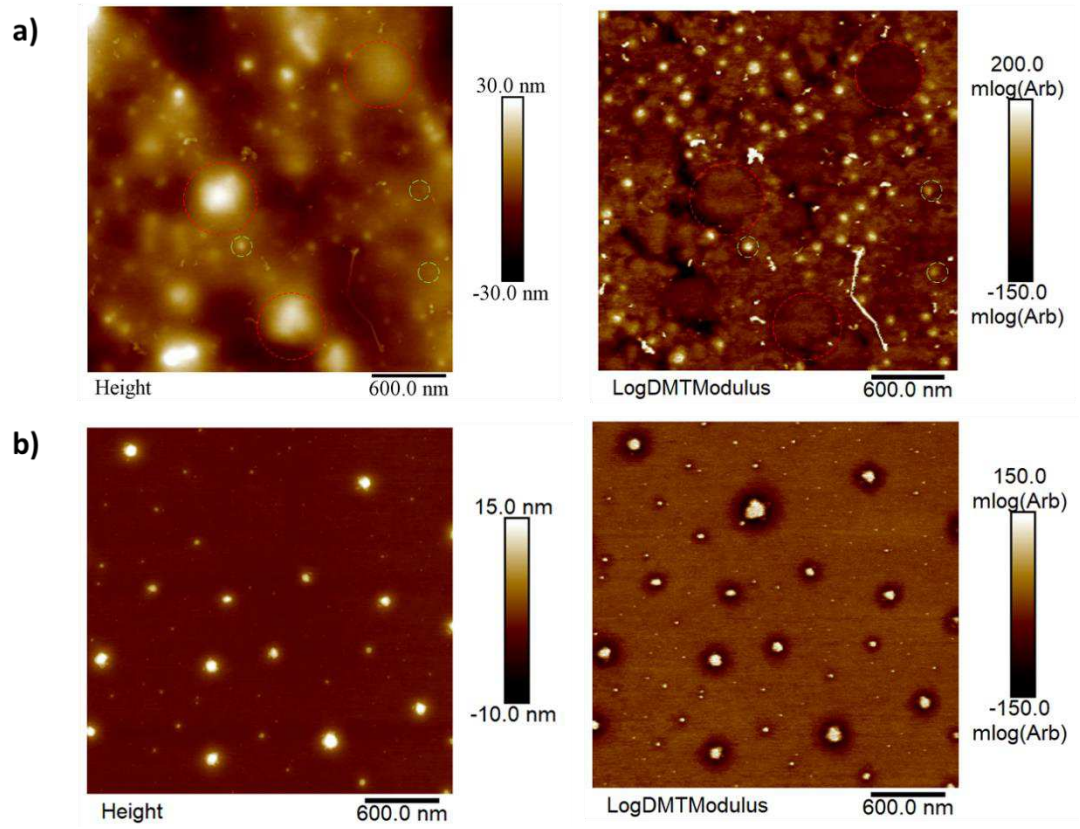

Figure 17 AFM images with contrast in function of the topography of the surface (left) or the stiffness of the surface (right). (a) Film made from an attempt of SiO_2@MG particles suspension. The red circles indicate the presence of big microgels particles whereas the green circles show the hidden small particles of glass, according to their rigidity. (b) Observation of isolated particles from purified SiO_2@MG particles' suspensions

The AFM images of the film surface (Figure 17*a*) show the presence of at least two different kind of colloids: big soft particles and hard smaller beads. The size of the big soft particles reminds the size of POEGMA-based microgel synthesized in classical precipitation polymerization, with an apparent diameter close to 400 nm. In contrast, the hard and smaller particle can be identified as the silica sphere embedded in its POEGMA matrix, due to their apparent higher rigidity. Their size appears slightly smaller than what could be expected to the measured hydrodynamic measurement (D_h = 180 nm), but could be caused by the matrix hiding the circumference of the embedded silica spheres.

The images of isolated particles display particles with sizes more in adequation with the hydrodynamic measurement of the silica seeds (Figure 17*b*). Interestingly, the AFM images with the surface contrast depending on the surface

rigidity show the presence of apparent core-shell particles, made of a hard core (whiter) and surrounded by a soft shell (darker).

A zoom on the isolated MG grafted silica spheres is presented with their homologues SiO_2-MPS seeds (Figure 18). It appears clearly the SiO_2-MPS spheres have spherical shapes, with sharp edges. No darkening of the outer part of the particle is apparent, at the opposite of the isolated SiO_2-MPS@MG particles. The whiter, stiffer cores have sizes coherent with the AFM observation of the seeds. Though this darker, softer identified shell can be identified as POEGMA layer, nothing indicates if a covalent bonding actually exists.

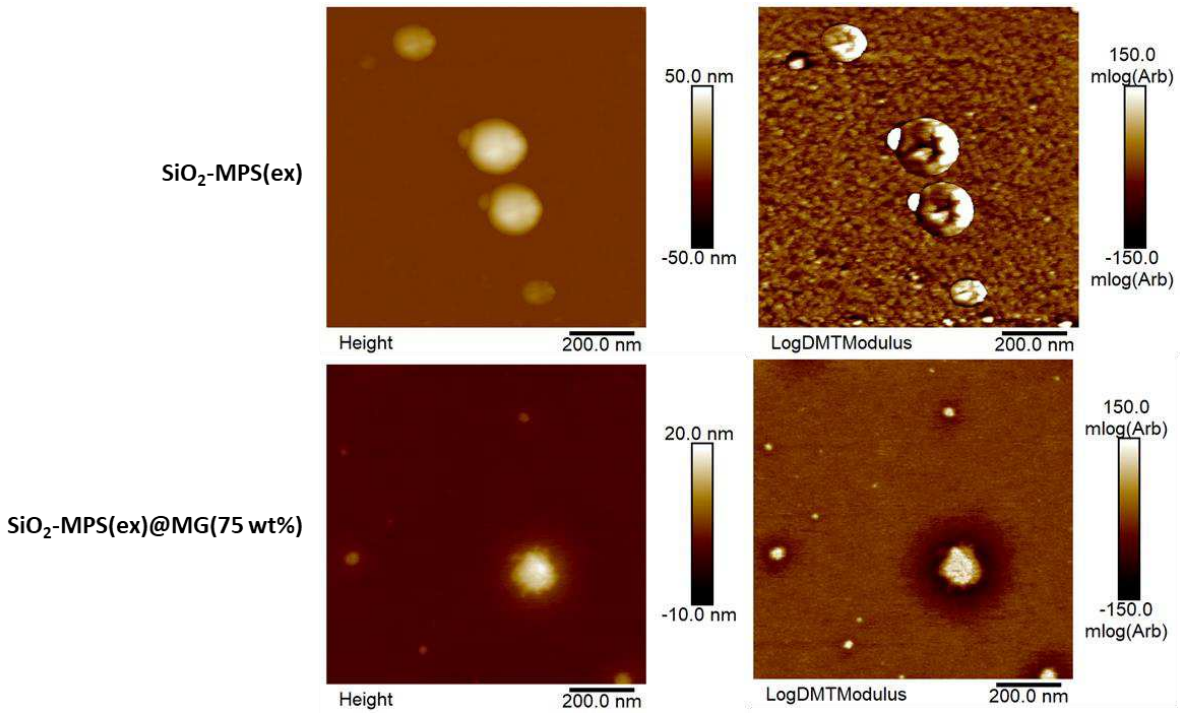

Figure 18 AFM images of isolated particles from purified SiO_2-MPS(ex) before and after the grafting attempt of POEGMA-based microgel shell. The volume fraction of microgel is aimed to be around 75 wt% in the film. On the right, the contrast is displayed in function of the surface topography, whereas on the right, the contrast is according to the surface rigidity.

The MG grafting step leads to the formation of relatively unstable suspensions, with a secondary nucleation of POEGMA-based microgel. However, among the object suspended, core-shell particles are identified, as a promise ensuring the controllable grafting of the multi-responsive and filmogenic layer is achievable with some efforts.

Conclusions

Among the lines of this chapter, an alternative design of colloidal particles is described for the conception of reddish photonic glasses. This design can be simply described as a composite particle, made of a hollow silica sphere, surrounded by a POEGMA-based microgel. The conception of these new colloids is related to at least three critical synthesis steps: (1) the formation of PS particles, surrounded by a controlled thickness of glass by seeded sol-gel precipitation, (2) the controlled calcination of the core-shell particles, achieving hollow silica spheres and (3) the effective grafting of the POEGMA-based microgel on the silica beads.

The two first steps have showed to be achievable, a peculiar attention has been brought on the size evolution of the colloids between each step. An evaluation of the grafting rate of silica material on the seeds by DLS and TEM has confirmed the robustness of the first step. The calcination protocol at a controlled heating rate offers the possibility to remove the PS template without any traces of broken silica hollow spheres, but with an increase of the particle size polydispersity due notably to residual intra/inter silanol condensation at high temperature.

The last step has been experimentally modelled on silica spheres with controlled sizes. Surface modified silica spheres were compared with bare silica particles for the grafting of the MG layer. In both cases, the suspensions obtained leaded to settling suspensions over 24 hours. However, the grafted attempt of MG on surface modified silica spheres leaded to the production of identifiable core-shell particles.

Some supplementary effort remains essential for the actual grafting of a POEGMA-based layer on silica spheres. Nevertheless, the present results pave the way toward the elaboration of this innovative colloidal architecture, lightening the possibility and the challenges to overcome for the conception of red photonic glass for skincare applications.

References

1. Kim, S.-H. *et al.* Inverse Photonic Glasses by Packing Bidisperse Hollow Microspheres with Uniform Cores. *ACS Applied Materials & Interfaces* **9**, 24155–24160 (2017).
2. Scott, G. D. & Kilgour, D. M. The density of random close packing of spheres. *Journal of Physics D: Applied Physics* **2**, 863–866 (1969).
3. Gorsd, M. N., Pizzio, L. R. & Blanco, M. N. Synthesis and Characterization of Hollow Silica Spheres. *Procedia Materials Science* **8**, 567–576 (2015).
4. Kim, S.-H. *et al.* Inverse Photonic Glasses by Packing Bidisperse Hollow Microspheres with Uniform Cores. *ACS Applied Materials & Interfaces* **9**, 24155–24160 (2017).
5. Baaziz, W. *et al.* Thermal behavior of Pd@SiO $_2$ nanostructures in various gas environments: a combined 3D and *in situ* TEM approach. *Nanoscale* **10**, 20178–20188 (2018).
6. Greasley, S. L. *et al.* Controlling particle size in the Stöber process and incorporation of calcium. *Journal of Colloid and Interface Science* **469**, 213–223 (2016).
7. Narayanasamy, J. & Kubicki, J. D. Mechanism of Hydroxyl Radical Generation from a Silica Surface: Molecular Orbital Calculations. *J. Phys. Chem. B* **109**, 21796–21807 (2005).
8. Inoubli, R. *et al.* 'Graft from' polymerization on colloidal silica particles: elaboration of alkoxyamine grafted surface by in situ trapping of carbon radicals. *Polymer* **46**, 2486–2496 (2005).
9. Zhuravlev, L. T. Concentration of hydroxyl groups on the surface of amorphous silicas. *Langmuir* **3**, 316–318 (1987).
10. Florea, N.-M., Lungu, A., Vasile, E. & Iovu, H. The influence of nanosilica functionalization on the properties of hybrid nanocomposites. *High Performance Polymers* **25**, 61–69 (2013).

Conclusion

In this work, we have studied the self-assembly of multi-responsive hybrid microgels spheres. It follows the line of previous works on the self-assembly properties of multi-responsive microgels based on poly(oligo(ethylene glycol) methacrylate)-based microgel. In this context, we raised the following question: *Would it be possible to develop the self-assembly properties of these microgels to make dried photonic crystal, with controllable and responsive interferential colors toward the conception of a skincare application?*

The first chapter reviews the natural photonic assemblies giving structural colors and exposes the fundamental concepts behind the structural coloration: the light scattering and diffraction. The diffraction description from the Maxwell's equation resolution has been compared to the simpler Bragg-Snell approach. This last approach has been identified as an affordable method to estimate the diffracted wavelength from experimental parameters. The size of the building blocks and the refractive indexes of the materials are essential for the control of the optical properties. From there, the presentation of accessible artificial photonic crystal by bottom-up approaches have brought our interest on the opal-like structures. Their formation through self-assembly have been described in the framework of solvent evaporation. In this context, without any external forces the self-assembly mechanism is controlled essentially by convection forces inside the drying suspensions and by surface tension interplaying between the particles and the solvent. The overview of bio-inspired and self-assembled photonic crystals have allowed the selection core-shell colloids as suitable design for making responsive and tunable structural colors. We have aimed the synthesis of hard-core@soft-shell particles made of polystyrene core surrounded by a poly(oligo(ethylene glycol) methacrylate)-based microgel shell. Seeded precipitation polymerization appears as the most accessible synthesis pathway for the conception of core-shell particles. Nonetheless, the synthesis of the shell layer *via* seeded precipitation polymerization is systematically preceded by a constraining purification step of the seeds. The review of the artificial photonic crystals has showed the experimental constraints behind responsive properties, as the mechanochromism. The self-assembled core-shell particles are systematically

(photo-)chemically reticulated to assure the film cohesion and responsivity through mechanical deformation.

The second chapter exposes seeded precipitation polymerization in water without intermediate seed purification to conceive of PS cores surrounded by a POEGMA-based microgel shell. The integration of an interlayer of PBA to promote the microgel adhesion hasn't led to an efficient grafting of the shell. This observation has led to a simplification of the colloidal design, *i.e.* without interlayer. With a peculiar attention on the seed nature and the synthesis method, core-shell particles have been produced with a shell grafting rate around 90 ± 9 wt%, without intermediate purification. This high grafting rate is correlated with the self-assembly quality of the film produced, giving more regular photonic crystals with more intense structural colors.

The third chapter focuses on the self-assembly properties of the colloids. Thanks to its robustness, the synthesis protocol of the core-shell particles allowed the control of the shell thickness, with a constant grafting rate. The alteration of the core/shell balance is a tool to tune the iridescent structural color, according to an aimed diffraction wavelength. These experimental observations have been coherent with theory and have opened the discussion about the crystallin structure of the self-assembly. The particles sizes were correlated with the optical properties of the films to bring forward the "hard sphere"-like self-assembly mechanism of this system. This mechanism is allowed by the thermo-responsivity of the shell and is driven by the convection forces during the solvent evaporation. The films have showed an astonishing tenacity through mechanical deformation, without any (photo-)chemical treatment. This cohesion is due to the visco-elastic properties of the shell, and give rise to an entanglement of the particles after drying. It confers spontaneous mechanochromism properties to the films, then able to color change through deformations.

The fourth chapter presents the works on the transfer of the photonic crystal technology into a skincare/cosmetic formulation. Two points were focused, the impact of essential additives on films' color and the refining of the colloidal suspensions into an applicable product for a consumer. We have pointed out the crucial control of the additive proportion against the quantity of hybrid microgel

to conserve the structural coloration. Above 20-25 wt% of liquid additives in the dried film, the self-assemblies are perturbed and loss their diffraction ability. The increase of the suspension solid content in the scope of an applicable product has led to dramatic conclusions. The rise of the suspensions' viscosity, controlled by the colloidal concentration, inhibit severely the mobility of the suspended objects. Photonic crystals were no more achievable in casting condition relevant for a skincare/cosmetic application. Instead of organized crystals, only blueish films made of disorganized colloidal arrangements were produced, so called *photonic glasses*.

The fifth chapter opens perspectives on the elaboration of photonic glasses made from a new colloidal design. It integrates the poly(oligo(ethylene glycol) methacrylate)-based microgel shell around hollow silica spheres to produce reddish photonic glasses. The first part treats the conception of hollow silica spheres (HSS) by seeded sol-gel condensation and successive annealing. Colloidal HSSs with controllable morphology are achievable, fitting the theoretical dimensions required for the conception of the aimed photonic glass. The second part discuss the actual grafting of the microgel on the colloidal silica through an experimental model with full spheres of colloidal silica. Bare silica and surface-modified silica have been investigated, but only the surface-modified samples have given encouraging results.

In conclusion, the present research work has achieved *the complete conception of hybrid microgels, with a controllable architecture, giving rise to colored films with tunable iridescent coloration and spontaneous mechanochromic properties*. From a fundamental point of view, the self-assembly mechanisms were investigated and have allowed the comprehension of the experimental parameters driving the colloidal crystallization. From an industrial point of view, the junction of the marketable casting conditions with the fundamental knowledge on this system allowed the identification of the self-assembly limits of colloidal objects.

In the perspective of further works, we could envision the development of novel colloidal design, targeting the elaboration of photonic glasses with controllable coloration. One could also aim the fine prediction of the color intensity according to the photonic glasses' thicknesses by Finite Difference Time Domain

involving the Maxwell's equation resolution, and bring critical information on their suitability for cosmetic/skincare application.

Appendices

1. Size control of PS beads through emulsion polymerization

The nucleation step of an emulsion polymerization is critical to control the final size of the colloidal objects. The higher the number of particles, the lower their final diameter. According to Smith-Ewart Theory, the number of particle (N_p) is in particular related to the surfactant concentration (*i.e.* [SDS]). Related to the classical nucleation theory, the modification of the surface energy impact directly the critical size of an emerging nuclei. In one hand, Smith-Ewart exposes $N_p \propto [SDS]^{3/5}$. In the other hand, the number of particles can be estimated considering the volume of monomer used with respect to the diameter of the particles (D_p), giving rise to $N_p \propto D_p^{-3}$. It can be thus estimated a power law relating the surfactant concentration and the particle size, as $D_p \propto [SDS]^{-x}$. In this theoretical context, x is a power factor with a theoretical value of 0.2, but that could vary depending on the nucleation/growth dynamic of the system[1].

With our experimental set-up the control of our seeds' size was performed through successive synthesis at different SDS concentrations. It allowed to calibrate the $D_p \propto [SDS]^{-x}$ equation (figure), with x values for PS-DVB & PS-EGDMA particles respectively of 0.442 and 0.605.

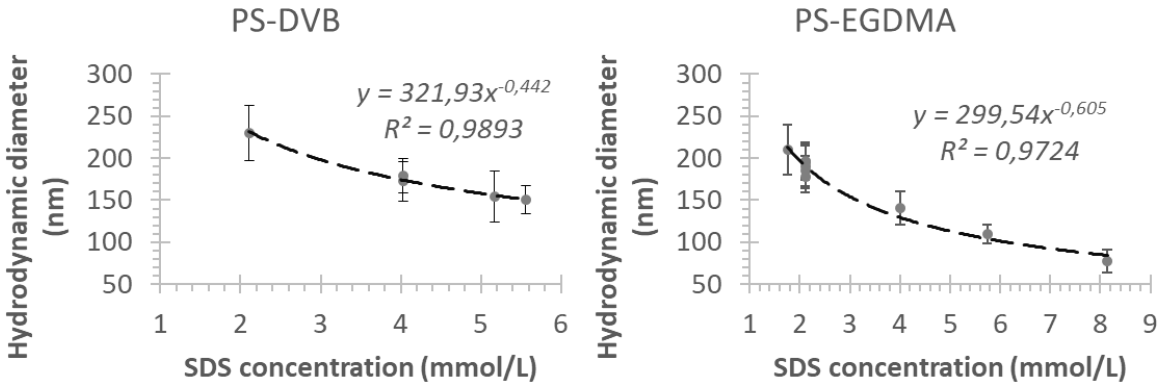

Figure 1 Hydrodynamic diameter of the seeds synthesized, according to the SDS concentration. At the exception of the SDS concentration, each synthesis of PS-DVB or PS-EGDMA series shared the same experimental conditions.

2. Atomic Force Microscopy

The samples were observed through Atomic Force Microscope (AFM) from Brucker© (MultiMode8®), on peak force modes. Each image was taken with a resolution of 512x512. Peak force mods imaging uses a vibrating cantilever.

In peak forces mode, the cantilever oscillates in order to touch the surface punctually with a constant force. The position of the cantilever is adjusted to keep always the same deflection of the laser beam corresponding to a force of 10 pN. Approaches and withdrawals of the tip on the surface allow to get mechanical information about the surface. Through the *Derjaguin-Muller-Toporov* (DMT) model of an elastic contact given below, it is possible to obtain the reduced Young's Modulus, E^* by fitting the experimental retract curve. In this equation, F_{tip} is the force on the tip, F_{adh} is the adhesion force, R is the tip end radius and d is the tip-sample separation. Consecutively, the *log(DMTmodulus)* images propose a representation of the relative variation of reduced Young's Modulus upon the surface.

$$F_{tip} = \frac{4}{3} E^* \sqrt{R d^3} + F_{adh}$$

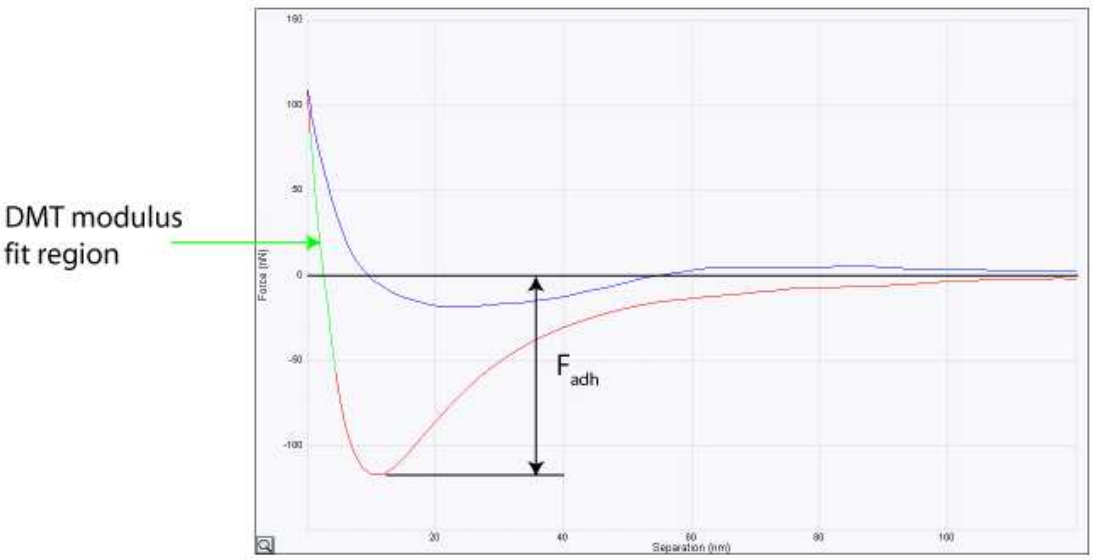

Figure 2. Force vs. Separation plot in peak force mode during the tip withdrawal

2.1. *AFM: tip deconvolution*

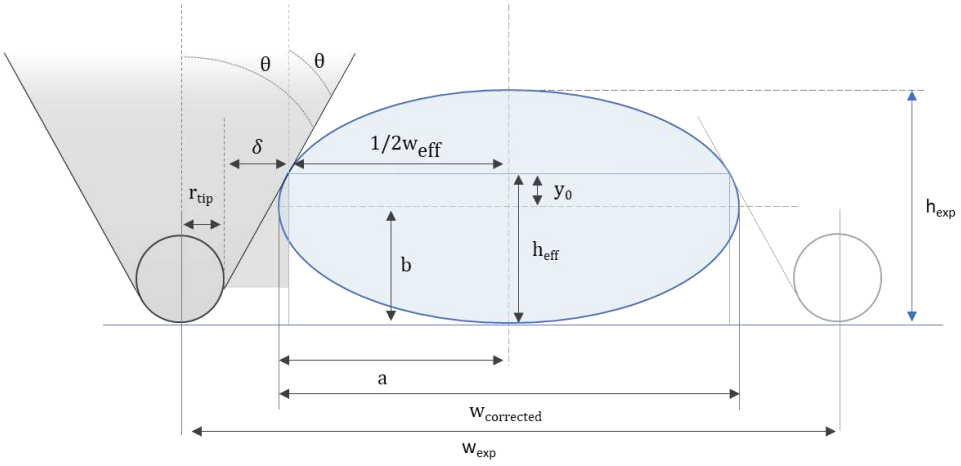

Figure 3 Schematic 2D representation of an AFM tip touching an ellipsoidal particle.

Due to the tip morphology, the images obtained by AFM trend to oversize the lateral dimensions of spherical objects (Figure 3). According to the work of Canet-Ferrer[2], the experimental width measured, w_{exp}, could be corrected to obtained a better evaluation of the size particle, w_{eff}.

$$w_{eff} = w_{exp} - 2(\delta + r_{tip})$$

Where r_{tip} is the radius of the tip's extremity and δ is the lateral distance separating the spherical extremity of tip and the contact point between the sphere and the tip's edge. This last lateral distance δ, can be evaluated considering the tip angle θ and an effective height h_{eff}.

$$\delta = (h_{eff} - r_{tip}) \times \tan(\theta)$$

Here we evaluate the spreading of the spherical object by evaluating the evolution of its width, compared to its height, thanks to section analysis. The particle section is thus modeled as an ellipse, characterized by a major radius, a and a minor radius, b.

Two main problem surround the application of the … method on spherical objects. Firstly, the h_{eff} must be evaluated the most accurately possible. It can be approximated according to the height experimentally measured, h_{exp} such as:

$$h_{eff} = h_{exp} \times \overline{\sigma_h}$$

However, the parameter correcting the height, σ_h, is not constant and depend of itself of the b/a ratio. Secondly, the effective width w_{eff} obtained doesn't consider the curvature of the spherical border, and thus may underestimate the experimental width of the object. Similarly, it can be corrected such as:

$$w_{corrected} = w_{eff} \times \overline{\sigma_w}$$

Here also, the parameter correcting the width σ_w, is a function of the b/a ratio and must be calibrated.

The parameters σ_h and σ_w have been calibrated thanks to the simulation of the contact of tip edges, modelled as affine curves, with ellipsoid sections defined by controlled b/a ratios.

The elliptic and affine functions, respectively y_{part} and y_{tip} was expressed as in a Cartesians (x;y) space:

$$y_{part} = b\left(1 - \left(\frac{x}{a}\right)^2\right)^{\frac{1}{2}}$$

$$y_{tip} = a'x + b'$$

Where a' is the defined according to the tip angle, such as $a' = tan(\theta)$ with $\theta = 12.5°$ and b' is considered as a fitting parameter. Indeed, the point of contact between the tip edge and the border of the particle imply $y_{tip} = y_{part}$. It can be developed as an 2nd degree equation:

$$\left(\left(\frac{b}{a}\right)^2 + a'^2\right)x^2 + 2a'b'x + b'^2 - b^2 = 0$$

The existence of only one contact point imply the 2nd degree discriminant, Δ must be null:

$$\Delta = (2a'b')^2 - 4\left(\left(\frac{b}{a}\right)^2 + a'^2\right) \times (b'^2 - b^2) = 0$$

This last equation defines a success condition for the fitting of b'. Consecutively, a model was designed, with a fixed value for the minor axis of the ellipse, b = 90 nm, and variables values for the major axis, a =

[90;100;110;120;130;140;150;160;170;180]. The b' values was thus fitted so that $\Delta = 0$ for those systems with b/a ratios between 1 and 0.5.

Each contact point was consecutively associated with coordinates (x_0;y_0).

$$x_0 = \frac{-a'b'}{\left(\frac{b}{a}\right)^2 + a'^2}$$

$$y_0 = b\left(1 - \left(\frac{x_0}{a}\right)^2\right)^{\frac{1}{2}}$$

According to the system designed, we obtain $w_{eff} = 2x_0$ and $h_{eff} = y_0 + b$. Consecutively, the parameters σ_h and σ_w are calculated for each b/a values with:

$$\sigma_h = \frac{y_0 + b}{2b}$$

$$\sigma_w = \frac{x_0}{a}$$

The Figure 4 shows the parameters σ_h and σ_w vary linearly with the b/a ratios, with slope coefficient respectively of around 0.11 and -0.04. As the slope are weakly pronounced, we chose to average the correcting parameter within the b/a ratios between the [0.5 - 1] value, giving rise to $\overline{\sigma_h} = 0.577$ and $\overline{\sigma_w} = 0.988$.

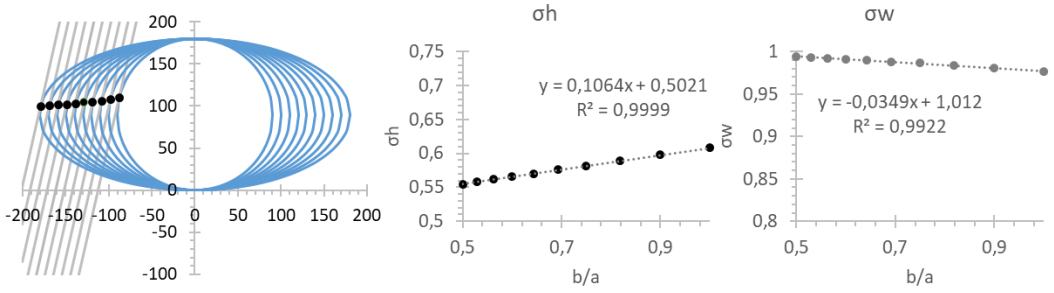

Figure 4 Variation of an ellipsoid particle section with b = 90 nm. The a *radius are between 90 and 180 nm, by step of 10 nm. Each black dot represents the calculated contact point between the edge of the tip (gray lines), according to the b/a ratios. Corresponding σ_h and σ_w are represented.*

3. FTIR-ATR analysis details

The FTIR spectroscopy quantification analysis obey to Beer-Lambert's law:

$$Abs(i) = \varepsilon_i \times l_i \times c_i$$

With *Abs(i)*, the measured absorbance of a chemical function, characterized by its extinction coefficient ε_i (m^2/kg), l_i (m) the thickness investigated through FTIR-ATR analysis and its concentration in the material c_i (kg/m^3).

Relative quantification consists in comparing an absorbed signal of a target, for instance named *Abs(i),* to a constant reference, for instance *Abs(j).* The ratio of interest, called $r_{i/j}$ can then be expressed as:

$$r_{i/j} = \frac{Abs(i)}{Abs(j)} = \frac{\varepsilon_i}{\varepsilon_j} \times \frac{l_i}{l_j} \times \frac{c_i}{c_j}$$

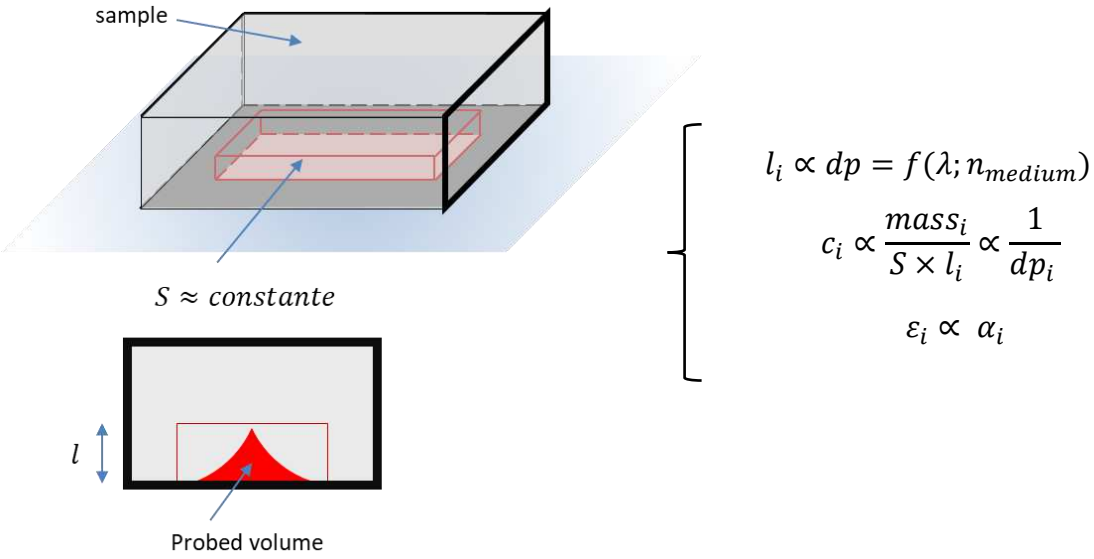

Figure 5 Schematic representation of the probe volume in a FTIR-ATR experiment. The open bracket expresses the dependence of the Beer-Lambert parameters with the depth penetration of the incident IR beam, and the polarizability on the chemical function.

From a practical point of view, the relative quantification search to relate for instance a mass ratio of two different compound and the corresponding *r(i/j)* ratio.

In such case, the mass information is integrated in the concentration parameter of the Beer-Lambert law. In such case, the concentration of the chemical function probed can be related to the mass of the associated chemical compound

against the volume probed by the IR beam. With ATR, the volume probed can be expressed as function of the contact surface between the set-up crystal and the sample S, supposed constant, and the depth penetration (dp). The depth penetration is directly related to the thickness investigated in classical Beer-Lambert's law (l_i) and can be expressed as a function of the refractive index of the medium, n_{medium} and the wavelength of the incident light, λ. Concerning the coefficient extinction of the chemical function probed (ε_i), it can be related to the polarizability of the chemical function, α_i.

We assume then the absorbance ratio $r_{i/j}$ can be related to the following equation:

$$r_{i/j} = \frac{Abs(i)}{Abs(j)} = \frac{m_i}{m_j} \times \tau^{\varepsilon}_{i/j} \times \tau^{l}_{i/j} \times \tau^{c}_{i/j} = \frac{m_i}{m_j} \times K_{i/j}$$

Where $\tau^{\varepsilon}_{i/j}$, $\tau^{l}_{i/j}$ and $\tau^{c}_{i/j}$ are respectively constants related to $\frac{\varepsilon_i}{\varepsilon_j}$, $\frac{l_i}{l_j}$ and $\frac{c_i}{c_j}$ ratios. As the polarizability in intrinsic to a chemical function, the first term shouldn't be significantly altered whatever the i/j proportion and may be assumed quite firmly as constant. However, the two other terms depend on the depth penetration of the beam and so on the average refractive index of the material. The average refractive index depends on the composition of the material. Those two last terms can thus be impacted significantly by the i/j ratio. That's why a calibration curve remain indispensable to assure that a linear relation exists effectively between the absorbances ratio, and the masses ratio.

4. Dynamic light scattering

The polydispersity and the average particle diameter are obtained from a Zetasizer nano ZS from Malvern Instruments. In the following sections, the fundamental equations of dynamic light scattering (DLS) analysis are briefly presented.

4.1. *Autocorrelation function*

Due to their size close to the wavelength, particles interact with light and scatter. This scattering decrease in intensity over time due to the Brownian motion

of particles. The dynamic information of the particles can be extract by the analysis of the second order auto-correlation curve whose the expression is:

$$g^2(q;\tau) = \frac{<I(t)I(t+\tau)>}{<I(t)>^2} \qquad \text{Equation 1}$$

In the *Equation 1*, $g^2(q;\tau)$ is the autocorrelation function at the second order, at a particular wave vector, "q" and delay time "τ". "I" is the scattered intensity and "t" the time variable.

The first approach is to treat the first order autocorrelation function as a single exponential decay. This treatment is appropriate for a monodisperse population.

$$g(q;\mathrm{r}) = \exp(-\Gamma\tau) \qquad \text{Equation 2}$$

In this *Equation 2*, "Γ" is the decay rate. The coefficient diffusion "D" is directly derived from this parameter at a single angle or at a range of angles depending on the wave vector "q"

$$\Gamma = q^2 D \qquad \textit{Equation 3}$$

With "q", a function of "η_0"the refractive index of the sample, "λ" the incident laser wavelength, and "θ" the angle which the detector is located with respect to the cell sample.

$$q = \frac{4\pi\eta_0}{\lambda}\sin(\frac{\theta}{2}) \qquad \textit{Equation 4}$$

4.2. *Strokes-Einstein relation*

The coefficient diffusion is usually exploited through the Stokes-Einstein equation to determine the hydrodynamic radius, R_h of the spherical particles. The *Equation 5* is a function of k_B, the Boltzmann constant, T the temperature, D the coefficient diffusion and η, the dynamic viscosity of the solvent.

$$R_h = \frac{k_B T}{6\pi D\eta} \qquad \textit{Equation 5}$$

4.3. *Cumulant method: description of the Z-average value*

The Cumulant method is a common method which consider the polydispersity of the system. It allows to obtain D_z, the average hydrodynamic diameter of the particles which can be expressed as below:

$$D_z = \frac{\sum I_i}{\sum \frac{I_i}{D_i}} \qquad \textit{Equation 6}$$

The *Equation 6* is a function of I_i, the scattered intensity of the particle *i,* and the radius of this particle, R_i.This interpretation appears as a reliable method to consider particles size fluctuation. Also, the following hydrodynamic results will always be presented as a result of this method.

5. Mie scattering: simulation

The scattering of particles is simulated the behavior of spherical particles into a medium. The software MiePlot developed by Philip Laven allow easily generate spectrum of scattered intensity in function of its wavelength. The particles diameter, refractive indexes of the medium and of the particles can be fixed, according to the nature of the system.

References

1. Chern, C.-S. *Principles and Applications of Emulsion Polymerization*. (John Wiley & Sons, Inc., 2008)..
2. Canet-Ferrer, J., Coronado, E., Forment-Aliaga, A. & Pinilla-Cienfuegos, E. Correction of the tip convolution effects in the imaging of nanostructures studied through scanning force microscopy. *Nanotechnology* **25**, 395703 (2014).